MAGNETIC AND MATERIAL LIMITER DISCHARGES IN TOKAPOLE II

by

RICHARD ALAN MOYER

A thesis submitted in partial fulfillment of the
requirements for the degree of

Doctor of Philosophy
(Physics)

at the
UNIVERSITY OF WISCONSIN - MADISON
1988

MAGNETIC AND MATERIAL LIMITER DISCHARGES IN TOKAPOLE II

Richard Alan Moyer
Under the supervision of Professor Stewart C. Prager

Disruptive instabilities have been studied in Tokapole II, a small poloidal divertor tokamak, in magnetic and material limiter configurations. In the magnetic limiter configuration, the divertor separatrix defines the tokamak current channel boundary. Limiters or neutralizer plates are not used to remove plasma in the scrape-off region. The relatively hot, dense plasma in the scrape-off region carries 5-20% of the current. In the material limiter configuration, limiter plates are inserted to the separatrix to remove plasma and current in the scrape-off region. The plates vary the tokamak current channel boundary condition in a controlled manner, and provide a benchmark for comparison with other tokamaks.

Internal and external disruptions have been studied, and several unique features in the magnetic limiter configuration have been identified. The magnetic limiter configuration enables routine passing of the stability barriers at $q(a) = 2$ and $q(a) = 1$, where $q(a)$ is the edge safety factor, without a close fitting wall, external windings, or detailed profile control techniques. Passing the $q(a) = 1$ barrier permits operation in the $q < 1$ regime where total reconnection of the sawtooth does not occur. Discharges with $q < 1$ are also obtained in the material limiter configuration, suggesting

that partial reconnection is characteristic of the sawteeth, and not the magnetic limiter configuration.

The magnetic limiter configuration suppresses current termination in a major disruption. Current termination occurs in material limiter discharges due to enhanced interaction with the inboard limiter following the post-disruptive shift in major radius.

These experiments have been compared with the results of a nonlinear resistive MHD code that includes current in the scrape-off region. Code results and experimental data suggest that the improved stability of the magnetic limiter configuration results from modification of the current profile near the separatrix. An additional stabilizing influence on the (2,1) tearing mode is the noncircularity of the flux surfaces near the separatrix. The (1,1) resistive kink is less sensitive to the edge boundary conditions and noncircularity.

ACKNOWLEDGMENTS

I wish to thank my major professor, Dr. Stewart Prager, for his guidance and enthusiasim throughout this research. His friendship and support during my rather difficult transfer to the Physics program are gratefully acknowledged. Dr. Richard Dexter provided valuable insight into topics as diverse as day-to-day machine operation, plasma spectroscopy, and computorized data acquisition and analysis. Dr. J. Clinton Sprott provided advice on machine operation and diagnostics, and directed the design and implementation of the device upgrade that made further work on this topic possible for others.

I am especially grateful to several plasma theorists for their close cooperation and assistance. Dr. James Callen was always available for discussion and provided many valuable insights. Eijiro Uchimoto developed the 3-D resistive MHD code RPD and used it extensively to simulate these experiments. Much of my understanding of the theoretical aspects of this work resulted from discussion and collaboration with Eijiro. Eijiro and I benefited from numerous discussions with Darrell Skinner, who did the initial magnetic field line stochasticity studies with the TUBE code.

I wish to thank Tom Lovell for his assistance in diagnostic hardware and software development, data reduction, and machine operation. Jim Morin, the technical staff, and graduate students

John Goetz and Ing Tan helped keep Tokapole II running, and greatly facilitated the data acquisition in the last year.

I have benefited from the assistance of several fellow graduate students on the Tokapole II experiment: Dave Kortbawi provided assistance on numerous diagnostic hardware and software issues, John Sarff developed the low drift active integrator circuit used in this work, and Saeed Assadi and Abdulgader Almagri provided assistance on magnetic pickup loop construction, calibration, and operation.

Since leaving the Nuclear Engineering Department, Dr. John Conrad, my former major professor, has provided support and guidance. His continued support and friendship are greatly appreciated.

Finally, I wish to acknowledge the love and support of my family and family to be. My parents have waited patiently for many years for me to receive this doctorate. Janie, my fiance, provided boundless amounts of encouragement, emotional support, and when the chips were down, cutting and pasting for the final copy! It would not have been possible without their support. Thank you—it will never happen again! I promise!

This work has been supported by the United States Department of Energy.

Chapter 1
INTRODUCTION

I.A. Disruptions in Tokamaks:

Tokamak plasmas are subject to instabilities that cause the abrupt loss of significant amounts of plasma thermal energy. In MHD theory, these disruptions result from helical perturbations to the toroidal equilibrium. In ideal plasmas with negligible resistivity, the magnetic field lines are "frozen" into the plasma and are convected along with the perturbation. Finite plasma resistivity permits the magnetic field to diffuse through the plasma, relaxing the perturbed field on the relatively long resistive diffusion time scale τ_R.

Finite resistivity can have a dramatic impact on plasma stability and confinement. Resistivity allows magnetic field lines to "tear" and reconnect in the helical perturbations. Magnetic reconnection alters the magnetic topology through the formation of magnetic islands that lower the energy stored in the magnetic field associated with the plasma current. By localizing this reconnection to a thin resistive layer in an otherwise ideal plasma, the instability is able to proceed on a much faster time scale than τ_R. Under certain conditions, this energy release is catastrophic.

Despite nearly thirty years of research, disruptions continue to generate considerable experimental and theoretical interest because of the fundamental limits they pose to tokamak operation.[1,2]

Magnetic reconnection may destroy the magnetic flux surfaces.[3,4,5] The rapid quench of the plasma current can generate large currents in the structural components and magnets of the tokamak. The resulting mechanical stresses are capable of severely damaging a reactor-grade device.

Less severe disruptions that affect only the plasma core have been seen in all tokamaks since their discovery in 1973.[6,7,8,9] These disruptions are called "sawteeth" due to the characteristic long rise and rapid collapse of the central soft x-ray emissivity and the repetitiveness of the disruptions. During a sawtooth, plasma thermal energy is redistributed from the plasma core to the periphery, rather than being expelled from the plasma. Thus, while sawteeth are less catastrophic, they limit the extent to which plasma profiles can be peaked for optimal performance.

The redistribution of plasma thermal energy to the periphery during a sawtooth can dominate plasma thermal transport in low q discharges, where q, the tokamak safety factor, is the ratio of toroidal to poloidal transits for the magnetic field lines. Low q operation is one possible path to high plasma β (Section II.A.3), where $\beta = P/[B^2/4\mu_0]$ is the ratio of plasma kinetic pressure P to the pressure of the magnetic field B. High β signifies efficient utilization of the magnetic field, an important consideration in a power generating device due to the high cost of magnetic systems.

The transport of plasma and energy from the core to the periphery in a sawtooth may have beneficial effects on discharge

stability. The sawtooth mixes core plasma with the periphery, expelling impurities from the plasma core. This prevents impurity accumulation near the axis of the discharge that would cause the formation of hollow current profiles due to increased plasma resistivity near the axis. Such profiles may trigger disruptions. If, however, the magnetic reconnection theories for sawteeth are correct, the sawteeth themselves may constrain the amount of plasma current near the axis by holding $q(0) \approx 1$.

I.B. Terminology of Disruptions:

Disruptive instabilities are generally divided into two categories: external disruptions, which affect the periphery of the discharge and may or may not affect the plasma core, and internal disruptions, which affect only the interior of the discharge. In resistive MHD theory, tearing modes are responsible for causing the disruptions. Tearing mode eigenfunctions of the perturbed radial magnetic field for modes with poloidal mode number $m > 1$ are centered about the surface containing field lines with the same pitch as the tearing mode. The eigenfunctions fall off as $(1/r)^{m+1}$ outside the surface, and fall to 0 inside the surface before reaching the magnetic axis. In contrast, the eigenfunction for the $m = 1$ tearing and resistive kink modes is roughly constant from the magnetic axis out to this surface, and drops sharply to 0 outside. The structure of these eigenfunctions suggests the identification of modes with $m > 1$ with external disruptions and modes with $m = 1$ with internal disruptions.

Disruptions are also classified by severity. A "major" disruption terminates the discharge abruptly. These are usually external disruptions involving resistive tearing modes with $m = 2$ or 3. In many cases, the external disruption expels large amounts of plasma thermal energy, but the discharge recovers. These disruptions are "minor" or "pre-disruptions".[5] The terms "hard" and "soft" are often used interchangeably with major and minor.

This terminology will be used throughout this thesis. The relationship of the various classifications is shown schematically in figure 1.1.

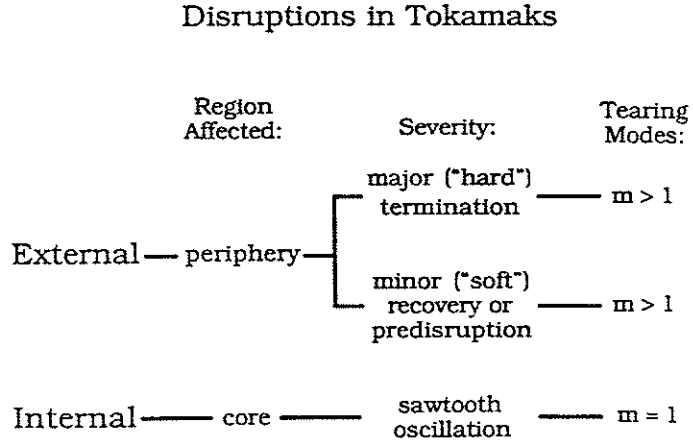

Figure 1.1: Schematic representation of disruption terminology used in this thesis.

I.C. Overview of Thesis Research:

I.C.1. Motivation:

This research has been motivated by both theoretical interests and experimental observations. It builds upon earlier work by several others, principally T.H. Osborne[10] and N.S. Brickhouse.[11] These authors identified several novel features of disruptive instabilities in the Tokapole II tokamak and conducted initial numerical simulations to understand them. These features are shown schematically in figure 1.2, modified from reference 10.

Key Features of Disruptive Behavior in Tokapole II Magnetic Limiter Discharges

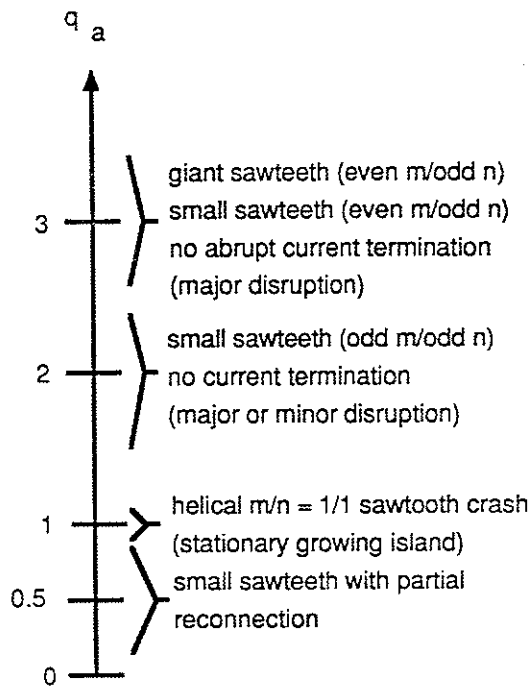

Figure 1.2: Key features of the dependence of disruptive behavior on q_a in magnetic limiter discharges (modified from reference 10).

Tokamak discharges have been obtained with $q < 1$ over most of the plasma cross section.[12,13] These discharges violate the edge safety factor $q(a) > 1$ Kruskal-Shafranov criterion for stability to ideal kink modes. The discharges display sawtooth oscillations on soft x-ray detectors but internal magnetic probe measurements indicate that, contrary to magnetic reconnection theories for sawtooth oscillations, the safety factor on the magnetic axis $q(0) \approx 0.6$ and remains essentially stationary throughout many sawtooth oscillations.[12,13]

In tokamak discharges with an effective edge safety factor $q_a \sim 1$, where q_a is the q at the edge of a straight, circular tokamak with the same plasma current and cross sectional area as Tokapole II discharges within the divertor separatrix, the sawtooth collapse has a helical $(m,n) = (1,1)$ structure.[14] Here, n is the toroidal mode number. These sawteeth agree well with the single helicity model of Kadomtsev[15] but disagree with experimental observations of an axisymmetric (0,0) collapse in other tokamaks.

Tokamak discharges with $1 \leq q_a \leq 2$ are routinely obtained without major or minor disruptions. Only internal disruptions on the soft x-ray detectors are seen.[10] These discharges are obtained without the benefit of the close fitting conducting wall or special operating techniques needed in other tokamaks for operation at $q(a) \leq 2$.

In tokamak discharges with $2.3 \leq q_a \leq 3$, "giant" sawtooth oscillations of long period and large amplitude are obtained with a

high degree of reproducibility. No major disruptions are seen under normal operation. These giant sawteeth are identified as external disruptions in this thesis, similar to major disruptions in other tokamaks except for the lack of current termination. In no other tokamak do external disruptions occur with the regularity and reproducibility of the giant sawteeth. The ability to suppress (or circumvent) abrupt current termination could have significant engineering benefits as pointed out in Section I.A.

Each of these observations concerns a topic of current interest in tokamak research. An increasing variety of sawtooth phenomena are being identified in the present-day, low resistivity tokamaks (TFTR, JET, JT-60, and DIII-D). These results challenge the range of validity of the sawtooth model first proposed by Kadomtsev and verified experimentally by Jahns, et al.,[9] and numerically by Sykes and Wesson.[17]

To date, safety factor profiles have been measured in only three other devices, TEXTOR,[18] TEXT,[19] and ASDEX.[20] In TEXTOR and TEXT, $q(0) \approx 0.7\text{-}0.8$ as in the Tokapole II experiments. Only in the ASDEX experiment was $q(0) \approx 1$ in agreement with magnetic reconnection theories of sawteeth. Several alternative models for the sawtooth relaxation have been developed recently.[21,22,23,24] Stochasticity of the magnetic field lines and plasma turbulence play crucial roles in these models.

The ability to avoid major disruptions in a reactor-grade device could prove beneficial. Of greater interest may be the ease

with which an external disruption-free operating regime of $q_a \leq 2$ can be obtained. Such low q(a) operation is favorable to enhance β since $\beta \propto 1/q^2$, but most tokamaks have difficulty reaching $q(a) \approx 2$ due to external disruptions.

The magnetic limiter configuration of the Tokapole II device has several features that could contribute to the uniqueness of the observed disruptive behavior. The divertor separatrix may influence the development of the tearing modes responsible for the disruptions. The identification of an "H" mode of high plasma confinement in neutral beam heated divertor tokamaks[25] and an associated disruptive instability, the "ELM" or "ERP" edge localized or relaxation mode, supports such a view. Simulations of magnetic islands in a divertor geometry suggest that the divertor separatrix may influence the tearing modes by producing significant stochastic field regions about the divertor separatrix that might lead to enhanced transport.[26] The recent identification of an H-mode in a device without a separatrix, the JFT-IIM tokamak,[27] suggests, however, that the H-mode may be only indirectly linked to the presence of the separatrix. The divertor magnetic topology in the plasma edge may "predispose" the plasma to the behavior necessary for H mode but such behavior might not be unique to the separatrix geometry.

While many tokamaks have operated with a poloidal divertor, the Tokapole II device is unique in its "magnetic limiter" configuration. No neutralizer plates or material limiters are inserted

into the region outside the separatrix to "scrape off" the plasma. Instead, significant amounts of plasma and toroidal current occupy this scrape-off region. The scrape-off plasma might act as a close-fitting conducting shell without the concomitant harmful effects of plasma-wall interactions. The shear of the magnetic field is very high near the divertor separatrix due to the presence of the separatrix "X-points" and may contribute to stabilizing some modes. The presence of the current outside the separatrix might be stabilizing to the tearing modes.[28]

The magnetic limiter configuration could also enhance tearing mode stability in several less direct ways. Moving the nearest limiter surface (divertor rings and vacuum vessel walls) far from the plasma edge decouples the core plasma from the detrimental effects of plasma-wall interactions that play a significant role in external disruptions. The lack of a material boundary at the plasma edge permits shallow gradients in plasma current and pressure at the periphery since these parameters are not constrained to zero at the edge. It is these gradients that drive the two principal classes of instabilities in a toroidal device: current and pressure driven modes.

The noncircularity of the flux surfaces in the plasma periphery near the divertor separatrix might also affect the tearing mode stability. Noncircularity has been shown to be stabilizing to tearing modes with poloidal mode number $m > 1$, although it appears to have little effect on $m = 1$ modes.[29]

Despite the uncertainties in the understanding of disruptive instabilities in tokamak devices, a large degree of experimental, theoretical, and numerical expertise concerning magnetic reconnection has been obtained in the past 10-20 years. Application of this expertise to study of the transition between the high q tokamak and $q << 1$ reversed field pinch (RFP) regimes might contribute to understanding magnetic reconnection processes in these devices as well. Relevant issues include the nature of the "dynamo effect" that sustains the RFP, mode coupling, plasma turbulence and transport, and localized structures of disruptive character in RFP plasmas.

From a practical standpoint, it is desirable to maximize the plasma current for a given toroidal field in order to optimize the plasma β. In addition, the fusion power production rate is proportional to $\beta^2 B^4$, so maximizing β also maximizes the fusion power production rate. Because of the obvious benefits of low q operation, several tokamaks have investigated this regime (DIVA, TOSCA, CLEO, TORUIT series, and REPUTE). Access to high β regimes through low q operation is under study at the DIII-D tokamak at GA Technologies.

I.C.2. Objective of This Thesis:

The objective of this thesis is to identify the importance of the magnetic separatrix, and plasma and current outside the separatrix, on disruptive stability in a tokamak device. Specifically,

this thesis seeks to identify the mechanisms leading to:

1. suppression of disruptive current termination in magnetic limiter $2 < q_a < 3$ discharges.
2. passing the $q_a \approx 2$ and $q_a \approx 1$ stability barriers easily and operating in an external disruption-free regime at $1 < q_a < 2$ without a close fitting conducting wall, external windings, or any special current ramp or profile control techniques; and
3. operation with $q(\psi) < 1$ throughout many sawtooth periods, in apparent contradiction of reconnection models of sawteeth.

Retractable limiter plates are used to remove the current and plasma outside the separatrix in a controlled manner. Comparison of disruptive behavior in the magnetic and material limiter configurations enables separation of the effects of plasma and current in the scrape-off region outside the separatrix from effects associated with the presence of the divertor separatrix. The interaction of the tearing modes with the divertor separatrix is changed by varying q_a, and consequently, the proximity of the mode rational surface to the divertor separatrix.

Use of the material limiters "peaks" the plasma profiles near the separatrix, enhancing the gradients near the separatrix. The presence of the limiter plates at the divertor separatrix also enhances the plasma/wall interaction and this effect has also been studied here with VUV measurements. Finally, a "benchmark" for

disruptive behavior in the Tokapole II device is provided by the similarity of the material limiter configuration to other tokamaks. This facilitates comparison with experimental results from other tokamaks.

I.C.3. Research Approach:

Disruptions are studied with conventional SXR detectors and Mirnov magnetic loops in both the magnetic and material limiter configurations. Variation of the plasma and current in the divertor scrape-off region is confirmed by magnetic and electrostatic probe measurements in the scrape-off region. In each configuration, disruptions are studied in three separate operating regimes, loosely characterized by q_a as $q_a < 1$, $1 < q_a < 2$, and $2 < q_a < 3$. The regimes $2 \leq q_a \leq 2.3$ in magnetic limiter discharges and $1.5 \leq q_a \leq 2$ in material limiter discharges are transitional regimes between discharges dominated by external disruptions and discharges free of external disruptions. Since the q_a limits of the transitional regimes vary with discharge conditions, these values are representative only, and importance should not be ascribed to the specific values reported (versus, e.g. $q_a = 2.4$ or $q_a = 1.4$).

This experimental research has been closely coupled to the development and use of a three dimensional, nonlinear resistive MHD code by another graduate student, Eijiro Uchimoto.[30] Since the Tokapole II device lacks the appropriate diagnostics for detailed profile measurements inside the divertor separatrix (probes either

do not work or are too perturbing), Uchimoto constructed pairs of similar equilibria, with and without plasma current outside the separatrix, to investigate the effects of scrape-off current and divertor geometry on the tearing mode behavior. The insight provided from the code runs, and where possible, qualitative comparison with experiment, has proven indispensable in this research. The results of reference 30 have been extensively extracted and presented throughout this thesis due to their direct relevance to the experimental work and for the convenience of the reader.

I.D. Organization of This Thesis:

This thesis has been organized into eight chapters. Chapter 1 is an introduction to the research, and discusses the motivation, objectives, and approach of this work. The present status of experimental and theoretical disruption research is summarized in Chapter 2. This chapter may be omitted by readers already familiar with most of this information. The Tokapole II device and experimental methods used in this research are described in Chapter 3. In Chapter 4, data are presented which characterize the plasma equilibria in each of the three operating regimes. Scrape-off profiles and global discharge parameters in both magnetic and material limiter configurations are compared for each regime to document the removal of plasma and current in the scrape-off region and any alteration in profile gradients near the separatrix. Data

pertaining to disruptions has been split into two chapters. In Chapter 5, all data for disruptions in which an m = 2 mode has been identified (external disruptions) is presented for each configuration. In Chapter 6, all data for disruptions in which an m = 1 mode has been identified (internal disruptions) is presented for each configuration. Key features and conclusions are summarized at the close of each chapter. Overall conclusions regarding the effect the divertor separatrix, and plasma and current in the scrape-off region, on stability are presented in Chapter 7. Directions for future investigations are also suggested in Chapter 7. This work would be performed on the Tokapole II upgrade device.

I.E. A Note on Thesis and PLP References:

Throughout this thesis, numerous references are made to Ph.D. theses from the University of Wisconsin—Madison and University of Wisconsin PLP reports. PLP reports are internal reports of the University of Wisconsin Plasma Physics research group in the Department of Physics. Copies of all Ph.D. theses and PLP reports may be obtained by writing to:

Plasma Physics Group
Physics Department
University of Wisconsin—Madison
1150 University Avenue
Madison, WI 53706.

Please include the PLP number in any request.

REFERENCES

[1]Current Disruption in Toroidal Devices, (Proc. IAEA Technical Committee Meeting, Garching, 1979), Max Planck Institut für Plasmaphysik, Garching, IPP—3/51 (1979).

[2]B.B. Kadomtsev, Plasma Physics and Controlled Fusion, 2, 217 (1984).

[3]A. Bondeson, "Disruptions in Tokamaks", Theory of Fusion Plasmas, (Proc. of the Course, Varenna, 1987), in press.

[4]F. Karger, et al., Plasma Physics and Controlled Fusion Research (Proc. 6th Int. Conf., Berchtesgaden, 1975), 1, (IAEA,Vienna, 1976), 267.

[5]S.V. Mirnov and I.B. Semenov, Plasma Physics and Controlled Fusion Research (Proc. 6th Int. Conf., Berchtesgaden, 1975), 1, (IAEA, Vienna, 1976), 291.

[6]V.A. Vershkov, C.E. Lisenko, I.B. Semenov, and A.T. Scherbac, PPPL Report MATT-TRANS 112 (1974).

[7]S. von Goeler, W. Stodiek, and N. Sauthoff, Physical Review Letters, 11, 1201 (1974).

[8]R.R. Smith, Nuclear Fusion, 16, 1053 (1976).

[9]G.L. Jahns, et al., Nuclear Fusion, 18, 609 (1978).

[10]T.H. Osborne, Ph.D. thesis, University of Wisconsin (1984).

[11]N.S. Brickhouse, Ph.D. thesis, University of Wisconsin (1984).

[12]T.H. Osborne, R.N. Dexter, and S.C. Prager, Physical Review Letters, 49, 734.

[13]T.H. Osborne, R.N. Dexter, and S.C. Prager, Physics of Fluids, 26, 350 (1983).

[14]N.S. Brickhouse, et al., Physics of Fluids, 28, 3429 (1985).

[15]B.B. Kadomtsev, Soviet Journal of Plasma Physics, 1, 389 (1975).

[16]R.A. Moyer, et al., Bulletin of the American Physical Society, 31, 1594 (1986).

[17]A. Sykes and J.A. Wesson, Physical Review Letters, 37, 140 (1976).

[18]G.H. Wolf, et al., Plasma Physics and Controlled Fusion, 28, 1413 (1986).

[19]W.P. West, D.M. Thomas, J.S. deGrassie, and S.B. Zheng, Physical Review Letters, 58, 2758 (1987).

[20]ASDEX paper at EPS Madrid meeting (1987).

[21]Equipe TFR, Plasma Physics and Controlled Fusion Research (Proc. 9th Int. Conf., Baltimore, 1981), 3, (IAEA, Vienna, 1982), 383.

[22]M.A. Dubois, A.L. Pecquet, and C. Reverdin, Nuclear Fusion, 23, 147 (1983).

[23]A.J. Lichtenberg, Nuclear Fusion, 24, 1277 (1984).

[24]W. Stodiek, Bulletin of the American Physical Society, (San Diego, most recently).

[25]Wagner et al., Physical Review Letters, 49, 1408 (1982).

[26]D.A. Skinner, et al., Physics of Fluids, 30, 1218 (1987).

[27]S. Sengoku, et al., Physical Review Letters, 59, 450 (1987).

[28]J.K. Lee, Physics of Fluids, 29, 1629 (1986).

[29]R.C. Grimm, et al., Plasma Physics and Controlled Fusion Research, (Proc. 9th Int. Conf., Balitmore, 1981), 3, (IAEA, Vienna, 1982), 35.

[30]E. Uchimoto, Ph.D. thesis, University of Wisconsin (1988).

Chapter 2
STATUS OF DISRUPTION RESEARCH

II.A. Preliminaries:

II.A.1. The Tokamak Confinement Concept:

One of the earliest magnetic confinement concepts for achieving controlled thermonuclear fusion was the linear z-pinch.[1] In this device, a large current was driven in a cylindrical plasma column parallel to the axis. The current heated the plasma and generated a poloidal magnetic field that contracted the plasma away from the device walls. Unfortunately, the longitudinal current was subject to two robust instabilities that either pinched off the current channel ("sausage" instability) or kinked the plasma column into the vessel walls (kink instability). These instabilities developed on the fast Alfvénic or ideal MHD time scale, $\tau_A = L\rho^{1/2}/B$ where L is a characteristic length, ρ is the mass density, and B is the magnetic field.

The addition of a close-fitting conducting shell and a strong longitudinal magnetic field, parallel to the plasma current, stabilized each of these modes. The magnetic field, however, led to rapid loss of the plasma out the ends of the device by flows parallel to the field lines. To circumvent these losses, the cylinder was bent into a torus.

A parameter of fundamental importance in tokamak stability is the ratio of stabilizing toroidal magnetic field B_t to the toroidal

plasma current I_p, expressed in terms of the dimensionless tokamak safety factor q:

$$q = \frac{2\pi}{\iota} \qquad (2.1)$$

where ι is the rotational transform of the magnetic field B. In a circular tokamak, q can be expressed in terms of the toroidal and poloidal magnetic field components as:

$$q = \frac{rB_t}{RB_p} \qquad (2.2)$$

where B_t and B_p are the toroidal and poloidal magnetic field components respectively, r is the minor radius, and R is the major radius. This coordinate system is shown in figure 2.1. In a noncircular cross section torus,

$$q = \lim \frac{\text{toroidal transits}}{\text{poloidal transits}} \qquad (2.3)$$

where the limit is taken to an infinite number of toroidal transits.

From equation 2.2, one can see that the tokamak represents the high q limit of the z-pinch. Plasma current is driven inductively in the torus, where the plasma acts as the secondary of a transformer. Bending the current into a ring generates a force that attempts to expand the ring in major radius to lower its inductance. This force arises due to the imbalance of magnetic field pressure on the small major radius and large major radius sides of the torus. To prevent the expansion of the plasma column into the vessel wall, a restoring force is generated either by image currents in a close-fitting conducting shell or, in modern tokamaks, by an

externally applied vertical magnetic field B_V (figure 2.2). The major components of the tokamak are shown in figure 2.3.

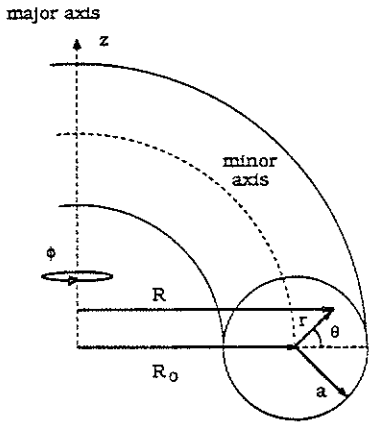

Figure 2.1: Tokamak coordinate system showing the major radius R, minor radius r, toroidal angle ϕ, and poloidal angle θ. The major and minor radii of the torus are designated by R_0 and a respectively.

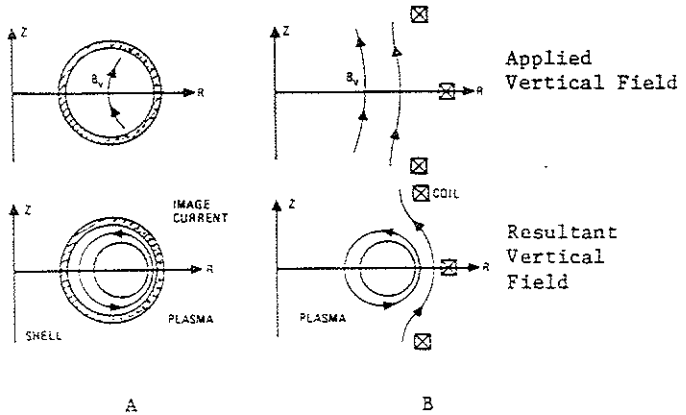

Figure 2.2: Plasma equilibrium in major radius can be maintained with either (A) a close-fitting conducting shell, or (B) an externally applied vertical magnetic field B_V. The applied vertical fields and resultant poloidal fields are shown for each configuration (from reference 2).

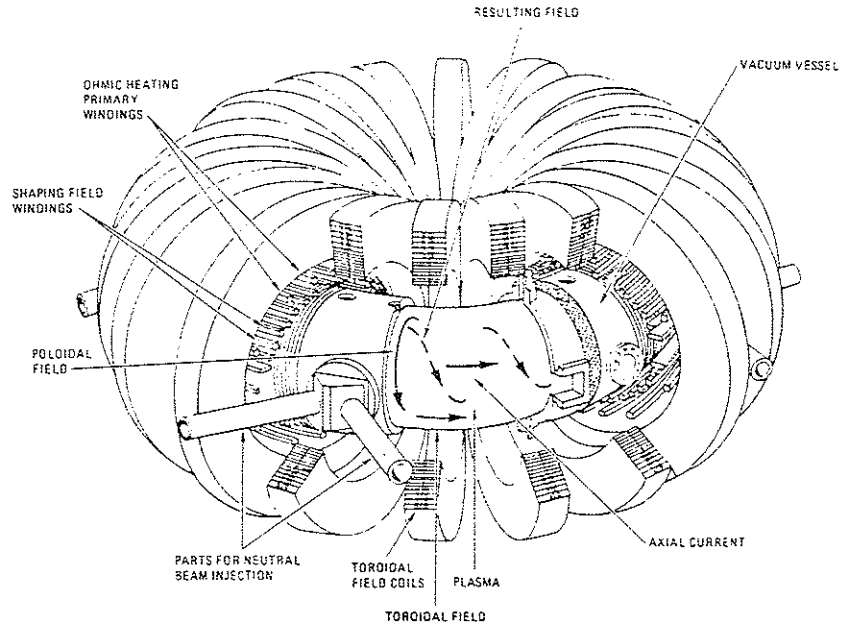

Figure 2.3: Basic components of the tokamak (from reference 3).

II.A.2. Instabilities in Toroidal Devices:

Plasmas are complex, many-body systems that exhibit collective behavior due to the electrostatic forces between the various species of charged particles. Considerable success in understanding the modes of collective excitation in plasmas has been achieved using the relatively simple magnetohydrodynamic (MHD) fluid model. In the model, the two major sources of free energy available to drive instabilities in toroidal devices are the current density gradient and the plasma pressure gradient.

Pressure driven modes include interchange modes, with constant amplitude along a magnetic field line (no field line bending) and ballooning modes, with variable amplitude along a field line. Stability to interchange modes is described in the limit R/r >> 1 by the Mercier criterion:

$$\frac{1}{4}\left[\frac{q'(r)}{q(r)}\right]^2 + 2\mu_o \frac{p'(r)}{rB_t}(1 - q^2) > 0 \qquad (2.4)$$

Shear (variable field line pitch) in the magnetic field produces a stabilizing force on the mode through the first term on the left hand side of equation (2.4). Thus, interchange modes are believed to be important only near the magnetic axis, where MHD instabilities may constrain the q and l_p profiles to be flat.

Due to the stabilizing influence of field line bending, ballooning modes are localized to regions of "bad" curvature on the large major radius side of the torus. The faster a field line travels from the bad to good curvature regions of the torus, the greater the field line bending. Thus, operation at low q is stabilizing to ballooning modes. An approximate limit on the attainable plasma β due to ballooning modes is given by $\beta \approx a/Rq^2$.

Current driven modes are divided into ideal modes for which the plasma resistivity η = 0, and resistive modes for which η is small but finite. The plasma resistivity may be expressed in terms of the dimensionless magnetic Reynolds number S:

$$S = \frac{\tau_R}{\tau_{Hp}} \qquad (2.5)$$

where $\tau_R = a^2/\eta$ is the resistive diffusion time and $\tau_{Hp} = a\rho^{1/2}/B_p$ is the poloidal Alfvén time, the time for a fast compressional wave to propagate across the minor cross section of the torus. In early tokamaks, typical values for S were 10^4-10^5. In the largest present-day tokamaks (TFTR, JET, JT-60, and DIII-D), S = 10^7-10^8. In this low resistivity regime, disruptive instabilities have become more complex as ideal modes appear to play a progressively more important role.

The ideal MHD modes essentially consist of external kink modes that disturb the plasma surface, and internal modes that leave the surface unaffected. These modes limit the parameter regime accessible to tokamak operation.[4] The modes have the approximate spatial dependence:

$$f(r)\exp[i(m\theta + n\phi)] \qquad \begin{cases} m = 0, 1, 2, \ldots \\ n = 0, 1, 2, \ldots \end{cases} \qquad (2.6)$$

where m and n are respectively the poloidal and toroidal mode numbers. The n = 0 axisymmetric modes are easily controlled by proper shaping and feedback control of the B_v field in modern tokamaks.

The remaining modes can lead to gross helical perturbations of the plasma whenever m/n = q at some point inside the vacuum vessel. For these mode numbers, the perturbation has the same pitch as the magnetic field lines, and the bending of magnetic field lines (a stabilizing effect) is minimized. In low β, circular cross section tokamaks, the (1,1) kink mode is unstable for "normal"

current density profiles that are peaked at the center if q = 1 anywhere inside the plasma. The stability condition q(r) > 1 imposes an upper limit on the plasma current:

$$I_p(MA) = \frac{rB_p}{2} < \frac{r^2 B_t}{2R} \qquad (2.7)$$

For r = a, equation 2.7 becomes the Kruskal-Shafranov condition:

$$I(MA) < \frac{a^2 B_t}{2R} \qquad (2.8)$$

The ideal modes with m/n > 1 may be unstable provided the point q(r) = m/n falls in the vacuum outside the plasma, or into the plasma periphery where resistivity becomes important. Here the kinks become resistive kink or tearing modes.

For resistive modes, the finite plasma resistivity plays a crucial role in the development of the instabilities that belies its low value. The finite resistivity permits tearing and reconnection of the magnetic field lines, leading to formation of magnetic islands and alteration of the magnetic topology. Under certain conditions, the magnetic flux surfaces can be completely destroyed.

While one might expect these resistive modes to evolve on the very slow resistive diffusion time scale $\tau_R \sim a^2/\eta \sim 100$ seconds, it is found that the modes evolve on a much faster hybrid time scale $\tau \propto \tau_A^{2/5}\tau_R^{3/5}$ or $\tau/\tau_A \propto S^{3/5}$.[5] This is possible because the resistive modes localize the magnetic reconnection to a thin layer δ about the singular surface q(r) = m/n. In typical tokamak experiments, $\tau_A \sim 10^{-6}$ seconds and $\tau_R \sim 100$ seconds.

II.A.3. Beta Limits in Tokamaks:

The limitations placed on tokamak operation by the ideal kink and internal modes are illustrated schematically in figure 2.4.[4] The limits are presented in terms of q(a), which determines the maximum plasma current, and q(a)/q(0), which corresponds to peaking of the profile for the parameterization $j(r) = j_0(1-r^2/a^2)^\nu$. For this profile, $q(a)/q(0) = \nu + 1$. Complete stability to m > 1 kink modes can be obtained for any q(a) > 1 with sufficient peaking of the profile ($\nu > 2.5$). Stability to internal modes requires q(0) > 1.

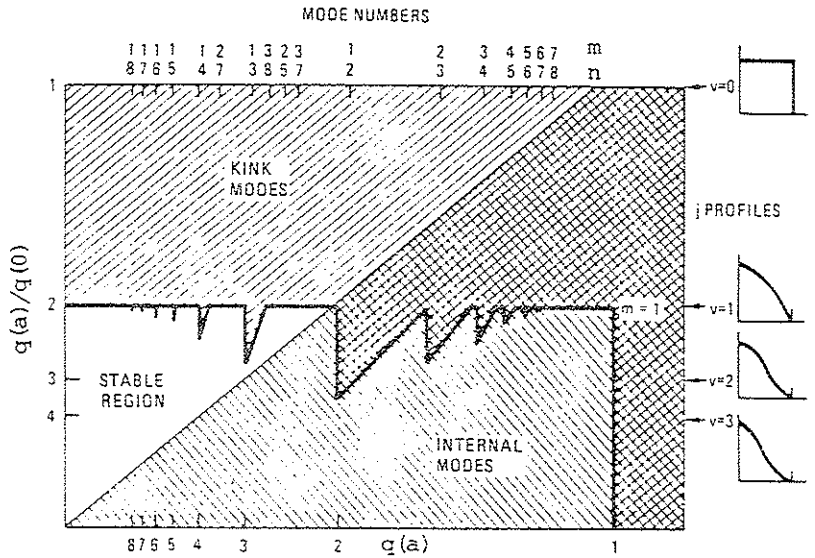

Figure 2.4: Stability diagram for ideal kink and internal modes. Stability to internal modes requires q(0) > 1; to m = 1 kinks requires q(a) > 1; and to m > 1 kink modes requires a minimum peaking of the current profile (from reference 4).

While the stable operating regime extends below q(a) = 3, for most tokamaks the effective limit is near q(a) ~ 3. Combined with

the ballooning mode limit $\beta \leq a/Rq^2$, this yields an effective limit of $\beta \leq a/9R \leq 2\text{-}5\%$.

Detailed calculations of β limits in tokamaks with optimized profiles yield the simple scaling law for the volume average β:

$$\beta_T(\%) \leq C \frac{I(MA)}{a(m)B(T)} \qquad (2.9)$$

for both n = 1 ideal external kink modes[7,8,9] and n = ∞ ideal ballooning modes.[8,9,10] The value of C differs for the two different modes and also among the various computations for each mode, but lies in the range 2.8-4.4. A survey of tokamak experimental data[11] over a wide range of discharge shape and topology, confinement modes, and heating methods, confirms a β limit in agreement with equation 2.9:

$$\beta(\%) \leq (3.5 \pm .5) \frac{I(MA)}{a(m)B(T)} \qquad (2.10)$$

Operationally, both "hard" and "soft" β limits have been observed. The hard β limits are major disruptions consistent with external kink or tearing modes. The soft β limits, arising from enhanced transport at high β, appear consistent with ballooning modes. The operational limits of several auxiliary heated tokamak experiments are plotted as volume average β_T in percent verses I/aB in figure 2.5, taken from reference 11. The excellent agreement of the results with equation 2.9 is evident.

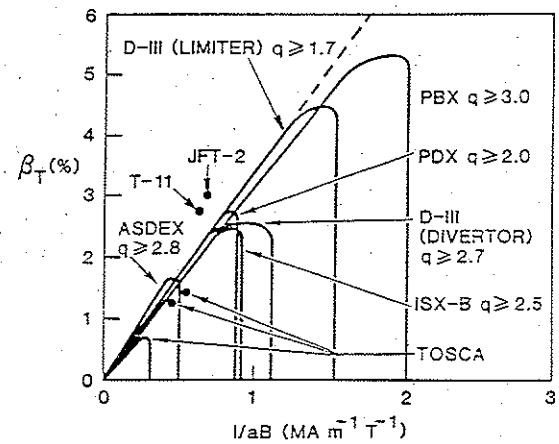

Figure 2.5: Operational limits of auxiliary heated tokamaks plotted as volume average beta $\beta_T(\%)$ versus I/aB, showing the validity of equation 2.9 (from reference 11).

II.B. External Disruptions:

II.B.1. Review of Experimental Results:

II.B.1.a. General Characteristics:

Any attempt to review the experimental studies of external disruptions in tokamaks is complicated by the fact that apparently similar final results can be obtained from discharges with differing MHD behavior prior to and during the disruption. A detailed study of disruptions on the PLT device using soft x-ray detectors[12] found no universal long wavelength MHD mode behavior, although m = 2 oscillations were a common feature.

To facilitate discussion of the experimental observations from many machines, the disruption is divided into precursor, transport, and termination phases. A schematic view of the plasma kinetic

and magnetic energy losses in the three phases of a major disruption is shown in figure 2.6.[14] The vertical lines separate the disruption into the precursor, transport, and termination phases in the figure. The time scales for the transport and termination phases are τ_{tq} ("thermal quench") τ_{mq} ("magnetic quench") respectively. Most of the plasma thermal energy is lost during the transport phase, mainly to the limiters (p^{kin}_{loss}). Most of the plasma magnetic energy is lost during the current rampdown in the termination phase, presumably to the walls through radiation and charge exchange (p^{mag}_{loss}).

One nearly universal observation during the precursor phase of disruptions on many different devices is the presence of magnetic oscillations in the poloidal field of character m = q(a), where n = 1 and m = 2[12,13,15-27] and more rarely, m = 3.[13] Major disruptions have also been seen in several devices without any precursors.[28,29] The (2,1) mode grows to a saturated state, rotating in the electron diamagnetic drift direction toroidally, poloidally, or both. Prior to disruption, the (2,1) mode rotation slows and often "locks" (stops rotating).[13,15,22,25,41] In other devices, the (2,1) mode is observed to grow explosively just before the disruption without apparently reaching a saturated state.

The (2,1) mode couples to other modes in many experiments. Often, a rapidly growing (3,2) mode is seen just before the disruption.[18,22,23,25] In TOSCA,[18] the (2,1) mode drove both the

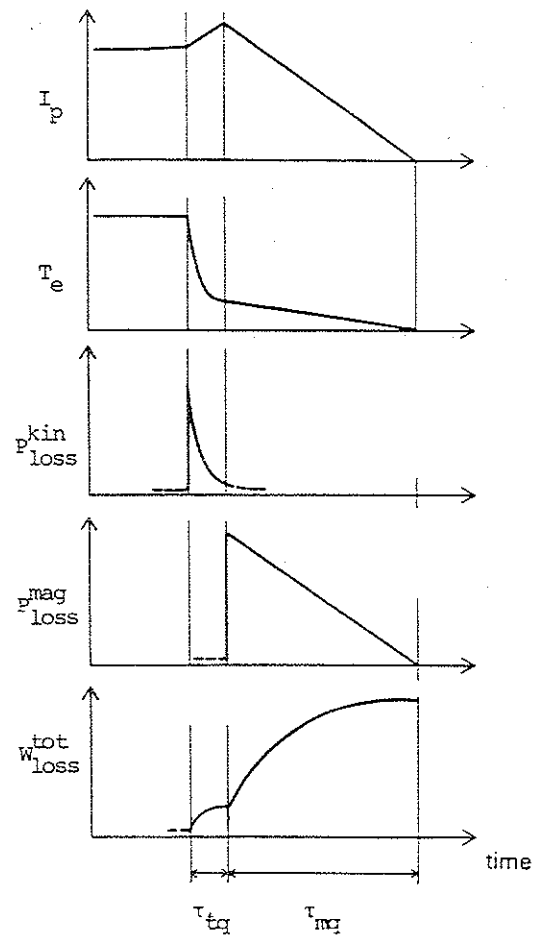

Figure 2.6: Schematic behavior of the plasma current I_p, central electron temperature T_e, thermal (kinetic) power loss p^{kin}_{loss}, magnetic power loss p^{mag}_{loss}, and total plasma energy loss W^{total}_{loss} in a major disruption. Time scales are indicated for the transport phase, τ_{tq}, and termination phase, τ_{mq}, (from reference 14).

(3,2) and (5,3) modes explosively unstable before the disruption. Coupling has also been seen between the (2,1) mode and the (1,1) mode in the interior of the discharge.[12,15-17,21,26,27] In PULSATOR, the (1,1) mode phase locked to the dominant (2,1) mode just before the disruption, as seen in figure 2.7 by the impression of the (2,1) mode frequency ("(INSIDE)(OUTSIDE) POLOIDAL FIELD") on the (1,1) mode on the SXR diodes.[15]

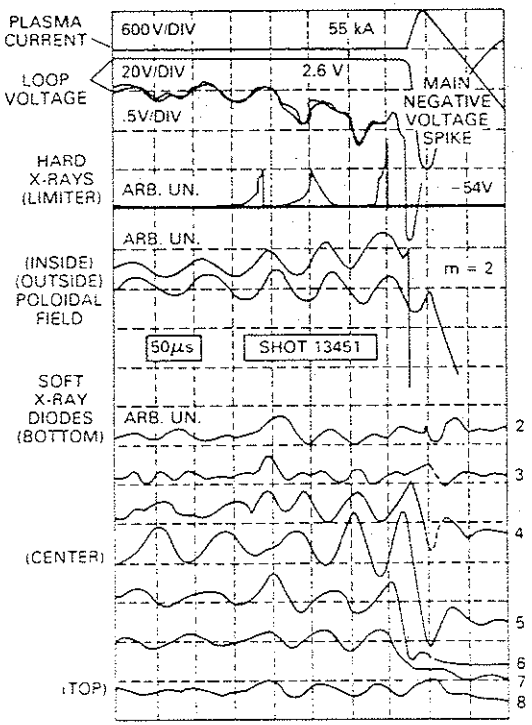

Figure 2.7: Expanded view of the last .5 ms before a major disruption in the PULSATOR device (from reference 30, after reference 15).

In a recent study of external disruptions using soft x-ray detectors on the JIPP TII device, Tsuji, et al.[27] distinguished between coupling of the (2,1) mode to the (3,2) mode and to the (1,1) mode. Coupling of the (2,1) and (3,2) modes led to a "partial" disruption (minor disruption) that redistributed the plasma current within the $q = 2$ and $q = 3/2$ surfaces, but did not affect the center of the discharge. Coupling of the (2,1) and (1,1) modes was observed to lead to a major disruption, destroying confinement to the center of the discharge.

In the PULSATOR study,[15] the precursor phase ended with a series of hard x-ray bursts ($E \geq 1$ MeV) from the limiter synchronized with the rotation of the island system (figure 2.7). The hard x-rays arose from the loss on successive passes of deeper and deeper layers of runaway electrons. The drift surfaces for the runaway electrons are displaced radially outward with respect to the magnetic surfaces (1.5 cm for 6 MeV) and are particularly susceptible to magnetic perturbations.

The transport phase begins with the abrupt drop in central T_e and the large negative loop voltage spike. In the PULSATOR study,[15] the drop of central T_e, as indicated by the soft x-ray central chord in figure 2.7, occurred 10-20 μs before the negative V_l spike. This indicates that the central confinement had already been destroyed by the time of the V_l spike.

The V_l spike arises due to the sharp drop in plasma poloidal β ($\beta_{pol} = P/[B_{pol}^2/2\mu_0]$) and expulsion of poloidal magnetic flux from

the discharge. The drop in β_{pol} due to the collapse of central T_e is insufficient to account for the magnitude of the V_l spike. The spike arises in part from a rapid expansion in minor radius, seen in enhanced H_α emission and fast neutral particle efflux. Due to the lowered inductance of the plasma column, the discharge shifts inward in major radius on a nearly ideal MHD time scale, seeking a new equilibrium position.

In older tokamaks, feedback control of the B_v system was often inadequate to maintain the equilibrium position of the discharge during the post-disruptive shift. Contact of the plasma with the inboard limiter terminated the discharge through rapid cooling and the influx of impurities.[15,16,21,31] In modern tokamaks, B_v feedback control systems are capable of maintaining plasma equilibrium position for disruptions with current rampdown rates $\Delta I_p/\Delta t \approx 50$ kA/ms.[27,32] While such systems effectively eliminate loss of equilibrium as a cause of discharge termination, it is found that major disruptions cannot be totally avoided.[27,32]

The termination phase is characterized by a nearly linear current rampdown rate $\Delta I_p/\Delta t$. The magnetic energy quench time τ_{mq} $(= I_p/[\Delta I_p/\Delta t])$ is plotted in figure 2.8 for a variety of tokamaks.[14] In early tokamaks, the strength of the current rampdown, and whether or not the disruption terminated the discharge, often depended only upon the magnitude of the central T_e drop and/or the strength of the plasma/limiter interaction.[15,31] In the T-4 device,[16,21] termination depended upon the strength of

the "pre-disruption", a type of minor disruption that affected only the plasma periphery. Major disruptions were observed to deeply mix the core plasma as well. This early work is echoed in the "partial" and major disruptions of reference 27. In either case, the major disruption appears to develop in two steps, with the occurrence of the final step—termination—depending upon the severity of the initial transport step. An interesting observation concerning the mechanism for the final termination phase was the observation on the T-10 device[33] that the disruptions left (1,1) helical patterns of damage on the liner.

The magnitude of $\Delta I_p/\Delta t$ in the PDX device[13,34] varied with the boundary conditions at the plasma edge. Operation against an inboard toroidal limiter produced $\Delta I_p/\Delta t$ rates four times larger than operation with either top and bottom rail limiters or an outboard scoop limiter. During divertor operation on both PDX[34] and ASDEX,[32,35] generally fewer disruptions occurred during current ramp-up or flattop. Instead, series of minor disruptions were often observed, particularly during the current rampdown. In both devices, these results were attributed to changes in impurity influx, both before and during the disruptions, and in the case of PDX, to the extent of plasma in the limiter scrape-off region. Longer scrape-off lengths were achieved with the rail and scoop limiters and the divertor, permitting shallower gradients in plasma parameters at the edge.

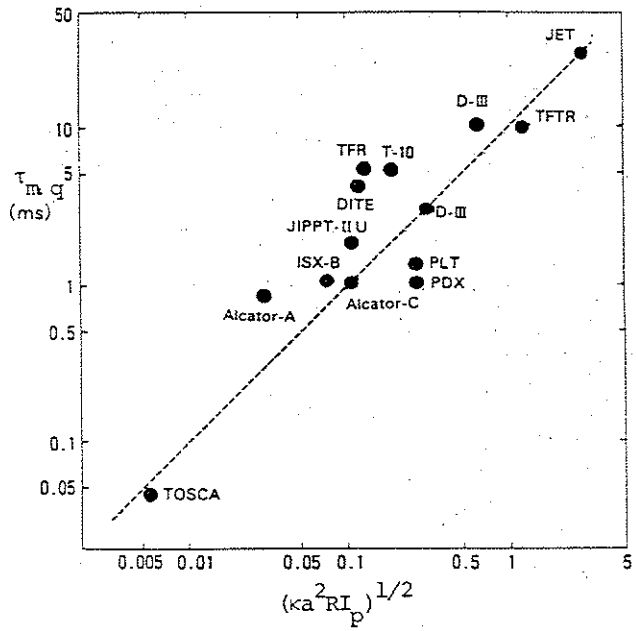

Figure 2.8: The magnetic quench time τ_{mq} verses $(\kappa a^2 R I_p)^{1/2}$ for a variety of tokamaks. τ_{mq}, a, R, and I_p have their previously defined meanings; κ is the plasma elongation. The dashed line is a theoretical fit from reference 14.

In the DIII device,[24,44] a noncircular tokamak with an unusual "open divertor", stability to major disruptions improved in the material limiter configuration, as demonstrated by the ability to achieve lower values of q(a). Here too more plasma was found outside the last closed flux surface in the favorable configuration. This suggests that the favorable influence may be related to edge profiles, and not to the presence of a divertor separatrix.

II.B.1.b. Current and Density Limit Disruptions:

With the elimination of loss of equilibrium as a cause of major disruption, it is found that major disruptions fall into two classes: current limit and density limit disruptions. The Hugill diagram is often used to indicate the range of stable tokamak operation, as shown in figure 2.9.[36] Tokamak operating parameters are plotted as $1/q(a)$ verses the "Murakami parameter"[37] nR/B_t, making the Hugill plot similar to the β limit plot of figure 2.5.

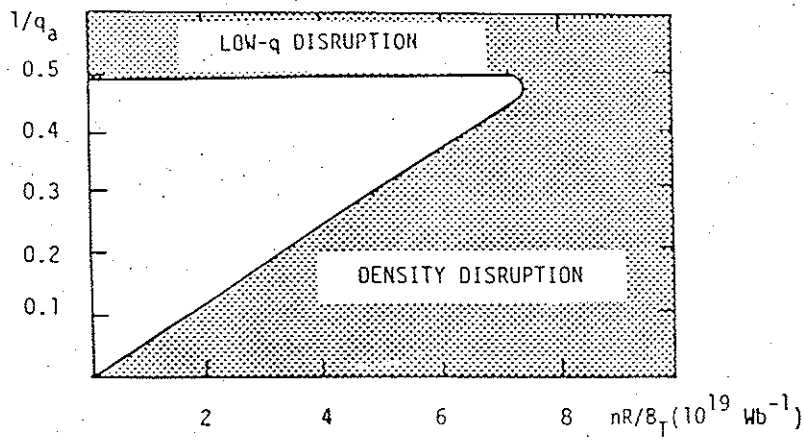

Figure 2.9: Schematic Hugill plot of the tokamak operating regime (from reference 36).

The current limit generally corresponds to $q(a) \geq 2$ (ignoring difficulties associated with $q(a) \approx 3$). The density limit is described by $n < CB_t(Wb/m^2)/R(m)q(a)$, where $C = 1\text{-}2 \times 10^{20}$ Wb^{-1} for ohmic heated plasmas. The density limit can been increased somewhat by neutral beam heating[38,39] and by pellet fueling (which reduces impurities).[39]

Disruptions at either limit are generally two step processes,

with the initial step involving an unstable (2,1) mode coupling to other modes (mostly (3,2) and (1,1) as described above). A significant difference between the limits is the duration of the precursor phase.[17,40] Current limit disruptions proceed more rapidly, with explosive growth of the (2,1) mode driving other modes unstable. Density limit disruptions have a much longer precursor phase, lasting up to 1 second on JET.[40] Generally, the (2,1) mode appears to saturate for some time, eventually slowing and locking as it begins to grow rapidly toward the disruption.[40,41]

The fundamental difference between the two limits, therefore, appears to be the mechanism destabilizing the (2,1) mode. In current limit disruptions, the stabilizing portion of the current density profile outside the q = 2 surface is lost as q(a) approaches 2. In density limit disruptions, radiative cooling of the plasma periphery reaches 100% of the input power,[42] causing the current profile to contract. Interaction of the (2,1) and (3,2) island may then lead to a further contraction of the profile as confinement is lost between the q = 2 and q = 3/2 surfaces due to island overlap. The resulting current density profile resembles a step function inside the q = 1 surface, and is highly unstable to (1,1) kinks.

Exact details of the Hugill plot vary from device to device, but the representation of figure 2.9 is generally valid. The Hugill plot for the FT tokamak[22] is shown in figure 2.10. Discharges in the shaded areas terminate in major disruptions. Operational limits are represented by solid and dashed lines. The narrow window to pass

the q(a) = 3 barrier is indicated between the dotted regions at 1/q(a) ≈ 3. The window to pass the q(a) = 2 barrier lies between the dotted and black regions at 1/q(a) ≈ 0.5 at the top of the operational space.

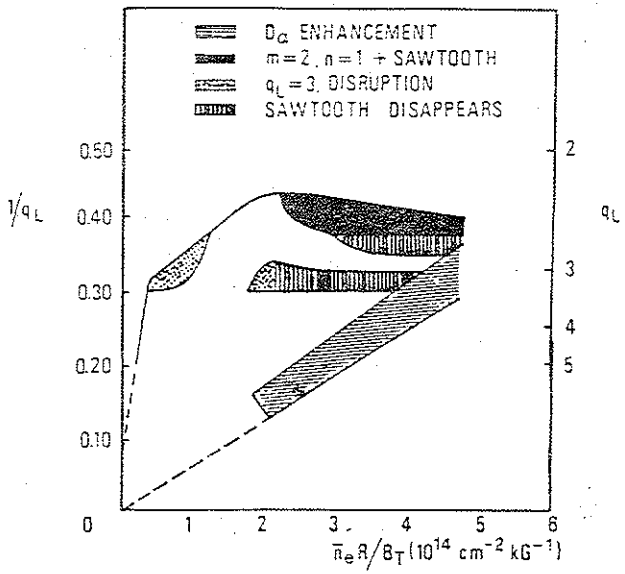

Figure 2.10: Hugill plot for the FT tokamak (from reference 22).

II.B.1.c. Disruption Control and Low q Operation:

Because of the interest in optimizing plasma confinement by maximizing β, many tokamaks have operated in the low q(a) ≤ 2 regime. Low q(a) operation maximizes β primarily by increasing the density limit. An additional benefit for those devices capable of operating with q(a) ≤ 1.5-1.8 is the absence of major disruption.

The lack of major disruption is generally attributed to the removal of the q = 2 surface from the plasma.

Access to the low q(a) regime is restricted by current limit disruptions, as shown, for example, in the Hugill plot of figure 2.10 for the FT tokamak. Therefore, some scheme to stabilize the (2,1) resistive tearing mode is needed. The wide variety of approaches utilized is summarized in Table 2.1.

Wall stabilization of the (2,1) tearing mode by a close fitting conducting wall with time constant τ longer than the discharge length has been used on T-6,[45] T-11,[46] and DIVA.[19] In TOSCA,[23] the resistive liner time constant $\tau \approx 7$ μs, but the mode rotation frequency $f \approx 50$ kHz was sufficiently high to permit the resistive liner to act as a conducting wall for the (2,1) mode.

Most devices have utilized extensive control of wall conditions and plasma-wall interactions to facilitate low q(a) operation. Heavy titanium gettering of the walls or liners has been used to reduce the level of heavy metallic impurities released into the discharge. In the DIVA experiments, 500 mg of titanium were evaporated onto the wall between each shot! In T-10[48] and CLEO,[47] high fluxes of light impurities (carbon, oxygen) from the plasma were beneficial to low q(a) operation by cooling the edge plasma and reducing the erosion of metals from the wall. Heavy gas puffing during the discharge, often feedback controlled by the level of (2,1) MHD activity in the plasma, had a similar effect on T-10,[48] T-11,[49] FT-2,[49] and CLEO.[47]

Table 2.1

METHODS FOR EXTERNAL DISRUPTON CONTROL:

Wall Stabilization:

Close-Fitting Conducting Wall: T-6,[45] T-11,[46] DIVA[19]

Mode Rotation: TOSCA[23]

Wall Conditioning/Interactions:

Titanium gettering: DIVA,[19] TOSCA,[23] CLEO,[47] TORUIT-4[52]

Cleaning (removal of heavy impurities): T-10[48]

Gas Puff Control: T-10,[48] FT-2,[49] T-11,[49] CLEO[47]

Resonant Fields:

m/n = 2 Fields: PULSATOR,[15] TOSCA,[23] TO-1,[50] HT-6B[51]

m/n = 3/2 Fields: JIPP TII-U[61]

Nonresonant Fields:

m/n > 2 (ergodization): TORUIT-4[52,53]

m/n < 2 (shear; helically assisted): CLEO,[47] TORUIT-5[52]

Separatrix/Magnetic Limiter: TOKAPOLE II[57-60]

High Fill Pressure: REPUTE,[56] DIVA,[19] TORUIT-4,5[52]

Fast Current Rise: CLEO,[47] TORUIT-4,[52] REPUTE[56]

ECH: T-10[54]

Electron Beam: SPAC[55]

Several techniques to directly influence the (2,1) magnetic island growth with applied external magnetic fields have been utilized. These techniques involve application of either resonant fields of helicity m/n = 2 or 3/2, or nonresonant fields with m/n ≠ 2 or 3/2.

The earliest attempt to control the (2,1) magnetic island growth with a resonant m/n = 2 winding was performed on the PULSATOR device.[15] At low coil current levels, the applied field induced the formation of a small (2,1) magnetic island that flattened the current density gradient about the q = 2 surface, saturating the (2,1) island at a nondangerous level. At higher coil currents, the external field led to a large, distorted (2,1) magnetic island that triggered major disruptions beyond a critical size. Similar results were also obtained in studies on TOSCA,[23,50] and HT-6B.[51]

Utilizing the observation that (2,1) and (3,2) mode interaction in the JIPP TII device led to partial disruptions that redistributed the plasma current between the q = 2 and q = 3/2 surfaces,[27] Yamazaki, et al.[61] used external coils of m/n = 3/2 helicity to deliberately drive the formation of a (3,2) island that overlapped the (2,1) island while the (2,1) island width was still small, triggering a "quick profile reorganization" partial disruption. The resulting current density profile was found to be stable to the (2,1) tearing mode.

Two classes of nonresonant applied fields have been used to

control major disruptions. For external coils of helicity m/n > 2, the applied magnetic field ergodizes the magnetic field lines in the plasma periphery. The enhanced transport in the stochastic fields flattens the current density gradient at the q = 2 surface and stabilizes the (2,1) tearing mode.[52,53] For external coils of helicity m/n < 2 the (2,1) tearing mode is stabilized by the addition of high shear to the magnetic field near the q = 2 surface. This technique is referred to as "helically assisted".[47,52] A somewhat related technique uses the magnetic separatrix of a poloidal divertor to influence the growth of the (2,1) island.[57-60]

The ability to operate at low q(a) has been enhanced in several devices by using high pre-fill gas pressures which reduce the magnetic Reynolds number S and increase dissipative effects.[19,52,56] In the CLEO,[47] TORUIT-4,[52] and REPUTE[56] devices, fast current ramp-up rates were also used successfully to reach the q(a) < 2 regime before the (2,1) tearing mode could develop. In REPUTE, the fast current ramp-up produced a paramagnetic pinch discharge (dq/dr < 0) that appeared to relax "quasistatically" to a less stable, peaked current profile (dq/dr > 0) typical of tokamak devices. Discharges with an initially peaked current profile could not pass the current limit at q(a) = 1 to reach the q(a) < 1 regime.

There is wide variation in the minimum q(a) obtained in these experiments. In general, however, major disruptions were no longer seen for q(a) < 2. In the range 2 > q(a) ≥ 1.3-1.4, most devices[19,23,47] obtained well confined discharges with $\tau_E \approx$ 300-500

μs, similar to τ_E in q(a) > 2 discharges. DIVA[19] reported τ_E as high as 5.7 ms, despite the dominant effect of the sawteeth on the transport. For 1.3 ≥ q(a) ≥ 1, τ_E drops to 50-100 μs.[19,23,47] Only the REPUTE[56] and TOKAPOLE II[57,59] devices were able to operate under stable conditions for q(a) < 1. In these discharges, $\tau_E \approx$ 50-100 μs as well.

In all devices operating at q(a) < 2, sawtooth oscillations dominated the energy transport. In a careful study of the energy confinement in the regime 1 ≤ q(a) ≤ 2 on the DIVA device,[19] an "ALCATOR-like" scaling:

$$\tau_E = n_l \sqrt{q(a)}\, a_{1/2}^2 \qquad (2.11)$$

where $a_{1/2}$ is the half-radius of the electron temperature profile, was obtained. This result is rather surprising, since generally sawteeth are insignificant for high q_a but not for low q_a. Thus, the physical mechanisms responsible for the transport are quite different for q(a) < and > 2. The result seems to arise from the scalings of sawtooth repetition and amplitude with n_l, q(a), and $a_{1/2}$.

II.B.2. Review of Theoretical Results:

There are essentially three classes of theoretical models to describe the triggering of disruptions in tokamaks: 1) single helicity (2,1) tearing mode interaction with a limiter or cold gas region, 2) nonlinear interaction of tearing modes of different helicities, and 3) coupling of tearing modes with transport effects induced by the

island structures. A significant difference in the multiple helicity calculations is the use of a plasma resistivity η = η(r) only. In each of the other classes, η is usually evolved self-consistently using some simple transport model for the effect of large scale MHD activity.

II.B.2.a. Single Helicity (2,1) Mode Simulations:

In one of the earliest models of major disruptions in tokamaks, Kadomtsev and Pogutse[62] found that the nonlinear development of ideal kink modes in a cylindrical plasma with a flat current profile (zero shear) trapped pockets of vacuum or cold plasma (so-called "vacuum bubbles") in the plasma boundary that are convected into the core by the plasma flows associated with the kinks. Shear, however, reduces the plasma distortion and Rosenbluth, et al.[63] concluded that ideal kink modes posed no threat to confinement in tokamaks.

With the inclusion of resistivity, the ideal kink modes become tearing modes. Under normal conditions, the (2,1) tearing mode is self-stabilizing due to its reduction of the destabilizing current density gradient. The (2,1) island saturates at a width w ≤ 0.4a for sufficiently high shear.[64] For low shear inside the q = 2 surface, however, very large islands are possible (w ≈ 0.7a for q(0) = 1.37).[64,65] When the plasma resistivity is evolved self-consistently to account for the effect of the large (2,1) islands, the hot central region is convected out to the edge while bubbles of cold plasma

move into the center, destroying confinement.[66]

In another early single helicity calculation, Sykes and Wesson[67] showed that the (2,1) tearing mode is strongly destabilized by contact with a limiter or cold gas region. The limiter contact cools the island and decreases the current density near the island O-point, enhancing the island growth. Since the (2,1) island grows mainly inward, such a scenario might correspond to a $q(a) \approx 2$ current limit disruption.

II.B.2.b. Multiple Helicity Tearing Mode Simulations:

In a series of classic multiple helicity resistive MHD simulations, Waddell and coworkers[68-70] found the nonlinear interaction of tearing modes of different helicities sufficient to trigger disruptions without evolving the plasma resistivity. Starting from an equilibrium highly unstable to both the (2,1) and (3,2) tearing modes, the (3,2) and higher order modes are strongly destabilized upon overlap with the (2,1) island. The (2,1), (3,2), and (5,3) island widths are plotted in figure 2.11 as a function of time, normalized to the resistive diffusion time τ_R. The island overlap leads to stochastic fields and the destruction of flux surfaces and confinement over a large portion of the plasma (figure 2.12).[71]

Although some authors have recently challenged the accuracy of the Oak Ridge calculations,[72-74] several independent simulations have verified the nonlinear destabilization of the (3,2) and higher

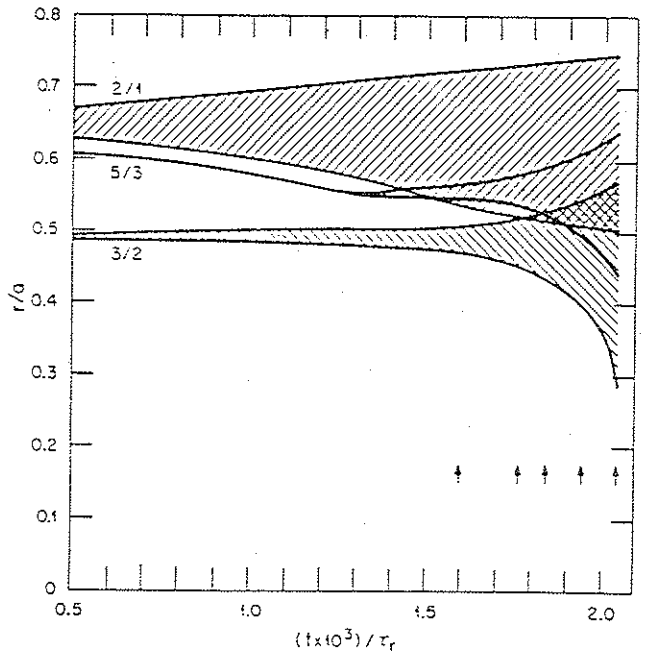

Figure 2.11: Evolution of the island widths for the (2,1), (3,2) and (5,3) modes in a multiple helicity simulation from reference 70. Growth of the (3,2) and (5,3) islands upon overlap with the (2,1) island is evident.

order modes, and subsequent development of short-wavelength turbulence.[71,75,76,77] Because of the constraints placed by numerical convergence,[71] it is not possible to follow the nonlinear development to the complete loss of confinement. Extrapolation of the result is needed to conclude that confinement is lost in the plasma core by this process. An additional difficulty with the multiple helicity simulations is the choice of an initial equilibrium highly unstable to the (2,1) and (3,2) modes, without stipulating how such an equilibrium could arise.[78]

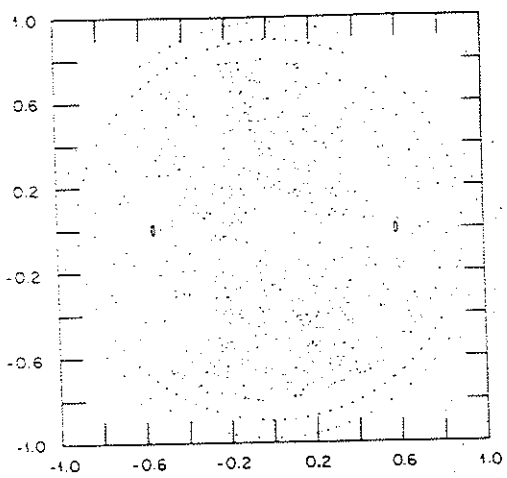

Figure 2.12: The magnetic field configuration at $t = {}_{685}\tau_{Hp}$ in a multiple helicity simulation. The magnetic field is stochastic in most of the region inside r/a = 0.8 (from reference 71).

II.B.2.c. Coupled Tearing Mode and Transport Simulations:

Several authors[79,80] have coupled transport processes to tearing mode calculations using relatively simple, one dimensional transport models to evolve the temperature profile self-consistently in the presence of large islands. The energy equation used to evolve the temperature includes thermal conduction, ohmic heating, and radiation losses. Island effects are included by flattening the temperature profile across the island. The effects of sawteeth are modeled by a large increase in thermal conductivity in the region where $q < 1$. The plasma current profile is evolved using a one dimensional diffusion equation with Spitzer resistivity, $\eta \propto T^{-3/2}$. In these simulations, the tearing modes of different helicity do not

interact directly, but effect each other through quasilinear modifications to the current profile. Hopcraft and Turner[80] initiated the simulations from an equilibrium with a saturated (2,1) island, rather than an axisymmetric equilibrium strongly unstable to the (2,1) and (3,2) modes. The plasma current was then increased in the simulation. This sequence more closely approximates experimental conditions than the initialization of the multiple helicity calculations.

In a typical simulation, a sequence of minor disruptions (pre-disruptions) leads to a major disruption at $t \approx 40$ ms (figure 2.13).[80] A minor disruption starts with the destabilization of the (2,1) tearing mode by an increasing current density gradient at the $q = 2$ surface. The growing (2,1) magnetic island flattens the current density profile about the $q = 2$ surface, advecting the current inward on the time scale of the island growth. The advected current increases the current density gradient inside the $q = 3/2$ surface, destabilizing the (3,2) tearing mode. The growth of the (3,2) island advects the current further inward, and actually stabilizes the (2,1) mode briefly by removing the current density gradient in the region $r < r(q = 2)$, as seen near $t \approx 24$ ms in figure 2.13. The rise in current at the axis, together with the restriction on the maximum current on axis by the $m = 1$ instability, forces the $q = 1$ surface outwards, transporting energy from the core to the edge and causing the temperature to drop. The cooling of the core dissipates the current near the axis and the $q = 1$ surface

contracts again.

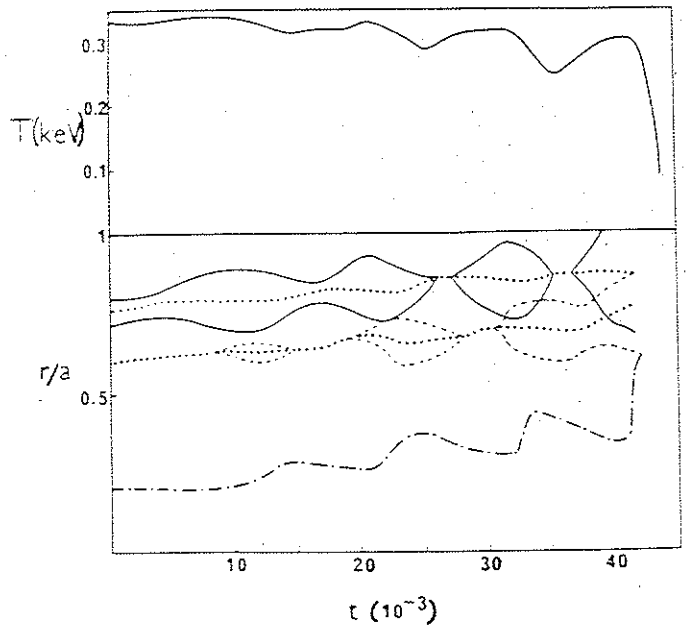

Figure 2.13: Evolution of the (2,1) (solid) and (3,2) (dashed) magnetic islands, together with the position of the q = 1 surface and central temperature (from reference 74).

The major disruption at 40 ms evolves somewhat differently. The (2,1) island contacts the limiter, leading to loss of the stabilizing portion of the current density gradient in the region $r > r(q = 2)$. The (2,1) island grows rapidly, intersecting the (3,2) island and thermally shorting the region $r > r(q = 3/2)$ to the limiter. The current profile contracts, moving the q = 1 surface outward until it connects with the (2,1) island. The entire plasma column is now thermally shorted to the limiter, and the central temperature falls abruptly.

These simulations suggest the following criteria for a major disruption:[80]

1) a large magnetic island intersecting a limiter or cold plasma mantle, most likely (2,1) for $q(a) \approx 2$-3.
2) an intermediate magnetic island resonant between the q = 2 surface and the magnetic axis, ensuring connection across the entire minor radius. This condition is sufficient, but not necessary for the disruption to proceed.
3) a method of restricting the amount of current flowing around the magnetic axis. This is provided by either the m = 1 instability (sawteeth) or, in discharges without sawteeth, by the accumulation of impurities near the magnetic axis.

When the one-dimensional transport model is replaced with a 3-D model,[76] the destabilization of the (3,2) and higher order modes takes the character of a shock moving inward from the q = 2 surface. In front of the shock, flux surfaces are intact but behind it the magnetic fields are stochastic and the plasma is turbulent. The shock appears to run out of driving energy when the q = 1 region is reached, and the $q \leq 1$ region is not penetrated. The central temperature drops in a sawtooth-like event due to the cold plasma surrounding the q = 1 surface. The resulting current density profile is essentially a step function inside the q = 1 surface.[76] This profile in a toroidal system is unstable to n = 1 ideal external kinks for

$q(0) > 1$, and the external kink terminates the discharge. In this model, the major disruption emerges naturally as a two step process, with the n = 1 external kink generating the negative voltage spike and the drop in plasma inductance.

II.B.2.d. Catastrophe Theory and Major Disruptions:

The weakest aspect of the theories outlined above is the mechanism for destabilizing the (2,1) tearing mode at the start of the disruption. For the multiple helicity calculations, some unspecified process creates the highly unstable equilibrium at the start of the simulation. This problem is particularly troublesome since under normal conditions, the (2,1) tearing mode is self-stabilizing, leading to a saturated final state.

Several authors[81,82] have attempted to explain the transition from a saturated island to disruption as a fold catastrophe. In linear theory, the measure of tearing mode instability is obtained by solving the equation:

$$\frac{1}{r}\frac{d}{dr}\left(r\frac{d\psi}{dr}\right) - \frac{m^2}{r^2}\psi - \frac{dj_o/dr}{B_{\theta o}(1 - nq/m)}\psi = 0 \quad (2.11)$$

where ψ is the perturbed flux function (α rB_r) for a mode with poloidal and toroidal mode numbers m and n, j_o and $B_{\theta o}$ are the equilibrium toroidal current density and poloidal magnetic field, and q is the safety factor. Solutions of equation 2.11 in the regions $r > r_s$ and $r < r_s$, where $r_s = r(q=m/n)$ is the resonant surface for the mode, are used to calculate:

$$\Delta' = \frac{\psi'}{\psi}\Bigg|_{r_s - \epsilon}^{r_s + \epsilon} \qquad \epsilon \to 0 \qquad (2.12)$$

If $\Delta' > 0$, the mode is unstable and a magnetic island forms. For small islands, the saturated island width w_s can be estimated from:

$$\Delta'(w_s) = \frac{\psi'}{\psi}\Bigg|_{r_s - w/2}^{r_s + w/2} = 0 \qquad (2.13)$$

as shown in figure 2.14a.[81] For large islands, the nonlinear modification of the equilibrium becomes important and the variables used in equation 2.11 are those consistent with the presence of the island. Equation 2.13 still gives the island width w_s but now there are two possible nonlinear equilibria with stability as indicated by the arrows in figure 2.14b. For varying conditions, there exists a family of such curves (figure 2.14c). When the catastrophe point w_{sc} is reached, there is no steady solution and the island grows disruptively. A series of such curves, calculated for disruptions at low q(a), is shown in figure 2.15. In figure 2.15b, the saturated island width is plotted as a function of 1/q(a), and clearly shows the catastrophic nature of the sudden growth in w at the critical q(a).

Although current limit disruptions arise naturally in several of the simulations considered above, none of the models predicts a critical density limit for stability. P.N. Guzdar[82] has formulated a catastrophe theory using a zero-dimensional electron energy

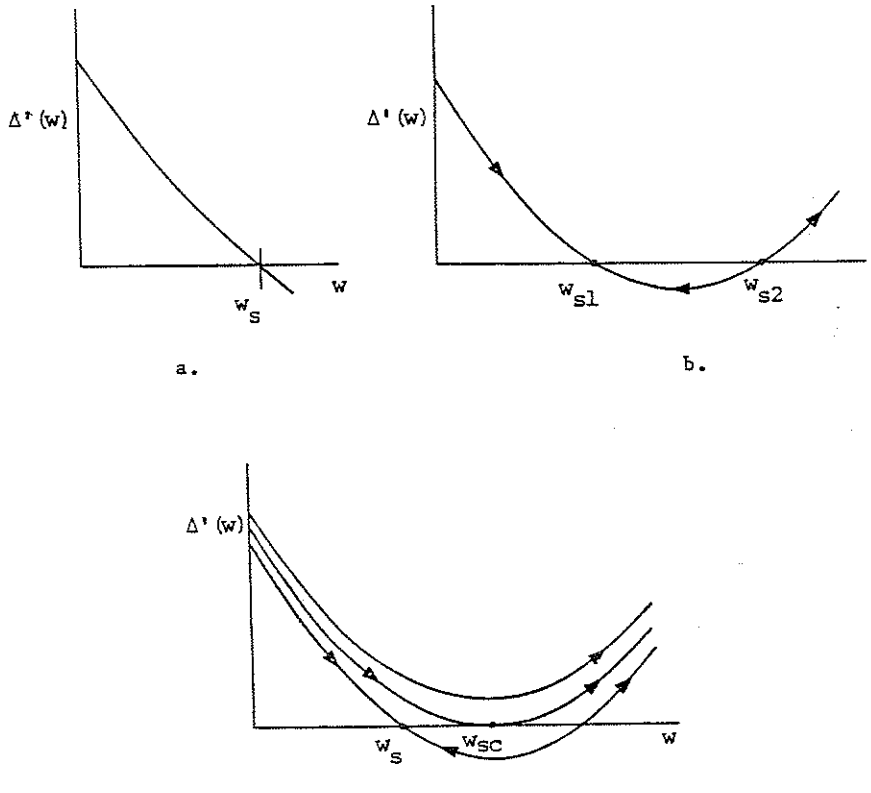

Figure 2.14: (a) Δ' versus island width w showing the determination of the saturation width w_s. The island grows until $\Delta'(w) = 0$. (b) Δ' versus w with inclusion of self-consistent modifications to the configuration. There are now two solutions, the stable w_{s1} and unstable w_{s2}. (c) Family of curves $\Delta'(w)$ for varying conditions, showing how w_s adjusts until the catastrophe point w_{sc} is reached. At w_{sc}, no steady solutions exist and the island grows disruptively (all from reference 81).

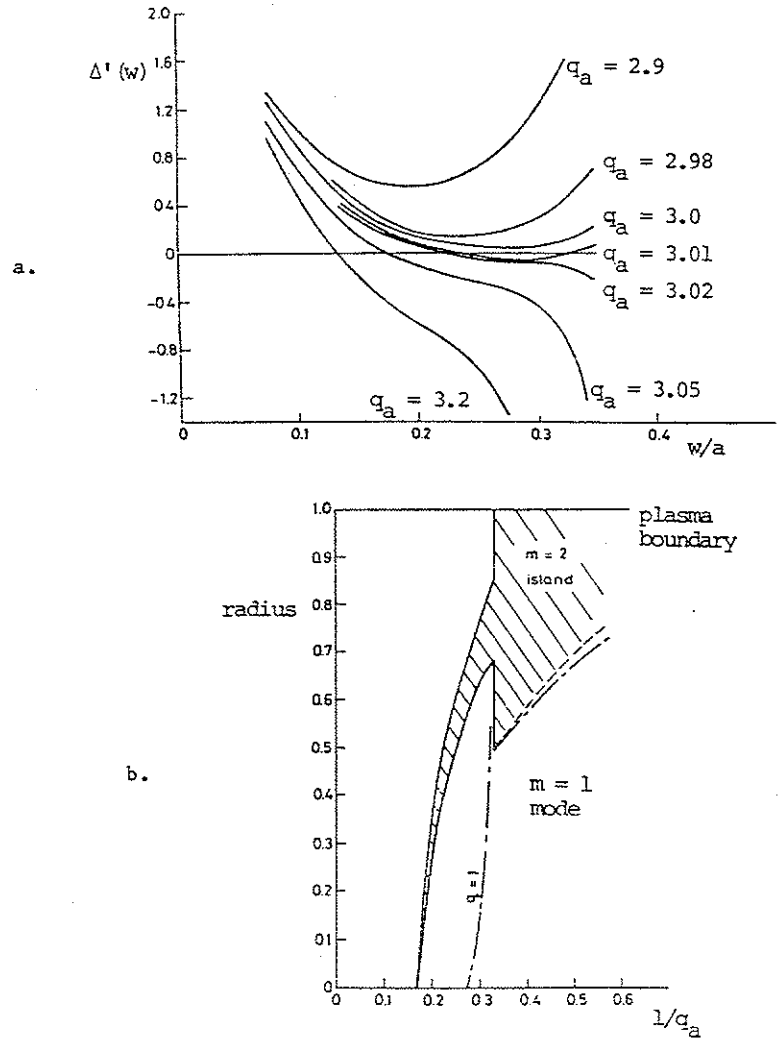

Figure 2.15: (a) Family of $\Delta'(w)$ curves for various values of q(a). (b) Saturated island width versus 1/q(a) showing the sudden change in w at the critical value of q(a) (from reference 81).

equation including anomalous heat conduction, ohmic heating, and

the electron-ion equilibration loss. For the two control parameters of density and toroidal field, the resulting cubic equation has two real roots that are physical (non-negative). The resulting equilibrium surface is shown schematically in figure 2.16.[82] The arrows indicate the stability in the upper and lower manifolds. Using this relatively simple model, Guzdar was able to obtain critical densities and time scales for disruption in reasonable agreement with both low density/high impurity and high density/low impurity tokamak experiments. One significant departure from experiment is the fact that the obtained critical densities are independent of plasma current.

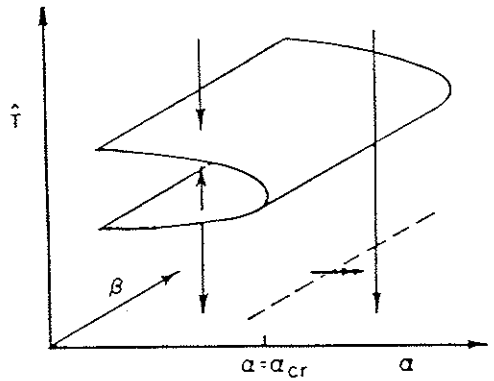

Figure 2.16: Equilibrium surface for a fold catastrophe with two control parameters α (n_l) and β (B_t). Catastrophe occurs as one crosses the bifurcation set (dotted line), as indicated by the double headed arrow. Stability in the upper and lower manifolds is indicated by the solid arrows (from reference 82).

Guzdar's calculations indicate that disruption arises from the

electron-ion equilibration losses overcoming the ohmic heating to the electrons. This suggests the remedy of converting this sink into a source by heating the ions to temperatures in excess of the electrons, as for instance with neutral beam or ion cyclotron heating.

II.B.2.e. Mode Locking and Stabilization by Resistive Walls:

The frequency with which the (2,1) precursor oscillations are observed to slow and lock just prior to disruption demands an explanation in terms of disruption models. The (2,1) tearing mode can be stabilized by resistive walls provided the mode rotates at a sufficiently high frequency. As long as the mode rotates fast enough, $\Delta' \rightarrow -\infty$ as $q(a) \rightarrow 2$ for a close-fitting wall, so that the (2,1) tearing mode becomes increasingly more stable as $q(a)$ is lowered toward 2. Eddy currents induced in the resistive wall, however, slow down the mode rotation, leading to destabilization of the mode as the rotation frequency drops.[83]

As long as the $q = 2$ surface is inside the conducting plasma, the rotation frequency is determined by the plasma flows locally at the resonant surface. If the $q = 2$ surface moves outside the conducting plasma, the mode can "slip" with respect to the plasma at the resonant surface. Wall stabilization is lost as the resonant surface reaches the wall and the mode locks to the wall, triggering the disruption.[76]

II.C. Internal Disruptions:

II.C.1. Review of Experimental Results:

One universal feature of tokamak operation is the observation of sawtooth oscillations in the central electron temperature and SXR emissivity. Because of the disruptive nature of the collapse, these oscillations are also called internal disruptions. Once believed to be well understood,[84,85] these oscillations display increasingly more complex behavior in present-day tokamaks as plasma resistivity decreases and dissipative effects become less important.[86-89]

II.C.1.a. Normal Sawteeth:

Sawtooth oscillations in most tokamaks are very regular and display similar characteristics (figure 2.17). There is a quiet phase during which the central temperature rises slowly due to ohmic heating and profile peaking and a precursor oscillation grows. This is followed by a disruptive collapse of the central temperature accompanied by a rise in the temperature in a ring around the central plasma. The precursor oscillations have a (1,1) structure, and the inversion of the central temperature collapse occurs at or near the q = 1 surface. The precursors result from a rotating (1,1) magnetic island at the q = 1 surface caused by the growth of the (1,1) resistive kink or tearing mode.

In the ORMAK device,[85] the precursor growth rate agreed well with the predicted linear growth rate of the (1,1) tearing mode up to the moment of collapse. The collapse was consistent with

complete reconnection, but the axisymmetric collapse was inconsistent with the single helicity heuristic model of Kadomtsev.[84] In low q discharges with $q_a \approx 1$ in TOKAPOLE II,[91] sawteeth displayed a helical (1,1) collapse consistent with complete reconnection in the Kadomtsev model.

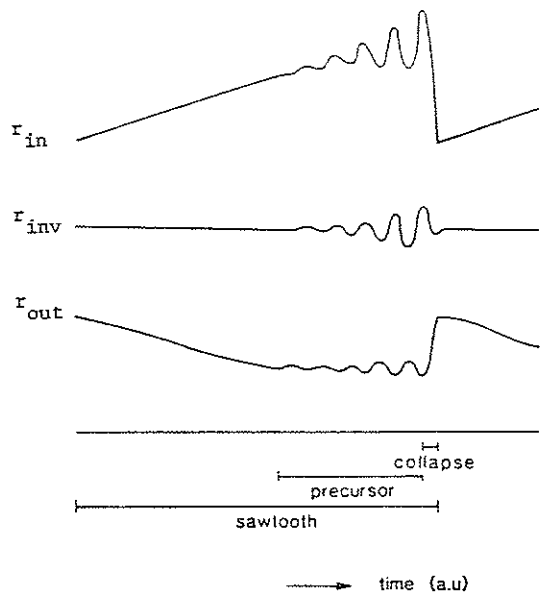

Figure 2.17: Evolution of SXR emissivity (or T_e) during a normal sawtooth cycle for three different plasma radii: inside (r_{in}), on (r_{inv}), and outside (r_{out}) the inversion radius where the sawtooth collapse changes sign.

In TFR,[92] however, the collapse could occur when the magnetic island was still very small. The collapse was best described not by complete reconnection but by a rapidly expanding zone of increased transport spreading through the plasma starting from the

separatrix of the island. Additional evidence for a collapse mechanism not associated with complete reconnection of the (1,1) island has been seen on T-10, where temperature profiles remained somewhat peaked following the collapse,[93] on TFR[92] and other devices[94] that display postcursor oscillations attributed to the island surviving the collapse, and on PLT,[95] where SXR tomography suggests the persistence of the island after the collapse.

Complete reconnection of the (1,1) tearing mode into the magnetic axis should relax q(0) to 1,[94,96] so accurate measurements of the current profile could provide valuable information on the question of complete reconnection. Current and safety factor profiles have been measured on only four tokamaks, TOKAPOLE II,[57,97] TEXTOR,[98] TEXT,[99] and ASDEX.[100] In TEXTOR and TEXT, q(0) was well below one, while in ASDEX, q(0) remained ≈ 1. Since the current profile can only evolve on the relatively long resistive diffusion time scale τ_R, it must be concluded that q can stay well below one throughout a sawtooth oscillation. Time resolved q profiles were obtained only in the TOKAPOLE II device, where q(0) remained stationary throughout several sawtooth oscillations.

II.C.1.b. Influence of Auxiliary Heating and Non-Inductive Current Drive:

Current profile effects on sawtooth dynamics have been investigated in several experiments by modifying the current profile

directly with non-inductive current drive or indirectly through alteration of the temperature profile with auxiliary heating. The localized nature of power deposition with electron cyclotron resonance heating (ECRH) makes it particularly suitable for the latter task.

In ECRH experiments on T-10[93] and CLEO,[101] heating well outside the q = 1 surface led to broad temperature profiles and stabilized sawteeth. In TFR,[102] however, neither heating inside or outside the q = 1 surface altered the sawtooth behavior. Instead, heating on the q = 1 surface slowed the precursor growth and in some cases saturated the (1,1) tearing mode at high power levels.

The most successful non-inductive current drive experiments have utilized lower hybrid current drive (LHCD). From experiments on ASDEX,[103] PETULA,[104] PLT,[105] and ALCATOR C,[106] it is found that sufficient LH power to non-inductively drive 30-50% of the total current stabilizes the sawteeth. On PETULA and ASDEX, the current profile broadens, and in the case of ASDEX, q(0) rises from just below 1 to just above 1 when the sawteeth disappear.[107] In the experiments on PLT and PETULA, however, an intermediate regime was observed where a saturated (1,1) oscillation remained after the sawteeth were stabilized.

II.C.1.c. Sawteeth in the Large Tokamaks:

In the largest tokamak devices (JET, TFTR, JT-60, and DIII-D), "compound" sawteeth with an intermediate collapse during the

main sawtooth rise are often seen (figure 2.18). The intermediate collapse leaves the central plasma unaltered and redistributes the energy in a ring around the sawtooth inversion radius. Both pre- and postcursor oscillations accompany the intermediate collapse, and often remain saturated until the next main collapse.

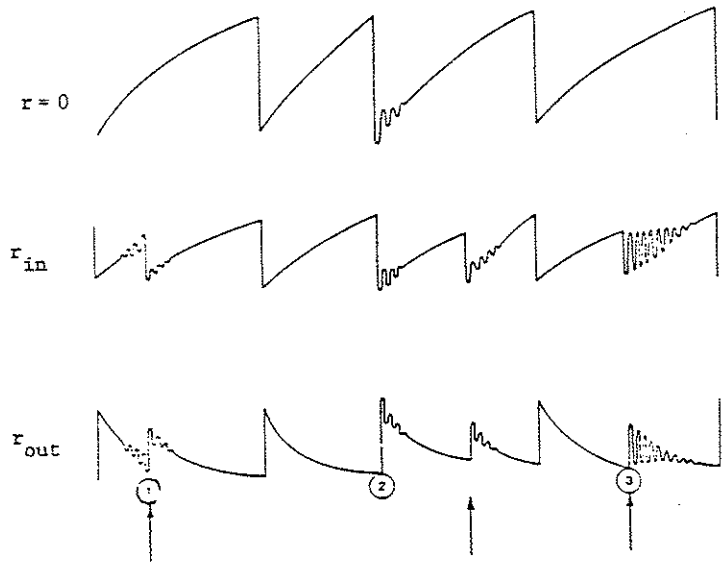

Figure 2.18: Compound sawtooth behavior observed in JET and TFTR at three different radii: axis (r_0) and inside (r_{in}) and outside (r_{out}) the inversion radius. The arrows indicate: (1) intermediate collapse with pre- and postcursor oscillations, (2) main collapse with postcursor oscillations, and (3) intermediate collapse with very large postcursor oscillations.

The main sawtooth collapse has no precursor, often has a postcursor, and in JET is very fast, typically 50-200 μs.[87] The temperature profile following the main collapse is either completely flat or hollow, and remains so if auxiliary heating is not applied.

Tomographic reconstructions[108] indicate that the fast collapse arises from a (1,1) kink of the hot plasma core that reaches a large amplitude in about 100 μs. A cold bubble is drawn into the discharge in the wake of the (1,1) kink. The kink saturates and mixes the hot plasma with the cold bubble in about 100 μs. Incomplete mixing leaves some poloidal asymmetry which gives rise to the postcursor oscillation.

Tomographic reconstructions of the intermediate collapse show a similar kink-like motion of the plasma core at the start of the collapse, but the kink never reaches a large amplitude. This suggests that the intermediate and main collapses have the same cause, but for some reason the collapse is stopped at an earlier stage during the nonlinear evolution.

II.C.2. Review of Theoretical Results:

Theoretical models for internal disruptions can be divided into two classes based upon the mechanism for the sawtooth collapse. In the first class, the collapse arises from mixing due to magnetic reconnection or plasma flows associated with the (1,1) ideal kink mode. In the second, the collapse is due to increased diffusive radial transport.

II.C.2.a. Reconnection and Mixing Models:

Kadomtsev first proposed the fast and complete reconnection of the helical flux inside and outside the q = 1 surface by the resistive

kink or tearing mode as the origin of the sawtooth collapse.[84] The basic validity of this model was verified in numerical simulations by Sykes and Wesson[6] (figure 2.19), but the reconnection time is too long for the collapse time observed on most tokamaks. Additionally, the heuristic model of Kadomtsev predicts a single helicity, (1,1) collapse, contrary to the axisymmetric collapse seen in most tokamaks.

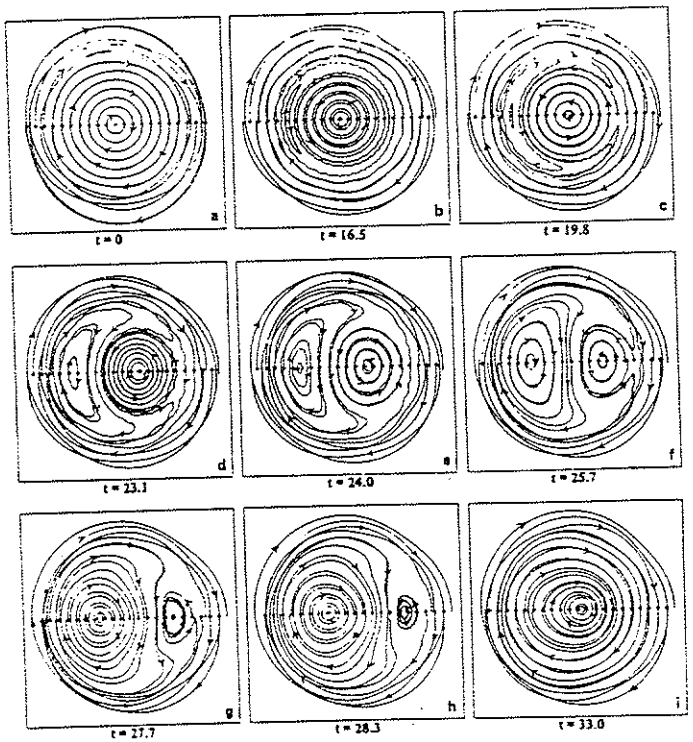

Figure 2.19: Sequence of magnetic field plots during one sawtooth oscillation, verifying the essential validity of the Kadomtsev reconnection model (from reference 6).

Jahns et al.[85] used this model to describe the sawtooth oscillations on the ORMAK device. The model predicts completely flattened or hollow profiles after the collapse and a rapid rise in q(0) to just above 1. These aspects are in contradiction to the peaked profiles after collapse seen in TFR and T-10 and with the TOKAPOLE II, TEXT, and TEXTOR measurements of q(0) much less than 1. This reconnection model is also unable to explain the compound sawteeth seen in the larger devices.

Several authors have extended the reconnection models to include compound and fast sawteeth. Compound sawteeth arise when two q = 1 surfaces exist in the plasma.[86,109] The extent of the reconnection is then determined by the details of the helical flux function ψ (figure 2.20). For a single q = 1 surface and $\psi(0) < \psi(q = 1)$, complete reconnection occurs. For two q = 1 surfaces and $\psi(r_2) \geq \psi(0)$, where r_2 is the radius of the outer q = 1 surface, the reconnection may still be complete (figure 2.20b and c). If $\psi(r_2) < \psi(0)$, the reconnection is localized to the region between the q = 1 surfaces and does not affect the plasma core (figure 2.20d).

The fast precursorless collapse of sawteeth in JET suggests an ideal MHD mechanism, and several authors have recently reinvestigated the m = 1 stability of tokamaks in an effort to explain the fast sawtooth collapses.[110-115] Complete understanding has been hindered by the complicated nature of m = 1 instability in toroidal systems.[114] Depending upon the details of the q profile, the magnetic Reynolds number S, the plasma β, and the aspect ratio,

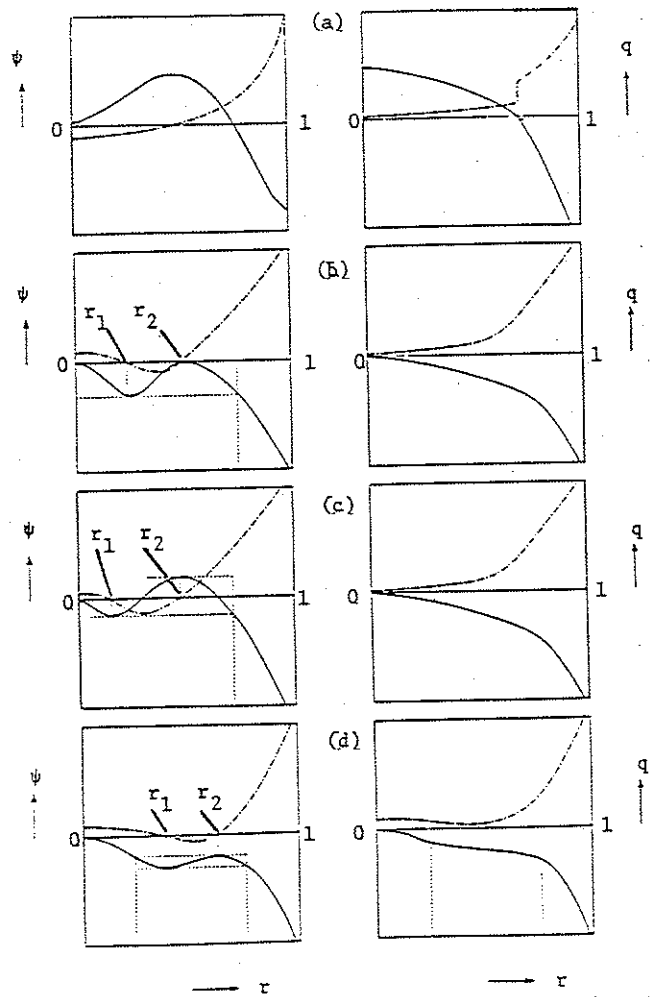

Figure 2.20: Different forms for the helical flux function ψ (solid) and q profile (dash-dot) before (left) and after (right) the sawtooth collapse leading to: (a) complete reconnection with a single q = 1 surface; (b) complete reconnection with q = 1 surfaces at r_1 and r_2 and $\psi(r_2) = \psi(0)$; (c) complete reconnection with q = 1 surfaces at r_1 and r_2 and $\psi(r_2) > \psi(0)$; (d) partial reconnection with q = 1 surfaces at r_1 and r_2 and $\psi(r_2) < \psi(0)$.

the m = 1 instability appears as the resistive kink, tearing mode, or ideal kink. Each form leads to different predictions for experimental observations.

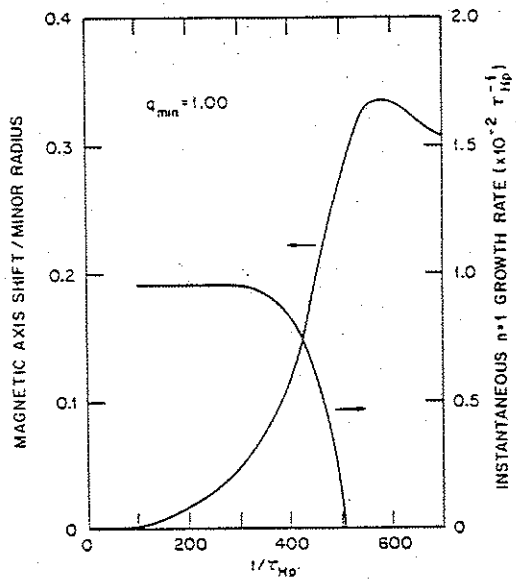

Figure 2.21: Instantaneous internal kink growth rate and magnetic axis shift versus time for q_{min} = 1.0 (from reference 114).

Nonlinear simulations in toroidal geometry[114] for hollow and low shear current profiles indicate that the m = 1 internal kink grows nonlinearly in the ideal linear time scale, several hundred to a thousand poloidal Alfvén times, consistent with the fast collapses observed on JET and TFTR. On this short time scale, magnetic surfaces are not broken by resistive effects. The instability saturates due to field line bending at finite amplitude, causing a helical shift of the magnetic axis (figure 2.21). The displacement

deforms the central flux surfaces into a crescent shaped region and carries outside flux surfaces into the center of the crescent, mixing the plasma (figure 2.22). Following saturation, magnetic reconnection proceeds on a slower time scale to relax the poloidal asymmetries.

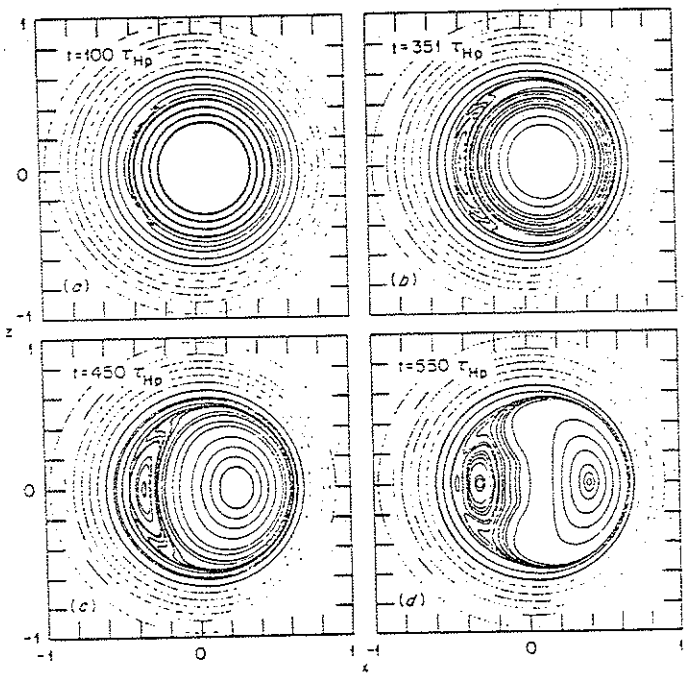

Figure 2.22: Magnetic field line plots of internal kink evolution for a hollow q profile in a circular cross section plasma (from reference 114).

The instability is sensitive to the q profile, and in low shear cases, to β. In the simulations, short time scales of order $10^3\tau_{Hp}$ and magnetic axis shifts of 20% of the minor radius can be obtained from q profile changes of only .003 from marginal stability. This

sudden transition from stability to robust instability with small changes in q is consistent with the rapid trigger of the experimentally observed fast sawtooth collapse.

II.C.2.b. Turbulent Models:

Several authors have proposed models of the sawtooth collapse based upon catastrophic increase in diffusive radial transport.[116-119] The turbulence arises from either microinstabilities when some threshold is exceeded[116,117] or from stochastisation of the magnetic field by secondary island overlap.[118,119] In each case, the turbulence is generated once the (1,1) island exceeds a critical size. Because the collapse is due to enhanced transport, the profiles remain peaked and the (1,1) island may persist after the collapse. Since the current profile need not change as dramatically as for complete reconnection, q(0) is not prevented from dropping well below 1.

II.C.3. Internal Disruption Summary:

There are clearly irreconcilable differences in both the experimental data and the theoretical models for sawteeth in tokamaks. These results suggest that sawteeth are not physically unique phenomena, but arise from two distinct mechanisms. In a high shear regime with q(0) well below 1 (e.g. TEXTOR, TFR, and T-10), profiles remain peaked and the sawtooth collapse likely arises from turbulent processes. In a low shear regime (e.g. TFTR and

JET), the temperature and density profiles are relatively broad and become flat or even hollow after a sawtooth collapse. These sawteeth, including compound and fast sawteeth, likely arise from reconnection and mixing processes.

REFERENCES

[1] S.W. Cousins and A.A. Ware, Proceedings of the Physical Society (London), A64, 159 (1951).

[2] Status of Tokamak Research, ed. by John M. Rawls, (U.S.D.O.E., Washington, D.C., 1979), 2-3 (1979).

[3] Status of Tokamak Research, ed. by John M. Rawls, (U.S.D.O.E., Washington, D.C., 1979), 1-2 (1979).

[4] J.A. Wesson, Nuclear Fusion, 18, 87 (1978).

[5] P.H. Rutherford, "Tearing Modes in Tokamaks", Physics of Plasmas Close to Thermonuclear Conditions, (Proc. of the Course, Varenna, 1979), 1, (Committee of the European Communities, Brussels, 1980), 129-142.

[6] A.Sykes and J.A. Wesson, Physical Review Letters, 37, 140 (1976).

[7] F.Troyon, et al., Plasma Physics and Controlled Fusion, 26, 209 (1984).

[8] T. Tuda, et al., Plasma Physics and Controlled Fusion Research, (Proc. 10th Int. Conf., London, 1984), 2, (IAEA, Vienna, 1985), 173.

[9] L.C. Bernard, et al., Nuclear Fusion, 23, 1286 (1981).

[10] A. Sykes, et al., Controlled Fusion and Plasma Physics, (Proc. 11th European Conference, Aachen, 1983), 7D Part 2, (European Physical Society, Geneva, 1983), 579.

[11] E.J. Strait, D.O. Overskei, and R.D. Stambaugh, Bulletin of the American Physical Society, 29, 1175 (1984).

[12] N.R. Sauthoff, S.von Goeler, and W. Stodiek, Nuclear Fusion, 18, 1445 (1978).

[13] K. McGuire, et al., Journal of Nuclear Materials, 121, 329 (1984).

[14] K. Yamazaki and G.L. Schmidt, Proc. of the 6th Int. Conf. on

Plasma Surface Interactions in Controlled Fusion Devices, Nagoya, 1984.

[15]F. Karger, et al., Plasma Physics and Controlled Fusion Research, (Proc. 6th Int. Conf., Berchtesgaden, 1976), 1, (IAEA, Vienna, 1977), 267.

[16]S.V. Mirnov and I.B. Semenov, Plasma Physics and Controlled Fusion Research, (Proc. 6th Int. Conf., Berchtesgaden, 1976), 1, (IAEA, Vienna, 1977), 291.

[17]Equipe TFR, Nuclear Fusion, 17, 1283 (1977).

[18]K.M. McGuire and D.C. Robinson, Physical Review Letters, 44, 1666 (1980).

[19]DIVA Group, Nuclear Fusion, 20, 271 (1980).

[20]A.A. Bagdasarov, et al., Plasma Physics and Controlled Fusion Research, (Proc. 9th Int. Conf., Baltimore, 1982), 3, (IAEA, Vienna, 1983), 281.

[21]S.V. Mirnov, Soviet Journal of Plasma Physics, 7, 436 (1981).

[22]F. Alladio, et al., Plasma Physics and Controlled Fusion Research, (Proc. 10th Int. Conf., London, 1980), 1, (IAEA, Vienna, 1981), 319.

[23]J.J. Ellis, et al., Plasma Physics and Controlled Fusion Research, (Proc. 8th Int. Conf., Brussels, 1980), 1, (IAEA, Vienna, 1985), 731.

[24]A.G. Kellman, et al., Bulletin of the American Physical Society, 29, 1363 (1984).

[25]S.B. Kim, T.P. Kochanski, and J.A. Snipes, University of Texas FRCR 256 (1984).

[26]TFR Group, Nuclear Fusion, 24, 784 (1984).

[27]S. Tsuji, et al, Nuclear Fusion, 25, 305 (1985).

[28]A.D. Cheetham, et al., Plasma Physics and Controlled Fusion Research, (Proc. 10th Int. Conf., London, 1984), 1, (IAEA, Vienna, 1985), 337.

[29]E.J. Strait, et al., Bulletin of the American Physical Society, 31, 1533 (1986).

[30]W.M. Manheimer and C. Lashmore-Davis, MHD Instabilities in Simple Plasma Configurations, (Naval Research Laboratory, Washington, D.C., 1984).

[31]K. Toi, et al., Nuclear Fusion, 22, 465 (1982).

[32]H. Niedermeyer, et al., Journal of Nuclear Materials, 93 & 94, 286 (1980).

[33]K.F. Alexander, et al., Nuclear Fusion, 24, 631 (1984).

[34]P. Couture and K. McGuire, PPPL-2380 (1986).

[35]M. Keilhacker, et al., Plasma Physics and Controlled Fusion Research, (Proc. 8th Conf., Brussels, 1980), 1, (IAEA, Vienna, 1981), 550.

[36]A. Bondeson, "Disruptions in Tokamaks", Theory of Fusion Plasmas, (Proc. of the Course, Varenna, 1987), in press.

[37]M. Murakami, J.D. Callen, and L.A. Berry, Nuclear Fusion, 16, 347 (1976).

[38]K.B. Axon, et al., Plasma Physics and Controlled Fusion Research, (Proc. 8th Int. Conf., Brussels, 1980), 1, (IAEA, Vienna, 1981), 413.

[39]JET Team, Plasma Physics and Controlled Fusion Research, (Proc. 11th Int. Conf., Kyoto, 1986), 1, (IAEA, Vienna, 1987), 31.

[40]D.J. Campbell, et al., Plasma Physics and Controlled Fusion Research, (Proc. 11th Int. Conf., Kyoto, 1986), 1, (IAEA, Vienna, 1987), 433.

[41]J.A. Snipes, et al., Controlled Fusion and Plasma Physics, (Proc. 14th Eur. Conf., Madrid, 1987), 11D, Part 1, (European Physical Society, Geneva, 1987), 69.

[42]D.E.T.P. Ashby and M.H. Hughes, Nuclear Fusion, 21, 911 (1981).

[43]F.W. Perkins and R.A. Hulse, Physics of Fluids, 28, 1837 (1985).

[44]A.G. Kellman, private communication, 1984.

[45]V.S. Vlasenkov, et al., Proc. 3rd Int. Symp. on Toroidal Confinement, Garching, 1973.

[46]A.G. Barsukov, et al., Controlled Fusion and Plasma Physics, (Proc. 10th European Conf., Aachen, 1983), 1, (European Physical Society, Geneva, 1983), 35.

[47]T. Edlington, et al., Plasma Physics and Controlled Fusion Research, (Proc. 9th Int. Conf., Baltimore, 1982), 3, (IAEA, Vienna, 1983), 241.

[48]A.B. Berlizov, et al., Plasma Physics and Controlled Fusion Research, (Proc. 8th Int. Conf., Brussels, 1980), 1, (IAEA, Vienna, 1981), 23.

[49]K.A. Razumova, Plasma Physics and Controlled Fusion, 26, 37 (1984).

[50]V.V. Arsenin, et al., Plasma Physics and Controlled Fusion Research, (Proc. 7th Int. Conf., Innsbruck, 1978), 1, (IAEA, Vienna, 1979), 233.

[51]Q.C. Zhao, et al., Plasma Physics and Controlled Fusion Research, (Proc. 10th Int. Conf., London, 1984), 1, (IAEA, Vienna, 1985), 345.

[52]H. Yamada, et al., Kakuyugo Kenkyu, 56, 341 (1986) [in English].

[53]Z. Yoshida, et al., Plasma Physics and Controlled Fusion Research, (Proc. 9th Int. Conf., Baltimore, 1982), 3, (IAEA, Vienna, 1983), 273.

[54]A.B. Berikov, et al., Plasma Physics and Controlled Fusion Research, (Proc. 8th Int. Conf., Brussels, 1980), 1, (IAEA, Vienna, 1981), 23.

[55]A. Mohri, et al., Plasma Physics and Controlled Fusion Research, (Proc. 10th Int. Conf., London, 1984), 3, (IAEA, Vienna, 1985), 395.

[56]Z. Yoshida, et al., NEUT Research Report 85-01.

[57]T.H. Osborne, R.N. Dexter, and S.C. Prager, Physical Review Letters, 49, 734 (1982).

[58]N.S. Brickhouse, et al., Plasma Physics and Controlled Fusion Research, (Proc. 10th Int. Conf., London, 1984), 1, (IAEA, Vienna, 1985), 385.

[59]T.H. Osborne, Ph.D. thesis, University of Wisconsin (1984).

[60]R.A. Moyer, et al., Bulletin of the American Physical Society, 31, 1594 (1986).

[61]K. Yamazaki, et al., IPPJ-796 (1986).

[62]B.B. Kadomtsev and O.P. Pogutse, Soviet Physics JETP, 38, 283 (1974).

[63]M.N. Rosenbluth, et al., Physics of Fluids, 19, 1987 (1976).

[64]R.B. White, D.A. Monticello, and M.N. Rosenbluth, Physical Review Letters, 39, 1618 (1977).

[65]J.F. Drake and R.G. Kleva, Physical Review Letters, 53, 1465 (1984).

[66]R.G. Kleva, J.F. Drake, and D.A. Boyd, Physics of Fluids, 29, 475 (1986).

[67]A. Sykes and J.A. Wesson, Physical Review Letters, 44, 1215 (1980).

[68]B.V. Waddell, et al., Physical Review Letters, 41, 1386 (1978).

[69]B.V. Waddell, et al., Physics of Fluids, 22, 896 (1979).

[70]B. Carreras, et al., Physics of Fluids, 23, 1811 (1980).

[71]H.R. Hicks, et al., ORNL/TM-9127 (1984).

[72]J.W. Eastwood and K.I. Hopcraft, Bulletin of the American Physical Society, 28, 1207 (1983).

[73]J.W. Eastwood and K.I. Hopcraft, Journal of Computational Physics, 60, 549 (1985).

[74]J.W. Eastwood and W. Arter, Physical Review Letters, 57, 2528 (1986).

[75]D. Biskamp and H. Welter, Plasma Physics and Controlled Fusion Research, (Proc. 9th Int. Conf., Baltimore, 1982), 3, (IAEA, Vienna, 1983), 373.

[76]A. Bondeson, Nuclear Fusion, 26, 929 (1986).

[77]R. Izzo, et al., Physics of Fluids, 26, 2240 (1983).

[78]J.W. Eastwood and W. Arter, CLM-P735 (1985).

[79]M.F. Turner and J.A. Wesson, Nuclear Fusion, 22, 1069 (1982).

[80]K.I. Hopcraft and M.F. Turner, Physical Review Letters, 56, 2372 (1986).

[81]J.A. Wesson, A. Sykes, and M.F. Turner, Plasma Physics and Controlled Fusion Research, (Proc. 10th Int. Conf., London, 1984), 2, (IAEA,Vienna, 1985), 23.

[82]P.N. Guzdar, Physics of Fluids, 27, 447 (1984).

[83]M.F.F. Nave and J.A. Wesson, Controlled Fusion and Plasma Physics, (Proc. 14th Eur. Conf., Madrid, 1987), 11D, Part III, 1103.

[84]B.B. Kadomtsev, Soviet Journal of Plasma Physics, 1, 389 (1975).

[85]G.L. Jahns, et al., Nuclear Fusion, 18, 609 (1978).

[86]W. Pfeiffer, Nuclear Fusion, 25, 673 (1985).

[87]D.J. Campbell, et al., Nuclear Fusion, 26, 1085 (1986).

[88]H. Yamada, et al., PPPL—2213 (1986).

[89]S.B. Kim, Nuclear Fusion, 26, 1251 (1986).

[90]M.A. Dubois, A.L. Pecquet, and C. Reverdin, Nuclear Fusion, 20, 1355 (1980).

[91]N.S. Brickhouse, et al., Physics of Fluids, 28, 3429 (1985).

[92]M.A. Dubois, A.L. Pecquet, and C. Reverdin, Nuclear Fusion, 23, 147 (1983).

[93]R. Sillen, et al., Nuclear Fusion, 26, 303 (1986).

[94]K. McGuire, private communication (1987).

[95]A. Compant La Fontaine, M.A. Dubois, and A.L. Pecquet, Plasma Physics and Controlled Fusion, 27, 229 (1985).

[96]N. Sauthoff, private communication (1987).

[97]T.H. Osborne, R.N. Dexter, and S.C. Prager, Physics of Fluids, 26, 350 (1983).

[98]G.H. Wolf, et al., Plasma Physics and Controlled Fusion, 28, 1413 (1986).

[99]W.P. West, D.M. Thomas, and J.S. DeGrassie, Physical Review Letters, 26, 2758 (1987).

[100]ASDEX Group, Controlled Fusion and Plasma Physics, (Proc. 14th Eur. Conf., Madrid, 1987), (European Physical Society, Geneva, 1987).

[101]A.C. Riviere, et al., 4th International Symposium on Heating in Toroidal Plasmas, 21—28 March, 1984, Rome, Italy, 2, 795.

[102]TFR Group and FOM ECRH Team, 13th European Conference on Controlled Fusion and Plasma Heating, 14—18 April, 1986, Schliersee, FRG, 2, 207.

[103]F.X. Soeldner, et al., 13th European Conference on Controlled Fusion and Plasma Heating, 14—18 April, 1986, Schliersee, FRG, 2, 319.

[104]D. van Houtte, et al., 13th European Conference on Controlled Fusion and Plasma Heating, 14—18 April, 1986, Schliersee, FRG, 2, 331.

[105]T.K. Chu, et al., Nuclear Fusion, 26, 666 (1986).

[106]M. Porkolab, et al., 13th European Conference on Controlled Fusion and Plasma Heating, 14—18 April, 1986, Schliersee, FRG, 2, 445.

[107]K. McKormick, et al., 13th European Conference on Controlled Fusion and Plasma Heating, 14—18 April, 1986, Schliersee, FRG, 2, 323.

[108]A.E. Edwards, et al., Physical Review Letters, 57, 210 (1986).

[109]R.E. Denton, et al., Physical Review Letters, 56, 2477 (1986).

[110]J.A. Wesson, Plasma Physics and Controlled Fusion, 28, 243 (1986).

[111]J.A. Wesson, P. Kirby, and M.F. Nave, Plasma Physics and Controlled Fusion Research, (Proc. 11th Int. Conf., Kyoto, 1986), 2, (IAEA, Vienna, 1987), 3.

[112]D. Biskamp and H. Welter, Plasma Physics and Controlled Fusion Research, (Proc. 11th Int. Conf., Kyoto, 1986), 2, (IAEA, Vienna, 1987), 11.

[113]M.N. Bussac, et al., Plasma Physics and Controlled Fusion Research, (Proc. 11th Int. Conf., Kyoto, 1986), 2, (IAEA, Vienna, 1987), 17.

[114]J.A. Holmes, et al., ORNL/TM-10585 (1987).

[115]A.Y. Aydemir, Physical Review Letters, 59, 649 (1987).

[116]A. Samain, Plasma Physics, 18, 551 (1976).

[117]M.A. Dubois and A. Samain, Nuclear Fusion, 20,1101 (1980).

[118]C. Mercier, Soviet Journal of Plasma Physics, 9, 82 (1983).

[119]A.J. Lichtenberg, Nuclear Fusion, 24, 1277 (1984).

Chapter 3
DEVICE DESCRIPTION AND EXPERIMENTAL METHODS

These experiments were conducted on Tokapole II[1] (figure 3.1), a poloidal divertor tokamak operating at the University of Wisconsin—Madison Physics Department since March, 1978. The engineering and physics considerations involved in the design of the device are covered elsewhere.[2,3] The features relevant to this work are presented in this chapter.

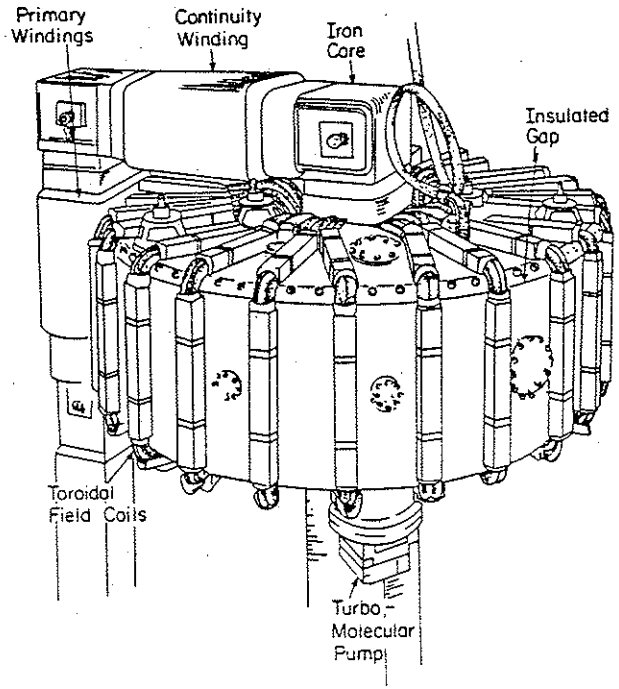

Figure 3.1: The Tokapole II device.

a.

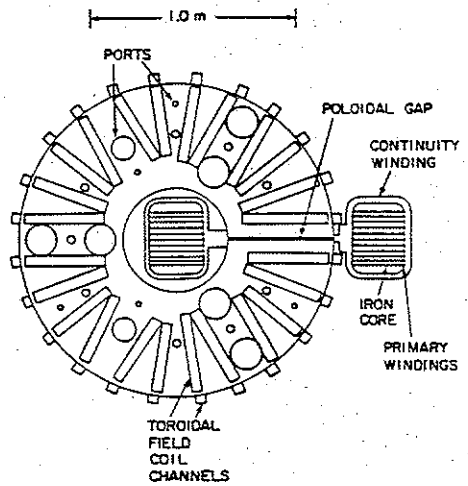

b.

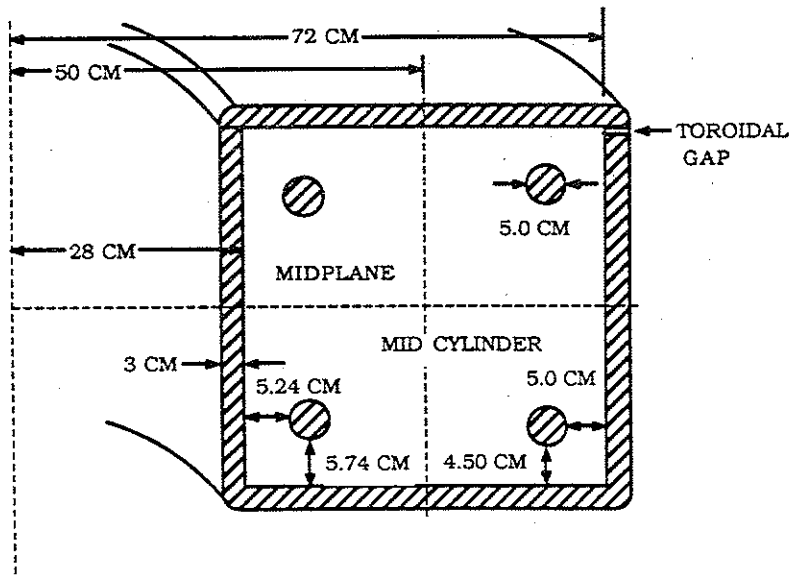

Figure 3.2: (a) Top view and (b) poloidal cross section of the Tokapole II vacuum vessel.

III.A. Tokapole II Device:

Tokapole II is a small tokamak with a major radius of 50 cm and a 44 square cm aluminum vacuum vessel (figure 3.2). The vessel walls are 3 cm thick and have two insulating breaks or "gaps", one poloidally and one toroidally, to allow the magnetic fields to penetrate. The vessel encloses four 5 cm diameter, chromium-copper toroidal rings each supported at three points toroidally by beryllium-copper rods.

The divertor field is obtained by driving toroidal current in the rings inductively in parallel with the plasma current through a 40:1 turns-ratio iron core transformer of .15 volt-seconds. The transformer primary current is supplied by a 7.4 mF, 5 kV capacitor bank and can be power crowbarred with a diode-switched .96 F, 450 V capacitor bank. Total ring currents range from 200 to 360 kA. The vacuum field from the rings produces an octupole pattern of poloidal flux contours, shown in figure 3.3a. Due to the position of the rings within the vacuum vessel, about half the poloidal flux encircles all four rings ("common flux") and half encircles a single ring ("private flux"), resulting in a vacuum electric field to drive the plasma current at the geometric axis that is about half the applied voltage across the poloidal gap.

The poloidal flux contours with plasma current are shown in figure 3.3b. In these experiments, plasma current varied from 8 to 50 kA. The divertor configuration of the poloidal magnetic field possesses two separatrices that together contain four saddle points

a.

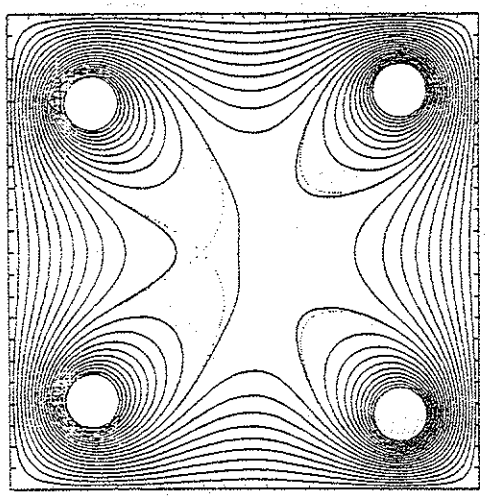

b.

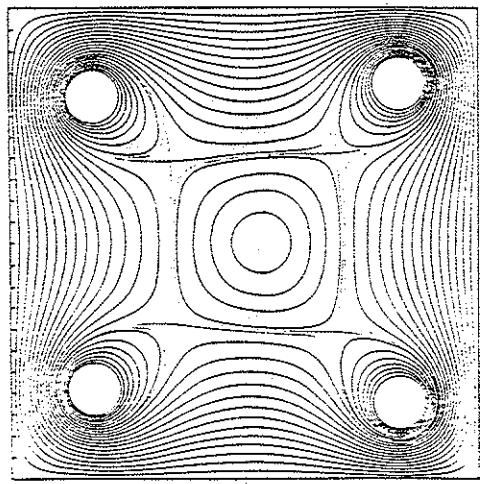

Figure 3.3: (a) Vacuum poloidal flux plot (ring currents only) and (b) equilibrium poloidal flux plot with plasma current present.

("x-points") where the poloidal field vanishes. These flux contours separate regions of topologically distinct flux contours. In this thesis, the region of flux contours inside the separatrices will be referred to as the "central current channel", the region outside the separatrices will be referred to as the "scrape-off region", and the inner and outer separatrices will be referred to for simplicity as the "separatrix".

Tokapole II is equipped with two retractable stainless steel limiter plates on the inner and outer walls that can be inserted beyond the separatrix at one toroidal azimuth. Two additional limiter plates are mounted on the lid and floor at the same azimuth but do not extend completely to the separatrix. The limiter plates allow operation of the Tokapole II in either of two configurations, "magnetic limiter" configuration with the plates retracted at least several centimeters beyond the separatrix and "material limiter" configuration with the plates inserted to the divertor separatrix. These configurations are shown in figure 3.4. The top and bottom limiter plates are also shown for reference in figure 3.4.

The limiter plates allow controlled variation of the plasma boundary conditions and interaction with the magnetic separatrix. In the material limiter configuration, the boundary of the central current channel is defined by the limiter plates which "scrape off" plasma and current outside the separatrix, while in the magnetic limiter configuration, the boundary is defined by the magnetic

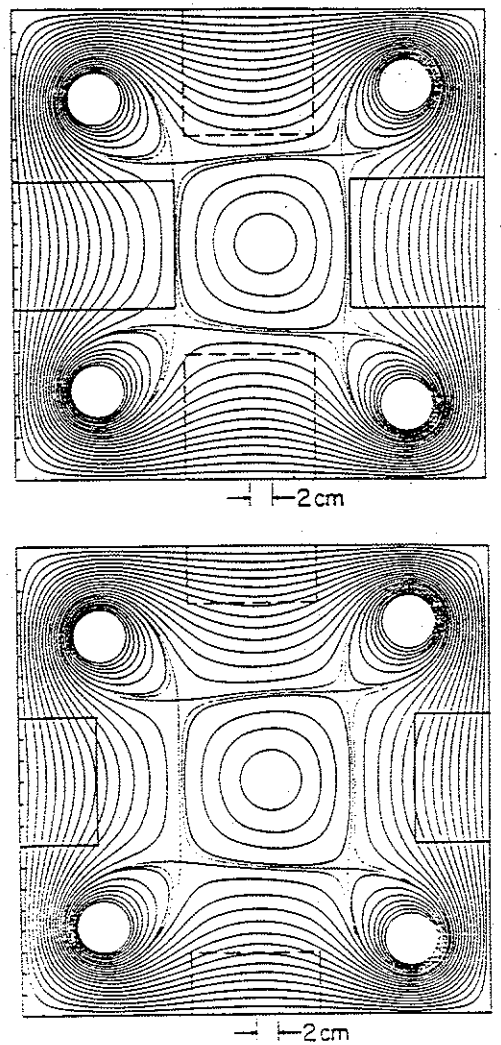

Figure 3.4: Poloidal cross section showing limiter plate configuration relative to the equilibrium poloidal flux plot in (a) material limiter discharges, and (b) magnetic limiter discharges, where the limiter plates are withdrawn at least halfway to the vacuum vessel wall. The top and bottom limiter plates (dashed) are shown for reference.

separatrix of the divertor. While the material limiter configuration is similar to many other tokamaks, the magnetic limiter configuration differs from most other divertor tokamaks in two respects: 1) aside from the rather small ring supports, the nearest material limiter is far from the edge of the plasma current channel, and 2) substantial toroidal plasma current may flow in the divertor scrape-off region beyond the separatrix, permitting shallow gradients in plasma parameters at the edge of the current channel. Since plasma current and pressure gradients are important in determining plasma stability, disruptions may be expected to behave significantly different in Tokapole II.

Because the divertor ring current is inductively driven rather than directly driven, determination of the plasma current and surface loop voltage in a non-perturbing manner is not possible. These, and other quantities, must be determined from the only signals directly measurable, the voltage applied across the poloidal gap V_{pg}, measured with a single turn flux loop around the iron core, and the primary current I_{pr}, measured with a .001 Ω resistive shunt in series with the primary windings.[4] To deduce the plasma and ring currents from these it is necessary to use some reasonable model of the plasma current profile. The model used, and the quantities derived from it, is presented in Section III.B.1.

In this experiment, disruptive behavior was studied as the effective edge safety factor q_a was varied over the range $3 \geq q_a > 0.5$. In the range $3 \geq q_a \geq 1$, this scan was achieved by fixing the

plasma density, toroidal field, and waveform of the voltage applied across the poloidal gap V_{pg}. The V_{pg} waveform and corresponding plasma current I_p and total divertor ring current I_r for a typical $q_a > 1$ discharge are shown by the solid lines in figure 3.5. The main capacitor bank voltage is critically damped by a resistor connected in series with the transformer windings and clamped by the crowbar capacitor bank through a diode when the main bank voltage has fallen to the crowbar bank voltage.

For fixed density and toroidal field, q_a could be lowered continuously from $q_a \sim 4$ to $q_a \sim 1$ by ramping the plasma current up with larger poloidal gap voltages. Unfortunately, due to mechanical strength limitations of the divertor rings and ring supports, it was not possible to lower q_a below 1 with the waveform in figure 3.5 at constant toroidal field. In order to obtain discharges with $q_a < 1$, the damping resistor was removed from the primary circuit, yielding the quarter sine wave shown by the dashed line in figure 3.5. The diode stack and crowbar capacitor bank were used to clamp the voltage to some value ≥ 0 V in this case as well, although with little effect due to the short duration of the discharges.

The toroidal field system consisted of 96 poloidal windings in 24 groups of 4 driven by a .52 mF, 5 kV capacitor bank. This bank is clamped by an ignitron across the windings when the bank voltage reaches zero. Typical on-axis toroidal field waveforms in high and low q_a discharges are also shown in figure 3.5. The toroidal field on

axis was lowered from 5 kG to 1.5 kG in order to attain the lowest q_a values studied.

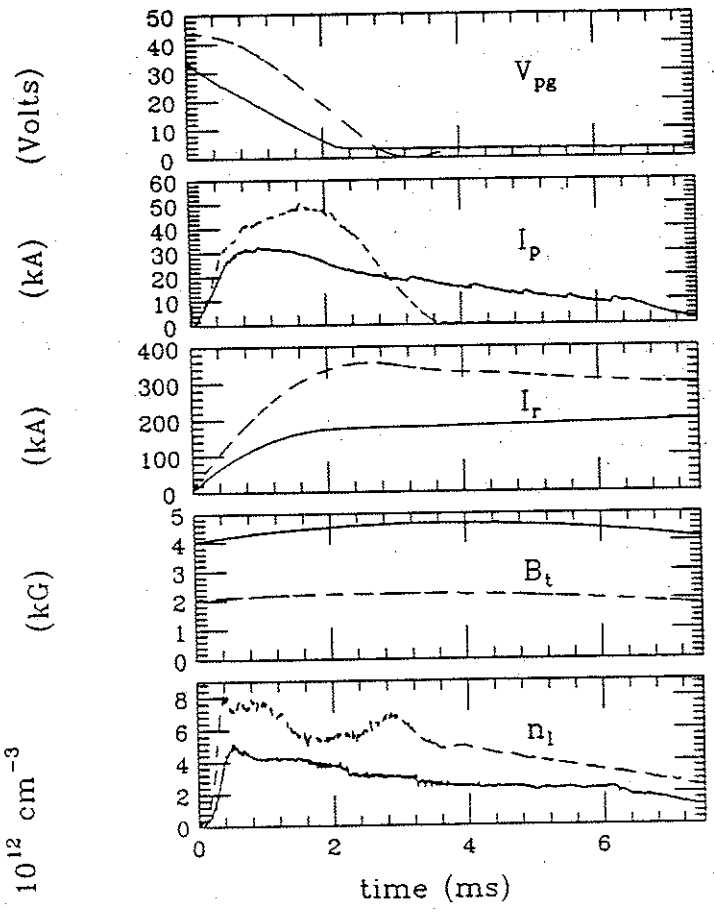

Figure 3.5: Typical waveforms of poloidal gap voltage V_{pg}, plasma current I_p, total divertor ring current I_r, toroidal field B_t, and line averaged electron density n_l in typical (solid) $q_a > 1$ magnetic limiter and (dashed) $q_a < 1$ magnetic limiter discharges.

Hydrogen gas is puffed into the vacuum vessel 16.66 ms before the discharge through a piezoelectric valve. Typical fill pressures are 3-10 $\times$ 10^{-4} torr. Refueling is accomplished via gas puffing utilizing feedback control of the piezoelectric valve. Preionization is accomplished with S, X, or K band microwaves, depending upon the toroidal field strength.

III.B. Diagnostics:

III.B.1. Routine Diagnostics:

As mentioned in Section III.A, the plasma and divertor ring currents must be determined from the poloidal gap voltage V_{pg} and the transformer primary current I_{pr} assuming some reasonable model of the plasma current profile. The justification for the model used is presented elsewhere;[5,6,7] briefly, the model assumes that the current profile is such that in some appropriate flux space average, the current can be treated as if it were all concentrated at the geometric axis (octupole null).

With this assumption and the circuit model shown in figure 3.6[7], the plasma and ring currents are given by:

$$I_p = \frac{N}{\alpha} I_{pr} - \frac{1}{\alpha L_r} \int V_{pg} dt + \frac{1}{\alpha L_r} \int I_r R_r dt \qquad (3.1)$$

$$I_r = N I_{pr} - I_p \qquad (3.2)$$

where α = private flux/common flux in the absence of plasma (~ .5), N is the primary turns ratio (typically 40), I_p is the plasma current (kA), I_r, R_r, and L_r are respectively the divertor ring

current (kA), resistance (ohms), and inductance (H), and V_{pg} is the poloidal gap voltage (V). An analog computer circuit solves these equations, including several other effects such as magnetic field soak-in to the rings and changing ring resistance.

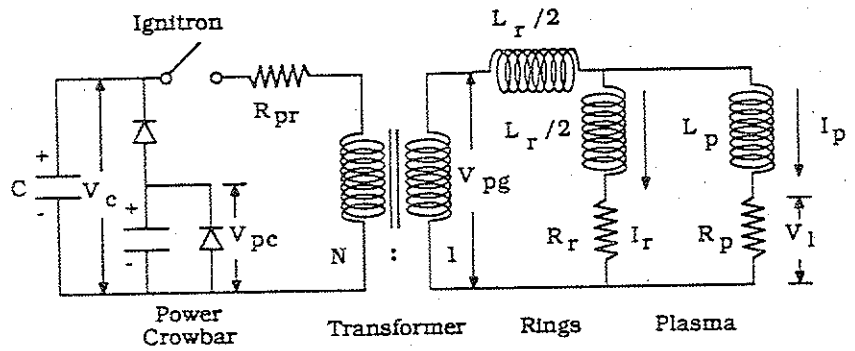

Figure 3.6: Circuit model from reference 7 to model Tokapole II.

From I_p, I_r, and V_{pg} one can derive the following quantities of interest:

$$a = 17.3 \left| I_p / (I_p + I_r) \right|^{1/4} \qquad (3.3)$$

where a is the radius in cm of a circle of the same cross-sectional area as that enclosed by the square-shaped plasma inside the separatrix (the central current channel).[8] By assuming that the plasma current density is uniform over the cross-section of a circle of radius a centered on the geometric axis, one can derive an "effective edge safety factor" q_a:

$$q_a = 10^{-4} a^2 B_t / I_p \qquad (3.4)$$

where B_t is the toroidal field in kG. Using the circuit model in figure 3.6, one can derive the resistive portion of the loop voltage V_l, the voltage around a contour encircling the machine toroidally at the magnetic axis, as:

$$V_l = \alpha V_{pg} + (1-\alpha) R_r I_r - \alpha(1-\alpha) L_r \frac{dI_p}{dt} - \frac{d}{dt}(L_p I_p) \qquad (3.5)$$

The quantity $L_p + \alpha(1-\alpha)L_r$ was measured experimentally to have a value of ~ 0.7 μH. That portion of the term $I_p dL_p/dt$ due to a simple expansion or contraction of the minor radius due to a change in plasma current was measured, but current profile changes, important in external disruptions, are not properly modeled Only the low frequency part of the loop voltage is therefore obtained.

Once the loop voltage is obtained, the electron conductivity temperature T_e^{cond} is determined from:

$$R_p = V_l / I_p \qquad (3.6)$$

where V_l is given by equation 3.5, I_p by equation 3.1, and the electron conductivity temperature is determined from the plasma resistivity R_p assuming Spitzer resistivity[9] and $Z_{eff} = 1$.

The poloidal ohmic heating rate follows from:

$$P_{oh} = V_l I_p \qquad (3.7)$$

The global energy confinement time is determined by assuming a steady state and equating the ohmic heating rate with the energy loss rate:

$$P_{oh} = P_{loss} = \frac{E_k}{\tau_E} \qquad (3.8)$$

yielding:

$$\tau_E = \frac{3/2<nk(T_i + T_e)>}{P_{oh}} \qquad (3.9)$$

where T_i is generally negligible compared to T_e ($T_i \approx 0.2\text{-}0.25\ T_e$ for $q_a > 1$), and the "< >" denote an average over the plasma volume inside the vacuum vessel, including the divertor scrape-off region.

The line average density n_l is measured with a 70 GHz microwave interferometer along a vertical chord from floor to ceiling passing through the center of the vacuum vessel at the midplane. To reduce ambiguities in plasma density arising from the large volume of moderate density plasma in the scrape-off region, the separatrix-to-separatrix line average density, designated by n_l^{core}, is obtained from n_l by subtracting the measured scrape-off profile contribution. Typical density traces are also shown in figure 3.5. Routine monitoring of several light impurity lines is discussed in Section III.B.4.

III.B.2. Electrostatic Probes:

Due to the low ion and electron temperatures in the Tokapole II device, it is possible to use probes for plasma diagnostics. Electrostatic and magnetic probes have been used extensively to study the properties of the scrape-off region plasma and, to a lessor extent, to study the properties of the central current channel plasma. Of considerable interest in this work was direct verification of the changes in the central current channel boundary conditions

through insertion of the material limiter plates. In this section, electrostatic probe techniques employed to measure plasma density, electron temperature, and kinetic pressure are briefly presented. Magnetic probe techniques are discussed in section III.B.3. Thorough discussions of electrostatic probe techniques can be found in references 10, 11, and 12.

A cutaway view of a typical electrostatic probe used in this work is shown in figure 3.7. The collecting area consists of one to three 5-10 x 10^{-2} cm^2 platinum wires mounted in an alumina rod. Typical tip-to-tip spacings are 2 mm. Vacuum feedthroughs consisting of teflon inserts in swagelock fittings are used at the back of the probe to bring the signals out from each tip. Electrostatic shielding between each tip is provided by braids on each wire and by the 1/4 inch outside diameter stainless steel tube which also functions as the vacuum boundary.

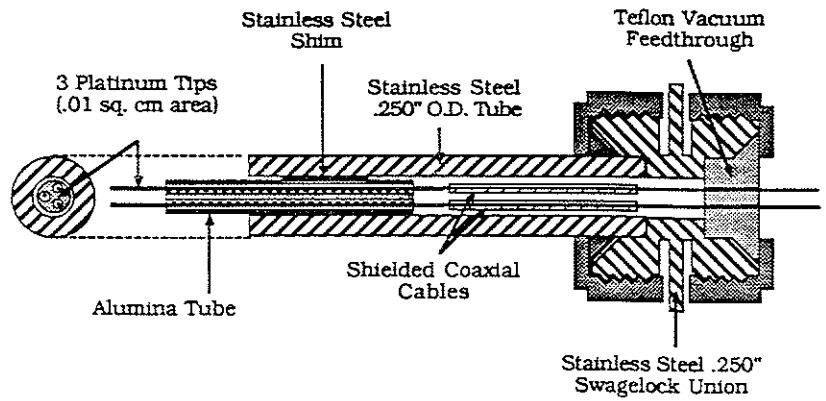

Figure 3.7: Cutaway view of electrostatic probe with three tips used in this experiment.

Components are cleaned ultrasonically in acetone and/or ethyl alcohol as appropriate for the materials prior to assembly. Before use, oils and contaminants are removed with ethyl alcohol. Under vacuum, additional cleaning is achieved by pulse discharge cleaning in 10-20 kA, mid-10^{12} cm^{-3} density discharges. Due to the presence of copper rings and ring supports within the vacuum vessel, glow discharge cleaning tends to deposit or "track" copper across the alumina, shorting the adjacent tips.

One or two of the probe tips are used to measure the ion saturation current I_{oi}:

$$I_{io} = j_{io} A = (\tfrac{1}{4} n e \bar{v}^*) C A \qquad (T_i \le T_e) \qquad (3.10)$$

where n is the plasma density in cm^{-3}, e is the fundamental charge, A is the collecting area, and $\bar{v}^*$ is the mean velocity of ions collected by the probe:

$$\bar{v}^* \approx \sqrt{\frac{8kT_e}{\pi m_i}} \qquad (3.11)$$

for a Maxwellian. Here, T_e is the electron temperature, k the Boltzman constant, and m_i the ion mass. The appearance of electron temperature and ion mass in equation 3.11 is physically reasonable since the force driving ions into the probe is the plasma pressure nkT_e.[11,13]

C is a correction factor for finite temperature and orbital motion effects.[14] For Tokapole II scrape-off plasma parameters and the probes used in this experiment,

$$10 \le \frac{R_p}{\lambda_{D-}} \le 20$$

$$3 \le \frac{e\phi_p}{kT_e} \le 4$$

$$.5 \le \frac{T_i}{T_e} \le 1$$

where R_p is the probe tip radius, λ_{D-} the electron Debye length, and ϕ_p the probe bias potential, C is between 1.8 and 2.1. The value C = 2.0 was selected for this work.

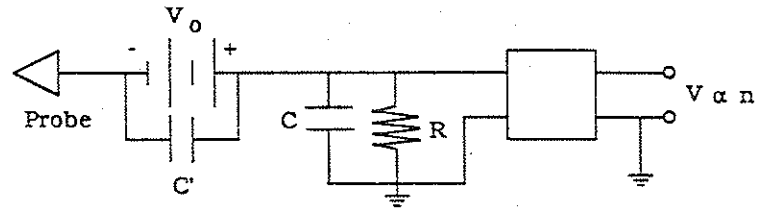

Figure 3.8: Electrostatic probe circuit for a single low impedance probe used to measure ion saturation current.

A typical probe circuit for a single low impedance probe is shown in figure 3.8. Proper operation of this probe requires that the bias voltage applied to the probe tip V_o and resistance through which the ion saturation current flows R satisfy the following conditions:

$$V_o >> kT_e / e \qquad (3.12)$$

$$R << V_o / I_{io} \qquad (3.13)$$

$$\frac{1}{2\pi f C} >> R \qquad (3.14)$$

Condition 3.12 assures that the probe is biased to saturation. Three to ten times the electron temperature is usually satisfactory; in these experiments, the scrape-off region electron temperature ranges from 10-40 eV, and the probes are biased to 80-100 V. Condition 3.13 ensures that the voltage on the probe tip remains at V_o even for large ion saturation currents I_{oi}. Typical values for R in this experiment were 1-10 Ω with ion saturation currents I_{oi} of ~ 2 A. Condition 3.14 defines the upper frequency limit of the probe. Since C in condition 3.14 is the cable capacitance and input capacitance of the coupling device used (typically tens of picofarads), the upper frequency limit is generally set by the maximum digitizing rate, 1 MHz. The probe signal was routinely low pass filtered to 300 kHz to avoid aliasing in the digitizer.

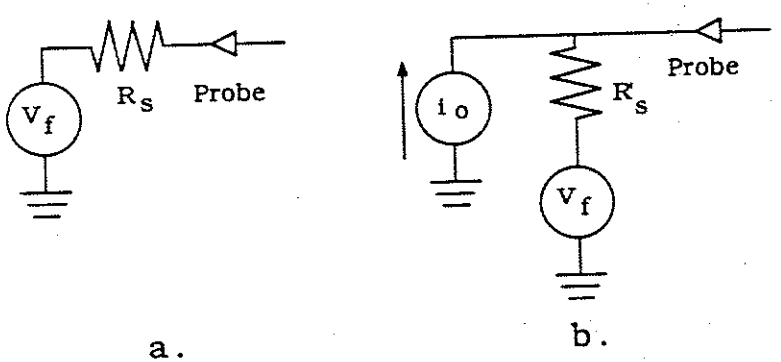

Figure 3.9: Equivalent electrical circuits for the plasma driving (a) a high impedance probe, and (b) a low impedance probe, showing the relationship between R_s and R_s'.

One serious drawback of a single low impedance probe is that

floating potential fluctuations produce a signal that cannot be distinguished from the signal proportional to density[11]. Proper operation of the probe in the presence of such potential fluctuations requires additionally:

$$V_o >> V_f \qquad (3.15)$$

$$I_{io} R_s' >> V_f \qquad (3.16)$$

where R_s', the effective sheath resistance, is the inverse slope of the V—I characteristic at the point $V = V_o$. The relationship between R_s' and the sheath resistance R_s measured at the floating potential V_f is indicated by the equivalent circuits of the plasma shown in figure 3.9. A calculation of R_s by Taylor series expansion has been done;[15] the result is:

$$R_s = \left[\frac{2\pi m_i}{kT^*}\right]^{1/2} = \frac{kT_e}{e}\,\frac{1}{j_{oi}A} \qquad (3.17)$$

where j_{oi} is the ion saturation current density drawn by the probe, A is the probe area, and:

$$T^* = \begin{cases} T_i & T_i > T_e \\ T_e & T_i < T_e \end{cases}$$

The resistance per unit area, R_s/A, is plotted for $T_i = T_e$ in figure 3.10. For Tokapole II plasmas, R_s is several tens to a few hundred ohms, and R_s' is typically ten times larger—a few hundred to a thousand ohms.

An alternative technique to overcome floating potential

variations is to use a double low impedance probe (figure 3.11). The basic concept of this probe is that the tips can be biased with respect to one another and the current read between them, while both tips float near V_f. Conditions 3.12, 3.13, and 3.14 still hold; in addition, adequate rejection of variations of V_1 due to V_f requires:

$$CMRR >> \frac{V_f}{I_{io} R} \qquad (3.18)$$

$$I_{oi} >> V_f / R_1 \qquad (3.19)$$

$$I_{oi} >> 2\pi f C_1 V_f \qquad (3.20)$$

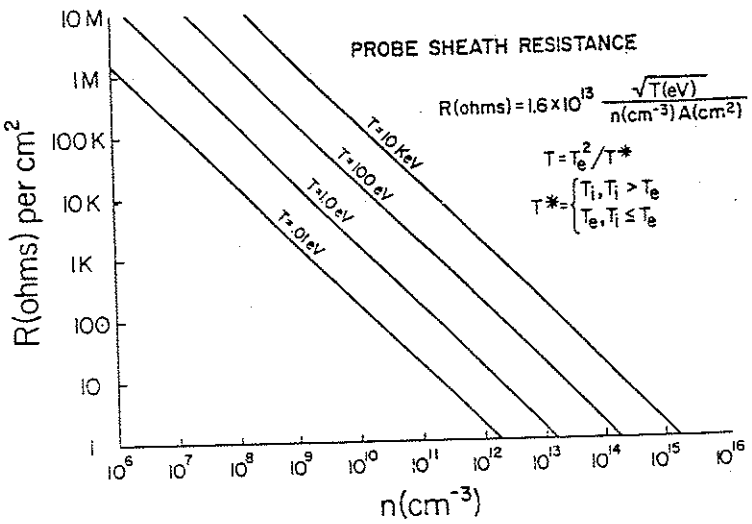

Figure 3.10: Sheath resistance per unit area versus plasma density and electron temperature for $T_i = T_e$.

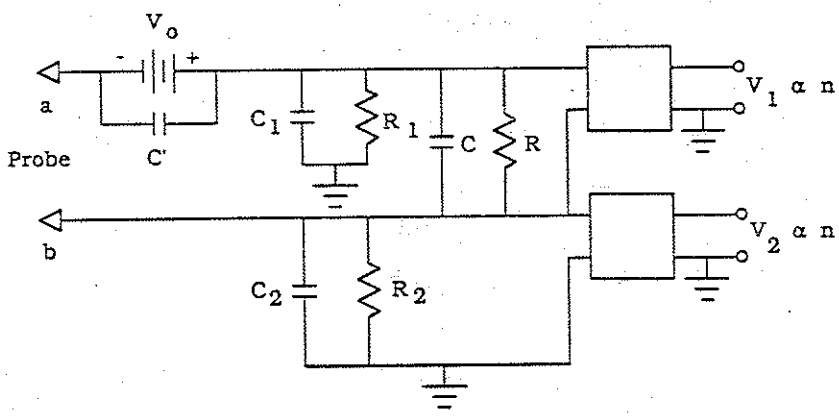

Figure 3.11: Electrostatic probe circuit for a double low impedance probe used to measure ion saturation current in the presence of floating potential fluctuations.

From equation 3.10, it can be seen that, if one can separately measure the electron temperature, then the ion saturation current measured by either technique above yields the plasma density. One tip of the electrostatic probe is used as an admittance probe.[16] This probe measures the slope of the V–I characteristic at the floating potential as follows. The current drawn by a plane electrostatic probe at a potential $V < V_p$, the plasma potential, is given by:

$$I = I_{oi} - I_{oe} \exp\left[e(V - V_p)/kT_e\right] \qquad (3.21)$$

Here, I_{oi} is the ion saturation current as before, and I_{oe} is the electron saturation current. Differentiating and evaluating at the floating potential,

$$Y = \frac{1}{R_s} = \left.\frac{dI}{dV}\right|_{V_f} = \frac{e I_{oi}}{kT_e} \qquad (3.22)$$

where Y has the dimensions of inverse resistance. The electron

temperature is then found from:

$$\frac{kT_e}{e} = I_{oi}R_s \qquad (3.23)$$

where the ion saturation current I_{oi} is measured by the other tips as described above. The plasma density is then found by equation 3.10.

The sheath admittance is measured with a capacitance bridge to insure that the probe remains at the floating potential. The output signal from an initially balanced capacitance bridge is proportional to the magnitude of the admittance |Y| added across one leg of the bridge provided |Y| is much less than the capacitive reactance of each leg of the bridge. The capacitive bridge used in this work is shown in figure 3.12. The unterminated cable is of the same type and length as that used for the probe tips. The bridge is driven at 400kHz, and C_1 is chosen to resonant with L_1 at this frequency. The resistor R_1 is added to reduce the Q and improve the frequency response of the circuit:

$$\tau = \frac{Q}{2\pi f} = R_1 C_{out} \qquad (3.24)$$

where C_{out} is the output capacitance of the bridge, measuring device, and cables. The probe is calibrated by placing various resistors between the probe tip and ground to establish the range over which the output signal is proportional to 1/R.

The admittance probe technique closely resembles the double probe technique[17] of measuring T_e in that it involves a measurement of both ion saturation current and the slope of the

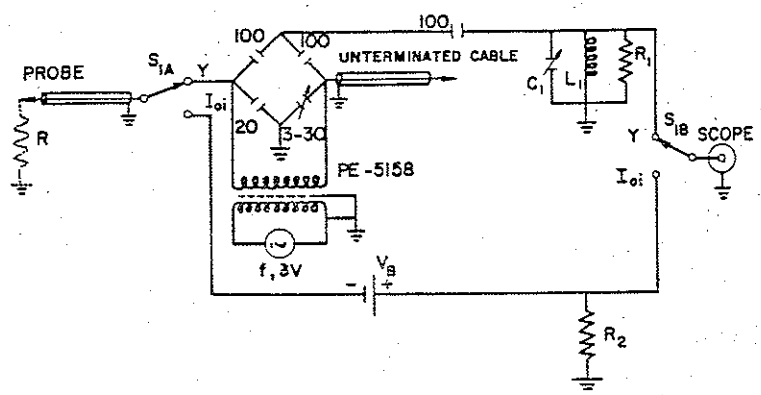

Figure 3.12: Admittance probe circuit used in this experiment.

V-I curve at the floating potential. Like the double probe, the admittance probe suffers from the disadvantage that only the most energetic electrons are sampled, and hence, for a non-Maxwellian distribution, the temperature inferred may not be representative of the bulk of the electrons.

III.B.3. Magnetic Probes:

Reviews of magnetic probe techniques for plasma diagnostics are presented in references 18, 19, and 20. Magnetic pickup loops are used in this research to make two types of measurements: fluctuations of the poloidal magnetic field just outside the separatrix (Mirnov oscillations[21]), and integrated coil signals to construct plasma current profiles and q profiles. The requirements on the pickup loops, electronics, and data acquisition system differ for these tasks and will be discussed separately.

Requirements for measuring Mirnov-type magnetic precursor oscillations are less complex than for obtaining flux surfaces, current profiles, or q profiles. A series of magnetic field pickup coils aligned to measure the fluctuating part of the poloidal field are distributed about the vacuum vessel in toroidal and poloidal arrays. The highest possible poloidal mode number m_{max} and toroidal mode number n_{max} that can be extracted from the measurements is related to the number of coils by:

$$k_{pol} = 2 m_{max} + 1 \qquad (3.25)$$

$$k_{tor} = 2 n_{max} + 1 \qquad (3.26)$$

where m_{max} and n_{max} are the largest poloidal and toroidal mode numbers measurable with poloidal and toroidal arrays of k_{pol} and k_{tor} coils respectively. No distinction between positive and negative mode numbers is made here. If, in addition, one is not interested in the m = 0 and n = 0 axisymmetric modes, a poloidal array of six coils and a toroidal array of four coils yield information on poloidal modes m = ± 1,2,3 and n = ± 1,2. Resistive tearing mode theory predicts that the modes of lowest mode number bend field lines the least and are therefore the most unstable;[22] the most commonly seen modes associated with disruptions on other tokamaks generally fall into these ranges.[23-30] Figure 3.13 shows the placement of the toroidal and poloidal arrays during much of this work. Additional work was performed with three coils at one toroidal azimuth (top midcylinder, outer midplane, and bottom midcylinder) yielding information on the evenness or oddness of the poloidal mode

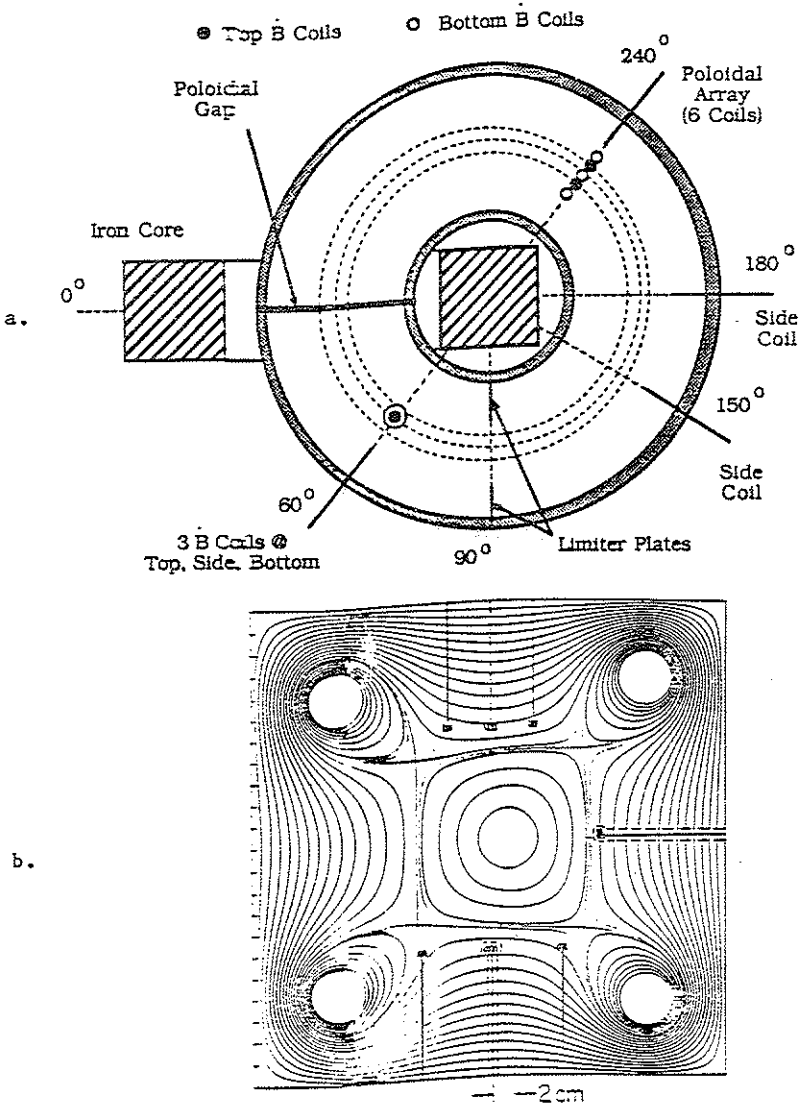

Figure 3.13: Placement of magnetic pickup coils for the (a) toroidal and (b) poloidal arrays used in this work. The location of three additional probes in a poloidal array at a toroidal angle of 60° (dashed lines) is also shown.

number, and occasionally with coils distributed about the vacuum vessel to "follow" the magnetic island structure.

The pickup coils used for these measurements consist of 50 turns of 40 gauge teflon coated wire wrapped on either G-10 or machinable ceramic forms. Typical d.c. resistances of the coils are 8 or 9 ohms, and typical effective areas are 4-6 cm^2. Structural support and electrostatic shielding is provided by a .005 inch thick, .125 inch outside diameter stainless steel tube. Coil leads are twisted together and wrapped in teflon tape to prevent abrasion and shorting to the stainless steel tube.

The design of a typical coil and vacuum envelop is shown in figure 3.14. The vacuum envelope is provided by a .250 inch outside diameter, .060 inch wall stainless steel tube. To maximize coil frequency response, minimize thermal loading to the coil, and to minimize degradation of the discharges, a boron nitride clad .005 inch wall stainless steel tube is 95/5 soldered into the end of the .250 inch tube and sealed at the tip with .004 inch stainless steel shim silver soldered in place. The .005 inch wall tubing has an .147 inch outside diameter and the boron nitride cladding is .050 inches thick. Typical temperature rises inside the vacuum envelop during a discharge are 150 C.

The output of a magnetic pickup coil is given by:

$$V = -\frac{d\Phi}{dt} = -\frac{d}{dt}\int \underline{B}\cdot d\underline{s} = -A_{eff}\frac{d\underline{B}_p}{dt} \qquad (3.27)$$

where Φ is the magnetic flux linked by the coil, $\underline{B}$ the magnetic

field, $d\underline{s}$ the element of coil area, and A_{eff} the effective area of the coil. For an ideal coil, $A_{eff} = NA$ where N is the number of turns in the coil and A is the area/turn. Due to attenuation in the electrostatic shield and the failure to wind each turn in precisely the same orientation, $A_{eff} \neq NA$ and is in general a function of frequency.

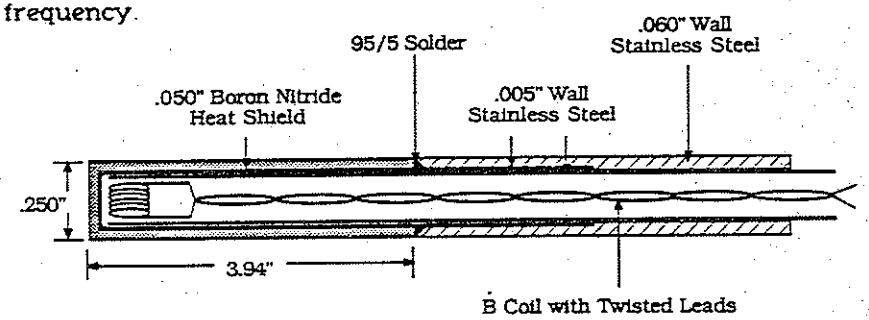

Figure 3.14: Cross section of a typical magnetic pickup coil and vacuum envelop used for Mirnov measurements in this work.

These effects can be accounted for by assuming the coil is ideal during calibration and including all variations in the factor $A_{eff}(\omega)$. The probes used in this work were calibrated using a Helmholtz coil set with an output of .56 G/A driven through 50 ohms by a Wavetech signal generator (figure 3.15). Measurements were made at 15 discrete frequencies from 500 Hz to 300 kHz. A typical coil calibration curve is shown in figure 3.16. The coil response is well represented between 10 and 300 kHz by a frequency independent A_{eff} of 4.652 ± .065 (1.4%) cm^2; during use, the output is low pass filtered at 10 kHz and high pass filtered at either 300 or 370 kHz to avoid aliasing in the 1 MHz digitizer.

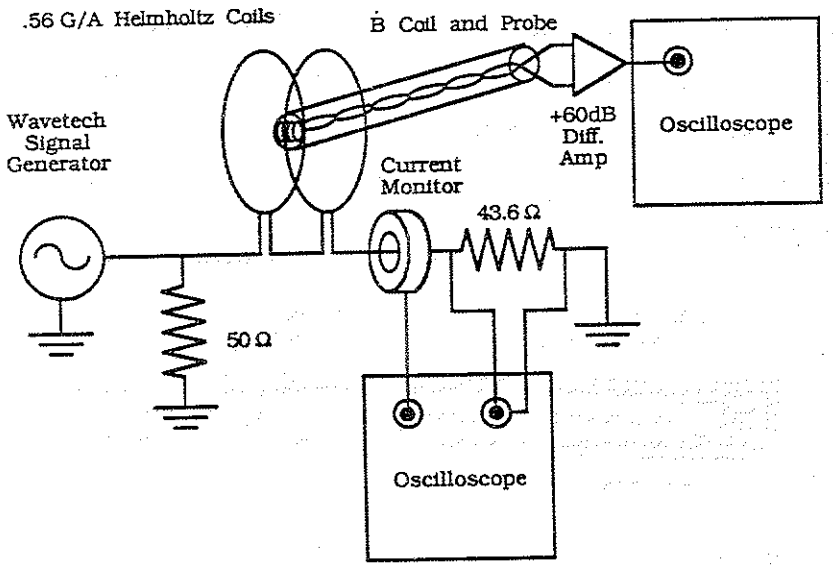

Figure 3.15: Magnetic pickup coil calibration setup. A .56 G/A Helmholtz coil set is driven through 50 Ω by a Wavetech signal generator. The 43.6 Ω resistor is a voltage shunt to monitor the Helmholtz current; a Rogowski coil is also used to monitor the current.

Derivation of equilibrium poloidal flux plots, plasma current profiles, and q profiles requires a frequency response of near d.c. (.1 Hz) to 100 kHz. At these lower frequencies, the coil output is sharply reduced and it is desirable to increase the effective area. The probe design shown in figure 3.14 was modified by removing the innermost stainless steel tubing from around the coil, decreasing the shielding to .005 inches, and by reducing the boron nitride cladding to .020 inches, increasing the available volume for the coil. Temperature rises with these thinner claddings were ~ 200 C. Coil

forms were machined from ceramic for transverse/axial and transverse/transverse coil sets. Typical effective areas were 10 cm^2 between .1 Hz and 300 kHz. Coil to coil alignments were maintained to within .1 degrees.

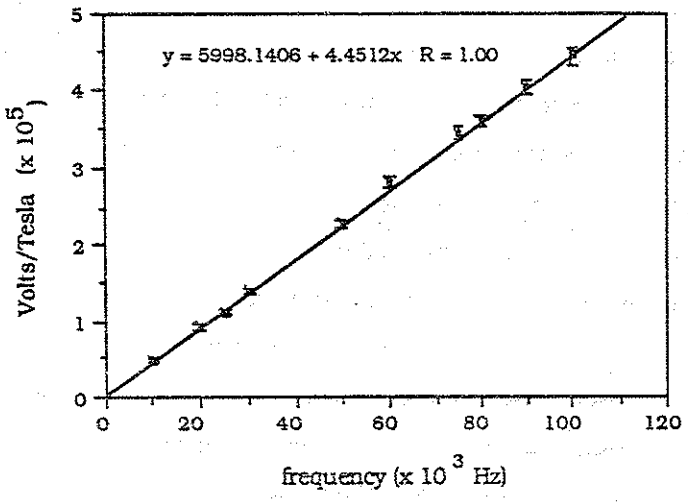

Figure 3.16: Typical calibration curve obtained with the setup shown in figure 3.15. The line is a least squares linear fit to the data. The slope is the effective area A_{eff} of equation 3.23.

Output from the equilibrium magnetic probes was actively integrated using the circuit shown in figure 3.17. This is a low drift, low offset, auto-zeroing integrator with an RC time constant of ~.0001 seconds. In the auto-zero state, switches S_1 and S_2 are closed and switch S_3 is open. The second op amp supplies a feedback voltage of $-R_f V_{io}/R$, where V_{io} is the input offset voltage of the integrating op amp, to the integrating op amp, canceling V_{io}. This

offset correction voltage is stored in the "sample and hold" capacitor $C_{s/h}$, buffered by the high input impedance voltage follower. To integrate, switches S_1 and S_2 are opened, memorizing the correction voltage on $C_{s/h}$, and switch S_3 is closed, returning the most recent correction voltage to the input of the integrator. The offset trim on the second amplifier is used to remove the residual offset voltage $-R_f V_{io}/AR$ from the output during the auto-zero state.

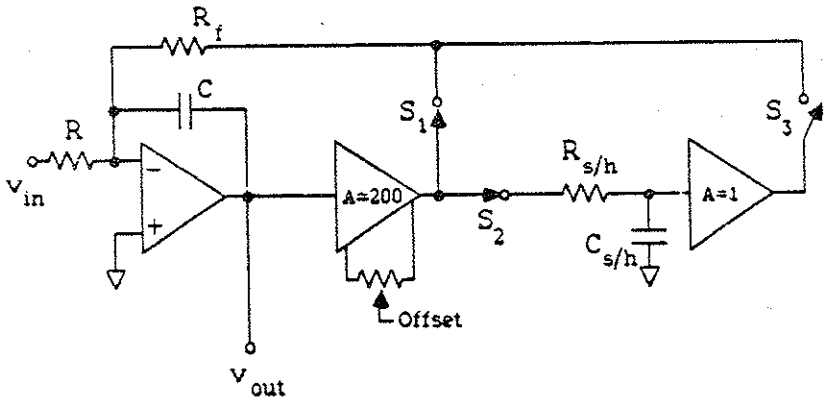

Figure 3.17: Circuit diagram for the analog integrator with auto-zero function used in this research.

The equilibrium magnetic probes were used to measure the safety factor q along the midplane of the central current channel in discharges with $q_a < 1$ without severely degrading the discharges. Attempts to repeat these measurements in discharges with $q_a > 1$ were not successful; in these discharges, measurements were limited to poloidal and toroidal magnetic field profiles in the divertor

scrape-off region outside the separatrix.

For $q_a < 1$ discharges, poloidal and toroidal magnetic field data was acquired along the midplane of the central current channel. The safety factor q was determined assuming circular flux surfaces:

$$q = \frac{r B_t}{R B_p} \qquad (3.28)$$

where r is the minor radius (with respect to the magnetic axis), R the major radius, B_t the toroidal field, and B_p the poloidal field.

Earlier work[31,32] in $q < 1$ plasmas mapped out the poloidal flux contours ψ in the poloidal cross section and averaged $q(\psi)$ over the flux contours to account for the noncircularity of the contours. The essential features of these measurements were that the q on the magnetic axis, $q(0)$, was significantly < 1 and remained unchanged throughout a sawtooth period,[33,34] indicating partial reconnection. Subsequent SXR measurements[35] indicated the existence of a large scale island over much of the discharge and a lack of axisymmetry just before and after a sawtooth crash, a fundamental assumption used in reconstructing flux contours from the magnetic probe data. Since this island apparently does not extend to the magnetic axis region, and since the flux surfaces near the axis are nearly circular, equation 3.28 should still yield information concerning the extent of the $q(0)$ relaxation during sawteeth in the $q < 1$ discharges.

Current density profiles were derived from the magnetic field data by subtracting the vacuum poloidal field of the divertor rings

and using Maxwell's equations on the resulting plasma magnetic field profiles. The cylindrical coordinate system (r,θ,z) centered on the minor axis is used to derive the toroidal current at the midplane (J_z) as shown in figure 3.18. In this system, the toroidal current J_t is given by:

$$J_t = J_z\Big|_{\substack{mid-\\plane}} = \frac{1}{r}\frac{\partial}{\partial r} r B_\theta - \frac{1}{r}\frac{\partial B_r}{\partial \theta} \qquad (3.29)$$

ignoring toroidal effects. The second term on the right hand side of equation 3.29 vanishes for circular flux surfaces. This term is difficult to measure directly. Neglecting noncircular effects, equation 3.29 reduces to:

$$J_t \approx \frac{1}{r}\frac{\partial}{\partial r} r B_\theta \qquad (3.30)$$

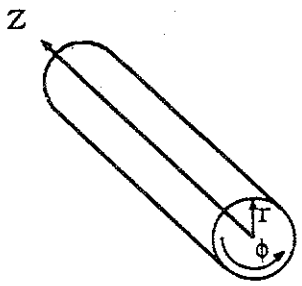

$$J_{tor} = J_z = \frac{1}{r}\frac{\partial r B_\theta}{\partial r} - \frac{1}{r}\frac{\partial B_z}{\partial \theta}\to 0$$

(for circular surfaces)

Figure 3.18: Coordinate system for calculating toroidal plasma current.

Due to the shot-to-shot variations and the difficulties in obtaining an adequate vacuum poloidal field subtraction, the resulting profiles have rather large uncertainties. These measurements could be improved by utilizing an array of coils to obtain the data in a single shot.

The probe perturbation was too severe in $q_a > 1$ discharges to allow insertion of the magnetic probes into the central current channel as described above. It was still of interest to verify the effectiveness of the limiter plates in removing toroidal current in the scrape-off region to determine the accuracy of q_a, and to determine the suitability of the equilibrium current distributions used in the 3-D resistive MHD initial value code RPD[36,37] that has been used to extensively to model these experiments.

Poloidal field profiles were obtained along the outer midplane from the separatrix to the wall. Equation 3.30 was used to obtain toroidal current profiles in magnetic and material limiter discharges. the resulting profiles have large uncertainties of order 10 A/cm^2, compared to J_t values of 10-30 A/cm^2. The measurements do, however, provide an upper bound on the current in the scrape-off region. Attempts to measure scrape-off poloidal current profiles were unsuccessful due to the small variation from the vacuum toroidal field in the discharges.

III.B.4. Soft X-Ray and Vacuum Ultraviolet Diagnostics:

While Mirnov probes provide information on magnetic field

structures at or near the edge of the plasma, it is desirable to also obtain direct measurements of magnetic field structure internal to the plasma. Because of the high thermal conductivity parallel to magnetic field lines, the electron temperature equilibrates quickly over new magnetic surfaces or ergodic regions. Radiation in the soft x-ray region comes primarily from sources that are strongly dependent on electron temperature,[38] so that even though soft x-ray detectors make chordal measurements, it is possible to image the internal magnetic structure with sufficient numbers of chords.

For Tokapole II discharges with a central electron temperature of about 100 eV, recombination radiation is expected to dominate bremsstrahlung.[39] Impurity doping experiments[40] indicate that the light impurities (carbon, nitrogen, oxygen) contribute less than 20% of the soft x-ray radiation. The dominant contribution is line radiation from metals, which is expected to vary approximately as[41]:

$$I_{SXR} \sim n_e n_i e^{-E/T_e} \qquad (3.31)$$

where I_{SXR} is the soft x-ray radiation intensity, n_e the electron density, n_i the density of the ith impurity charge state, and E the photon energy. In an impurity doping experiment, Groebner and Dexter[40] found that for Tokapole II plasmas, equation 3.31 becomes:

$$I_{SXR} \sim n_e n_i e^{-280/T_e} \qquad (3.32)$$

The SXR detectors used on Tokapole II are surface barrier diodes with polypropylene filters that transmit photon energies

between about 60-300 eV.[42] The diodes are operated in current mode and are biased to -5 V to improve the frequency response by reducing the diode capacitance. The frequency response was bench set to ~ 300 kilohertz for each of the diode amplifiers.

The detector systems consisted of a 7 chord poloidal array, located on the outer wall at a toroidal angle of 60 degrees from the poloidal gap, and several movable detectors that could be mounted on swivel ports about the machine. The side poloidal array diodes are separated by 3.18 cm, and have a spot size at the midcylinder of ~ 2 cm. The movable detectors have a range of swivel of ± 25° and a spot size at the machine center (midplane or midcylinder) of ~ 0.5 cm. The chords of view of these SXR detectors relative to the equilibrium poloidal flux plot is shown in figure 3.19.

In addition to the SXR detectors discussed above, impurity radiation was also monitored with a set of four photomultiplier tubes with filters to view the C III 464.7 nm, N III 450.9 nm, O III 376.3 nm, and, from the divertor rings and supports, Cu I 324.7 nm lines. Qualitative monitoring of a series of oxygen vacuum ultraviolet lines (VUV), O III 70.3 nm, O IV 79.0 nm, O V 63.0 nm, and O VI 103.2 nm, and hydrogen Lyman α 121.5 nm with a VUV monochromator was also performed to obtain indications of changes in electron temperature and impurity behavior.

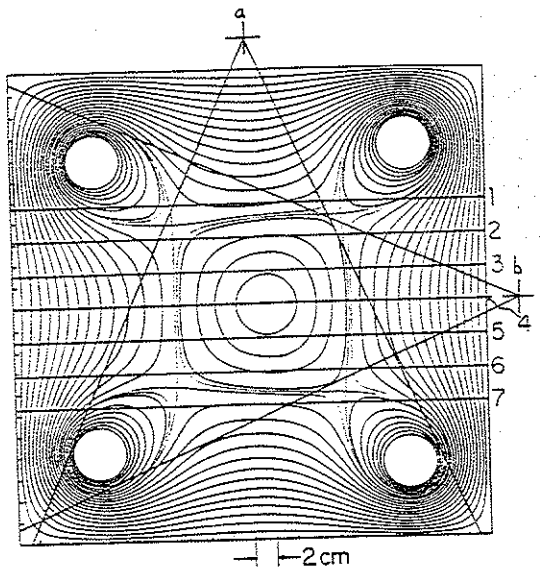

Figure 3.19: Layout of SXR detector chords in a poloidal cross section. The seven chords of the poloidal side array at the toroidal angle of 60° are designated by "1" through "7". The range of chords available to (a) top and (b) side swivel port mounted detectors is also shown.

III.C. Discharge Characteristics:

Typical plasma parameters for high q_a and low q_a discharges are shown in table 3.1. Electron temperatures are 100-120 eV, determined by modeling the time evolution of oxygen line ratios (OI-OVI).[3] Ion temperatures, determined by Doppler broadening measurements[3] on the 468.6 nm He II and 464.8 nm C III lines and charge exchange measurements,[43] are 20-70 eV. Typical Z_{eff} values are 2.5-3.[3] The variation of the electron conductivity temperature T_e^{cond}, determined as described in Section III.B.1, and ion temperature T_i, determined by neutral particle charge exchange

measurements, versus effective edge safety factor q_a is shown in figure 3.20. While the electron conductivity temperature drops from 100-120 eV at $q_a > 1$ to about 70 eV at $q_a < 1$, the ion temperature rises from 20-30 eV to nearly 60 eV in the $q_a < 1$ discharges. The time evolution of plasma current I_p, loop voltage V_l, q_a, edge and central chord SXR signals, and a Mirnov signal for discharges with $q_a \sim 3$, $q_a < 2$, and $q_a < 1$ are shown in figure 3.21a, b, and c respectively.

Table 3.1:

Tokapole II Parameters

	q < 1:	q ~ 3:
Toroidal Field:	~ 3 kG	~ 5 kG
Plasma Current:	30 – 40 kA	15 kA
Line Ave. Density:	$10^{13}/cm^3$	6 x $10^{12}/cm^3$
Electron Temperature	100 eV	120 eV
Ion Temperature:	70 eV	40 eV
Pulse Length:	~ 4 ms	~ 10 ms
Loop Voltage:	15 V	2 V
Magnetic Reynolds #:	< 10^4	~ 10^4
Energy Confinement Time:	.05 ms	.600 ms

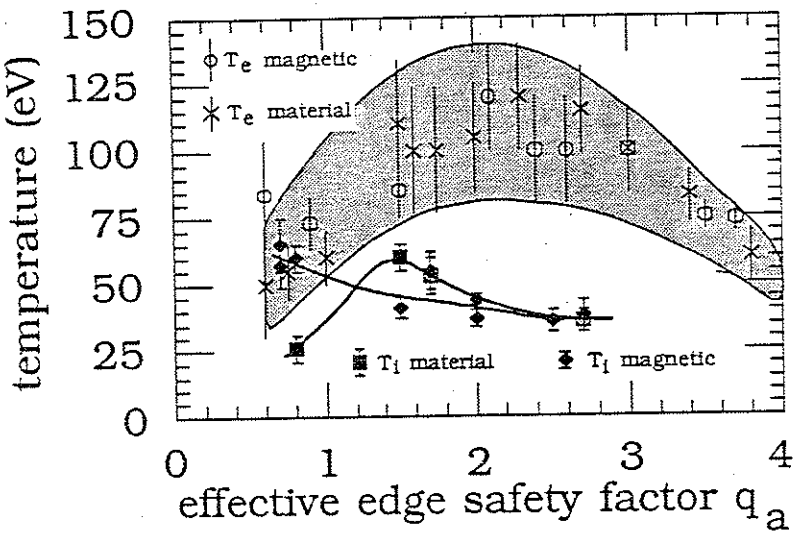

Figure 3.20: Variation of electron conductivity temperature T_e^{cond} and ion temperature T_i with effective edge safety factor q_a in Tokapole II magnetic and material limiter discharges. T_e^{cond} is essentially equal in the two configurations. The vertical bars and shaded area indicate the range of operating parameters, not uncertainties in individual measurements.

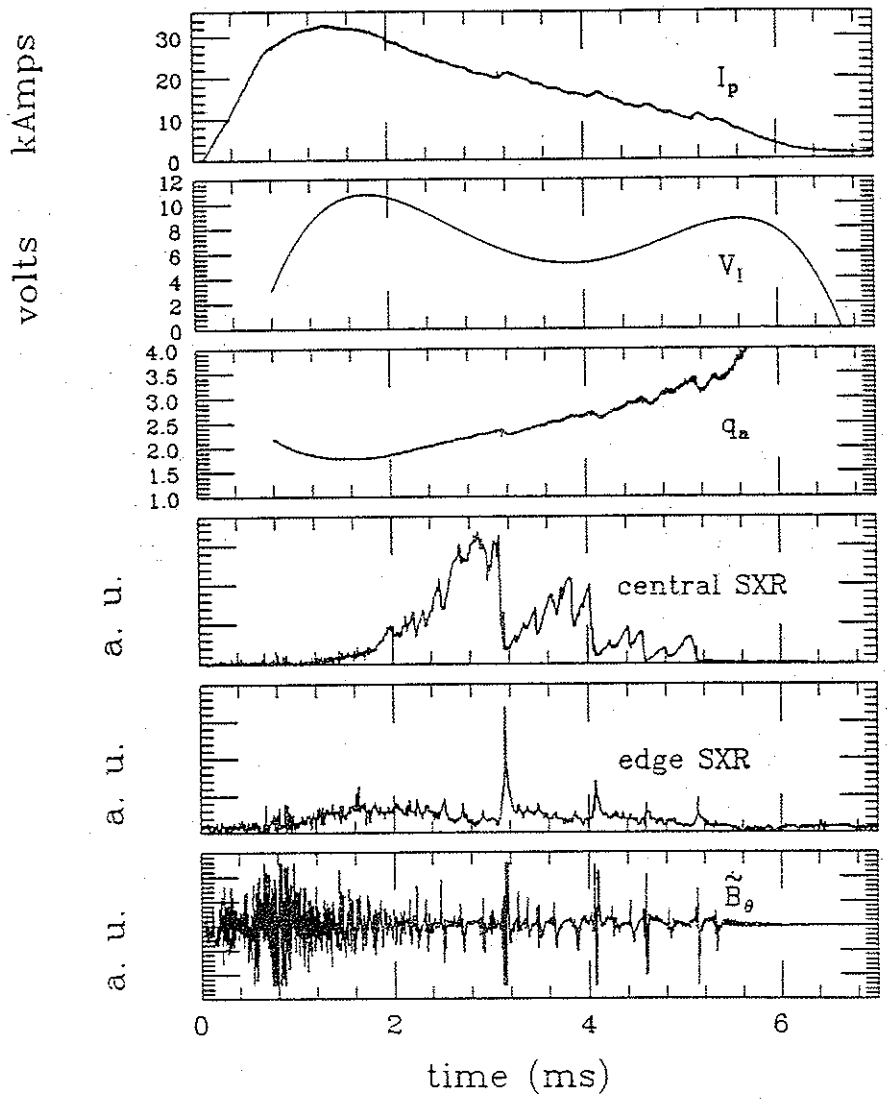

Figure 3.21a: Typical waveforms of plasma current I_p, loop voltage V_l, q_a, edge and central chord SXR signals, and Mirnov signal in a discharge with $q_a \sim 3$.

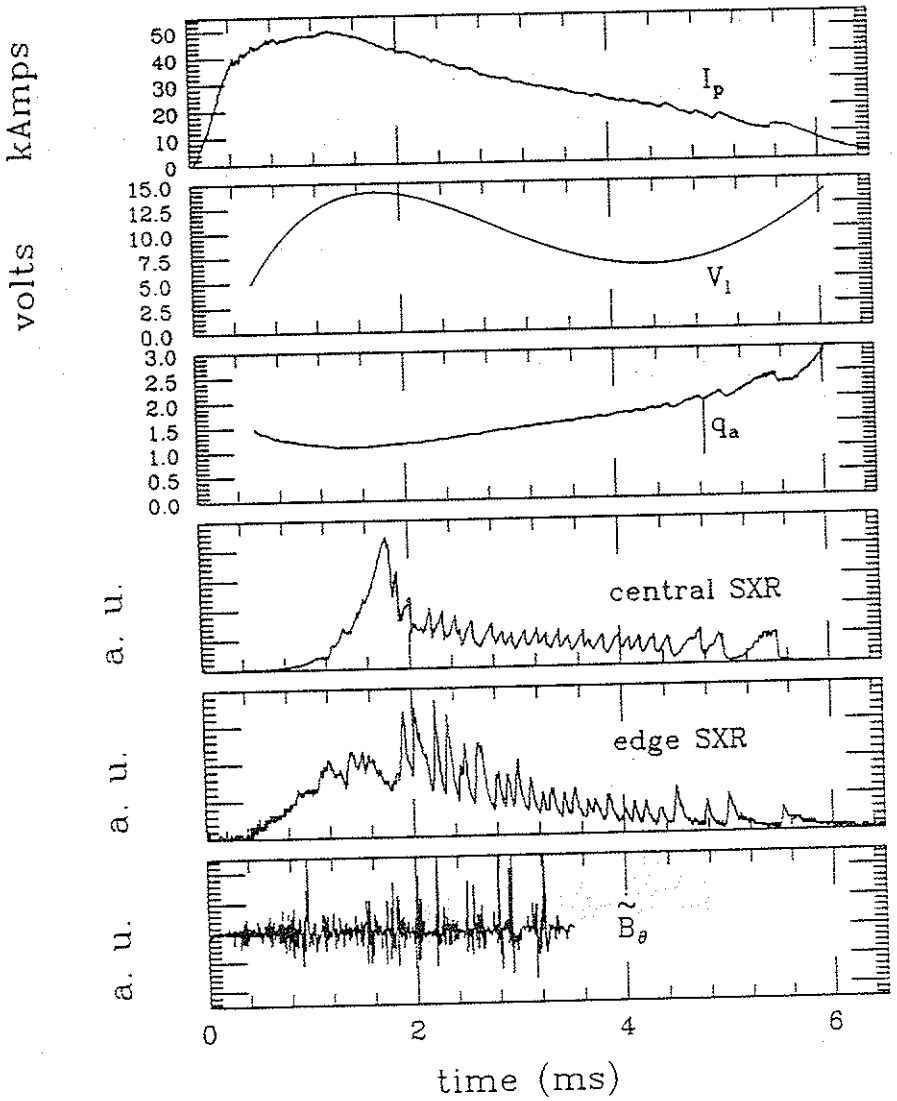

Figure 3.21b: Typical waveforms of plasma current I_p, loop voltage V_l, q_a, edge and central chord SXR signals, and Mirnov signal in a discharge with $q_a < 2$.

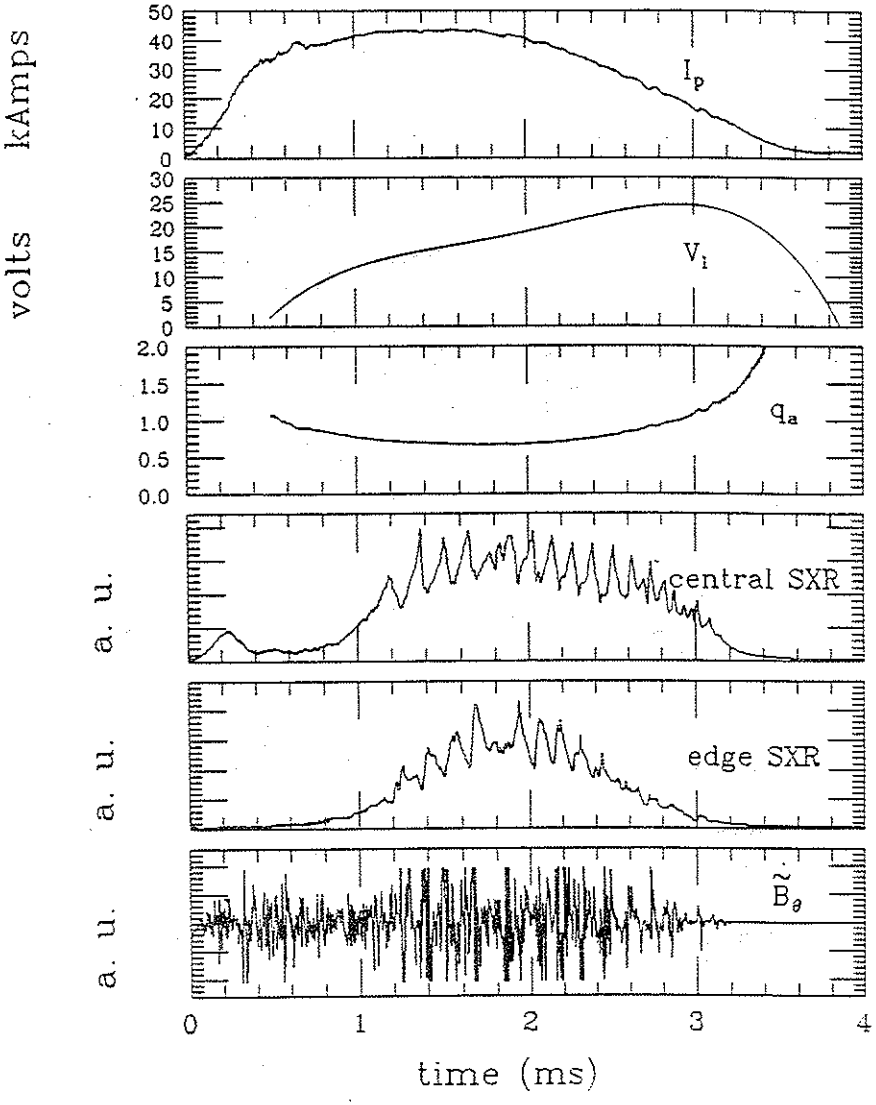

Figure 3.21c: Typical waveforms of plasma current I_p, loop voltage V_l, q_a, edge and central chord SXR signals, and Mirnov signal in a discharge with $q_a < 1$.

REFERENCES

[1]A.P. Biddle, et al., Nuclear Fusion, 19, 1509, (1979).

[2]J.C. Sprott and T.W. Lovell, University of Wisconsin—PLP 744 (1978).

[3]R.J. Groebner, Ph.D. Thesis, University of Wisconsin (1979).

[4]J.C. Sprott, University of Wisconsin—PLP 889 (1983).

[5]J.C. Sprott, University of Wisconsin—PLP 712 (1978).

[6]S.C. Prager, et al., University of Wisconsin—PLP 756 (1978).

[7]J.C. Sprott, University of Wisconsin—PLP 777 (1979).

[8]J.S. Sarff, University of Wisconsin—PLP 1003 (1987).

[9]L. Spitzer, Physics of Fully Ionized Gases, John Wiley and Sons, (1962).

[10]F.F. Chen, Plasma Diagnostic Techniques, Ed: R.H. Huddlestone and S.L. Leonard, (Academic Press, Inc., New York, 1965), 113 - 200.

[11]J.C. Sprott, University of Wisconsin—PLP 88 (1966).

[12]F.F. Chen, IPPJ—750 (1985).

[13]F.F. Chen, Princeton University Plasma Physics Laboratory Report MATT—77.

[14]J.G. LaFramboise, UTIAS Report N. 100, 48 (1966).

[15]J.C. Sprott, Reviews of Scientific Instruments, 37, 897 (1966).

[16]J.C. Sprott, Reviews of Scientific Instruments, 39, 1569 (1968).

[17]E.O. Johnson and L. Malter, Physical Review, 80, 58 (1950).

[18]R.H. Lovberg, Annals of Physics, 8, 311 (1959).

[19]R.H. Lovberg, Plasma Diagnostic Techniques, Ed: R.H. Huddlestone and S.L. Leonard, (Academic Press, Inc., New York, 1965), 69 - 112.

[20]W. Botticher, Plasma Diagnostics, Ed: W. Lochte-Holtgreven, (North Holland Publishing Co., Amsterdam, 1969), 617 - 667.

[21]S.V. Mirnov, Soviet Atomic Physics, 30, 22 (1971).

[22]R.B. White, Reviews of Modern Physics, 58, 183 (1986).

[23]F. Karger, et al., Plasma Physics and Controlled Fusion Research (Proc. 6th Int. Conf., Berchtesgaden, 1975), 1, (IAEA, Vienna, 1976), 267.

[24]TFR Group, Nuclear Fusion 17, 1283 (1977).

[25]S.V. Mirnov and I.B. Semenov, Plasma Physics and Controlled Fusion Research (Proc. 6th Int. Conf., Berchtesgaden, 1975) 1, (IAEA, Vienna, 1976), 291.

[26]N.R. Sauthoff, S. von Goeler, and W. Stodiek, Nuclear Fusion, 18, 1445 (1978).

[27]J.J. Ellis, et al., Plasma Physics and Controlled Fusion Research, (Proc. 8th Int. Conf., Brussels 1980), 1, (IAEA, Vienna, 1981), 731.

[28]K. McGuire, et al., Journal of Nuclear Materials, 121, 329 (1984).

[29]S.B. Kim, T.P. Kochanski, and J.A. Snipes, University of Texas at Austin FRCR 256 (1984).

[30]S. Tsuji, et al., Nuclear Fusion, 25, 305 (1985).

[31]B. Lipschultz, Ph.D. Thesis, University of Wisconsin (1979).

[32]T.H. Osborne, Ph.D. Thesis, University of Wisconsin (1984).

[33]T.H. Osborne, R.N. Dexter, and S.C. Prager, Physical Review Letters, 49, 734 (1982).

[34]T.H. Osborne, R.N. Dexter, and S.C. Prager, Physics of Fluids, 26,

350 (1983).

[35]T.H. Osborne and N.S. Brickhouse, University of Wisconsin—PLP 908 (1983).

[36]E. Uchimoto, J.D. Callen, and L. Garcia, Bulletin of the American Physical Society, 30, 1421 (1985).

[37]E. Uchimoto and J.D. Callen, Sherwood Theory Meeting, paper 1D18 (1987).

[38]S. von Goeler, Diagnostics for Fusion Experiments (Proc. of the Course, Varenna, 1978), Ed: E. Sindoni and C. Wharton, (Pergamon Press, Oxford, 1979), 79—109.

[39]W.R. Wing, Plasma Diagnostics and Data Acquisition Systems (Proc. of the Course, Varenna, 1975), Ed: A. Eubank and E. Sindoni, (Editrice Compositori, Bologna, 1975), 87.

[40]R.J. Groebner and R.N. Dexter, University of Wisconsin—PLP 770 (1978).

[41]G.M. McCracken and P.E. Stott, Nuclear Fusion, 19, 889 (1979).

[42]N.S. Brickhouse, Ph.D. Thesis, University of Wisconsin, 1984.

[43]R.A. Moyer, et al., Bulletin of the American Physical Society, 31, 1594 (1986).

Chapter 4
PLASMA EQUILIBRIA IN TOKAPOLE II

Characteristics of the plasma equilibria for magnetic and material limiter discharges in the three operational regimes studied are presented in this chapter. Data presented here include global discharge parameters, central current channel SXR emissivity profile evolution, and evolution of scrape-off density, electron temperature and pressure profiles, and plasma current profiles. Equilibria in the external disruption dominated $2 < q_a < 3$ regime are presented in Section IV.A. Equilibria in the $1 < q_a < 2$ regime are presented in Section IV.B. Equilibria in the internal disruption dominated $q_a < 1$ regime are presented in Section IV.C. The effects of varying the boundary conditions in $0.5 < q_a < 3$ discharges are summarized in Section IV.D.

IV.A. Equilibria with $2 < q_a < 3$:

IV.A.1. Global Discharge Parameters:

The most significant difference between $2 < q_a < 3$ magnetic and material limiter discharges is the abrupt current termination following the giant sawtooth in the material limiter discharge (figure 4.1). Magnetic limiter discharges survive three to seven giant sawteeth, depending upon discharge length. The overshoot in I_p in the first 1.5 ms in the magnetic limiter discharge lowers q_a somewhat initially, but q_a relaxes to values similar to the material

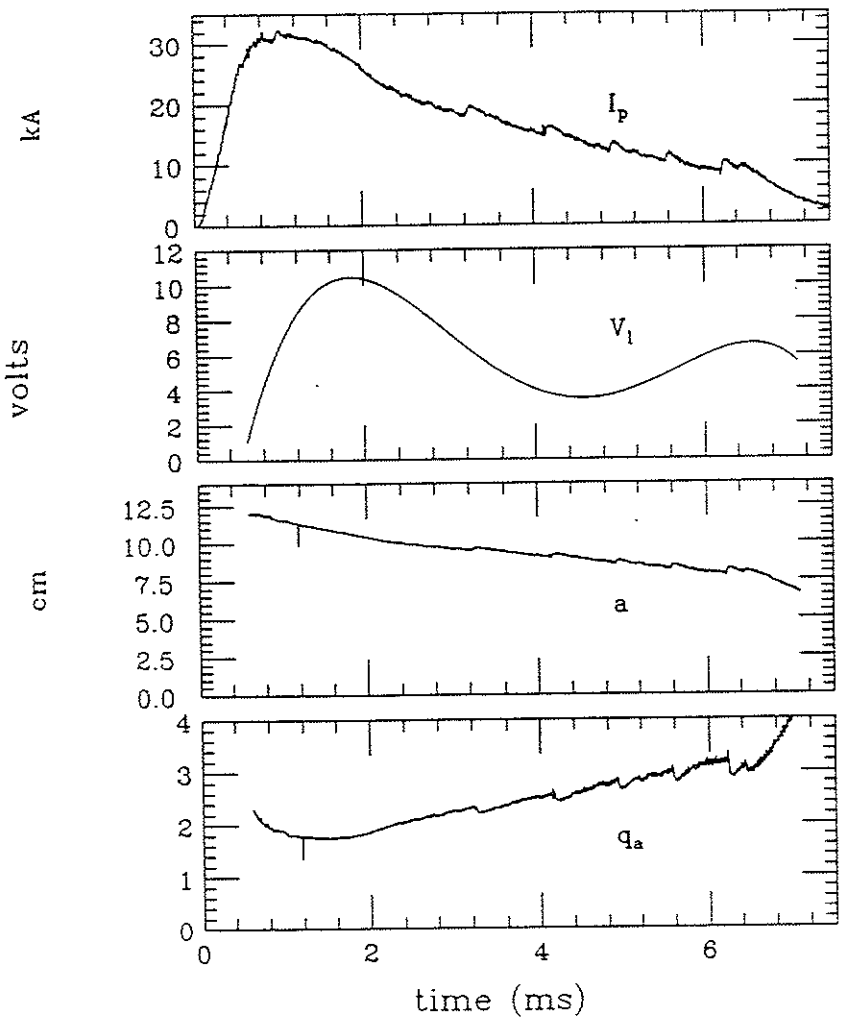

Figure 4.1a: Plasma current I_p, loop voltage V_l, equivalent minor radius a, and effective edge safety factor q_a determined with the circuit model of Section III.B.1 for a typical magnetic limiter $2 < q_a < 3$ discharge. Toroidal field B_t = 5.5 kG.

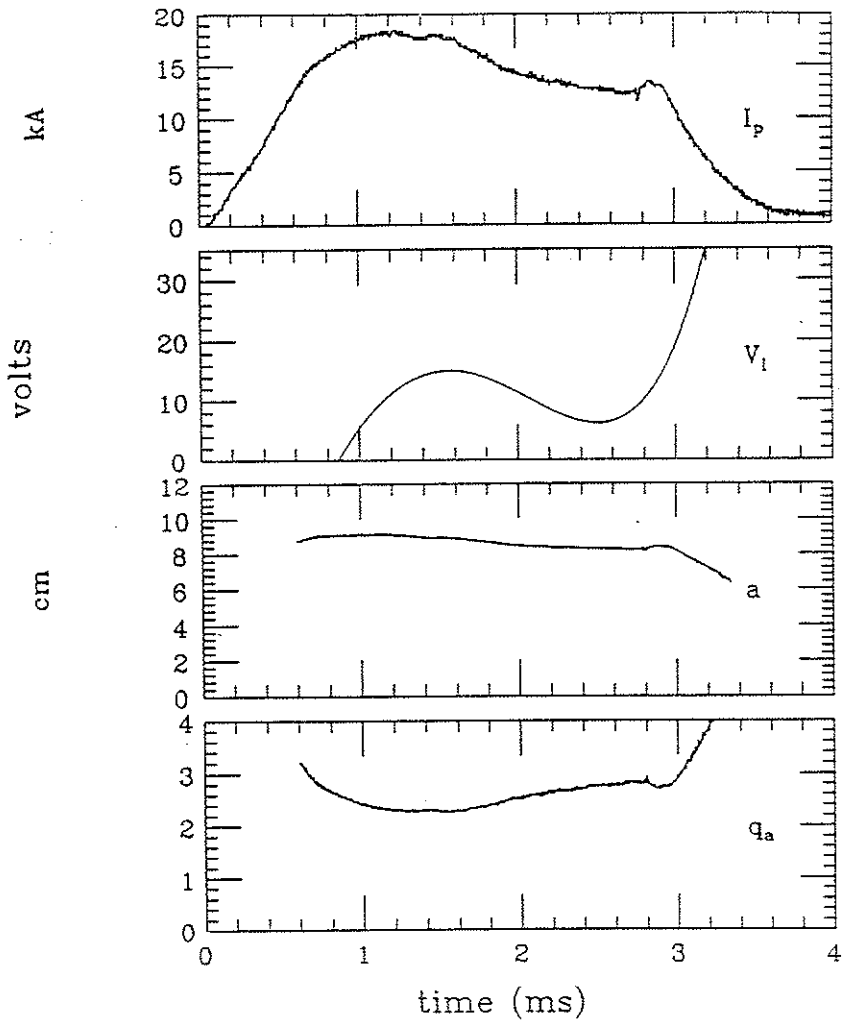

Figure 4.1b: Plasma current I_p, loop voltage V_l, equivalent minor radius a, and effective edge safety factor q_a determined with the circuit model of Section III.B.1 for a typical material limiter $2 < q_a < 3$ discharge. Toroidal field B_t = 5.5 kG.

limiter configuration by the onset of the SXR sawteeth.

The constant gap voltage drive and mismatch between the plasma and divertor ring resistances result in a plasma current during "flattop" that is generally slowly decaying for the magnetic limiter configuration. Discharge duration is therefore sensitive to impurity levels and alters the number of giant sawteeth that will occur. The repetitive nature of the giant sawteeth in the magnetic limiter configuration is therefore suggestive of the repetitive minor disruptions seen on PDX during current rampdown in divertor discharges.[1] In reference 1, these disruptions were associated with current gradient changes that resulted from changes in discharge shape. Such current profile changes cannot be entirely ruled out here.

Line average density n_l, electron conductivity temperature T_e^{cond} (using the previously measured $Z_{eff} \approx 2.5$ (Section III.C)), ohmic heating power P_{oh}, and global energy confinement time τ_E are shown in figure 4.2 for the discharges of figure 4.1. The material limiter discharges are degraded by the presence of the limiter plates, with T_e^{cond} dropping ~ 25 eV and τ_E dropping from ~ 400 μs to ~ 200 μs. This degradation arises from increased metallic impurity levels in the central current channel; evidence for impurity accumulation is discussed in Section V.B.3.

Neutral particle charge exchange measurements show no degradation in ion temperature T_i in the material limiter discharges (figure 4.3). Because the ion distribution function is measured

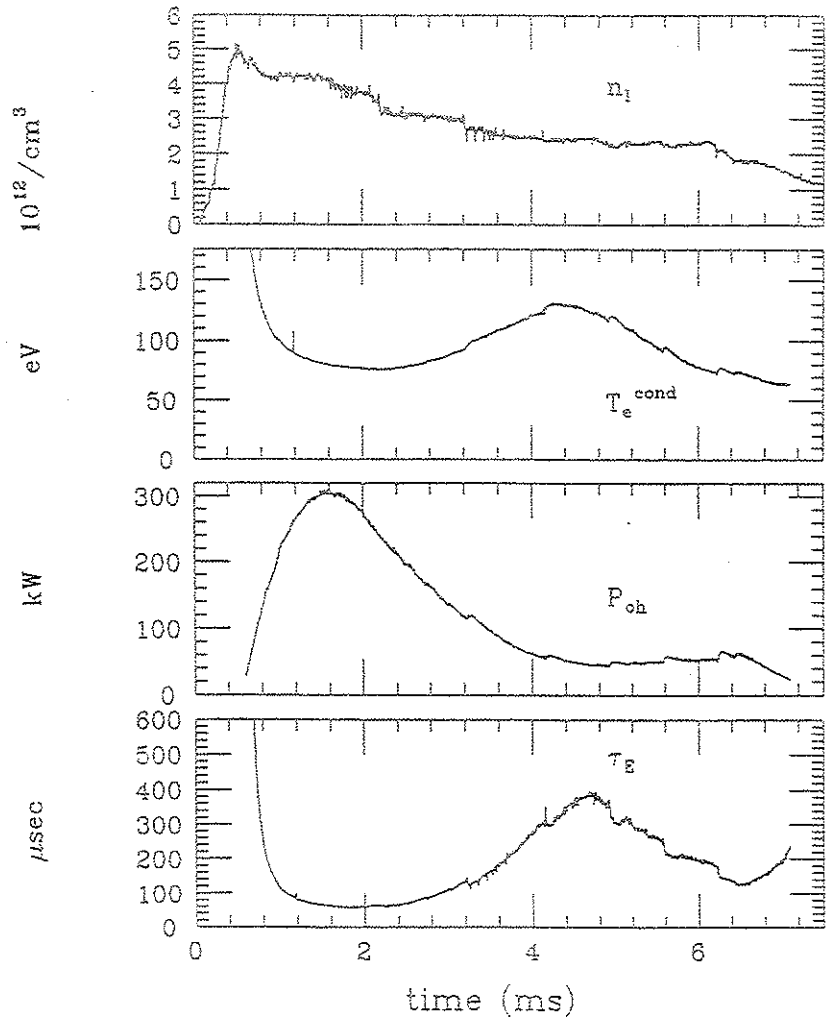

Figure 4.2a: Line average density n_l, electron conductivity temperature T_e^{cond}, ohmic heating power P_{oh}, and global energy confinement time τ_E for the same magnetic limiter discharge as figure 4.1a.

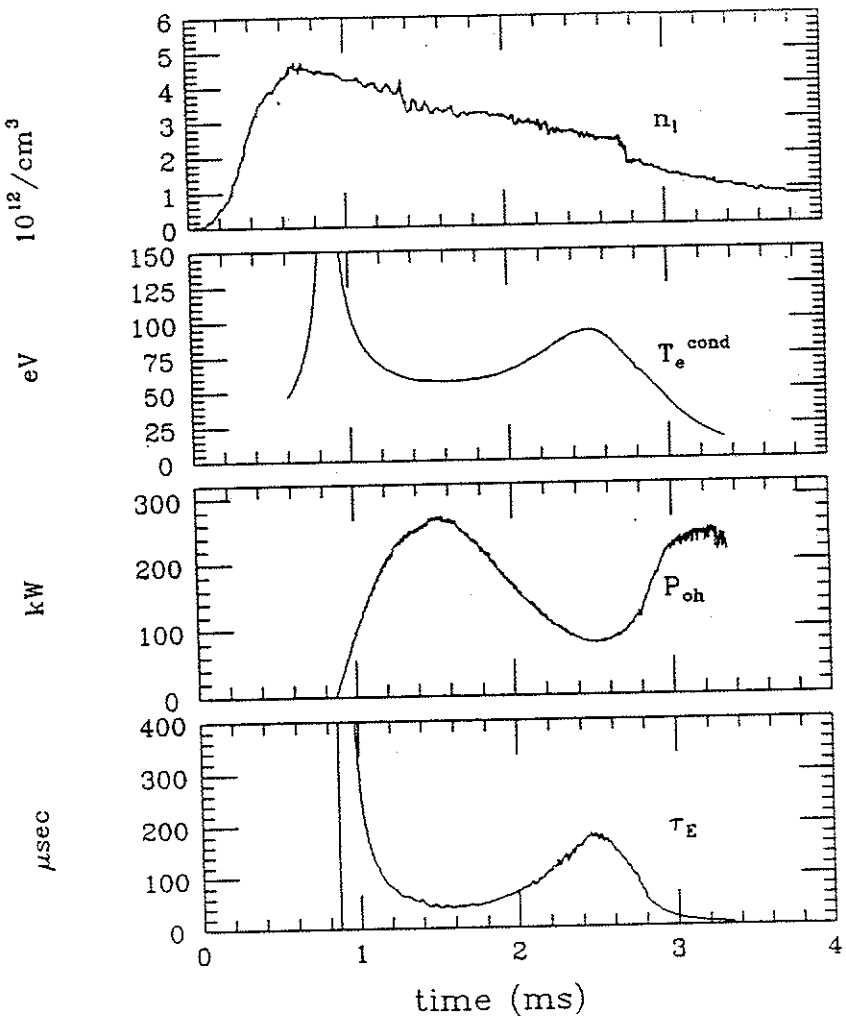

Figure 4.2b: Line average density n_l, electron conductivity temperature T_e^{cond}, ohmic heating power P_{oh}, and global energy confinement time τ_E for the same material limiter discharge as figure 4.1b.

shot-to-shot, the apparent increase in T_i at the time of the giant sawtooth collapse (2-2.5 ms) may not be real and might arise from lack of adequate reproducibility of neutral particle and plasma density profile changes during the giant sawtooth collapse.

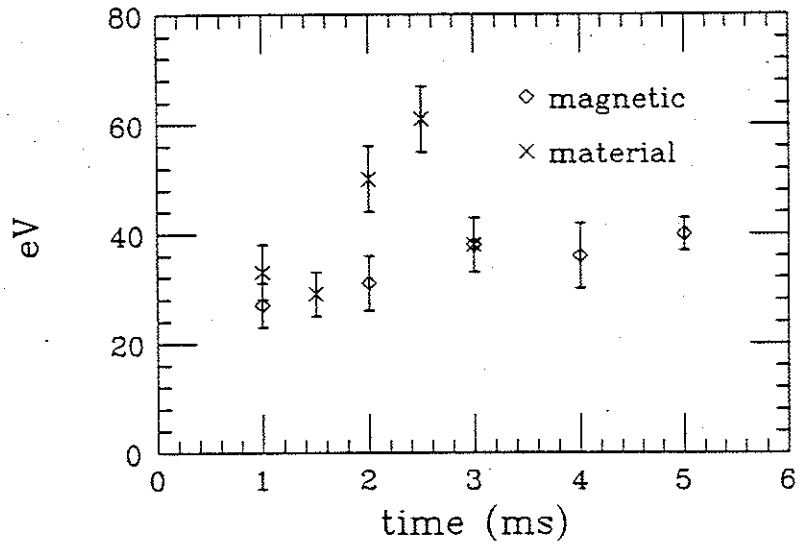

Figure 4.3: Evolution of ion temperature T_i, measured by neutral particle charge exchange analysis, in magnetic and material limiter $2 < q_a < 3$ discharges.

IV.A.2. SXR Emissivity Profiles:

SXR emissivity profiles in the material limiter configuration are more peaked and somewhat more centered than in the magnetic limiter configuration (figure 4.4). The profiles shown in figure 4.4 are taken shot-by-shot with a swiveling SXR detector 100

μs prior to the first giant sawtooth in each configuration. Effects of the small sawteeth are removed by averaging over 100 μs. A fixed central chord SXR detector is used to select shots with similar (± 20%) low frequency SXR emissivity. Variations within this range are normalized out. The "shoulders" on the material limiter SXR profile in figure 4.4 are not always present, and are associated with small sawteeth which invert at the shoulder inside the giant sawtooth inversions (Section V.B.1.a).

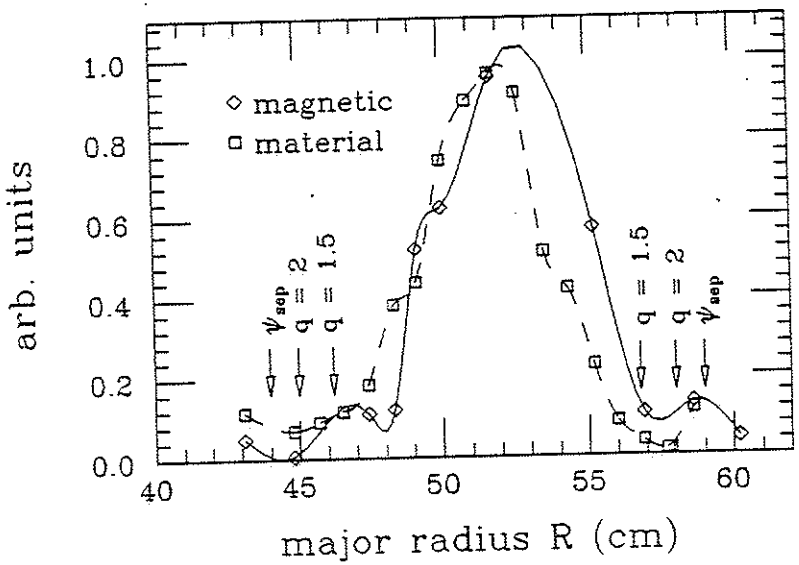

Figure 4.4: SXR emissivity profiles 100 μs before the first giant sawtooth in (solid) magnetic and (dashed) material limiter $2 < q_a < 3$ discharges. The locations of the separatrix and the q = 1.5 and 2 surfaces inferred from the equilibrium fit are indicated in the figure.

Most of the SXR emissivity is lost in each giant sawtooth in the magnetic limiter discharges, with the profile broadening and moving inward. After the giant sawtooth, the profile peaks and shifts out to nearly the original shape and radius. Over a series of giant sawteeth, the peak emissivity decreases, the profile broadens, and the peak drifts inward. This evolution is shown in 100 μs steps in figure 4.5.

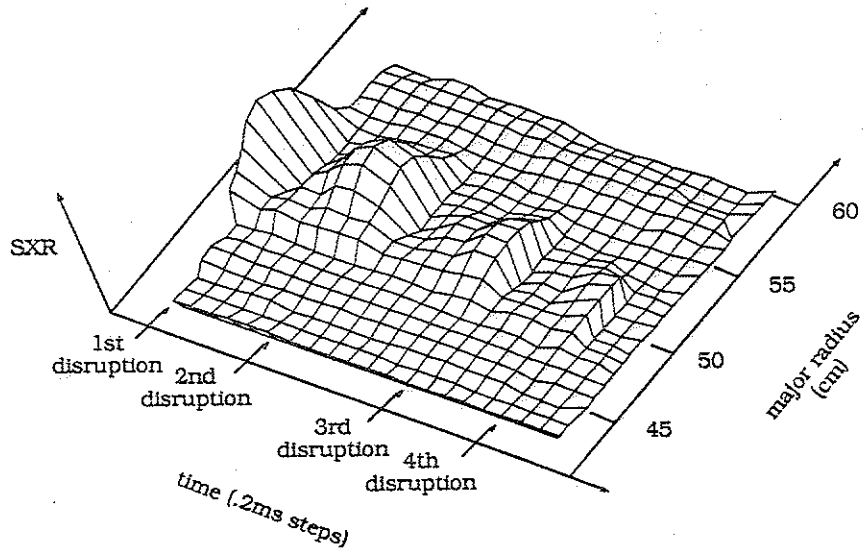

Figure 4.5: Surface plot of the SXR emissivity profile evolution in 200 μs time steps after each giant sawtooth in a typical magnetic limiter discharge. The last time step before each giant sawtooth is adjusted to fall 200 μs before the corresponding collapse.

IV.A.3. Scrape-off Density, Temperature, and Pressure Profiles:

The limiter plates decrease the plasma density, temperature,

and pressure in the divertor scrape-off region as shown by the profiles in figures 4.6, 4.7, and 4.8. The profiles shown were measured at ϕ = 240 degrees, with limiters at ϕ = 90 degrees. Scrape-off profiles have also been measured at ϕ = 60, 180, and 330 degrees with similar results, confirming the axisymmetry of the profiles. The limiters were inserted to r = 10 cm $\approx r_{sep}$.

The profiles were constructed from 30-50 similar shots, selected from data sets of 100-200 shots, with three to five shots per radial position. Values at each time step were averaged over 375 μs. The time average was varied from 100 μs to 1 ms to check the sensitivity of the profiles to the range used. The resulting profiles were insensitive to the range between 250 μs and 500 μs due to the small effect (short duration and small amplitude) of the small sawteeth on the scrape-off plasma (Section V.B.1.d), and the reproducibility of the giant sawtooth phasing (± 100-300 μs). The limiter plates were withdrawn to the vacuum vessel wall for the magnetic limiter discharges (figures 4.6a, 4.7a, and 4.8a) and inserted to the separatrix in material limiter discharges (figures 4.6b, 4.7b, and 4.8b). B_t was 5.5 kG in each configuration.

For similar $n_I \approx$ 4-5 $\times 10^{12}$ cm^{-3}, n_I^{core} (Section III.B.1) in material limiter discharges are 20-25% larger than in magnetic limiter discharges. The material limiter $n_I^{core} \approx$ 1-1.2 $\times 10^{13}$ cm^{-3} are near the Murakami limit[2] of 1-1.3 $\times 10^{13}$ cm^{-3}. No density limit disruptions have been seen on Tokapole II. Higher densities are achieved until the increased fill pressure and gas feed during the discharge prevents adequate breakdown of the gas. The scrape-off density profiles and n_I^{core} suggest that the density gradient is significantly steeper inside the separatrix in the material limiter configuration.

Central current channel T_e profiles (inferred from the SXR emissivity profiles of Section IV.A.2 using equation 3.33 with constant impurity density n_I and constant electron density $n_e \approx n_I^{core}$) are similar for the two configurations (figure 4.7). The T_e profiles were normalized at the peak to T_e^{cond}. Generally, the inferred T_e profiles don't fall off quite fast enough near the separatrix to match the measured scrape-off profiles. This is quite reasonable given the assumption of constant n_e and n_I. The scrape-off T_e profiles are flat for both magnetic and material limiters, although T_e is reduced about a factor of 2 by the limiter plates.

The scrape-off electron pressure profile is also reduced by the limiter plates (figure 4.8).

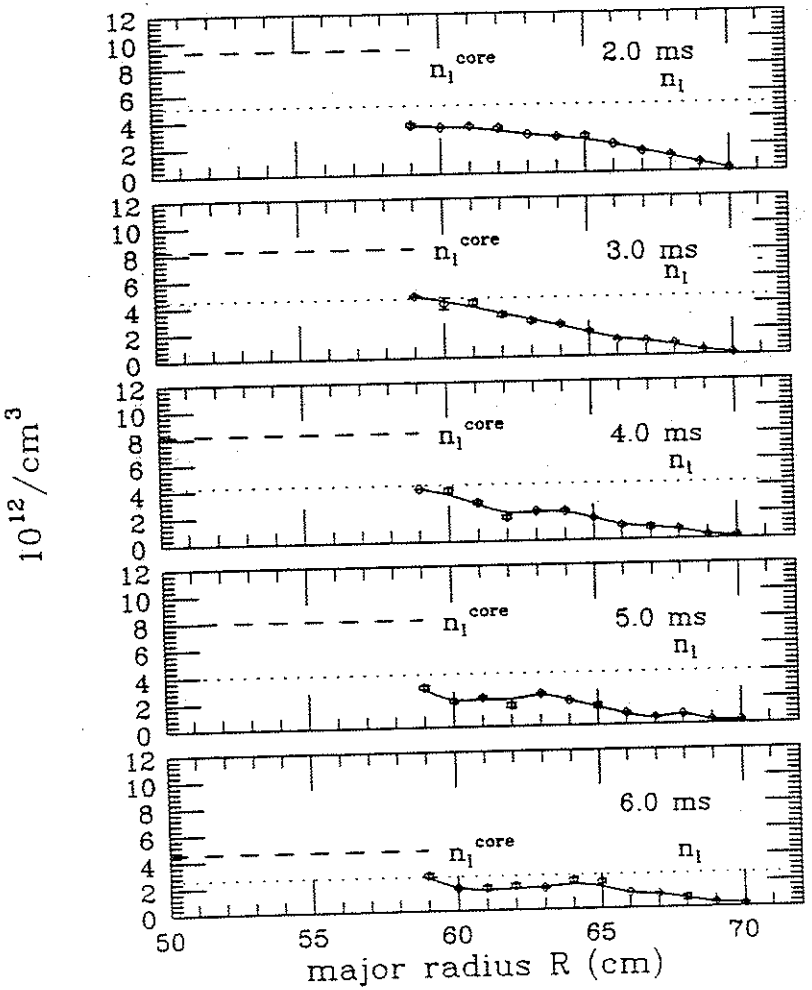

Figure 4.6(a): Scrape-off ion density n_i profiles in 1 ms steps from 2 ms in a typical magnetic limiter discharge. The line average density n_l (dotted line) and line average central current channel density n_l^{core} (dashed line) are shown.

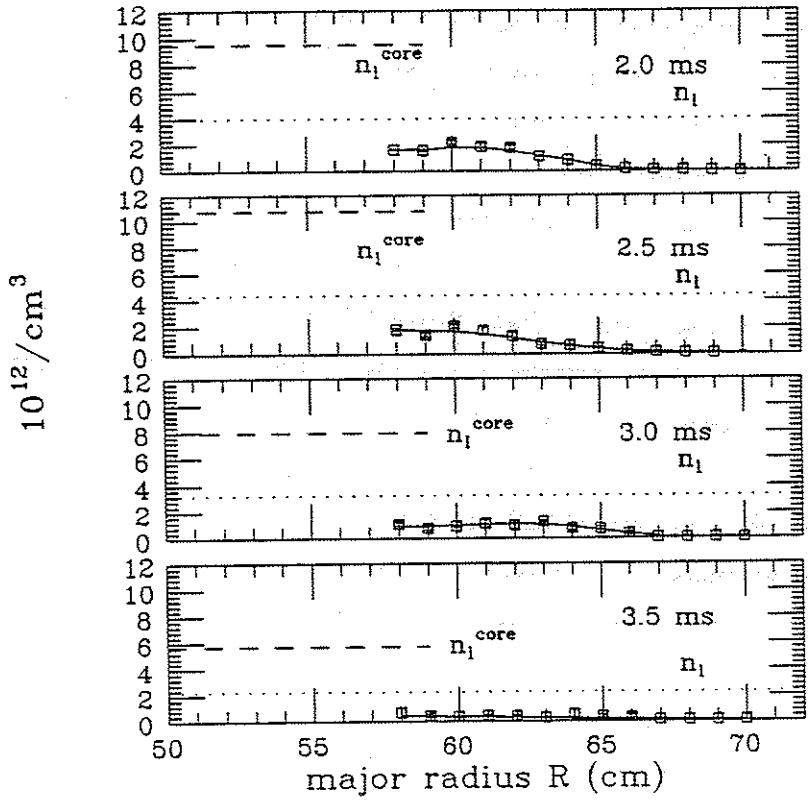

Figure 4.6(b): Scrape-off n_i profiles in 0.5 ms steps from 2 ms in a typical material limiter discharge. The discharge terminates disruptively at 3.2 ms. The line average density n_l (dotted line) and line average central current channel density n_l^{core} (dashed line) are shown.

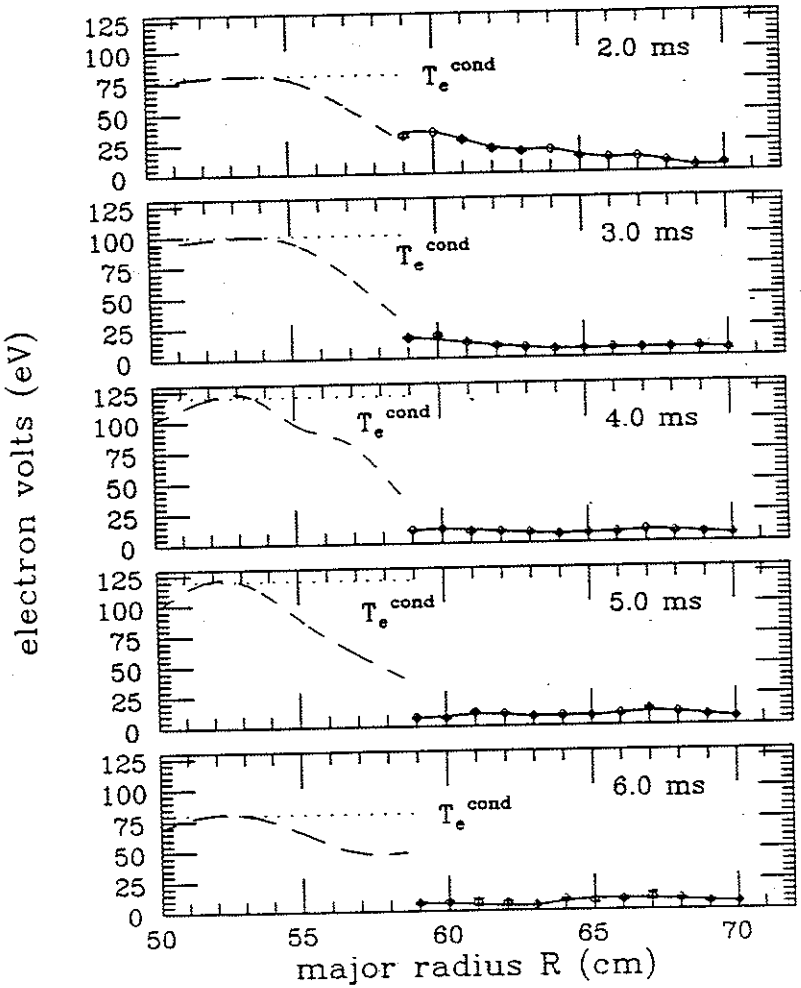

Figure 4.7(a) Scrape-off electron temperature T_e profiles in 1 ms steps from 2.0 ms in a typical magnetic limiter discharge. The electron conductivity temperature T_e^{cond} (dotted line) and central current channel T_e profile, inferred from the SXR emissivity profiles of figures 4.4 and 4.5 using equation 3.33 (dashed line), are shown.

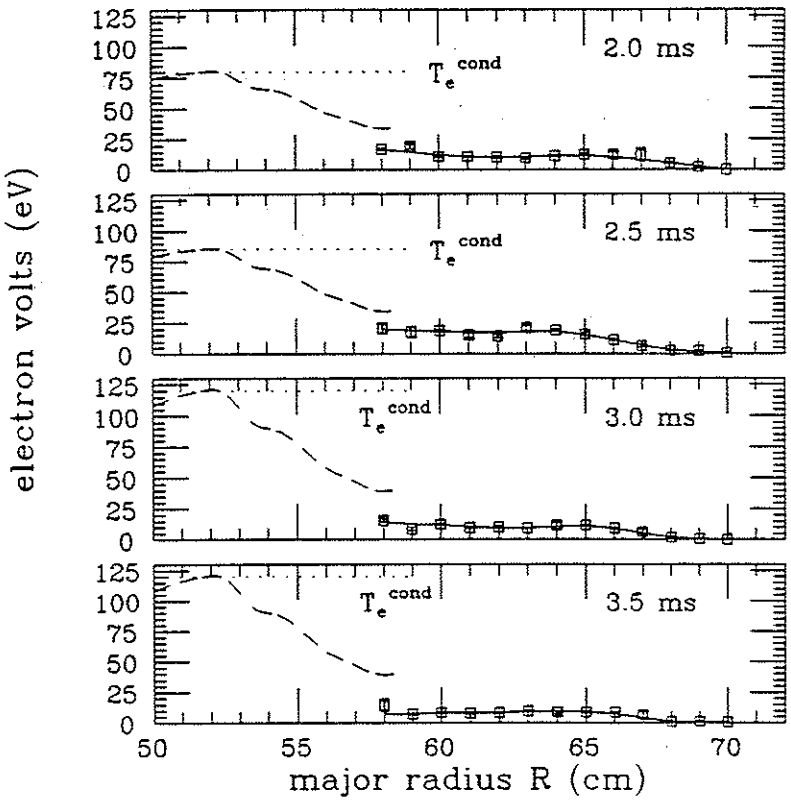

Figure 4.7(b) Scrape-off T_e profiles in 0.5 ms steps from 2 ms in a typical material limiter discharge. The material limiter discharge terminates disruptively at 3.2 ms. The electron conductivity temperature T_e^{cond} (dotted line) and central current channel T_e profile, inferred from the SXR emissivity profiles of figures 4.4 and 4.5 using equation 3.33 (dashed line), are shown.

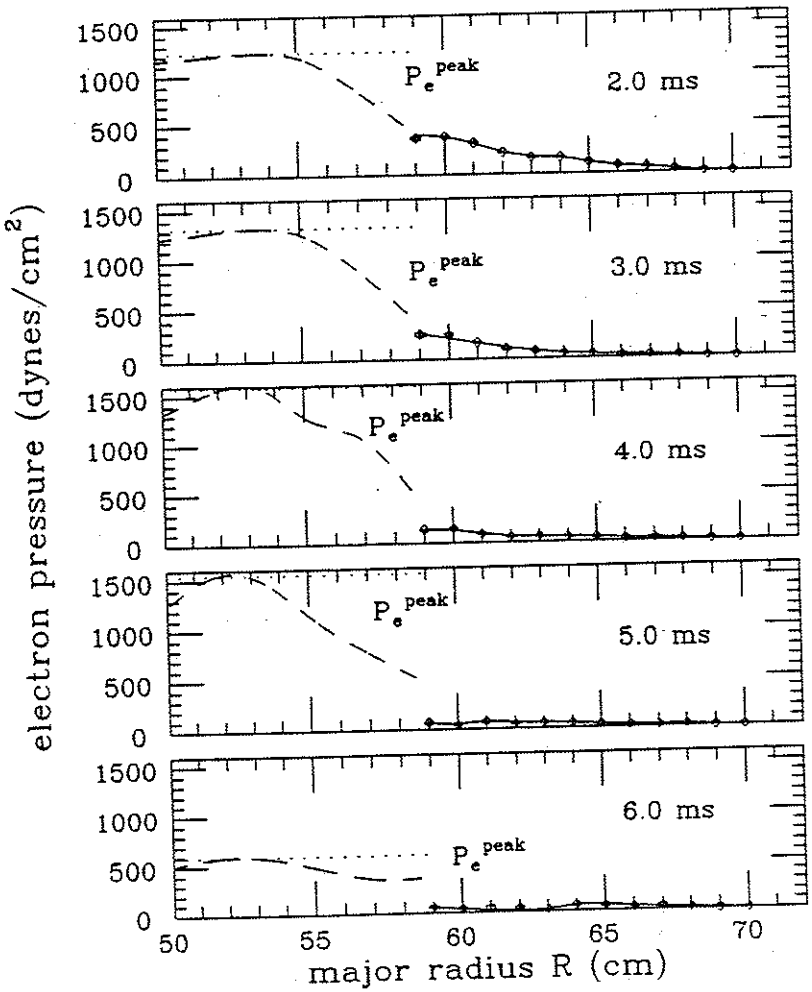

Figure 4.8(a): Scrape-off electron pressure P_e profiles in 1 ms steps from 2.0 ms in a typical magnetic limiter discharge. The "peak" pressure P_e^{peak} (dotted line), obtained using n_l^{core} and T_e^{cond}, and central current channel P_e profiles inferred from n_l^{core} and the inferred central current channel T_e profiles (figure 4.7) (dashed line) are also shown.

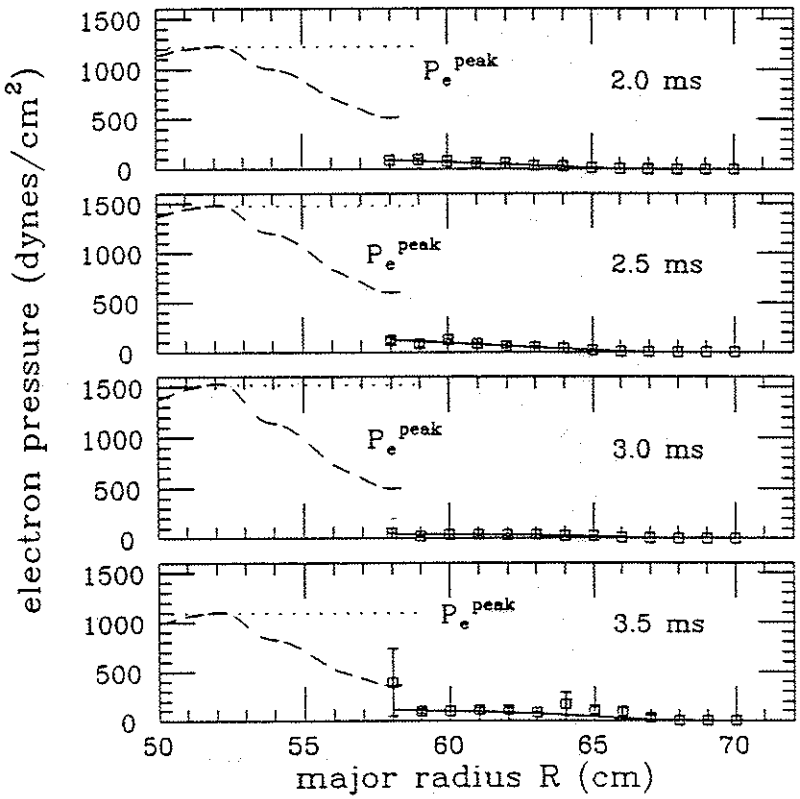

Figure 4.8(b): Scrape-off P_e profiles in 0.5 ms steps from 2.0 ms in a typical material limiter discharge. The material limiter discharge terminates at 3.2 ms. The "peak" pressure P_e^{peak} (dotted line), obtained using n_l^{core} and T_e^{cond}, and central current channel P_e profiles inferred from n_l^{core} and the inferred central current channel T_e profiles (figure 4.7) (dashed line) are also shown.

IV.A.4. Scrape-off Current Profiles:

Knowledge of the amount of plasma current in the scrape-off region is desirable because the presence of current outside the separatrix may influence the tearing mode stability, and a significant amount of current outside the separatrix yields an inaccurate q_a, since the model of Section III.B.1 considers all plasma current to be inside the separatrix.

Scrape-off profiles of toroidal current for magnetic and material discharges show the following features (figure 4.9): 1) early in the discharge ($t < 2$ ms), substantial toroidal current (15-30%) flows outside the separatrix in the magnetic limiter discharges. This current is not seen in material limiter discharges, and accounts for the excess current in the magnetic limiter configuration early in time. 2) After 2 ms, the current profile contracts and less current remains outside the separatrix (5-10%). Consequently, by the time the giant sawteeth onset (typically between 2 and 3 ms), the estimate of q_a is reliable; although the plasma current inside the separatrix is larger in the magnetic limiter configuration until $t \approx 5$ ms, the minor radius is larger as well. These effects compensate, yielding similar values for q_a.

Due to inadequate reproducibility, the uncertainties in the obtained profiles are rather large, 5-10 A/cm^2 versus measured values of 0-30 A/cm^2. The irreproducibility is also seen in the "zero" of the profiles near the wall at 22 cm, which typically ranged from 0 to -5 A/cm^2.

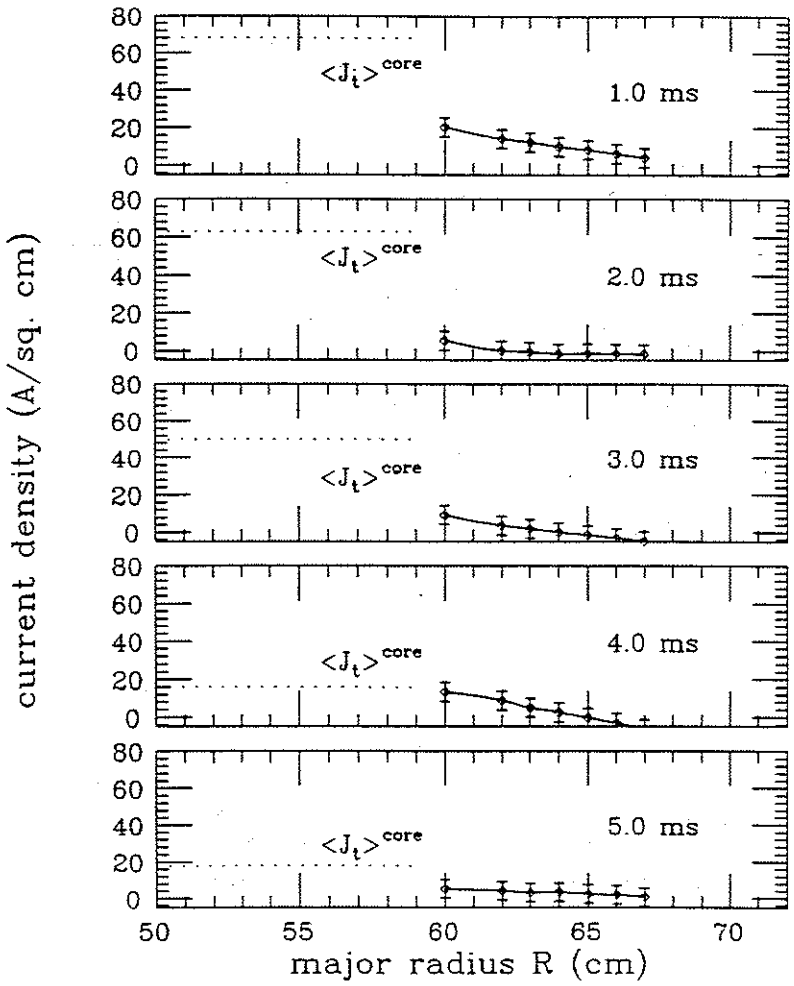

Figure 4.9(a): Toroidal plasma current density J_t profiles in 1 ms steps from 1 ms to the end of the discharge in magnetic limiter discharge. The dotted line is the average toroidal current density $\langle J_t \rangle^{core}$ in the central current channel inferred from the scrape-off profile and I_p.

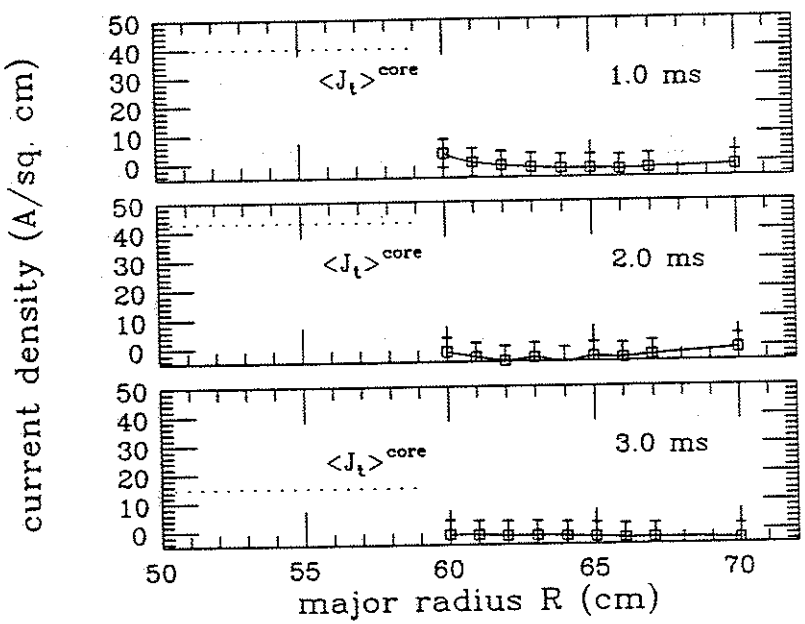

Figure 4.9(b): Toroidal plasma current density J_t profiles in 1 ms steps from 1 ms to the end of the discharge in a material limiter discharge. The dotted line is the average toroidal current density J_t^{core} in the central current channel inferred from the scrape-off profile and I_p.

IV.A.5. Summary for $2 < q_a < 3$ Discharges:

To facilitate comparison of the profile gradients between the magnetic and material limiter configurations, the n_i (figure 4.10), T_e (figure 4.11), P_e (figure 4.12), and J_t (figure 4.13) profiles are plotted normalized to the best estimate of the corresponding central

values during the "flattop" portion of the discharge (3 ms in magnetic limiter discharges; 2 ms in material limiter discharges). While the limiter plates are effective in removing plasma and current outside the separatrix, the material limiter discharges appear to have steeper gradients near the separatrix. This makes separation of profile-dependent effects from those directly caused by the divertor separatrix and plasma current in the scrape-off region difficult.

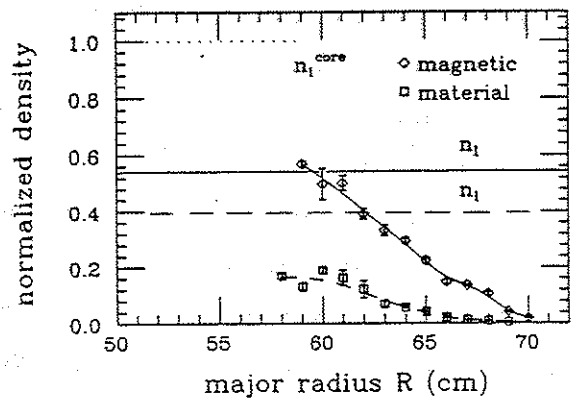

Figure 4.10: Density profiles (figure 4.6) during "flattop" in magnetic (solid) and material (dashed) limiter $2 < q_a < 3$ discharges. The profiles are normalized to n_i^{core} (dotted) to remove changes in overall magnitude. The line average densities are also shown.

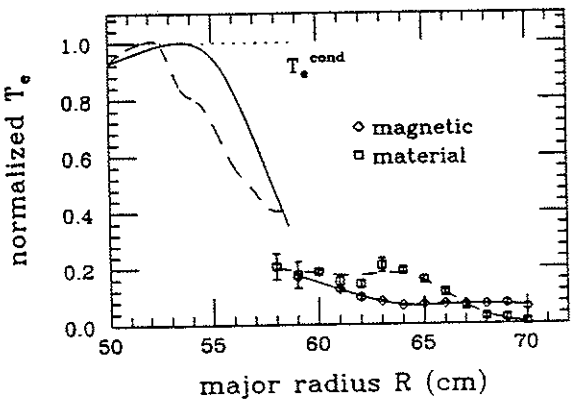

Figure 4.11: T_e profiles (figure 4.7) during "flattop" in magnetic (solid) and material (dashed) limiter discharges. The profiles are normalized to T_e^{cond} (dotted) to remove changes in magnitude. The inferred central current channel T_e are also shown.

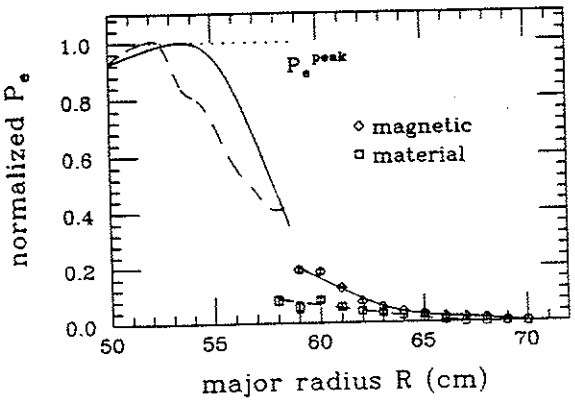

Figure 4.12: P_e profiles (figure 4.8) during "flattop" in magnetic (solid) and material (dashed) limiter discharges. The profiles are normalized to $n_i^{core} k T_e^{cond}$ to remove changes in magnitude. The inferred central current channel P_e are also shown.

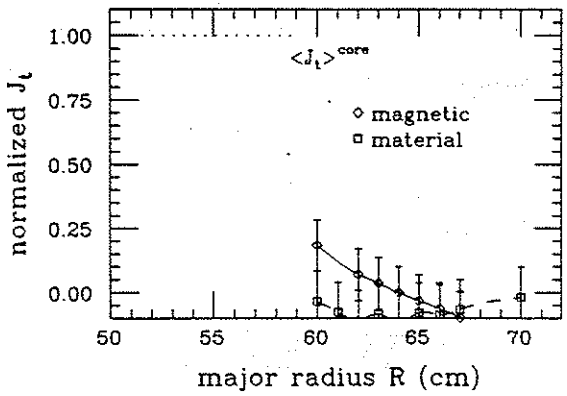

Figure 4.13: J_t profiles (figure 4.9) during "flattop" in magnetic (solid) and material (dashed) limiter discharges. The profiles are normalized to J_t^{core} to remove changes in overall magnitude.

Using n_i^{core}, T_e^{cond}, and T_i, the peak β at the magnetic axis is estimated to be:

$$\beta(0) = \frac{n_i^{core} k (T_i + T_e^{cond})}{B^2(0)/4\mu_o} = .4\% \qquad (4.1)$$

in these discharges.

Osborne[4] used an equilibrium code[3] that places all plasma current within the separatrix to model these discharges. I_p, I_r, B_t at the wall, and the inversion radius of the giant sawteeth

(inferred to be the q = 2 surface) were input to the code. The quality of the fit is presumably better for the material limiter configuration (no current outside the separatrix). The equilibrium poloidal flux contours and safety factor profile $q(\psi)$ are shown in figure 4.14. Attempts to match the discharge parameters with the giant sawtooth inversion radius identified as the q = 1 surface yielded unrealistically peaked current profiles.[4] The inferred q on axis is $1.1 \leq q(0) \leq 1.3$.

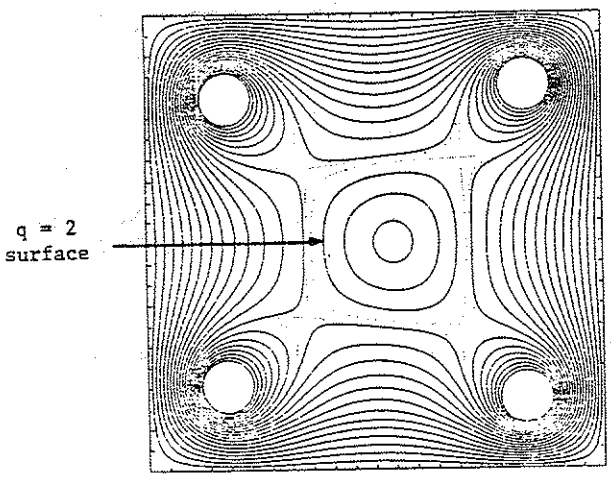

Figure 4.14(a): Equilibrium poloidal flux ψ contours and generated by an equilibrium code fit to the discharge parameters at the time of the first giant sawtooth in a $2 < q_a < 3$ discharge. The toroidal current profile is zero beyond the divertor separatrix in the equilibrium code. The location of the q = 2 surface is indicated on the flux plot.

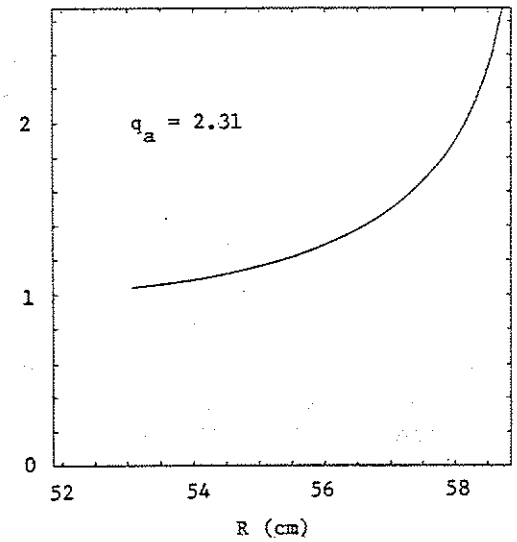

Figure 4.14(b): Midplane safety factor profile q(R) corresponding to the equilibrium poloidal flux plot in figure 4.16a generated by an equilibrium code fit to the discharge parameters at the time of the first giant sawtooth in a $2 < q_a < 3$ discharge.

IV.B. Equilibria with $1 < q_a < 2$:

IV.B.1. Global Discharge Parameters:

The most significant difference between the magnetic and material limiter discharges is the increase in V_l in the material limiter discharge after q_a rises above 1.6 (figure 4.15). Sawteeth become progressively more "giant" and the discharge terminates in a soft disruption near $q_a \approx 1.9$. As I_p decays in the magnetic

limiter discharge, q_a rises above 2 and the traces in figure 4.15a appear like those in $2 < q_a < 3$ magnetic limiter discharges (figure 4.1a).

The loop voltage is 10-15 V, compared to 3-5 V in the $2 < q_a < 3$ discharges of figure 4.1. In addition to the increased I_p, the effective radius increases from ~ 10 cm to ~ 12 cm in magnetic limiter discharges and from ~ 8 cm to ~ 10 cm in material limiter discharges. This increase is also seen in the SXR emissivity profiles (Section IV.B.2).

Line average density, electron conductivity temperature, ohmic heating power, and global energy confinement time are shown in figure 4.16 for the discharges of figure 4.15. The material limiter discharges are degraded from the magnetic limiter discharges. T_e^{cond} drops from 80-125 eV in magnetic limiter discharges to 60-75 eV in material limiter discharges. τ_E drops by a factor of 2-3 from 200-300 μs to 100μs or less. The magnetic limiter $\tau_E \approx$ 200-300 μs agrees well with values obtained in helically assisted $q_\psi \approx 1.5$ discharges in the CLEO device.[5] No degradation in T_i is seen in material limiter $1 < q_a < 2$ discharges (figure 4.17). The material limiter discharges used to obtain figure 4.17 ended at 4 ms, while the magnetic limiter discharges lasted until 6 ms, which is the cause of the difference seen after 3.5 ms in the figure.

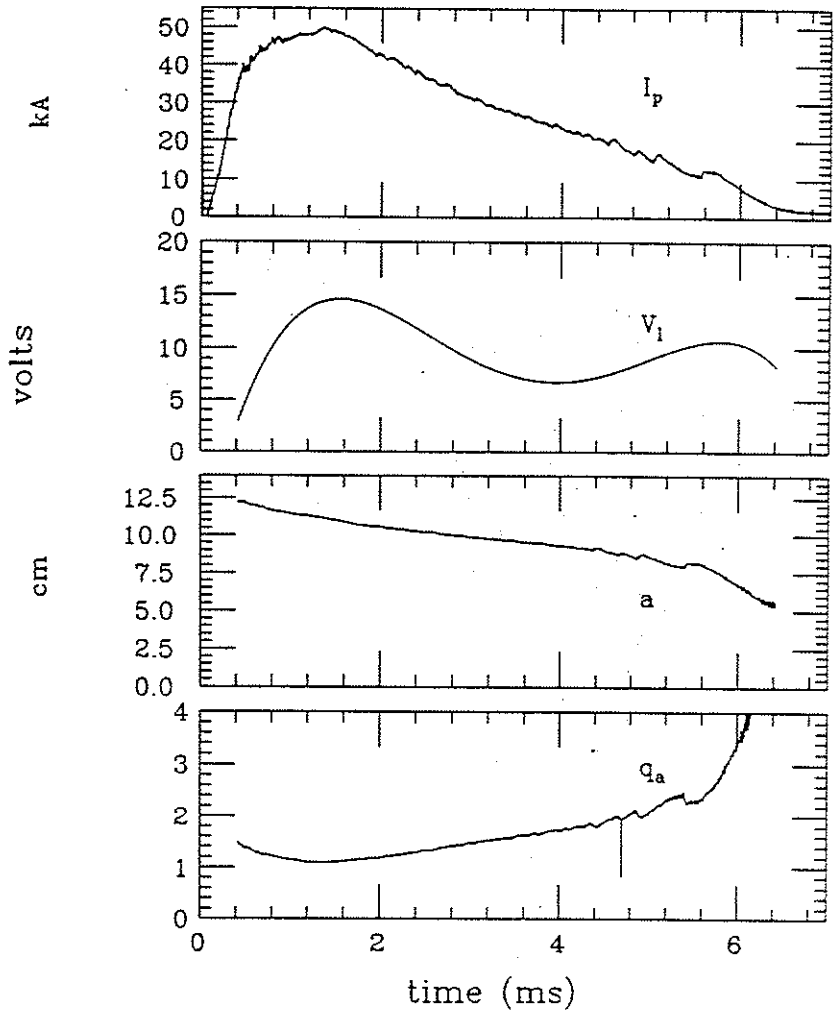

Figure 4.15a: Plasma current I_p, loop voltage V_l, equivalent minor radius a, and effective edge safety factor q_a for a typical magnetic limiter discharges. Toroidal field B_t = 4.8 kG.

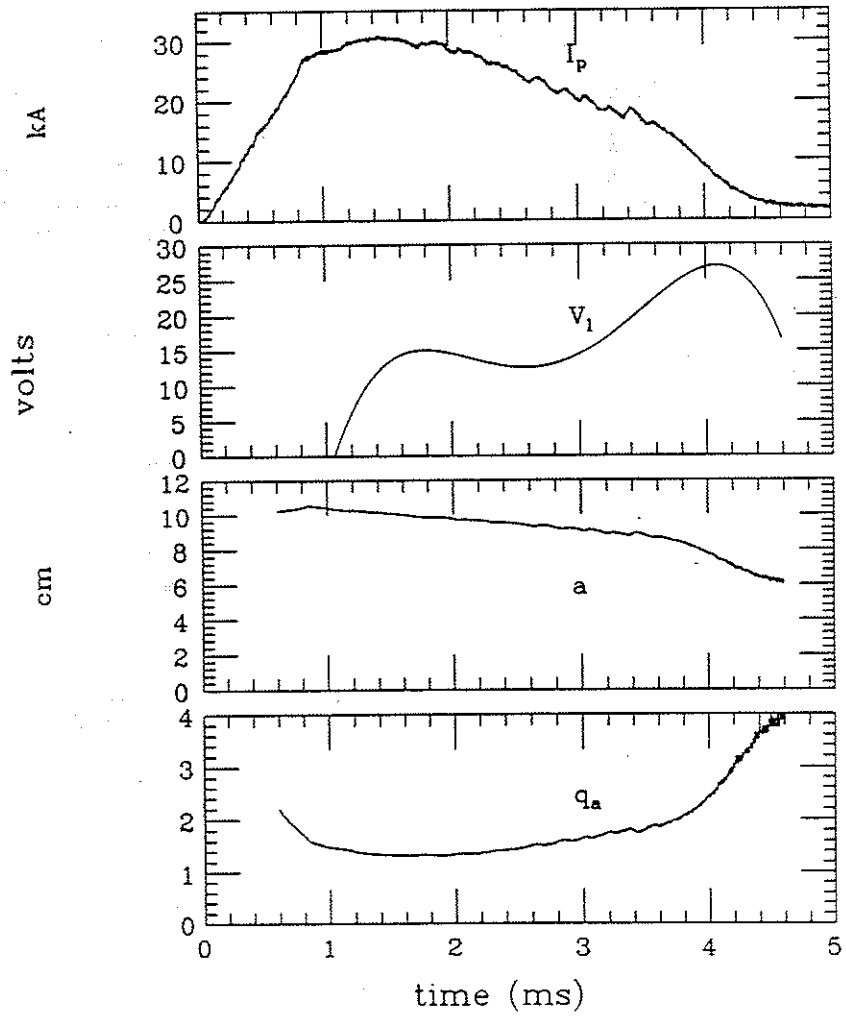

Figure 4.15b: Plasma current I_p, loop voltage V_l, equivalent minor radius a, and effective edge safety factor q_a for a typical material limiter discharge. Toroidal field B_t = 4.8 kG.

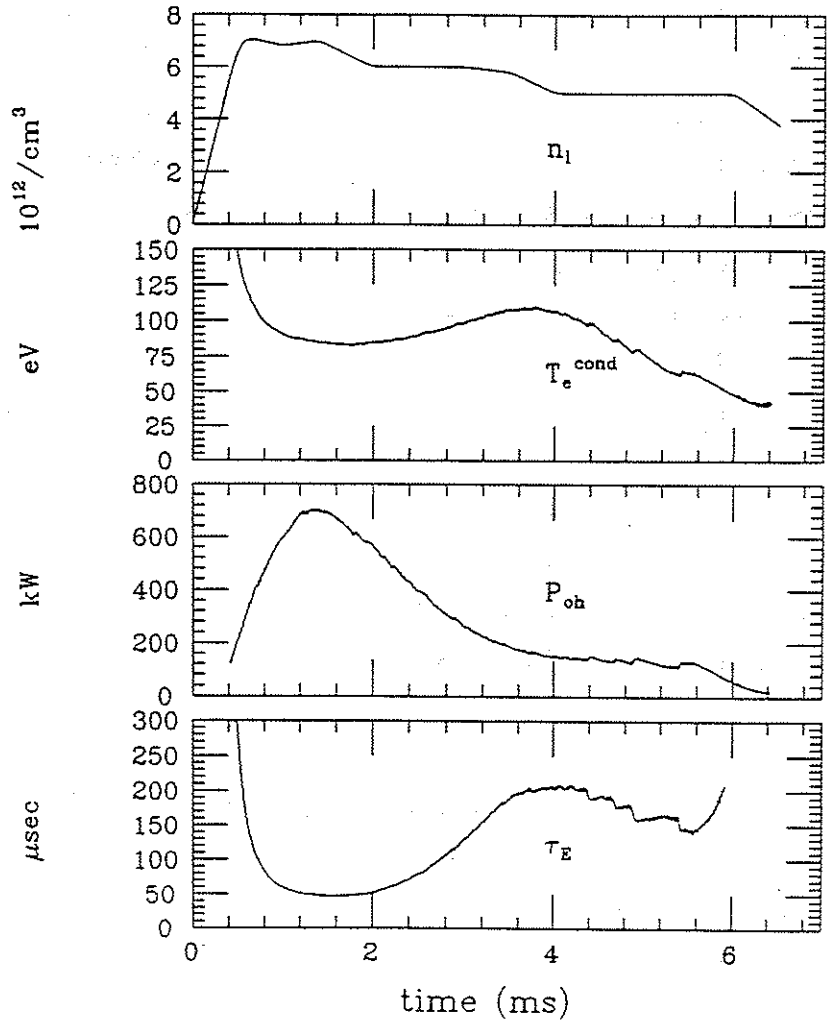

Figure 4.16(a): Line average density n_l, electron conductivity temperature T_e^{cond}, ohmic heating power P_{oh}, and global energy confinement time τ_E for the same magnetic limiter discharge as figure 4.15a.

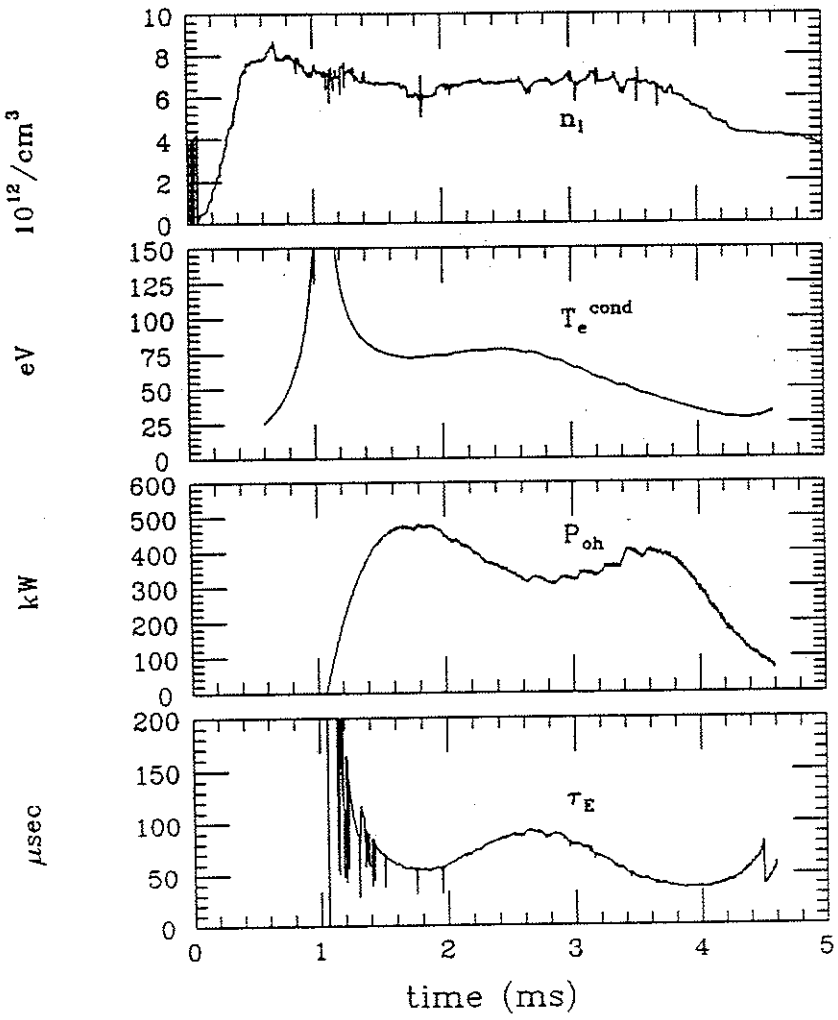

Figure 4.16b: Line average density n_l, electron conductivity temperature T_e^{cond}, ohmic heating power P_{oh}, and global energy confinement time τ_E for the same material limiter discharge as figure 4.15a.

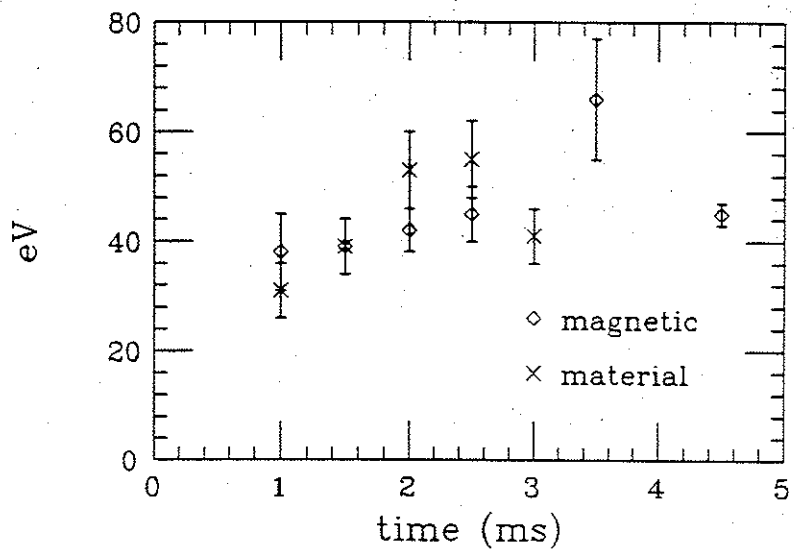

Figure 4.17: Evolution of ion temperature T_i, measured by neutral particle charge exchange analysis, in magnetic and material limiter $1 < q_a < 2$ discharges.

IV.B.2. SXR Emissivity Profiles:

SXR emissivity profiles in both magnetic and material limiter discharges are broader and shifted outward 2-3 cm relative to the $2 < q_a < 3$ profiles (figure 4.18). The magnetic limiter profile (figure 4.18a) shows a strong "inverse-D" shape (asymmetric profile with a long tail on the small R side), consistent with higher β. These changes are consistent with the 20% increase in effective minor radius seen in figures 4.1 and 4.15, and have been well documented in other low-q tokamak experiments.[6-8]

Stability to the (2,1) tearing mode in a tokamak with a

conducting wall at $r_{wall}/a = 1.2$ and $q_{lim} = 1.8$ requires a broad current density profile and flat q profile over most of the discharge interior (figure 4.19).[9] This marginally stable profile is maintained during ohmic heating by internal disruptions which efficiently mix the plasma inside the q = 1 surface and may hold q(0) > 1 on average. The material limiter SXR profile is more peaked than the magnetic limiter profile, suggesting that these discharges may not be as stable to the (2,1) tearing mode.

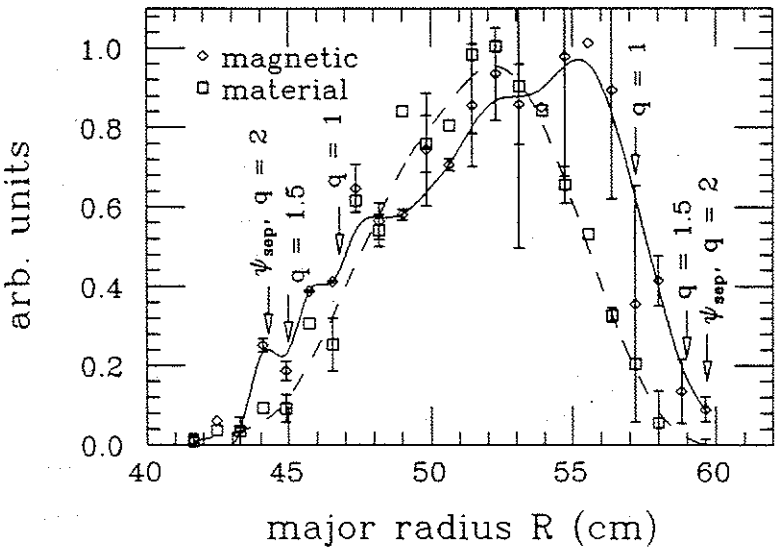

Figure 4.18a: Comparison of SXR emissivity profiles in the midplane for (solid) magnetic and (dashed) material limiter $q_a \sim 1.5$ discharges. The positions of the separatrix and the q = 2, 1.5, and 1 surfaces in the equilibrium code fit are shown.

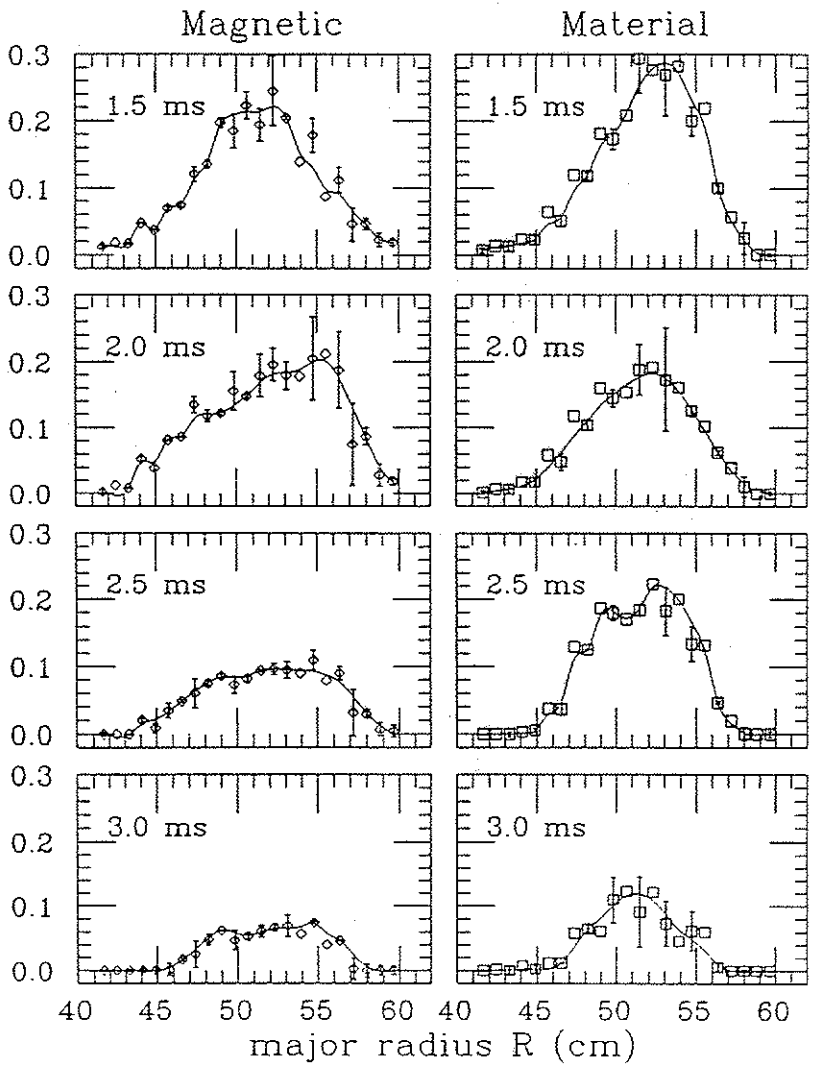

Figure 4.18b: Sequence of SXR emissivity profiles in 0.5 ms steps during the "flattop" portion of (left) magnetic and (right) material limiter $q_a \sim 1.5$ discharges.

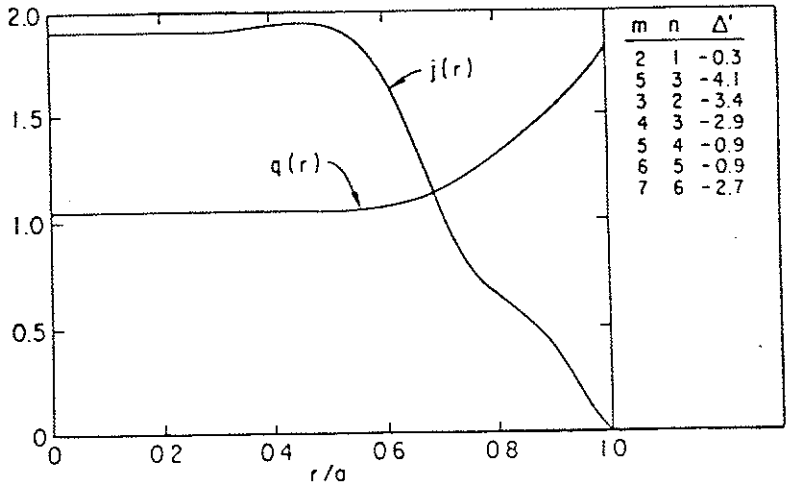

Figure 4.19: Optimized current and safety factor profiles for complete stability with a conducting wall at $r_{wall}/a \sim 1.2$. Δ' for modes with $2 \leq m \leq 7$ and $1 \leq n \leq 6$ are shown (from reference 9).

IV.B.3. Scrape-off Density, Temperature, and Pressure Profiles:

The limiter plates are effective in reducing plasma density, temperature and pressure in the scrape-off region in $1 < q_a < 2$ material limiter discharges, as shown in figures 4.20, 4.21, and 4.22. The magnetic limiter profiles have steep gradients outside the divertor separatrix, flatten across the separatrix, and are inferred to be broad and relatively flat across the central current channel. The material limiter profiles are flat or slowly rising outside the separatrix, flat across the separatrix, and are inferred to be more peaked inside the separatrix than the magnetic limiter profiles.

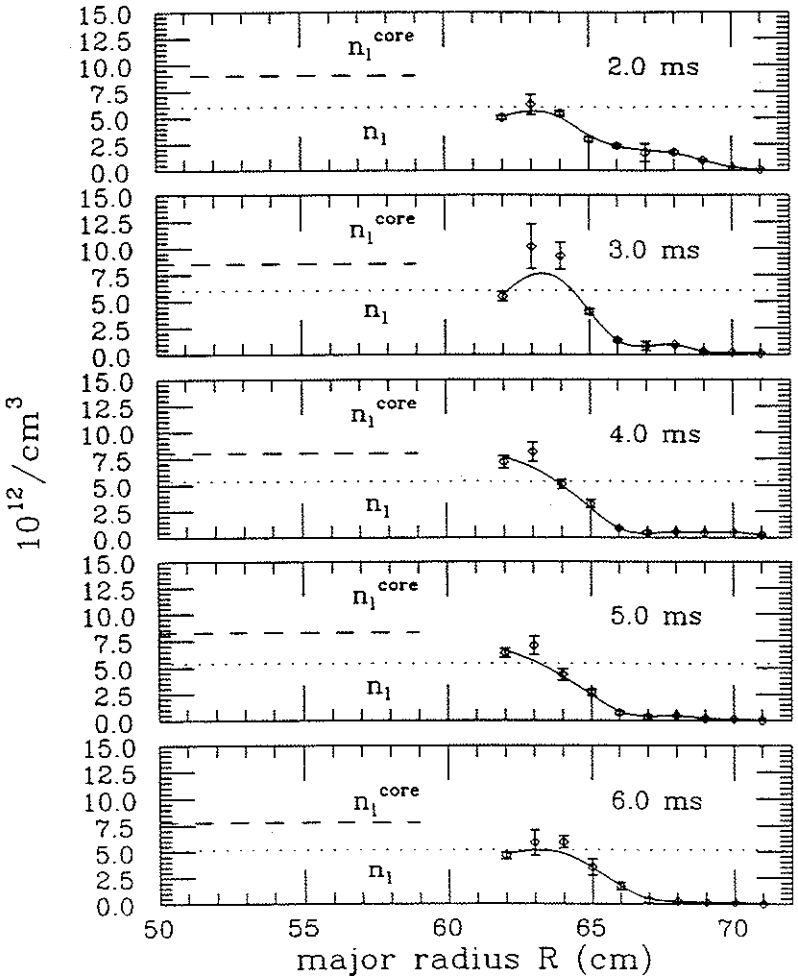

Figure 4.20(a): Scrape-off ion density n_i profiles in 1 ms steps from 2 ms in a typical magnetic limiter discharge. The line average density n_l (dotted line) and the line average central current channel density n_l^{core} (dashed line) are shown.

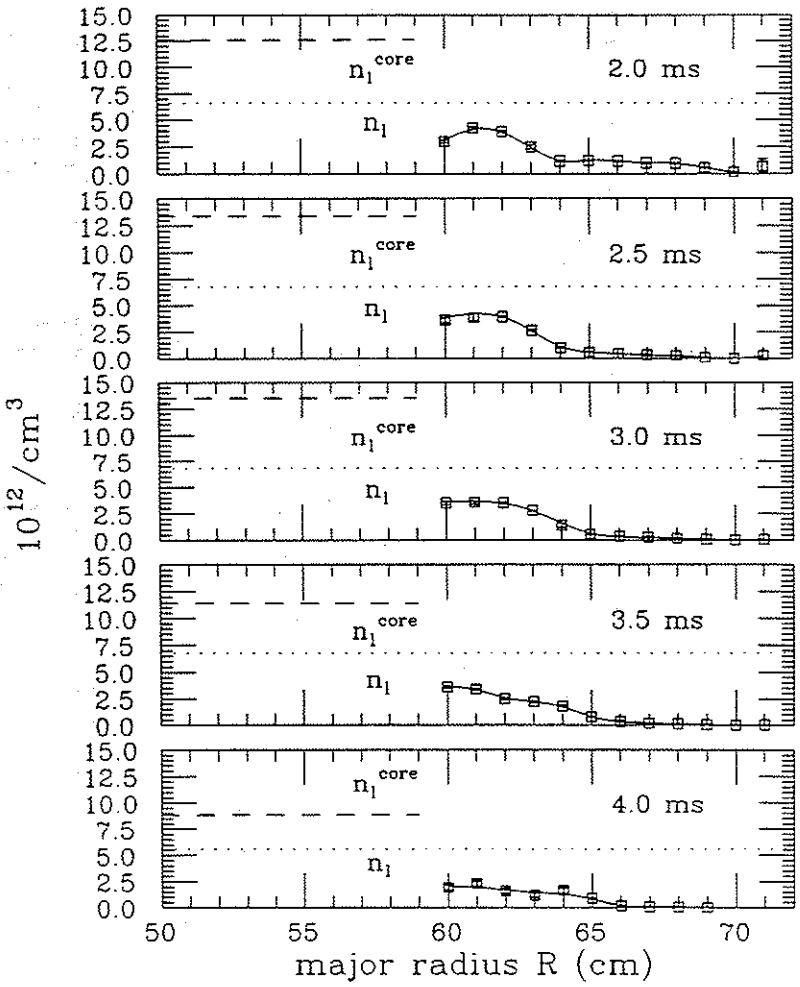

Figure 4.20b: Scrape-off density profiles in 0.5 ms steps from 2 ms in a typical material limiter discharge. The line average density n_l (dotted line) and the line average central current channel density n_l^{core} (dashed line) are shown.

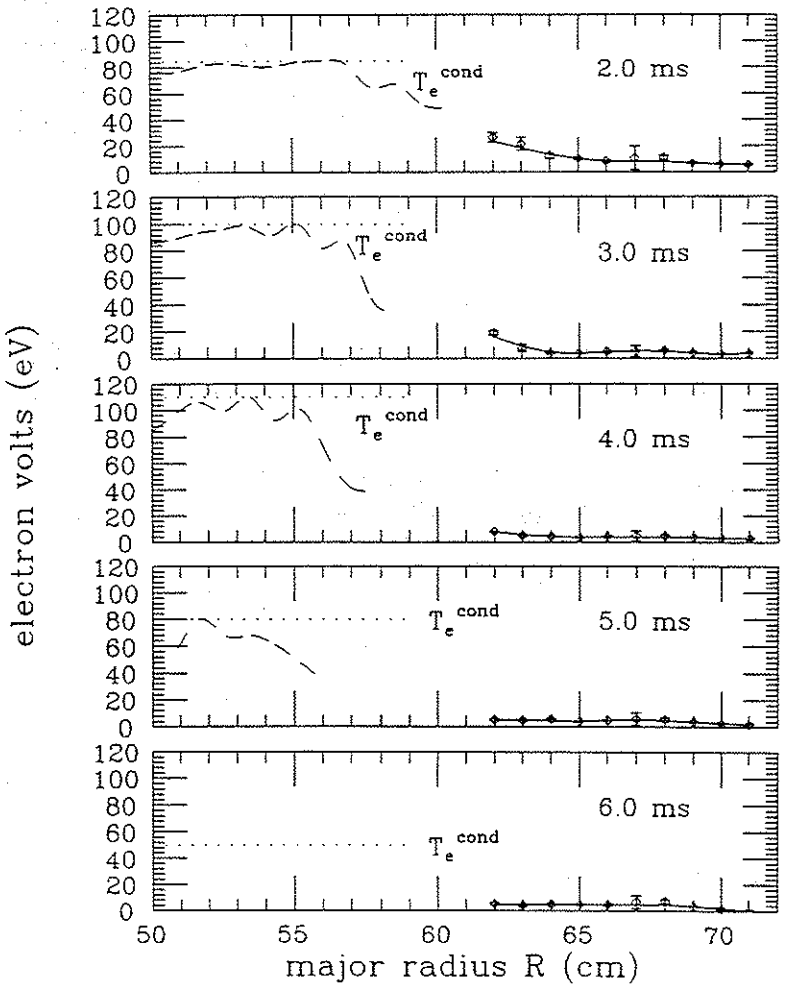

Figure 4.21a: Scrape-off electron temperature T_e profiles in 1 ms steps from 2 ms in a typical magnetic limiter discharge. T_e^{cond} (dotted line) and central current channel T_e profile, inferred from the SXR emissivity profiles of figure 4.18 using equation 3.33 (dashed line), are shown.

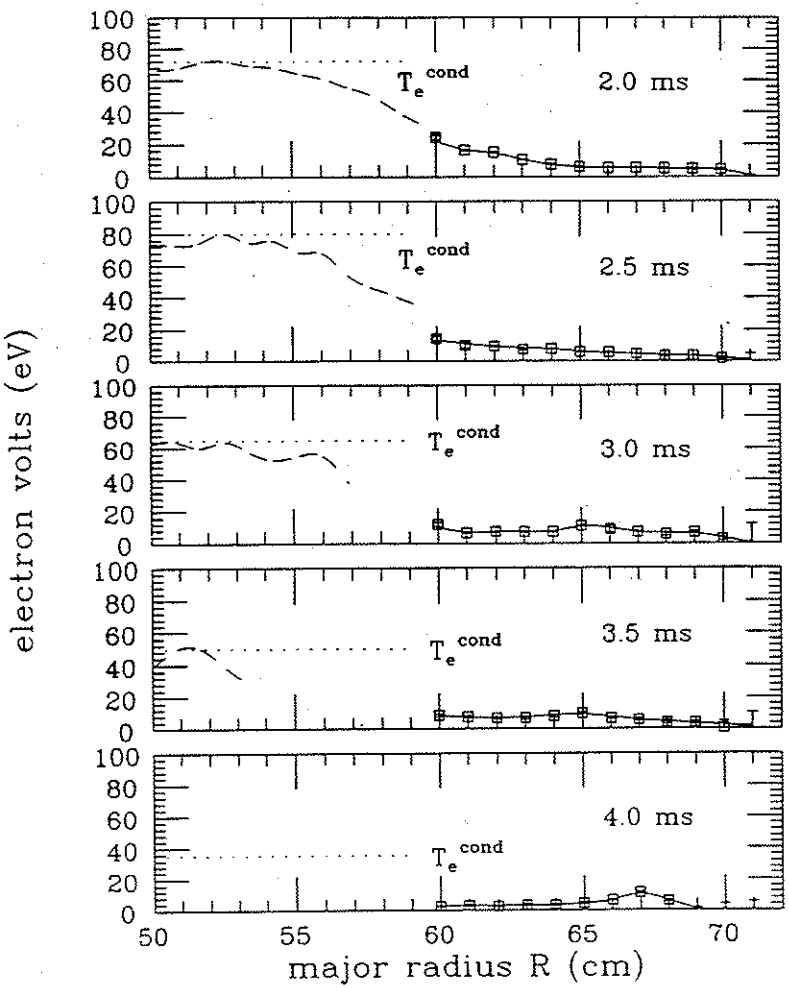

Figure 4.21b: Scrape-off T_e profiles in 0.5 ms steps from 2 ms in a typical material limiter discharge. T_e^{cond} (dotted line) and central current channel T_e profile, inferred from the SXR emissivity profiles of figure 4.18 using equation 3.33 (dashed line), are shown.

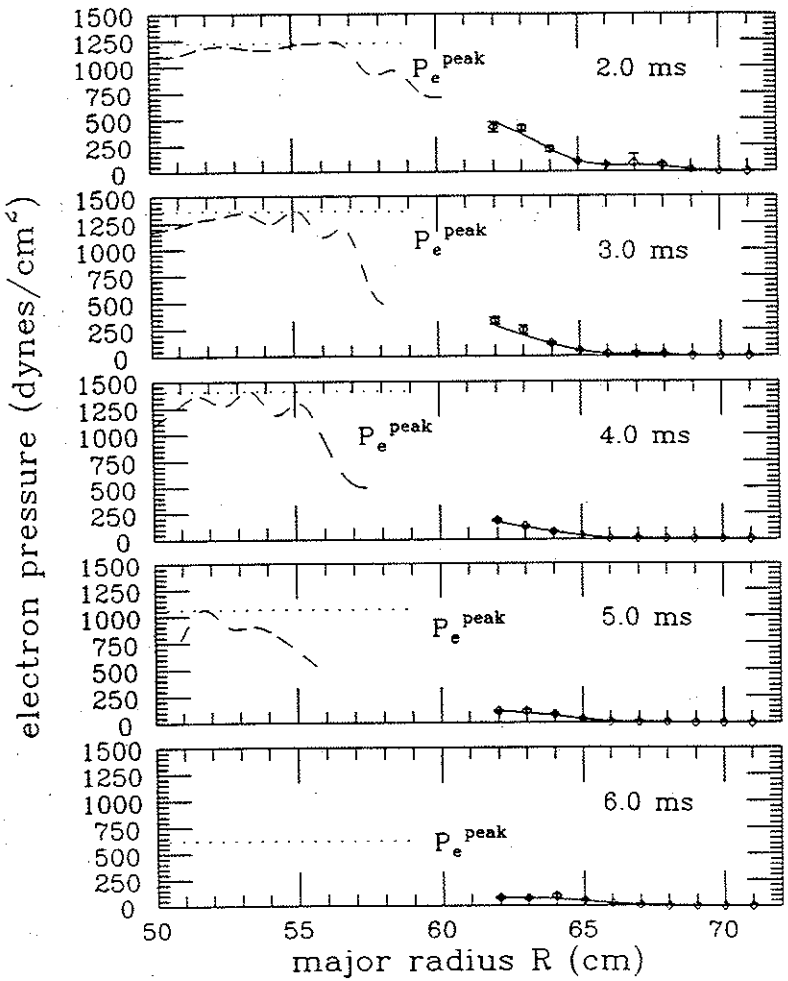

Figure 4.22a: Scrape-off electron pressure P_e profiles in 1 ms steps from 2 ms in a typical magnetic limiter discharge. The "peak" pressure P_e^{peak} (dotted line) and central current channel P_e profiles inferred from n_l^{core} and the inferred central current channel T_e profiles (figure 4.21) (dashed line) are also shown.

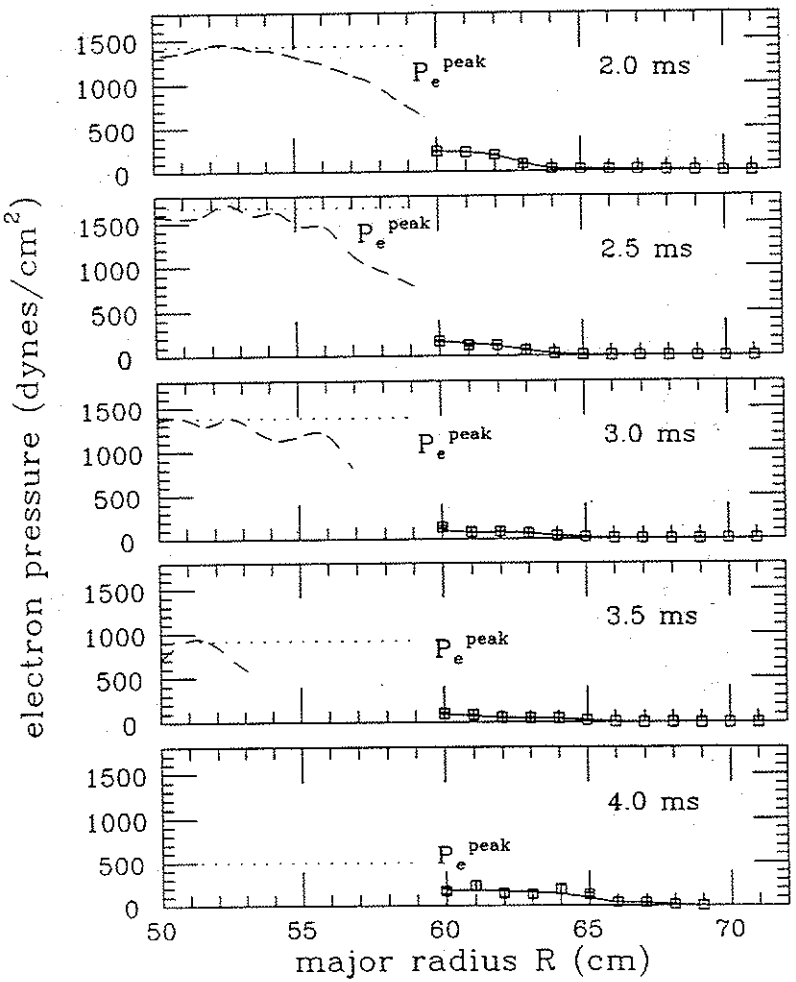

Figure 4.22b: Scrape-off P_e profiles in 0.5 ms steps from 2 ms in a typical material limiter discharge. The "peak" pressure P_e^{peak} (dotted line) and central current channel P_e profiles inferred from n_l^{core} and the inferred central current channel T_e profiles (figure 4.22) (dashed line) are also shown.

The line average densities of 7-9 x 10^{12} cm^{-3} are 50-60% higher than in the $2 < q_a < 3$ discharges. The n_l^{core} are correspondingly larger as well; $n_l^{core} \approx 1.2\text{-}2 \times 10^{13}$ cm^{-3}. For these discharges, B_t = 4.8 kG and the Murakami limit[2] is 1-1.3 x 10^{13} cm^{-3}. The facility of obtaining high densities at low-q was identified in one of the first low-q tokamak experiments on the DIVA[6] device, and has been used extensively to help obtain high β in other devices.[5,8,10-14]

The scrape-off T_e profiles (figure 4.21) are flat in both configurations and are similar to those obtained in the $2 < q_a < 3$ discharges. The central current channel T_e profile inferred from the SXR profile is significantly more peaked in the material limiter configuration. Peak electron temperatures inferred from T_e^{cond} are similar to those obtained at $2 < q_a < 3$.

P_e is 2-4 times larger in the scrape-off region than in $2 < q_a < 3$ in each configuration. Peak P_e values inferred from n_l^{core} and T_e^{cond} are larger due to similar T_e^{cond} and somewhat larger n_l^{core} in these discharges.

IV.B.4. Scrape-off Current Profiles:

Except for early in time (before 2 ms), the toroidal current is quite small in both the magnetic and material limiter configurations (figure 4.23). As was the case for $2 < q_a < 3$ discharges, the excess toroidal current outside the separatrix before 2 ms accounts for most of the increase in I_p in the magnetic limiter configuration. Prior to 2 ms, 30-50% of the toroidal current flows in the scrape-off

region. After 2 ms, this drops to typically less than 10%.

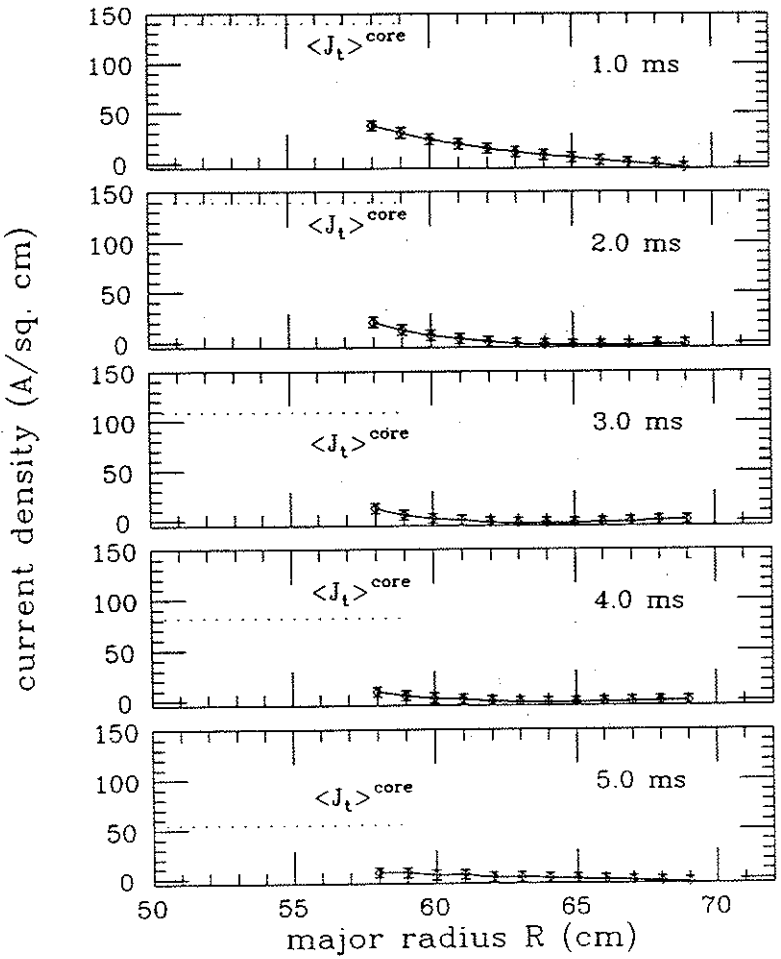

Figure 4.23a: Toroidal plasma current density J_t profiles in 1 ms steps from 1 ms to the end of the discharge in a magnetic limiter discharge. The dotted line is the average toroidal current density $\langle J_t \rangle^{core}$ in the central current channel inferred from the scrape-off profile and I_p.

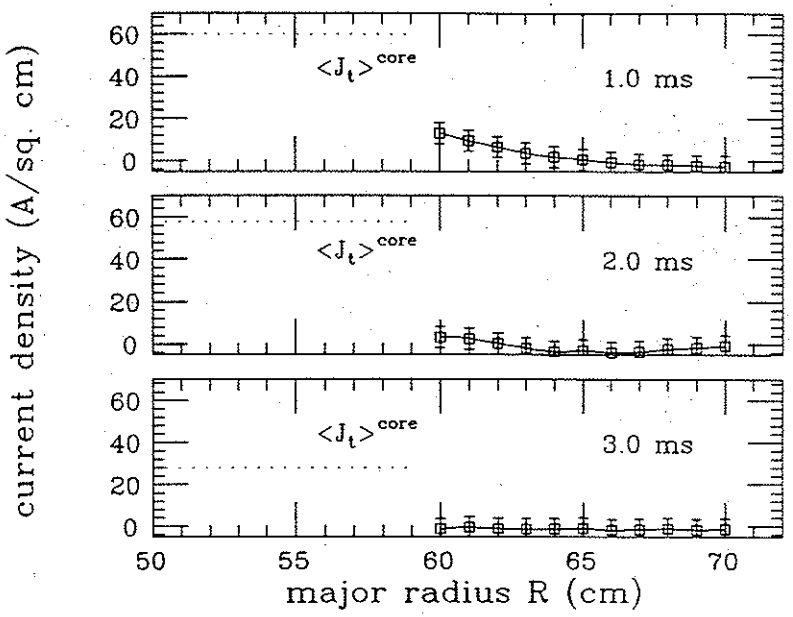

Figure 4.23b: Toroidal plasma current density J_t profiles in 1 ms steps from 1 ms to the end of the discharge in a material limiter discharge. The dotted line is the average toroidal current density $\langle J_t \rangle^{core}$ in the central current channel inferred from the scrape-off profile and I_p.

IV.B.5. Summary for $1 < q_a < 2$ Discharges:

To facilitate comparison of the profile gradients between the magnetic and material limiter configurations, the n_i (figure 4.24), T_e (figure 4.25), P_e (figure 4.26), and J_t (figure 4.27) profiles are plotted normalized to the best estimate of the corresponding central values during the flattop portion of the discharges (3 ms in

magnetic limiter and 2 ms in material limiter discharges). The limiter plates are effective in reducing plasma density, temperature, and pressure outside the separatrix, but the resulting profiles appear to have significantly steeper gradients within the separatrix than the magnetic limiter profiles, as was the case at 2 < q_a < 3 (Section IV.A.5). The current density profiles are similar in the two configurations after 2 ms. The broad wing of current prior to 2 ms in the magnetic limiter discharges (figure 4.23) may play a role in enabling passing of the q = 2 barrier during this time.

Using n_l^{core}, T_e^{cond}, and T_i in equation 4.1 for the peak β yields $\beta(0)$ of 0.9% in magnetic and 0.7% material limiter discharges.

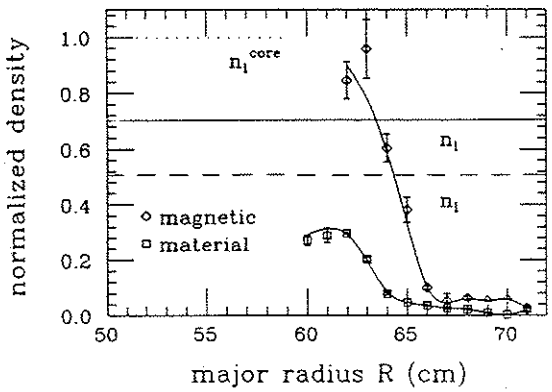

Figure 4.24: n_i profiles (figure 4.20) during flattop in magnetic (solid) and material (dashed) limiter 1 < q_a < 2 discharges. The profiles are normalized to n_l^{core} to remove changes in magnitude. The line average densities n_l are also shown.

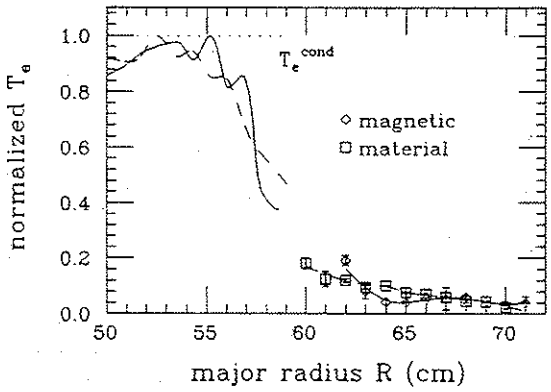

Figure 4.25: T_e profiles (figure 4.21) during flattop in magnetic (solid) and material (dashed) limiter discharges. The profiles are normalized to T_e^{cond} to remove changes in magnitude. The inferred central current channel T_e are also shown.

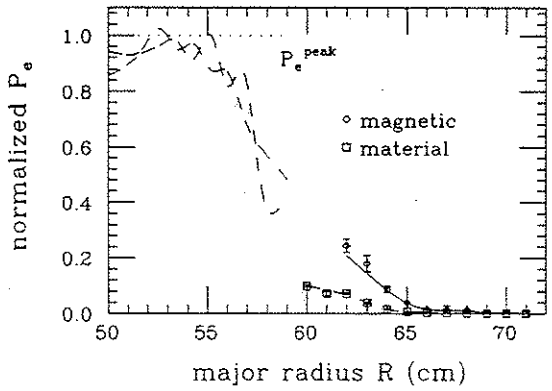

Figure 4.26: P_e profiles (figure 4.22) during flattop in magnetic (solid) and material (dashed) limiter discharges. The profiles are normalized to $n_l^{core}kT_e^{cond}$ to remove changes in magnitude.

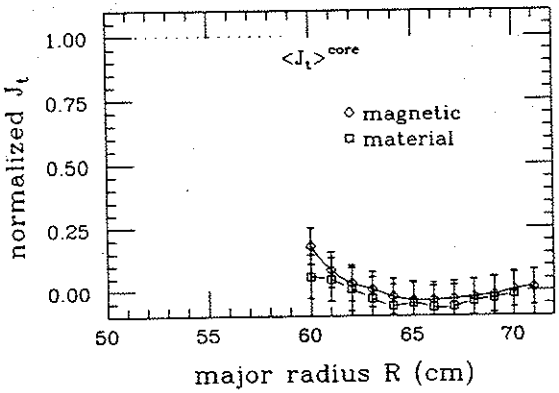

Figure 4.27: J_t profiles (figure 4.23) during flattop in magnetic (solid) and material (dashed) limiter $1 < q_a < 2$ discharges. The profiles are normalized to $\langle J_t \rangle^{core}$ to remove changes in magnitude.

An equilibrium code fit by Osborne[4] to I_p, I_r, B_t at the wall, and the inversion radius of the SXR sawteeth (inferred to be the q = 1 surface), in a discharge with $q_a = 1.88$ is shown in figure 4.28. The safety factor on the magnetic axis q(0) is 0.7 and the q = 2 surface is only ~ .25 cm from the divertor separatrix (figure 4.28b). This is consistent with local q measurements in the separatrix vicinity that place the q = 2 surface about 0.5 cm from the separatrix. The proximity of the q = 2 surface to the divertor separatrix significantly affects the linear stability of the (2,1) tearing mode, as will be seen in Section V.C.1.

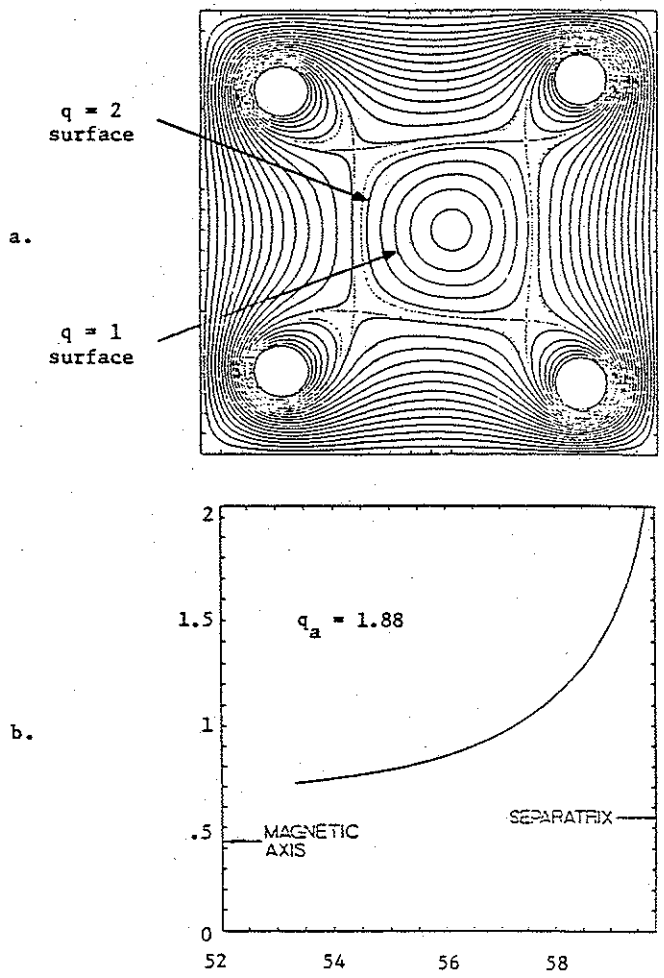

Figure 4.28: (a) Equilibrium poloidal flux contours and (b) safety factor profile q(R) generated by an equilibrium code fit to the discharge parameters during flattop in a $q_a \approx 1.88$ discharge. The toroidal current is zero beyond the separatrix in the fit. The q = 1 and q = 2 surfaces are indicated on the flux plot.

IV.C. Plasma Equilibria with $q_a < 1$:

IV.C.1. Global Discharge Parameters:

The most significant difference in the $q_a < 1$ magnetic and material limiter discharges is a 40% reduction in I_p from 50-60 kA to ~ 30 kA (figure 4.29). There is a reduction in minor radius from 11-12 cm to 8-10 cm. To obtain similar q_a values, B_t is reduced from 2.75 kG in the magnetic limiter configuration to 2.5 kG in the material limiter configuration.

The V_{pg} waveform is changed in $q_a < 1$ discharges (Section III.A) to a quarter sine wave that is power crowbarred at 2.3 ms. Because the maximum available crowbar voltage is only 5 V, which is inadequate to sustain the $q < 1$ discharges, the discharges last ~ 4 ms.

Confinement properties of the $q_a < 1$ discharges determined from the circuit model of Section III.B.1 are relatively insensitive to the presence of the limiter plates (figure 4.30). P_{oh} drops from 700 kW to 500 kW, but T_e^{cond} and τ_E remain essentially unaltered at values of 80-90 eV and 50-75 μs for discharges with $n_l \approx .8\text{-}1.4 \times 10^{13}$ cm^{-3}.

The facility of attaining high density at low-q, demonstrated for $1 < q_a < 2$, is also seen in the $q_a < 1$ discharges. Due to the reduced B_t, the Murakami limit in these discharges is only 6-8 × 10^{12} cm^{-3}. Considerable density pumpout is seen during startup while $1 \geq q_a > .75$, similar to the CLEO device[5] for $q_\psi = 2$ or 1.5. Density pumpout is overcome as in reference 5 by increased gas

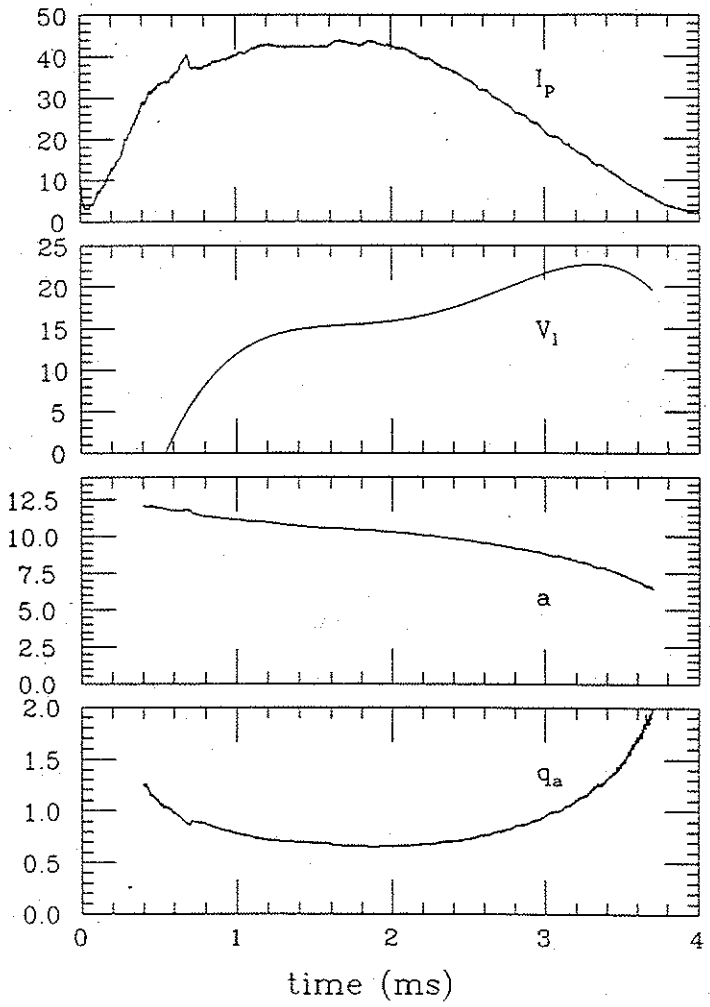

Figure 4.29a: Plasma current I_p, loop voltage V_l, equivalent minor radius a, and effective edge safety factor q_a for a typical magnetic limiter discharge. Toroidal field B_t = 2.75 kG.

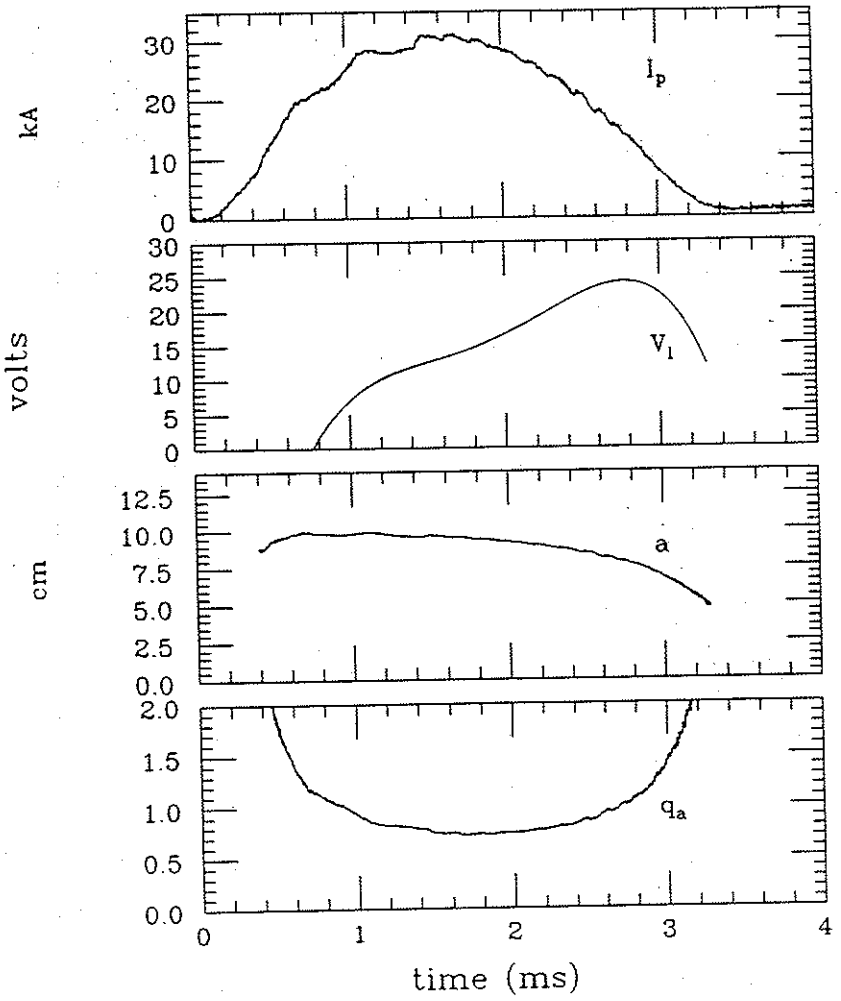

Figure 4.29b: Plasma current I_p, loop voltage V_l, equivalent minor radius a, and effective edge safety factor q_a for a typical material limiter discharge. Toroidal field B_t = 2.5 kG.

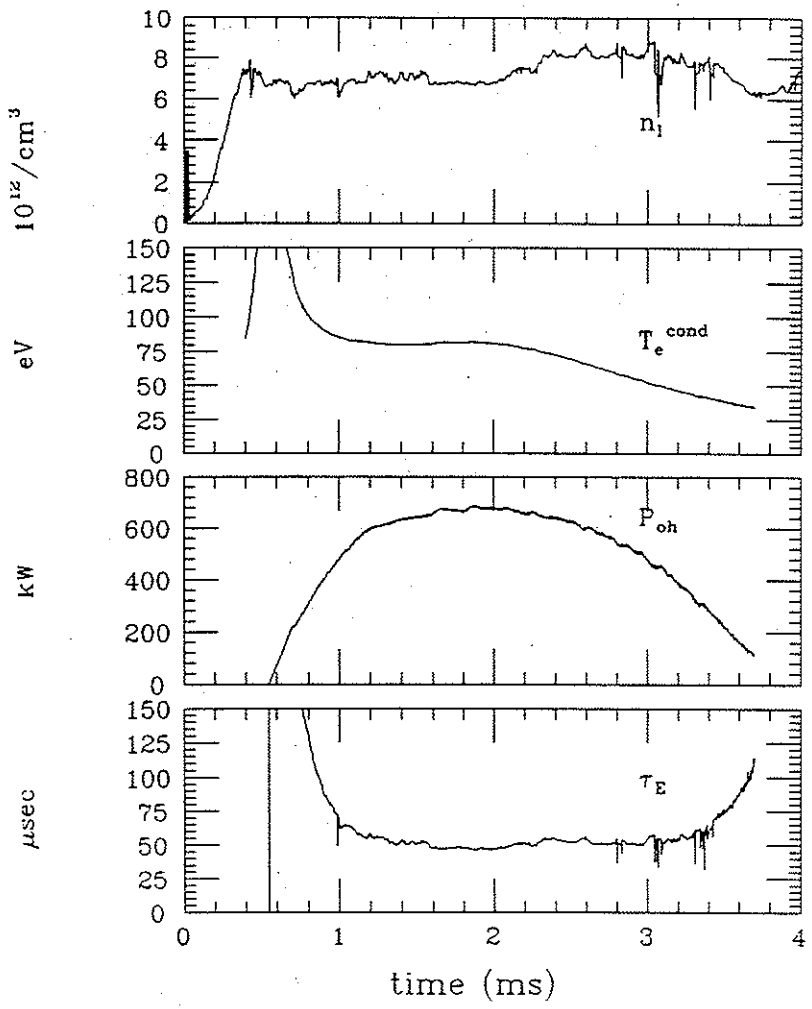

Figure 4.30a: Line average density n_l, electron conductivity temperature T_e^{cond}, ohmic heating power P_{oh}, and global energy confinement time τ_E for the same magnetic limiter discharge as figure 4.29.

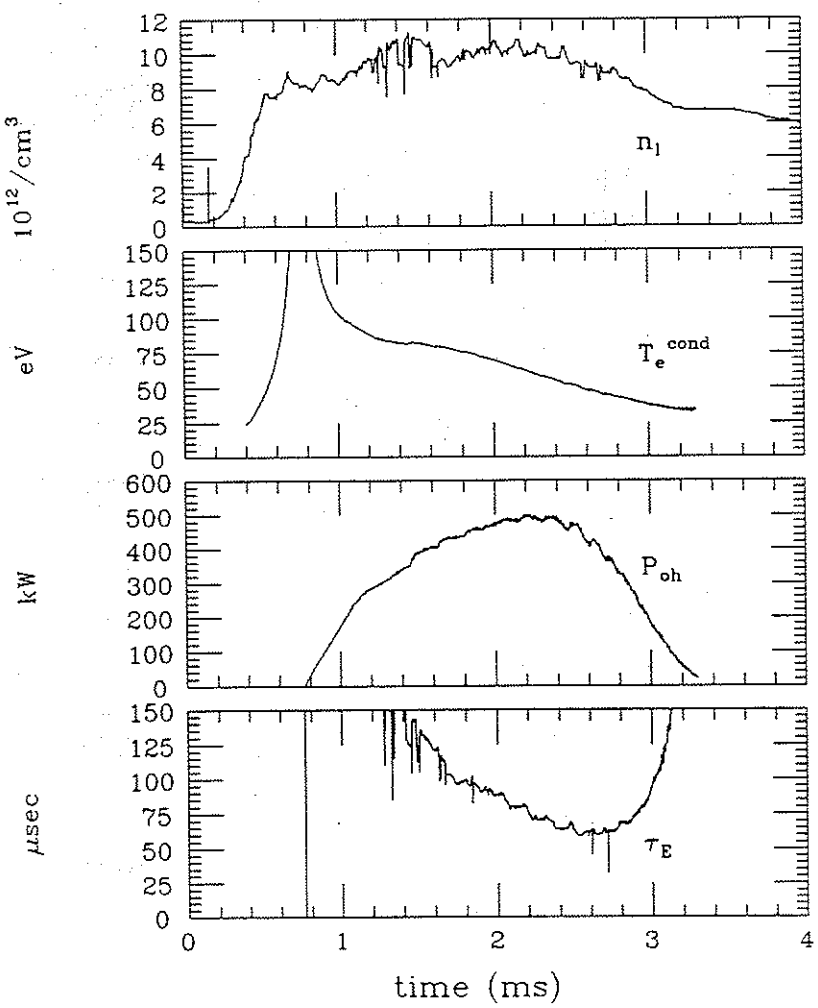

Figure 4.30b: Line average density n_l, electron conductivity temperature T_e^{cond}, ohmic heating power P_{oh}, and global energy confinement time τ_E for the same material limiter discharge as figure 4.29b.

puff during the discharge. Higher gas puff is required to "fill in" the density in the material limiter configuration. The global electron energy confinement time τ_E ~ 50-75 μs is in very good agreement with values obtained on the DIVA[6] and REPUTE-1[15] devices.

Although the circuit model parameters are similar in the magnetic and material limiter discharges, T_i drops by a factor of 2-3 in the material limiter discharges (figure 4.31). Qualitative VUV measurements of the oxygen series O III-O VI (figure 4.32) suggest decreased core electron temperatures as well, despite an essentially unchanged T_e^{cond}. In the magnetic limiter configuration, $T_i/T_e \approx .65$, compared to $T_i/T_e \approx .25$ for all other regimes in both configurations. Edlington, et al.[5] attributed $T_i \approx T_e$ in high-density, low-field discharges to increased classical ion heat conduction. In reference 5, $\tau_{Ei} \approx 500$ μs while $\tau_{Ee} \approx 200$-350 μs, producing an equipartition time less than the confinement time and $T_i \sim T_e$.

The ion contribution to equation 3.9 for τ_E in the circuit model is no longer negligible in the $q_a < 1$ magnetic limiter discharges. Including the measured T_i yields $\tau_E \approx$ 80-120 μs in the magnetic limiter configuration, versus 60-90 μs in the material limiter configuration. Thus, the global energy confinement time drops 25% in the material limiter configuration.

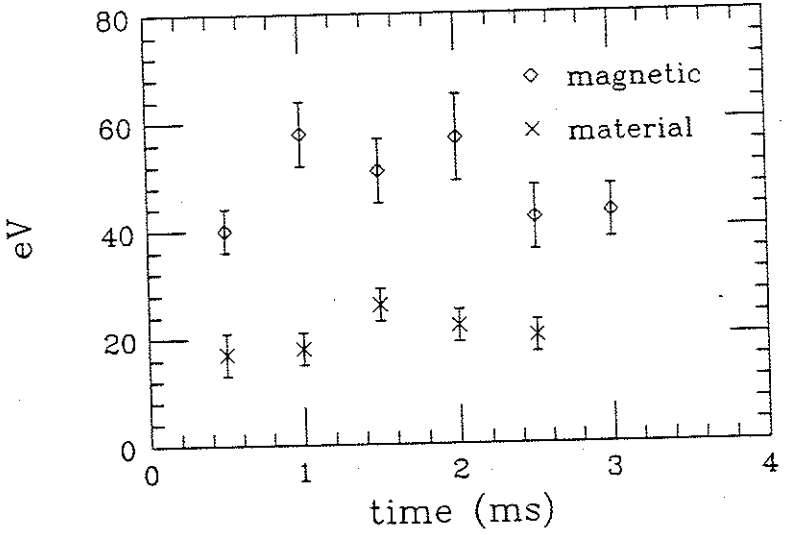

Figure 4.31: Evolution of ion temperature T_i, measured by neutral particle charge exchange analysis, in magnetic and material limiter $q_a < 1$ discharges.

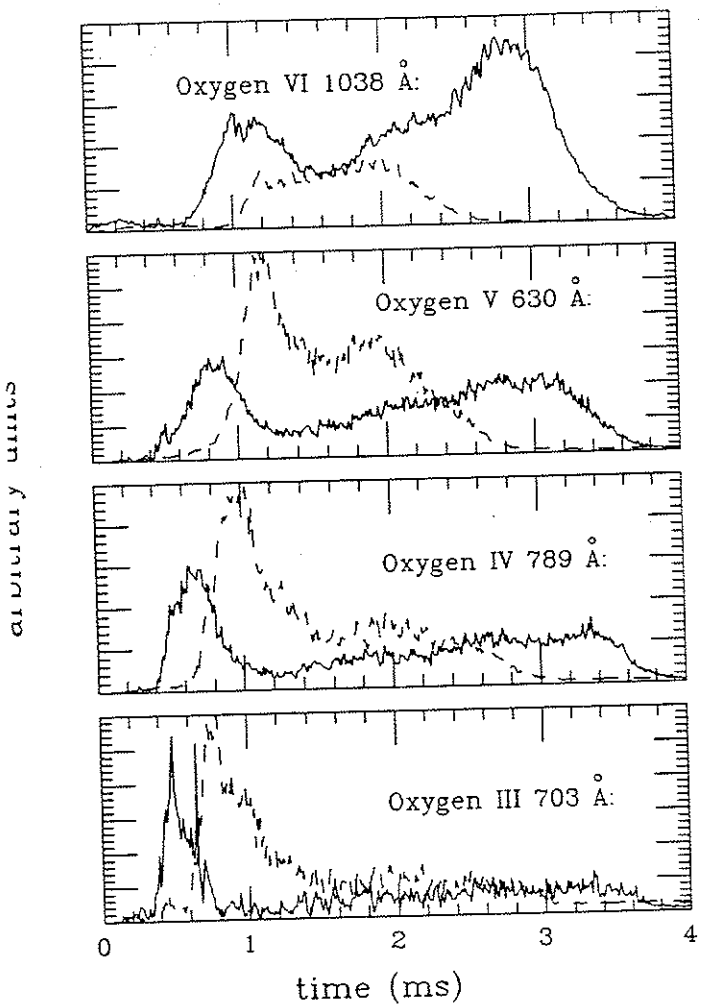

Figure 4.32: Evolution of VUV line emission from the oxygen series O III, O IV, O V, and O VI in (solid) magnetic and (broken) material limiter $q_a < 1$ discharges. The O V line is not "burned through" and little O VI emission is seen in the material limiter configuration, indicating a reduction in T_e.

IV.C.2. SXR Emissivity Profiles:

SXR emissivity profiles in both magnetic and material limiter $q_a < 1$ discharges are broad and flat across the central current channel (figure 4.33). The material limiter profiles have steeper gradients near the divertor separatrix. In each configuration, the profiles are nearly centered in the vacuum vessel midplane and midcylinder.

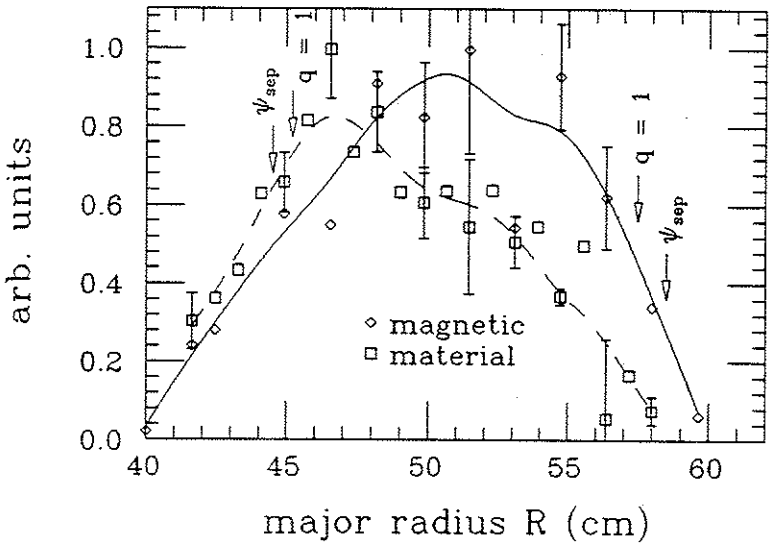

Figure 4.33a: Comparison of SXR emissivity profiles in the midplane for (solid) magnetic and (dashed) material limiter $q_a < 1$ discharges.

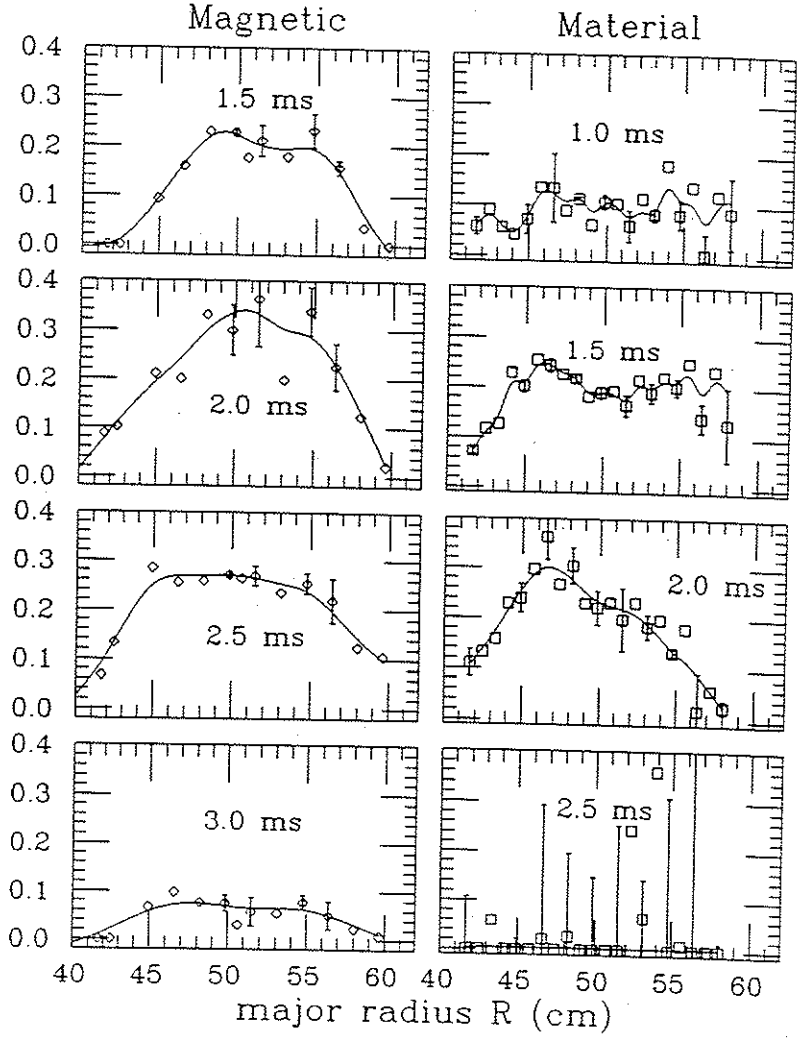

Figure 4.33b: Sequence of SXR emissivity profiles in 0.5 ms steps during the "flattop" portion of (left) magnetic and (right) material limiter $q_a < 1$ discharges.

IV.C.3. Scrape-off Density, Temperature, and Pressure Profiles:

While the limiter plates are effective in reducing plasma density, temperature, and pressure in the divertor scrape-off region in the material limiter configuration (figures 4.34, 4.35, and 4.36), a toroidal asymmetry appears in the density profiles at $q_a <$ 1 in both configurations (figure 4.37). This asymmetry appeared at ϕ = 240 degrees, and was not seen at 60, 180, or 330 degrees. It may result from field errors caused by a large port (6 inch diameter) in the floor of the vacuum vessel at that azimuth.

The magnetic limiter density profiles are broad and flat inside the separatrix, with the gradient rising much more rapidly outside the separatrix at 60 degrees toroidally (figure 4.34a). In contrast, most of the density gradient in the material limiter configuration lies inside the separatrix, with the inferred central current channel profile being significantly more peaked (figures 4.34b and 4.37b). Inferred values for n_l^{core} are 0.9-1.2 $\times$ 10^{13} cm^{-3} in the magnetic limiter configuration and 2-3 times larger in the material limiter configuration, n_l^{core} = 2.5-2.8 $\times$ 10^{13} cm^{-3}. It was not possible to match n_l^{core} in the two configurations due to the enhanced density pumpout in the material limiter configuration that required higher gas puff.

In the magnetic limiter configuration, the T_e profile rises near the wall ($R \geq 66$ cm), is flat across the scrape-off region to the separatrix ($R_{sep} \approx 10$ cm), and is quite flat across the central current channel, as inferred from the SXR emissivity profile (figure

4.33a). In the material limiter configuration, T_e is flat and pedestal-like at $T_e \approx 10$ eV beyond the separatrix. The central current channel profile inferred from the SXR emissivity profile is broad and flat near the axis, suggesting a sharp drop near the separatrix to match the scrape-off T_e profiles.

Due to the density profile asymmetry, the P_e profiles also display a toroidal asymmetry, with the profile broadening several centimeters at ϕ = 240 degrees (figure 4.37). The material limiter profiles are somewhat more peaked with most of the gradient occurring within several centimeters of the separatrix. In the magnetic limiter configuration, the gradient is "spread" over the entire scrape-off region. The pedestal plasma outside the separatrix in the material limiter configuration, possibly sustained by "fill-in" from the poorly confined central current channel, might have a significant effect on free boundary modes in these discharges.

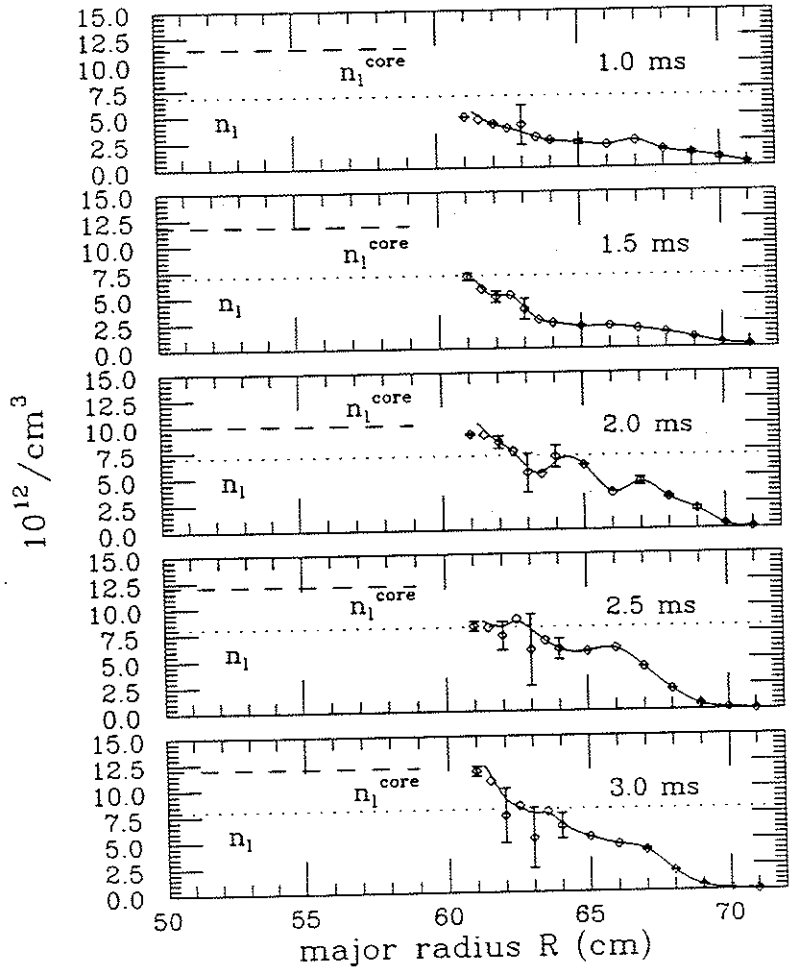

Figure 4.34a: Scrape-off ion density n_i profiles in 0.5 ms steps from 1 ms in a typical magnetic limiter discharge. The line average density n_l (dotted line) and the inferred line average central current channel density n_l^{core} (dashed line) are shown.

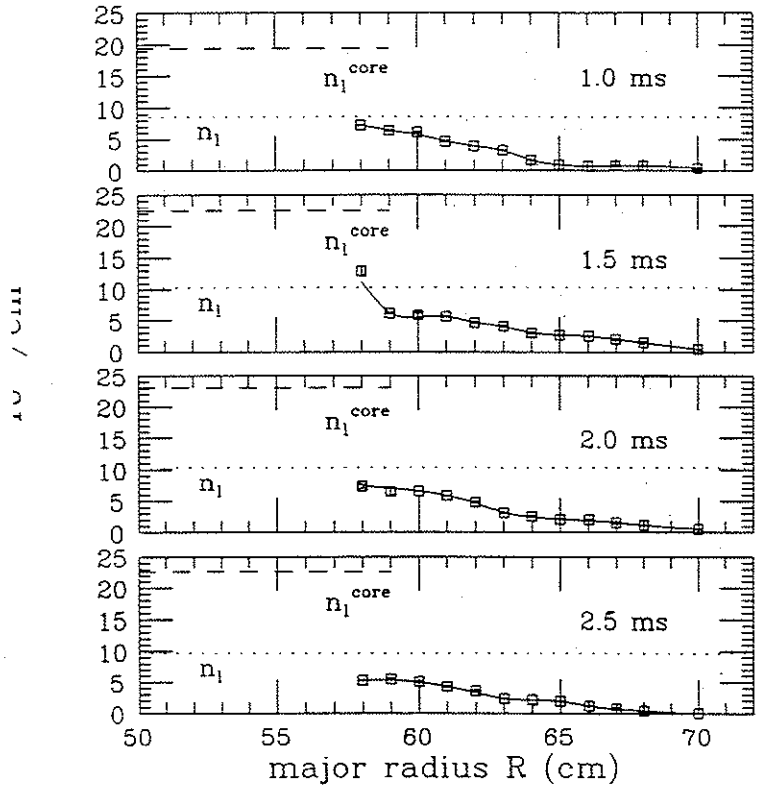

Figure 4.34b: Scrape-off ion density n_i profiles in 0.5 ms steps from 1 ms in a typical material limiter discharge. The line average density n_l (dotted line) and the inferred line average central current channel density n_l^{core} (dashed line) are shown.

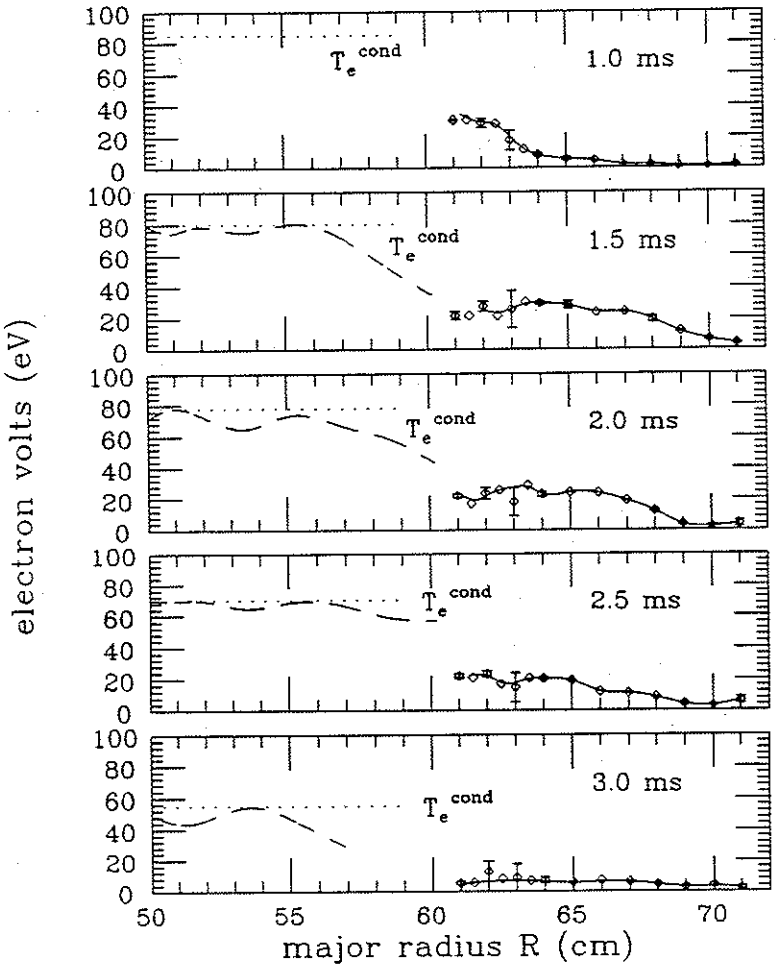

Figure 4.35a: Scrape-off electron temperature T_e profiles in 0.5 ms steps from 1 ms in a typical magnetic limiter discharges. T_e^{cond} (dotted line) and central current channel T_e profile, inferred from the SXR emissivity profiles of figure 4.33 using equation 3.33 (dashed line), are shown.

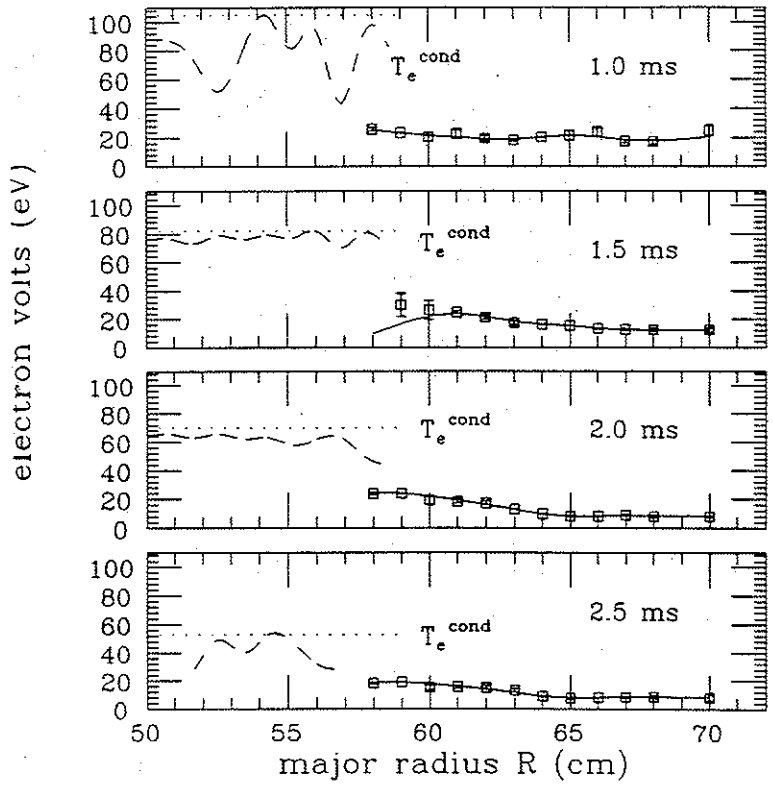

Figure 4.35b: Scrape-off electron temperature T_e profiles in 0.5 ms steps from 1 ms in a typical material limiter discharge. T_e^{cond} (dotted line) and central current channel T_e profile, inferred from the SXR emissivity profiles of figure 4.33 using equation 3.33 (dashed line), are shown.

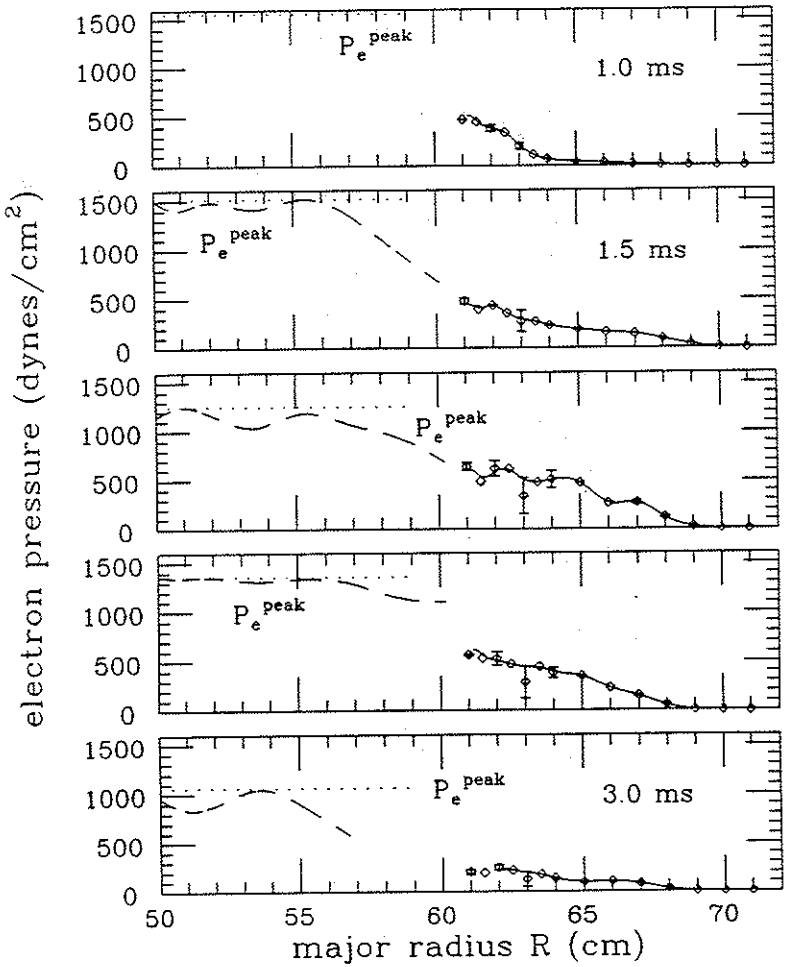

Figure 4.36a: Scrape-off electron pressure P_e profiles in 0.5 ms steps from 1 ms in a typical magnetic limiter discharge. The "peak" pressure P_e^{peak} (dotted line) and central current channel P_e profiles inferred from n_l^{core} and the inferred central current channel T_e profiles (figure 4.35) (dashed line) are also shown.

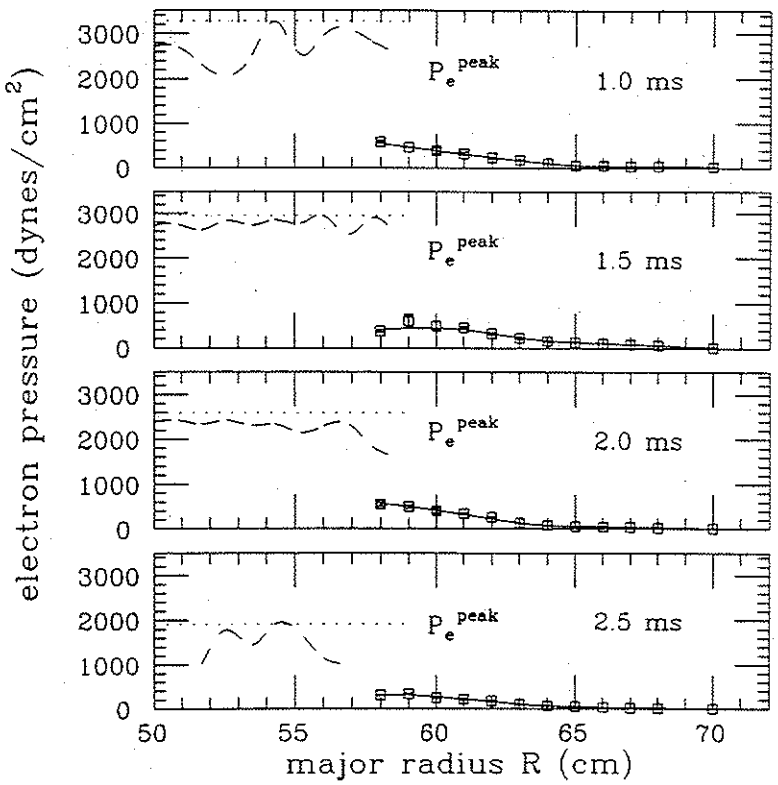

Figure 4.36b: Scrape-off electron pressure P_e profiles in 0.5 ms steps from 1 ms in a typical material limiter discharge. The "peak" pressure P_e^{peak} (dotted line) and central current channel P_e profiles inferred from n_l^{core} and the inferred central current channel T_e profiles (figure 4.35) (dashed line) are also shown.

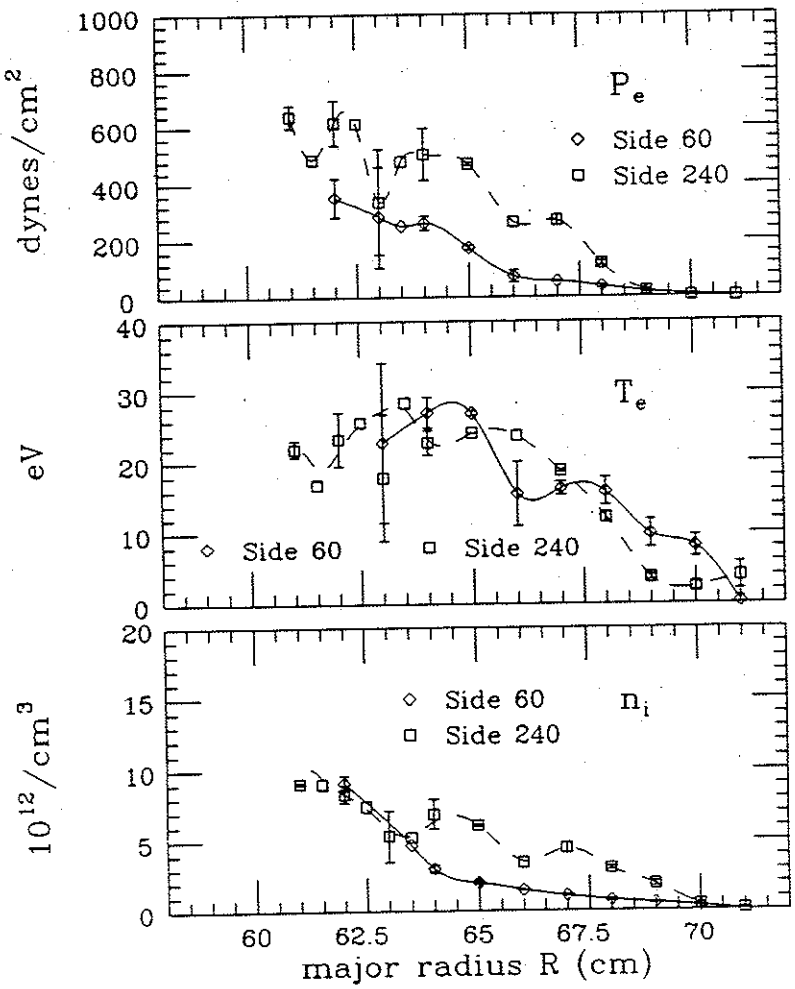

Figure 4.37a: Scrape-off n_i, T_e, and P_e profiles at toroidal azimuths of (solid) 60 degrees and (dashed) 240 degrees in magnetic limiter discharges.

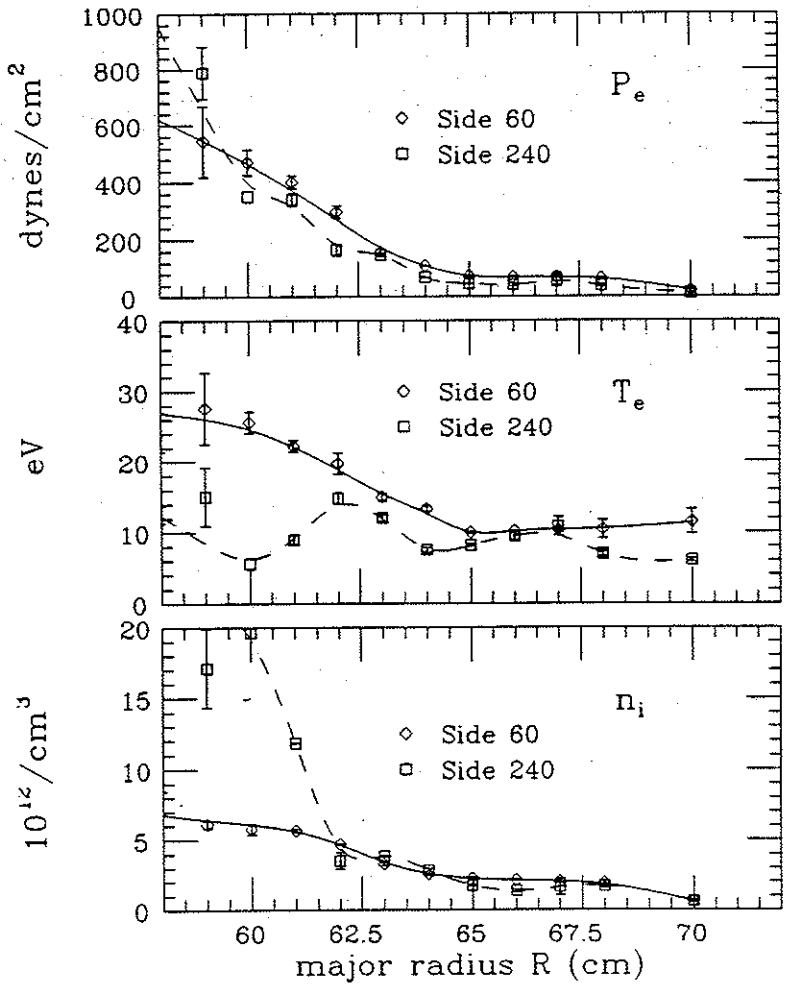

Figure 4.37b: Scrape-off n_i, T_e, and P_e profiles at toroidal azimuths of (solid) 60 degrees and (dashed) 240 degrees in material limiter discharges.

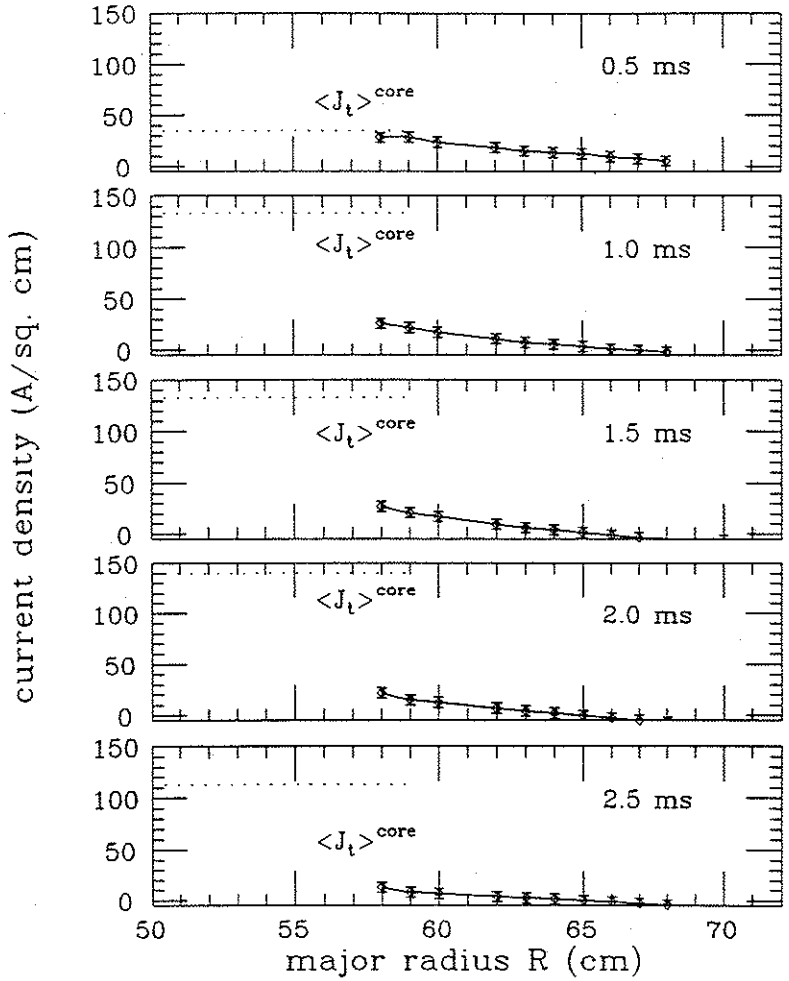

Figure 4.38a: Toroidal current density J_t profiles in 0.5 ms steps from 0.5 ms to the end of the discharge in magnetic limiter discharges. The dotted line is the average toroidal current density $\langle J_t \rangle^{core}$ in the central current channel inferred from the scrape-off profile and I_p.

IV.C.4. Scrape-off Current Profiles:

The scrape-off toroidal current profiles are similar in both the magnetic and material limiter configurations (figure 4.38). Early in the discharges ($t < 1$ ms), as much as half the discharge current flows outside the separatrix. After 1 ms, the current in the scrape-off region drops to 10-20% of the discharge current. Due to the significantly reduced I_p in the material limiter configuration, it should be pointed out that 10-20% of the discharge current corresponds to a total scrape-off toroidal current of only 1-3 kA, beyond the accuracy of the measured profiles ($\pm$ 5 A/cm^2 yielding $\pm$ 5 kA).

Current density profiles have also been obtained from magnetic field measurements in the central current channel of the material limiter configuration. The resulting profile (figure 4.39a) is broad across the central region, with a peak value of ~ 90 A/cm^2. The total current represented by this profile is 17 kA. Linearly extrapolating this profile from 6 cm to 10 cm adds an additional 10 kA. The total plasma current in these discharges was 29-30 kA at this time. These measurements predict a total toroidal current outside the separatrix of 2-3 kA, in good agreement with the scrape-off profiles of figure 38. The result of a similar measurement in the magnetic limiter configuration by Osborne displays a similarly shaped profile (figure 4.39b), although no absolute magnitude was computed.

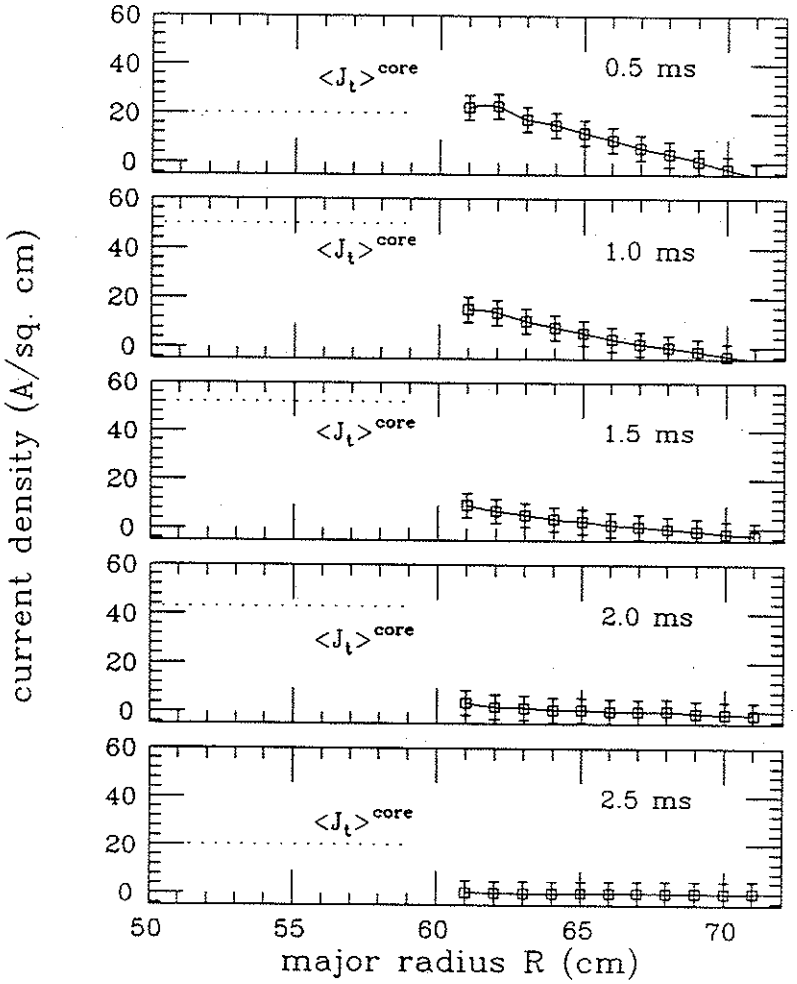

Figure 4.38b: Toroidal current density J_t profiles in 0.5 ms steps from 0.5 ms to the end of the discharge inmaterial limiter discharges. The dotted line is the average toroidal current density $\langle J_t \rangle^{core}$ in the central current channel inferred from the scrape-off profile and I_p.

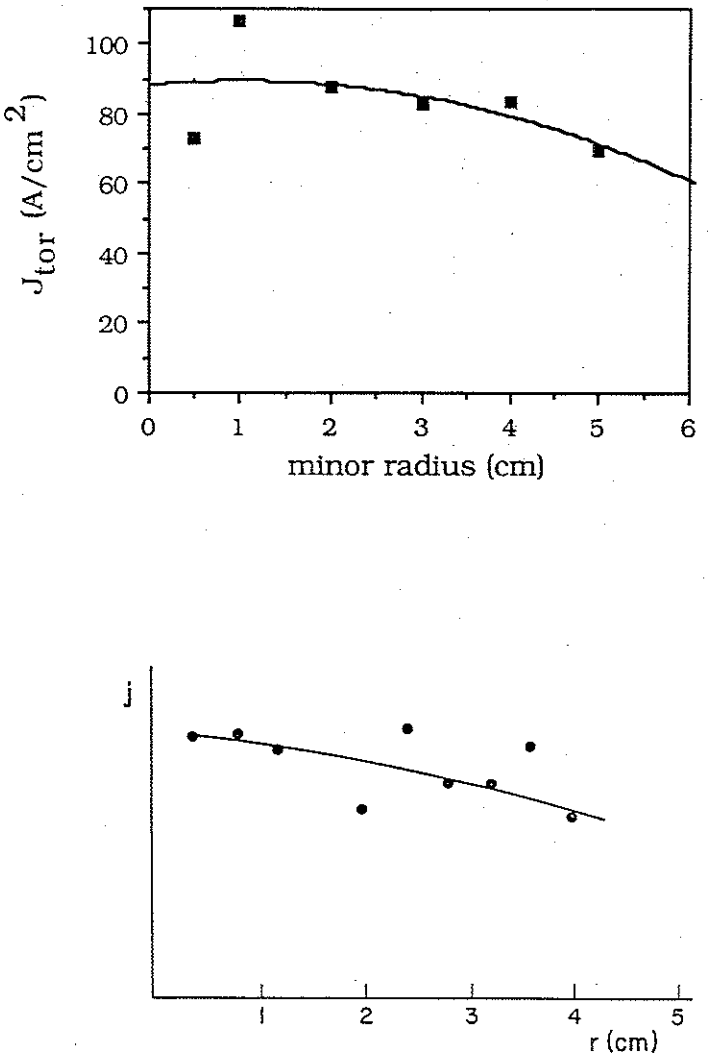

Figure 4.39: Experimentally measured toroidal current density profiles in (a) material and (b) magnetic limiter discharges. The magnetic limiter profile provides the shape only.

IV.C.5. Summary for $q_a < 1$ Discharges:

To facilitate comparison of the profile gradients between the magnetic and material limiter configurations, the n_i (figure 4.40), T_e (figure 4.41), P_e (figure 4.42), and J_t (figure 4.43) profiles are plotted normalized to the best estimate of the corresponding central values at peak I_p. While the limiter plates are effective in reducing plasma density, temperature, pressure, and current outside the divertor separatrix, the material limiter profiles show a low density, relatively high temperature ($T_e \approx 10$ eV) pedestal in the scrape-off region and steeper gradients near the separatrix.

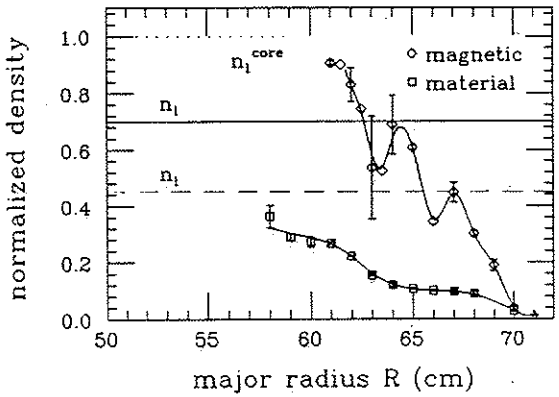

Figure 4.40: n_i profiles (figure 4.34) during flattop in magnetic (solid) and material (dashed) limiter discharges. The profiles are normalized to n_i^{core} to remove changes in magnitude.

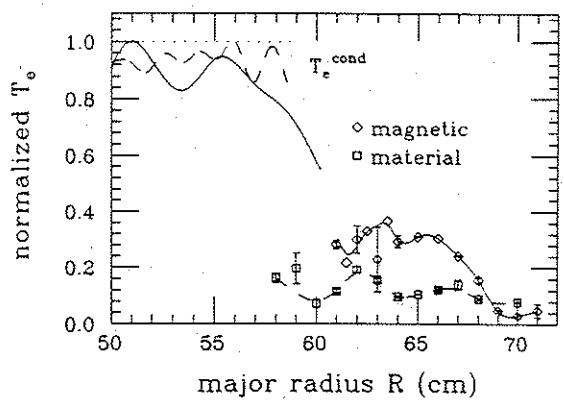

Figure 4.41: T_e profiles (figure 4.35) during flattop in magnetic (solid) and material (dashed) limiter discharges. The profiles are normalized to T_e^{cond} to remove changes in magnitude.

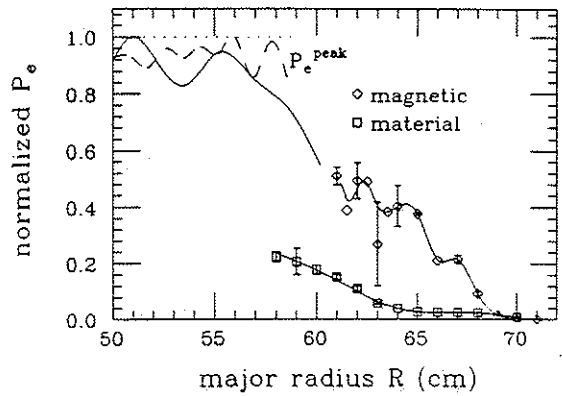

Figure 4.42: P_e profiles (figure 4.36) during flattop in magnetic (solid) and material (dashed) limiter discharges. The profiles are normalized to $n_i^{core} kT_e^{cond}$ to remove changes in magnitude.

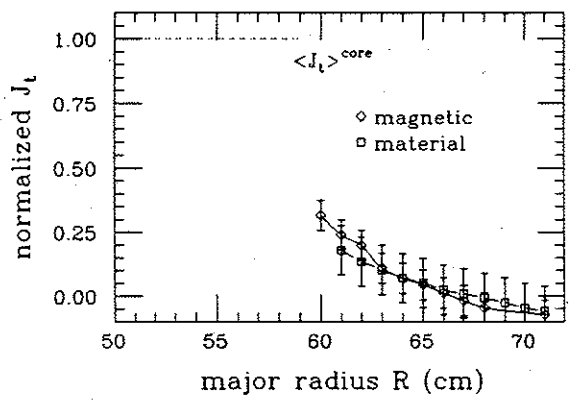

Figure 4.43: J_t profiles (figure 4.38) during flattop in magnetic (solid) and material (dashed) limiter discharges. The profiles are normalized to $<J_t>^{core}$ to remove changes in magnitude.

Using the values of n_i^{core}, T_e^{cond}, and T_i in equation 4.1 for the peak β yields $\beta(0) \approx 1.9\%$ in the magnetic limiter configuration and $\beta(0) \approx 2.6\%$ in the material limiter configuration.

Experimentally measured equilibrium poloidal flux plots of the central current channel are shown just before (figure 4.44a) and just after (figure 4.44b) a sawtooth in a magnetic limiter $q_a < 1$ discharge.[4] The corresponding flux surface averaged q profiles are designated by the solid and open circles respectively in figure 4.45.[4] The flux plots are in good agreement with the results of an equilibrium code fit to the discharge parameters by Osborne, as shown in figure 4.44c.

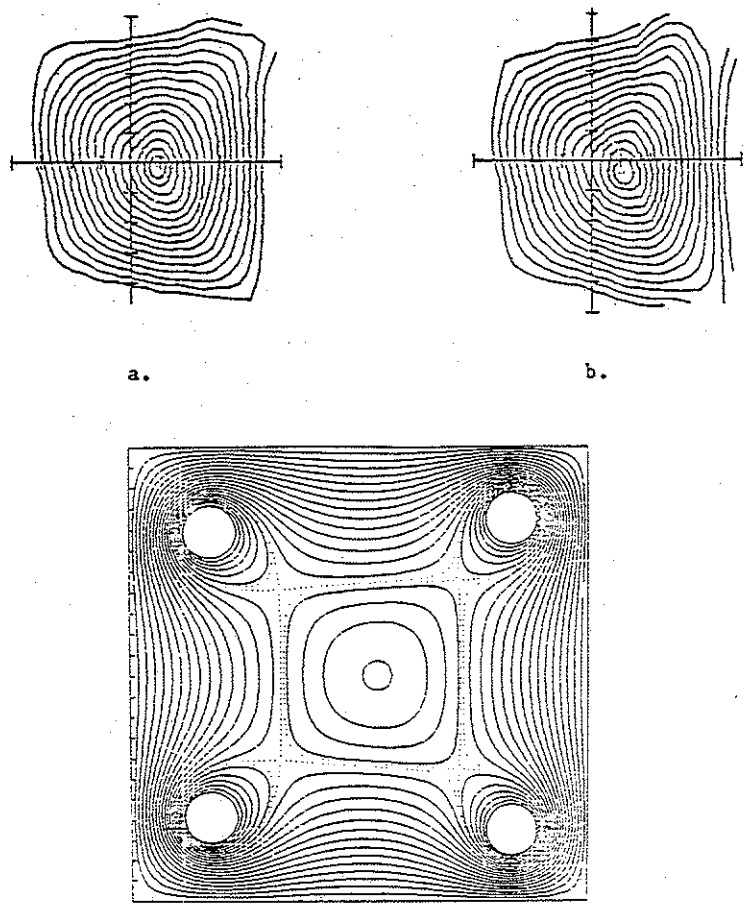

Figure 4.44: Experimentally measured equilibrium poloidal flux ψ contours (a) just before and (b) just after a sawtooth in a $q_a < 1$ discharge. (c) Equilibrium poloidal flux plot generated by an equilibrium code fit to the discharge parameters.

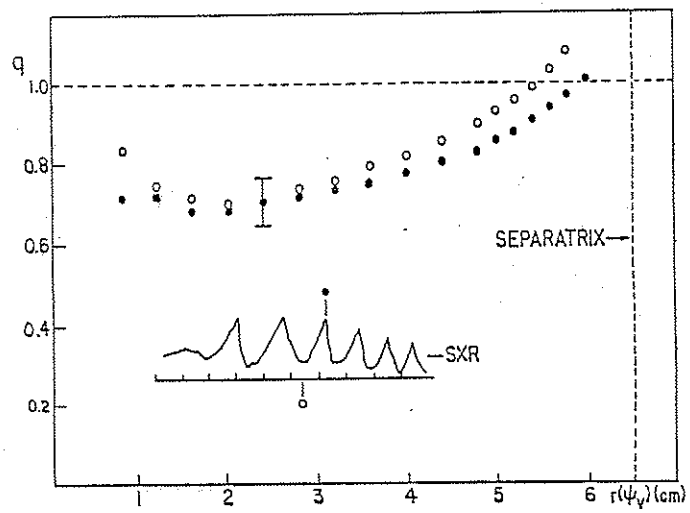

Figure 4.45: Experimentally measured flux surface averaged q(ψ) profile in magnetic limiter configuration just before (black circles) and just after (open circles) a sawtooth collapse.

Experimentally measured local q profiles along the vacuum vessel midplane in material limiter discharges are shown in figure 4.46a. For comparison, the corresponding local q profiles in magnetic limiter discharges are also shown (figure 4.46b). The local q profiles do not rise near the separatrix ($r \approx 8$ cm) as do the flux surface averaged profiles since the singularity in the poloidal field at the X-points has no effect on local measurements along the midplane. The similarity of the q profiles suggests that the current profiles inside the separatrix are essentially the same in each configuration, as seen in figure 4.39. Differences in tearing mode

stability then should arise from the changes to the boundary condition induced by the limiter plates.

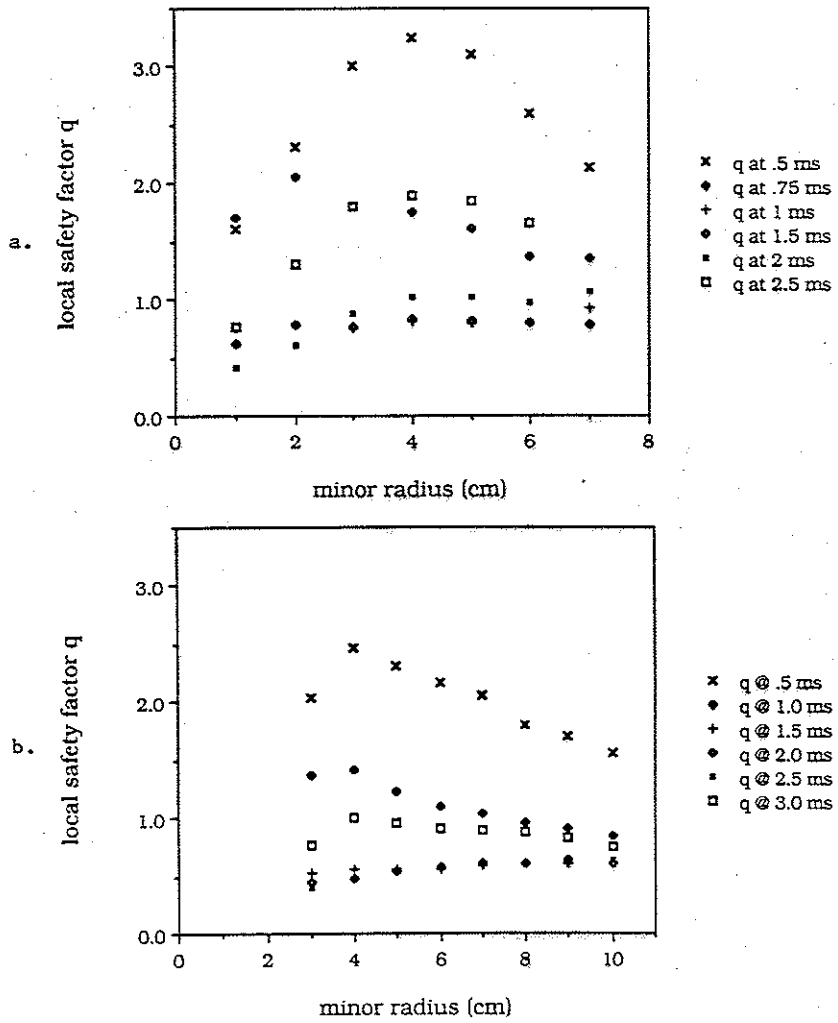

Figure 4.46: Experimentally measured local q(r) profiles along the vacuum vessel midplane in (a) material limiter and (b) magnetic limiter $q_a < 1$ discharges.

IV.D. Summary: Equilibria in $0.5 \leq q_a < 3$ Discharges:

The retractable limiter plates are effective in reducing plasma density, temperature, pressure, and current in the divertor scrape-off region for all regimes studied, $0.4 < q_a < 3$. A "pedestal" of 10 eV, 2-3 $\times 10^{12}$ cm^{-3} plasma ($n(r) \approx .3n_l^{core}$) remains outside the separatrix in the $q_a < 1$ material limiter discharges, possibly due to the poor confinement in the central current channel, and may influence stability to free boundary modes. In the higher q_a regimes, the scrape-off plasma is less than $.1n_l^{core}$ over most of the scrape-off region.

The central current channel boundary conditions have been varied in a controlled manner by removing plasma and current outside the divertor separatrix in $q_a > 1$ material limiter discharges and by removing current outside the separatrix in $q_a < 1$ material limiter discharges. Unfortunately, the central current channel profiles are also more peaked ($2 < q_a < 3$) or display enhanced gradients just inside the separatrix for the material limiter discharges. This complicates separation of profile effects on the tearing mode stability from separatrix and scrape-off current effects.

Access to the regimes $q_a < 1$ and $1 < q_a < 2$ in magnetic limiter discharges is routine. No close-fitting wall, external windings, or special profile control techniques, beyond the magnetic limiter configuration, are employed to allow the stability barriers at $q = 2$ and $q = 1$ to be passed. As a consequence, the majority of

discharges in the Tokapole II device lie beyond the bounds of the Hugill plot for most other tokamaks. This provides the most emphatic demonstration that the magnetic limiter configuration provides some measure of instability control. This topic will be investigated in subsequent chapters.

Global discharge parameters for $0.4 \leq q_a \leq 2$ are in good agreement with results at low-q (~ 2, ~ 1) in similar sized devices. The facility of attaining high density discharges at low-q is clearly demonstrated. The results are suggestive of higher β provided T_e is essentially constant, although no attempt was made to optimize β in these experiments. In each configuration and operating regime, the estimated peak $\beta(0)$ is less than that predicted by equation 2.9. $\beta(0)$ is plotted versus I/aB in figure 4.47; for comparison, the Troyon limit C = 2.8 is also shown. Apparently, pressure driven modes play no role in these discharges.

Detailed energy confinement data are not available on Tokapole II. In particular, the circuit model τ_E presented in this chapter does not distinguish between confinement in the central current channel and the divertor scrape-off region. If τ_E is plotted versus the "ALCATOR-like" scaling of equation 2.9, an approximate linear dependence is seen in each distinct regime, although the regimes are distinctly separate and have different slopes (figure 4.48a). In each regime, the density n_l^{core} (and n_l as well) is roughly constant. The largest change in density occurs between q regimes. If the variations in $a_{1/2}$ are ignored ($a_{1/2}$ is taken here as the half

radius of the SXR emissivity), a similar result is obtained. τ_E does display a linear dependence on $(q_a)^{1/2}$ down to $q_a \approx 1$, will all regimes described by a single line (figure 4.48b). These results suggest that the dependence of τ_E on density follows the DIVA result (equation 2.9) in each regime, but that this expression cannot describe the results across the different q regimes. This would not be entirely unsuspected, as the influence of sawteeth on transport might increase as q_a is lowered.

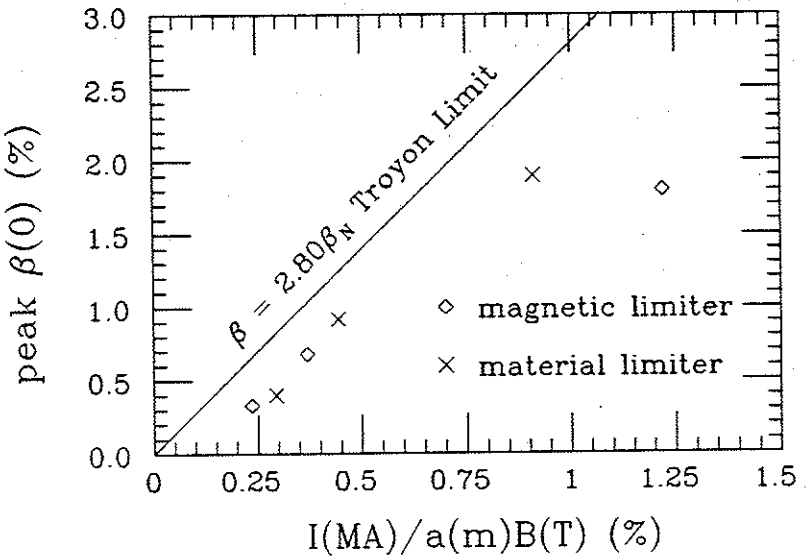

Figure 4.47: Peak β(0) (equation 4.1) versus β_N = I(MA)/a(m)B(T) for magnetic and material limiter configurations over the operating range $0.4 < q_a < 3$. The dashed line is the Troyon n = 1 ideal external kink mode β limit C = 2.8.

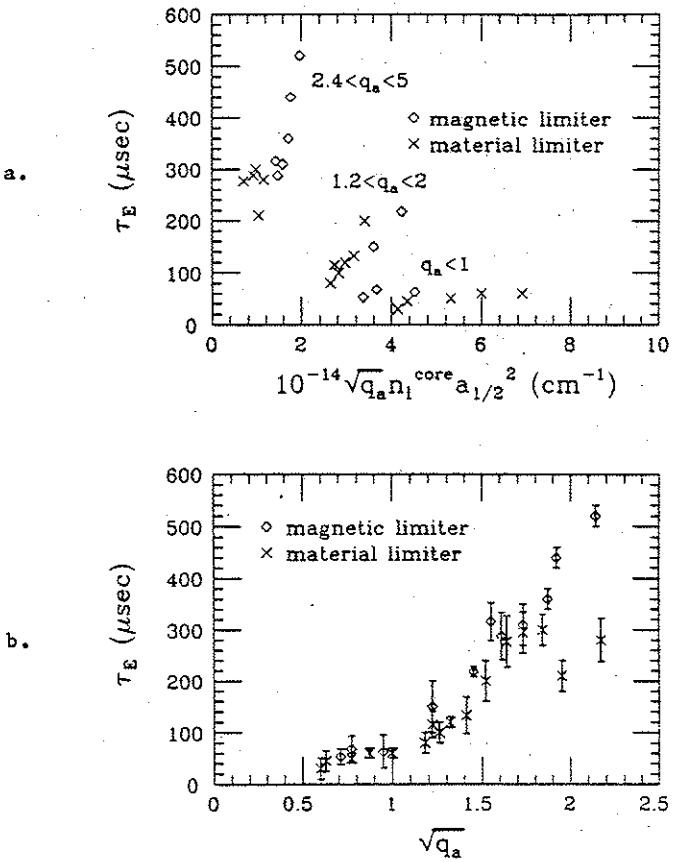

Figure 4.48: Global energy confinement time τ_E determined from the circuit model of Section III.B.1 versus (a) the "ALCATOR-like" scaling of the DIVA experiment[6] and (b) $q_a^{1/2}$ in discharges with 4×10^{12} cm^{-3} $\leq n_i \leq 8 \times 10^{12}$ cm^{-3}.

REFERENCES

[1]P. Couture and K. McGuire, PPPL-2380 (1986).

[2]M. Murakami, J.D. Callen, and L.A. Berry, Nuclear Fusion, 16, 347 (1976).

[3]M.W. Phillips, University of Wisconsin—PLP 765 (1978).

[4]T.H. Osborne, Ph.D. Thesis, University of Wisconsin (1984).

[5]T. Edlington, et al., Plasma Physics and Controlled Fusion Research, (Proc. 9th Conf., Baltimore, 1982), 3, (IAEA, Vienna, 1983), 241.

[6]DIVA Group, Nuclear Fusion, 20, 271 (1980).

[7]A.B. Berlizov, et al., Plasma Physics and Controlled Fusion Research, (Proc. 8th Conf., Brussels, 1980), 1, (IAEA, Vienna, 1981), 23.

[8]K.A. Razumova, Plasma Physics and Controlled Fusion, 26, 37 (1984).

[9]P.H. Rutherford, Physics of Plasmas Close to Thermonuclear Conditions, (Proc. of the Course, Varenna, 1979), 1, (Comm. of the European Communities, Brussels, 1980), 129.

[10]R. Birch, et al., Controlled Fusion and Plasma Physics, (Proc. 9th European Conf., Oxford, 1979), 2, (European Physical Society, Brussels, 1979), 71.

[11]J.J. Ellis, et al., Plasma Physics and Controlled Fusion Research, (Proc. 8th Conf., Brussels, 1980), 1, (IAEA, Vienna, 1981), 731.

[12]A.A. Grossman, et al., International Conference on Plasma Physics, Lausanne, Switzerland, 1, paper P6-10 (1984).

[13]A.G. Kellman, et al., Bulletin of the American Physical Society, 29, 1363 (1984).

[14]E.J. Strait, et al., Bulletin of the American Physical Society, 31, 1533 (1986).

[15]Z. Yoshida, et al., NEUT Research Report 85-01.

Chapter 5
EXTERNAL DISRUPTIONS IN TOKAPOLE II

To ascertain the effects of the divertor separatrix and the plasma and current in the scrape-off region on the stability of the (2,1) tearing mode, external disruptions have been studied in the material limiter configuration and the results compared with those in the magnetic limiter configuration. Data pertaining to disruptions for which a (2,1) mode has been identified are presented in this chapter. The principal conclusions of this study are:

1) The magnetic limiter configuration permits routine access to the external disruption-free regime $q_a \leq 2$. The (2,1) tearing mode is controlled by lowering q_a to 2 or less, moving the $q = 2$ surface within ≈ 0.5 cm of the separatrix.
2) A similar external disruption-free regime is obtained in the material limiter configuration by lowering q_a below 1.5. The accessibility of this regime even in the material limiter configuration demonstrates that the accessibility is not the result of plasma and current in the scrape-off region.
3) Discharge termination (major disruption) is suppressed in the magnetic limiter configuration by the elimination of plasma/wall interactions and the concomitant rapid cooling of the discharge. The plasma/wall interactions are eliminated by placing the nearest material surface several centimeters beyond the central current channel boundary, and by restricting the post-disruptive major radius shift to 2-3 cm. This shift is less than 40% of the shortest distance to a material boundary (across the X-points to the divertor rings) and less than 25% of the distance to the vacuum vessel walls. Any reflux of hydrogen or impurities from these surfaces is readily ionized in the $1\text{-}4 \times 10^{12}$ cm^{-3}, 15-30 eV plasma in the scrape-off region and confined by the magnetic field in the scrape-off region. This insulates the central current channel from the deleterious effects of such interactions.

Characteristics of external disruptions in $2 < q_a < 3$ and $1 < q_a < 2$ discharges are presented in Sections V.A.1 and V.A.2 respectively. Discharge termination is discussed in Section V.A.3. Comparison of the experimental results with (2,1) tearing mode computations in the magnetic and material limiter configurations using the resistive MHD initial value code RPD[1,2] is presented in Section V.B. Discussion and conclusions are presented in Section V.C.

V.A. Characteristics of External Disruptions with $q_a > 1$:

V.A.1. $2 < q_a < 3$ Discharges:

Magnetic and material limiter discharges with $2 < q_a < 3$ display two types of external disruptions, small and giant sawteeth. A striking difference between the configurations is the discharge termination (major disruption) at the giant sawtooth collapse in the material limiter configuration. Both types of sawteeth are remarkably regular in magnetic limiter discharges, despite the loss, in a giant sawtooth, of much of the density and thermal energy in the central current channel. In material limiter discharges, small sawteeth are often absent; when they are present, they are usually less regular than in magnetic limiter discharges. In some material limiter discharges, there are indications that the small sawteeth might by internal disruptions rather than external disruptions.

V.A.1.a. Small SXR Sawteeth:

The small sawteeth observed in magnetic limiter discharges, and occasionally in material limiter discharges, are external disruptions that appear to differ from giant sawteeth only in terms of the sawtooth amplitude and the degree of distortion of the (2,1) magnetic precursor detected on the Mirnov coils (Section V.A.1.c). The small sawteeth share some features of the partial disruptions seen in the JIPP TII-U device,[3] but unlike partial disruptions, do not rearrange the current profile to one stable to external disruptions, since both small and giant sawteeth reoccur shortly afterwards. The extent of the (2,1) magnetic island growth into the plasma core is known to be extremely sensitive to shear inside the

$q = 2$ surface.[4] Thus, details of the plasma current profile are likely responsible for determining the amplitude of the sawtooth collapse.

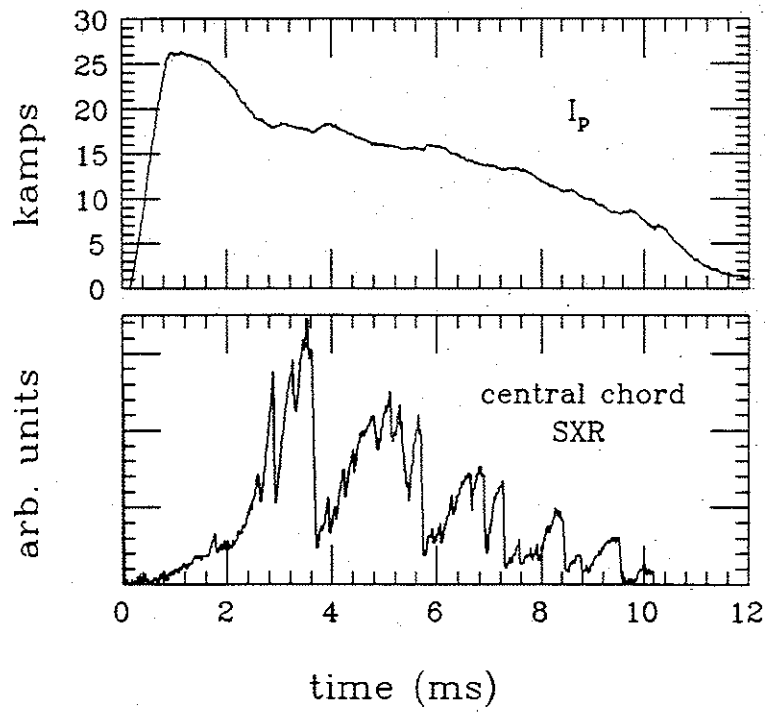

Figure 5.1: Plasma current I_p and central chord SXR signal for a typical magnetic limiter discharge, showing both small and giant sawteeth.

The small and giant sawteeth in a magnetic limiter discharge are shown in figure 5.1. Small sawteeth have an amplitude of $\Delta I/I \approx$ 5-20% and a period $\tau \sim$ 200-250 μs. The sawtooth collapse inverts near $x-x_o = \pm 5.2 \pm 0.5$ cm and $y-y_o = \pm 6.2 \pm 0.5$ cm, where x

and y are distances along the midplane and midcylinder from the geometric axis and (x_0, y_0) = (+2.5,0) cm is the position of the magnetic axis inferred from the SXR emissivity profile. These inversions are near but generally outside the giant sawtooth inversions, and the collapse appears to propagate inward from the inversion surface (figure 5.2).

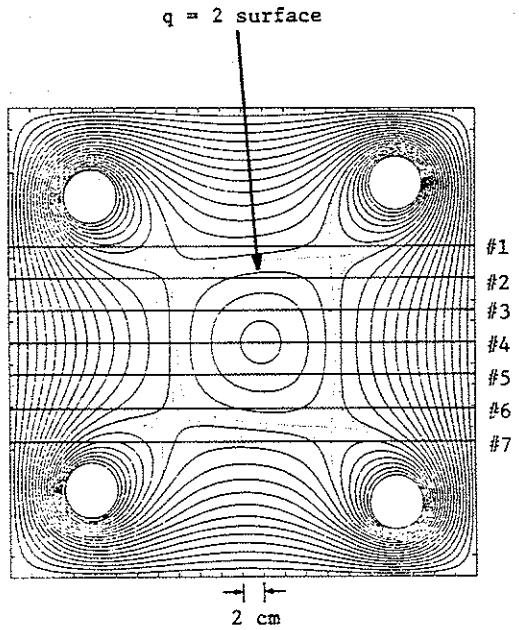

Figure 5.2(a): Equilibrium poloidal flux plot for a magnetic limiter discharge that matches the position of the q = 2 surface to the measured SXR inversion radii. If the magnetic axis is slightly below the geometric axis (typical case), the order of sawtooth collapses for inward propagation from the q = 2 surface is 2,6,3,5,4.

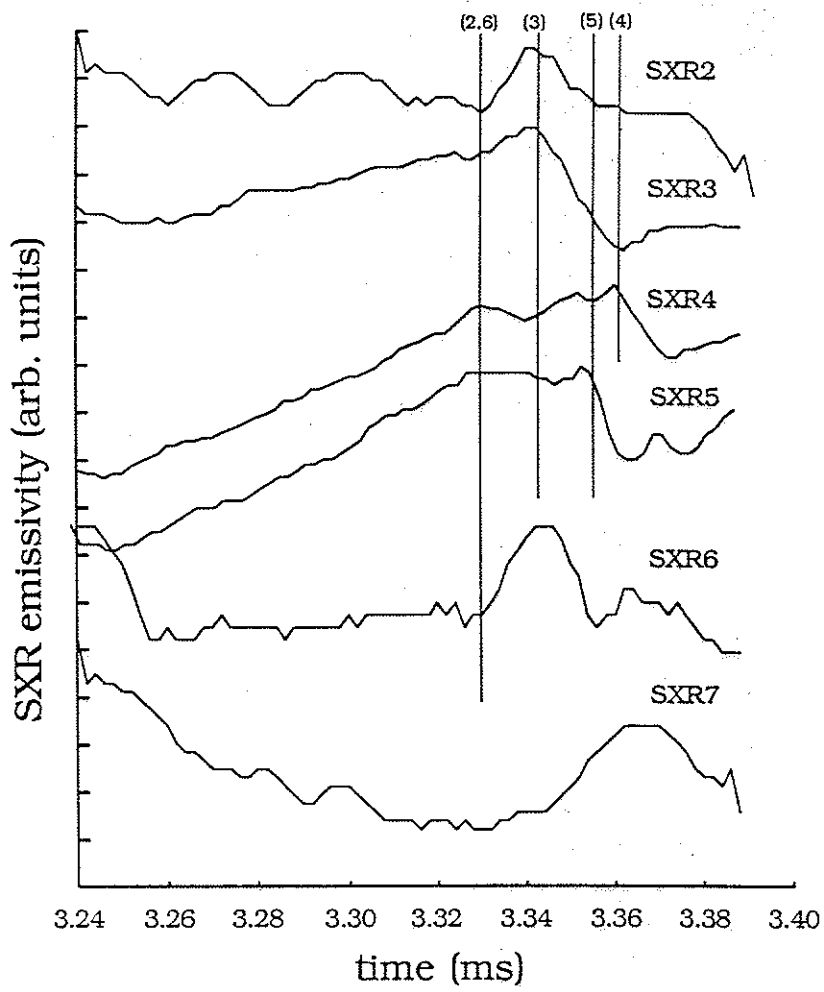

Figure 5.2(b) Small sawtooth showing inward propagation from the inversion surface in a discharge centered just below the midplane. Sequencing of the collapses is indicated by the vertical lines.

McGuire and Robinson have derived an empirical expression for the sawtooth period τ_{saw} that fits sawteeth from many devices of varying size:[5]

$$\tau_{saw} \sim 3 \tau_R^{3/7} \tau_A^{2/7} \tau_h^{2/7} \qquad (5.1)$$

Here, τ_R is the resistive "skin" time ($\tau_R = r_s^2/\eta$), τ_A the Alfvén transit time ($\tau_A = R\rho^{1/2}/B_t$), τ_h the heating time ($\tau_h = 3nT_e/2\eta j^2$), r_s the radius of the mode rational surface, η the plasma resistivity, ρ the mass density, and j the central current density. Using an average of the inversion radii in equation (5.1) yields a period τ_{saw} ~ 200 μs, in agreement with the observed period, despite the association of the small sawteeth with the (2,1) tearing mode, not a (1,1) tearing or resistive kink mode.

The small sawteeth seldom display precursor or successor oscillations on SXR (figure 5.2). Exceptions occur just before a giant sawtooth collapse and are either low frequency precursor oscillations of even (20 kHz) or odd (50 kHz) poloidal mode number $m > 1$[6] (figure 5.3), or high frequency oscillations that onset before the third or later giant sawtooth and survive the small sawtooth collapse (figure 5.4). The high frequency oscillations are ~ 140 kHz, onset with a growth rate of 2-3 × 10^4 s^{-1}, and appear to saturate shortly before the small sawtooth collapse. During the collapse, the frequency increases to ~ 175 kHz. The oscillations survive the small sawtooth collapse, returning to ~ 140 kHz during the reheat to the giant sawtooth collapse. The oscillations invert phase across the center of the discharge (SXR4 and SXR5) implying odd m, but, as

with the low frequency precursors, there are not enough chords with adequate signal-to-noise level to fix the poloidal mode number.

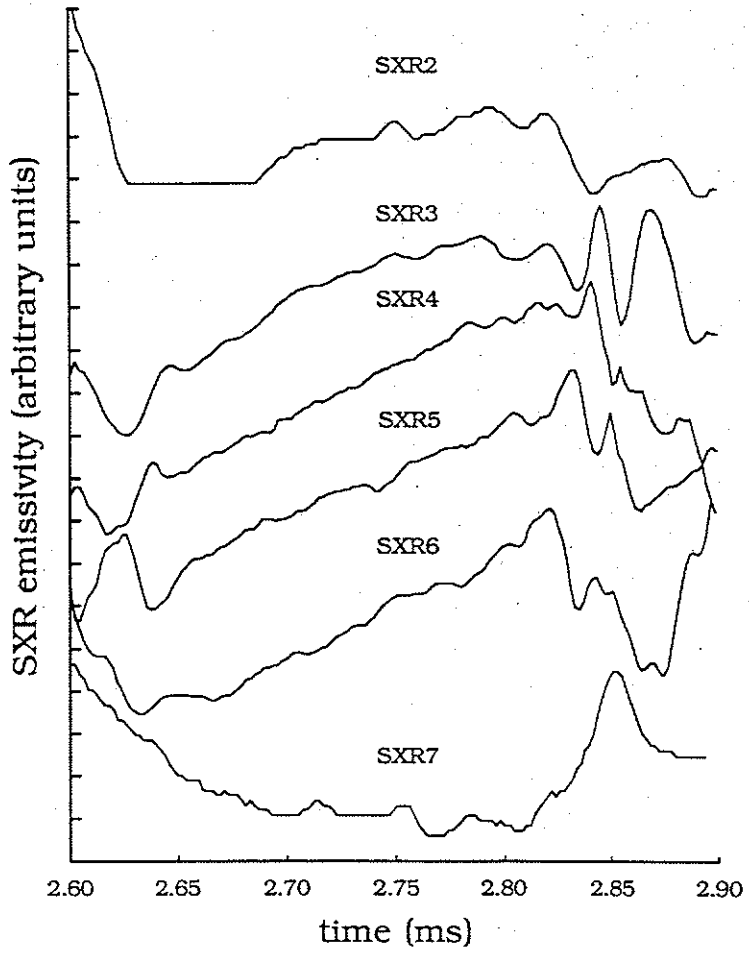

Figure 5.3: Expanded view of the last small sawtooth before a giant sawtooth in a magnetic limiter discharge displaying an odd m > 1 precursor of frequency f ~ 50 kHz. The phase of the precursor inverts between channels 3 and 4 and again between channels 5 and 6.

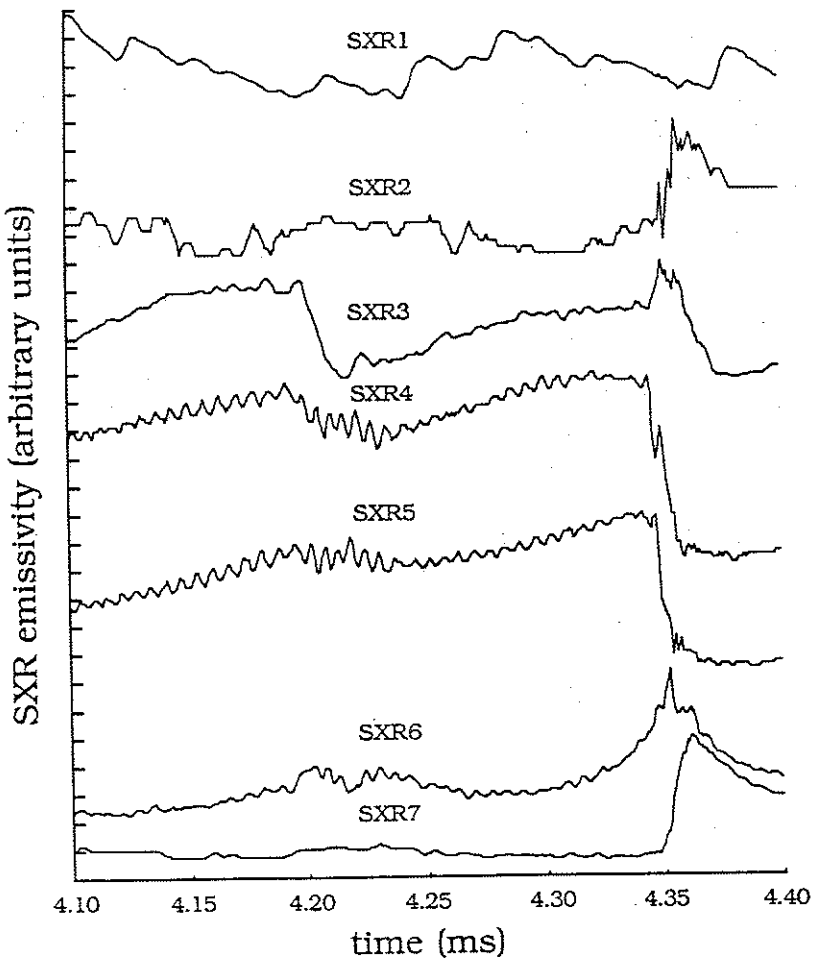

Figure 5.4: Rapid odd m SXR oscillations during the last small sawtooth before the third giant sawtooth in a magnetic limiter discharge. The 140 kHz mode survives the small sawtooth, and appears to "lock" prior to the giant sawtooth.

The small sawteeth typically have the largest amplitude $\Delta I/I$ near the inversion radius (SXR3 in figures 5.2, 3, and 4), with the amplitude less on the inner chords. In figure 5.4, the small sawtooth collapse at 4.22 ms is nearly zero on the central chords (SXR4 and SXR5). This is consistent with the partial disruptions seen on JIPP TII-U, which were localized to the region between the $q = 3/2$ and $q = 2$ surfaces,[3] and appears similar to the compound sawteeth associated with internal disruptions on other devices. The rounded off collapse evident in figure 5.4 on the central chords is consistent with the diffusion of the perturbation associated with the collapse into the interior.

Simulations of the (2,1) tearing mode in a low shear tokamak discharge with $q(0) > 1.5$[4] produce "sawtooth-like" behavior when the $q = 2$ surface is sufficiently far from the plasma edge. In the simulations, the (2,1) island destroys confinement in the plasma core but deposits the thermal energy in the periphery, permitting the discharge to survive. This picture may apply at the highest q_a values studied ($q_a > 3$), but equilibrium fits to the $2 < q_a < 3$ discharges (Section IV.A.1) suggest that $1.1 \leq q(0) \leq 1.3$.

Although accurate current profile data are needed to distinguish between $q = 2$ sawteeth and partial disruptions, the appearance of small sawteeth shortly after a giant sawtooth collapse (within 1 small sawtooth period), and most regularly in the magnetic limiter configuration, suggest that the current profile is rather flat, and possibly hollow. A low shear profile in the plasma

core should permit the (2,1) island to extend rapidly into the plasma core, making the partial disruption explanation more likely.

Reproducible small sawteeth are seldom seen in material limiter discharges. This may be because there is seldom more than one giant sawtooth in these discharges, and the rise to the first giant sawtooth is usually much more rapid and irregular than in magnetic limiter discharges.

The SXR emissivity profile (figure 4.4) in material limiter discharges is narrower, more peaked, and somewhat more centered than the magnetic limiter profile. If the small sawteeth are external disruptions whose amplitude is restricted by details of the current profile in the interior, then the absence of small sawteeth might result from the more peaked current profile inferred from the SXR emissivity in the material limiter configuration.

Small sawteeth have been seen in material limiter discharges that survived the first giant sawtooth without terminating. In this case, the small sawteeth invert at $x = -1.5$ cm and +3.0 cm for a discharge centered at $x_0 = +1.3$ cm. These inversions are inside the giant sawtooth inversions at $x = -3.5$ cm and +5.8 cm ($x-x_0 = \pm 4.5$ cm). The inward shift of the small sawtooth inversions relative to the giant sawtooth inversions, while the latter remained essentially unchanged with respect to the discharge center (±4.5 cm versus ± 5.2 cm with ±.5 cm resolution), also suggest that the current profile in the interior changes significantly with the insertion of the limiters.

The profile may be sufficiently peaked that $q(0) < 1$ and that the small sawteeth are internal disruptions. The small sawtooth period $\tau \sim 200$ μs fits the empirical formula (equation 5.1) and agrees with the period of internal disruptions seen at $1 < q_a < 2$. Unlike the internal disruptions at $1 < q_a < 2$, however, the small sawteeth do not usually have a precursor.

The localized flattening of the SXR emissivity profile at the small sawtooth inversions is suggestive of the presence of a magnetic island. Since the profiles in figure 4.4 were acquired shot-by-shot with a swivel SXR detector, detailed study of the SXR profile evolution during a small sawtooth was not possible due to inadequate reproducibility. The profiles shown were averaged over 100 ± 50 μs before the first giant sawtooth collapse in each configuration, and therefore represent an average effect of the small sawtooth on the profile.

V.A.1.b. Giant SXR Sawteeth:

Giant sawteeth are remarkably reproducible and are independent of density. They are generally one of two types, shown in figure 5.5. The first type (figure 5.5a) either rise continuously (especially in material limiter discharges) or saturate prior to the fast collapse on the central chord SXR signal. These giant sawteeth often display an odd $m > 1$ SXR precursor of 25-30 kHz, as shown in figure 5.5a. Edge SXR chords and electrostatic probes biased to collect ion saturation current in the divertor scrape-off region just

outside the separatrix rise sharply at or after the central chord collapse, but not before.

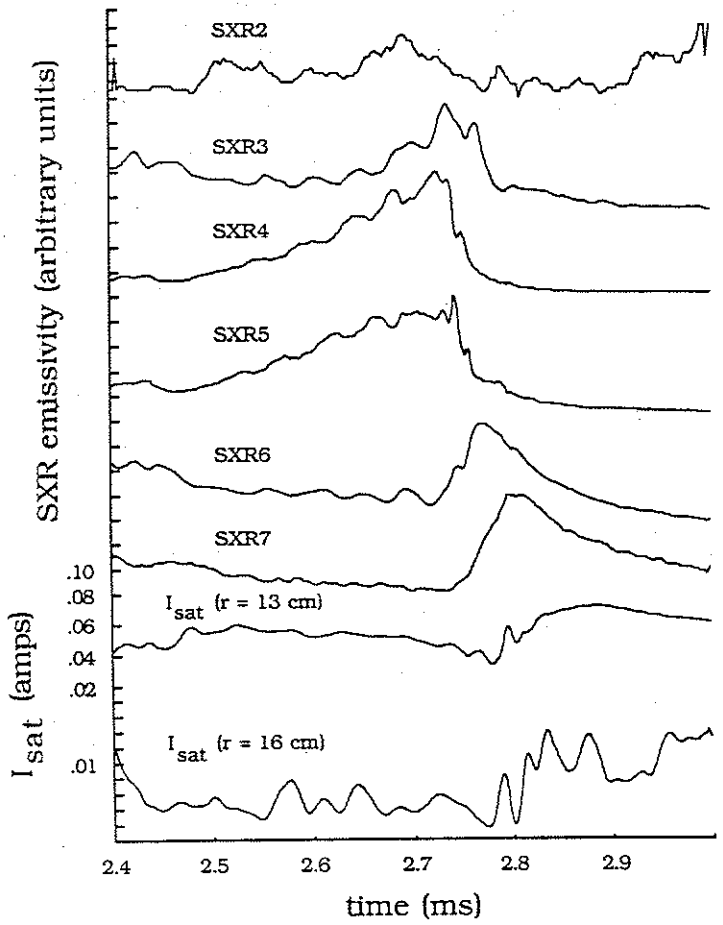

Figure 5.5a: One of two types of giant sawteeth. Early in the discharge, the central chord SXR signal drops sharply while inverted sawteeth are seen on edge SXR chords and on electrostatic probes biased to collect ion saturation current in the scrape-off region just beyond the separatrix ($r_{sep} \approx 10$ cm). Most giant sawteeth in material limiter discharges are of this type.

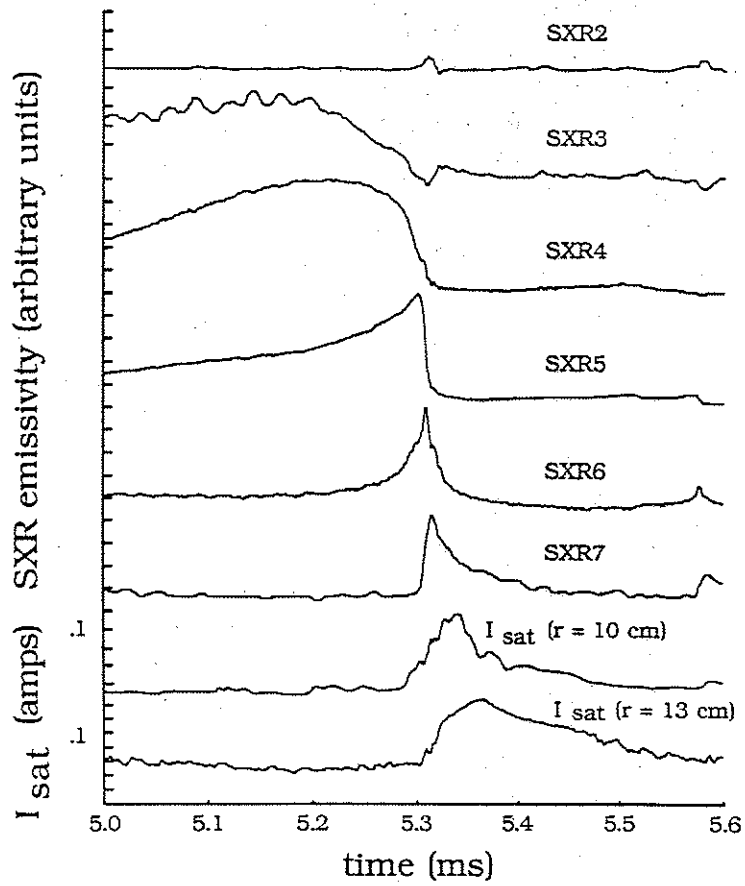

Figure 5.5b: One of two types of giant sawteeth. Late in a magnetic limiter discharge, after the appearance of the fast odd-m mode on the SXR signals (figure 5.4), the giant sawtooth collapse is rounded off and falls diffusively prior to the fast collapse. SXR chords just outside the inversion radius begin rising slowly before the fast collapse on the central chord SXR signal.

The second type of giant sawtooth (figure 5.5b) begins to drop slowly before the fast collapse of the central chord SXR. This slow drop is matched by a slow rise on the SXR chords just outside the inversion radius (SXR6 in figure 5.5b). Beyond the separatrix, the SXR and ion saturation current signals rise at or after the central chord fast collapse as for the first type. These giant sawteeth always appear after the onset of the fast SXR oscillation of figure 5.4. The mode saturates on the SXR chords for several hundred microseconds (tens of oscillation periods) as shown in figure 5.4. Often, the fast oscillation stops and subsequent giant sawteeth round off as much as 50% of the drop in the central chord SXR. The SXR signals suggest the presence of a large saturated island near the $q = 2$ surface that degrades confinement even before the giant sawtooth collapse.

Giant sawteeth in both magnetic and material limiter configurations have a period $\tau \sim 1$ ms, shortening to 0.6 ms by the end of the discharge. The time to the first giant sawtooth is 0.5-0.8 ms shorter in material limiter discharges than in magnetic limiter discharges, and the period is also smaller by 20-25% ($\tau \sim 0.5$-0.8 ms). The central chord SXR signal is enhanced in material limiter discharges, probably due to increased impurity accumulation in the center of the discharge. T_e^{cond}, n_i, and n_i^{core} are comparable in the two configurations, although an increase in $T_e(0)$ cannot be entirely ruled out. Such accumulation would restrict the current rise near the axis and steepen the current density gradient in the

central current channel edge near the giant sawtooth inversion radius (Section II.B.2.c). This, combined with the steepened gradients near the separatrix for the material limiter discharges inferred in Section IV.A, should lead to a larger growth rate for the (2,1) mode in material limiter discharges, as seen in Section V.B.1.c.

As described in Section V.B.1.a, the giant sawteeth invert near or just inside the small sawteeth in magnetic limiter discharges. For discharges centered at $x_0 = +$ 2-3 cm, the inversions are at $x-x_0 = \pm$ 5.2 $\pm$ 0.5 cm. In material limiter discharges, the magnetic axis shifts to $x_0 =$ 1-1.5 cm with inversions at $x-x_0 = \pm$ 4.5 cm. The reduction of the inversion radii in material limiter discharges suggests peaking of the profile, inconsistent with flattening near the axis due to impurity accumulation, but is not much outside the limits of the detector spatial resolution and shot-to-shot variability.

Attempts to fit the magnetic and material limiter discharges using an equilibrium code[7] (Section IV.A.5) suggest the association of the small and giant sawtooth inversion radii with the $q = 2$ rational surface. The tendency of the giant sawteeth to invert somewhat inside the small sawteeth might suggest the interaction of the (2,1) island with magnetic surfaces inside the $q = 2$ surface during the collapse. Interpretation of the inversions as the $q = 1$ surface requires unphysically peaked current profiles.[6]

V.A.1.c. Mirnov Oscillations:

Identification of both the small and giant sawteeth as external disruptions is provided by the detection of dominant magnetic precursors of (2,1) structure prior to the sawtooth collapses. The (2,1) magnetic precursor is seen in both the magnetic and material limiter configurations, although the details of the mode activity are different.

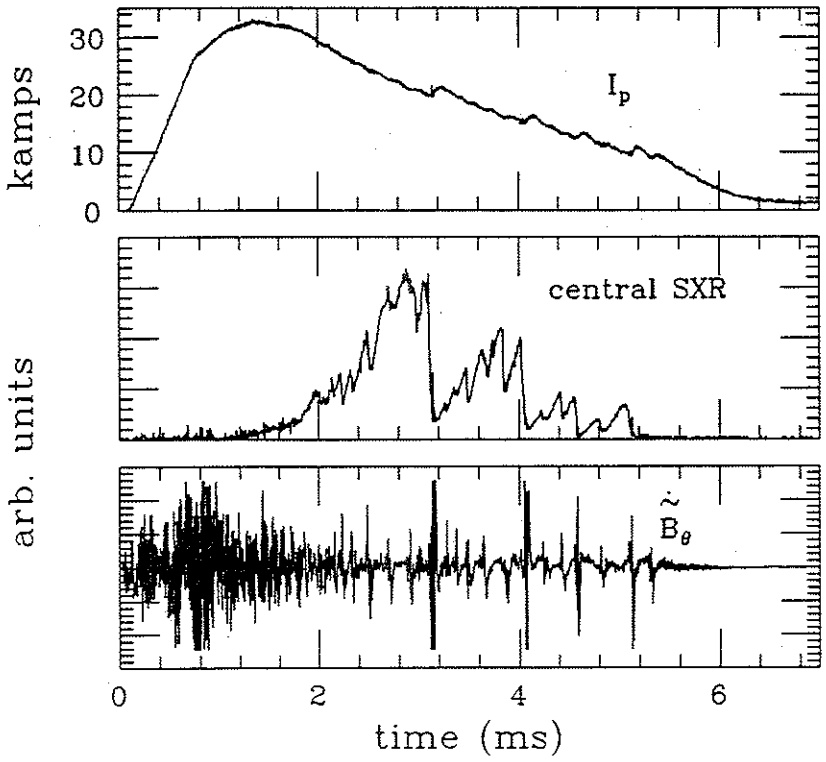

Figure 5.6a: Central chord SXR and Mirnov signals in a typical magnetic limiter discharge.

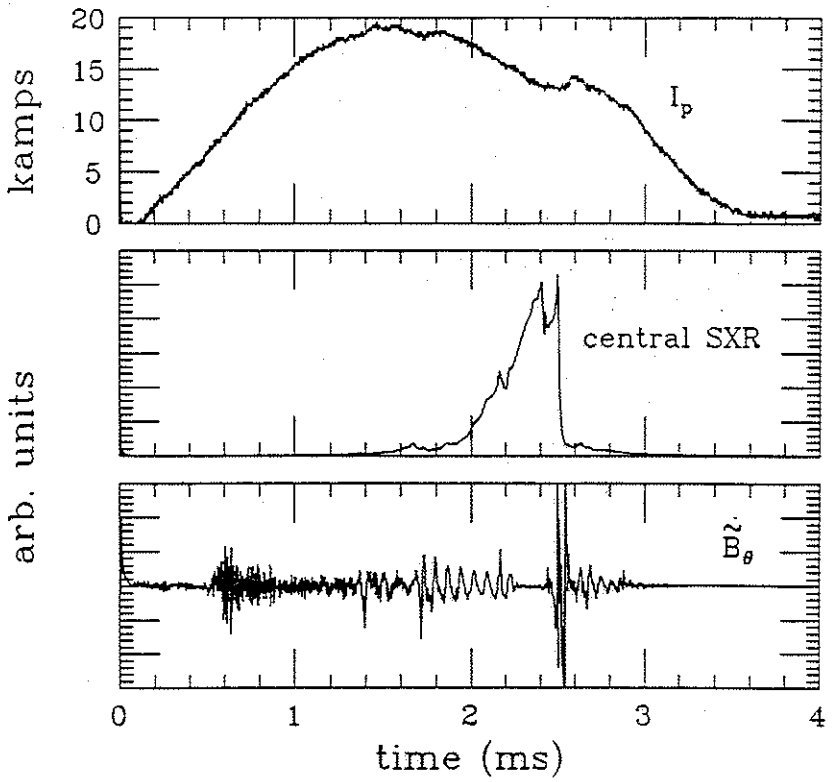

Figure 5.6b: Central chord SXR and Mirnov signals in a typical material limiter discharge.

Bursts of Mirnov activity are correlated with both the small and giant sawteeth in the magnetic limiter discharges (figure 5.6a). In material limiter discharges, a coherent mode grows and saturates during the SXR rise to the first giant sawtooth collapse, appears to lock or go away prior to the collapse, and reappears in the magnetic energy quench phase of the disruption (figure 5.6b).

Small sawteeth in magnetic limiter discharges display a (2,1)

magnetic precursor with a frequency of 25-30 kHz, accelerating to 40-50 kHz just before the sawtooth collapse (figure 5.7).

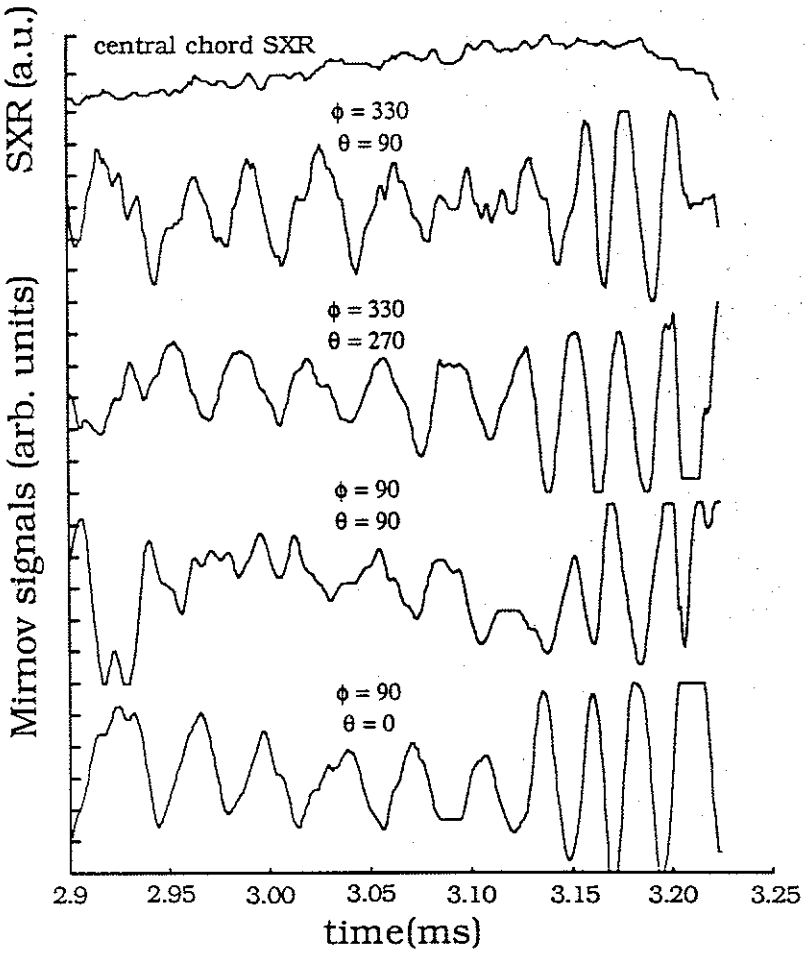

Figure 5.7a: Mirnov oscillations during a small sawtooth in a magnetic limiter discharge. Four probes spaced 90 and 180 degrees apart poloidally, showing the m = 2 character of the oscillation.

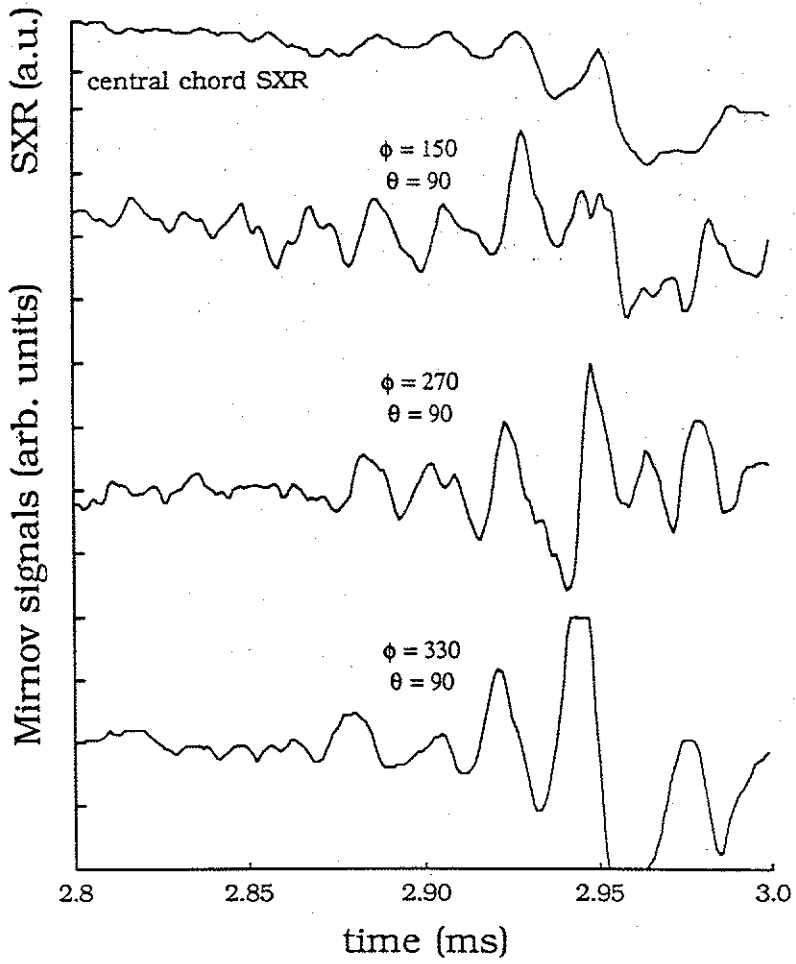

Figure 5.7b: Mirnov oscillations during a small sawtooth in a magnetic limiter discharge. Four toroidally spaced probes on the outer midplane, showing the n = 1 character of the signal.

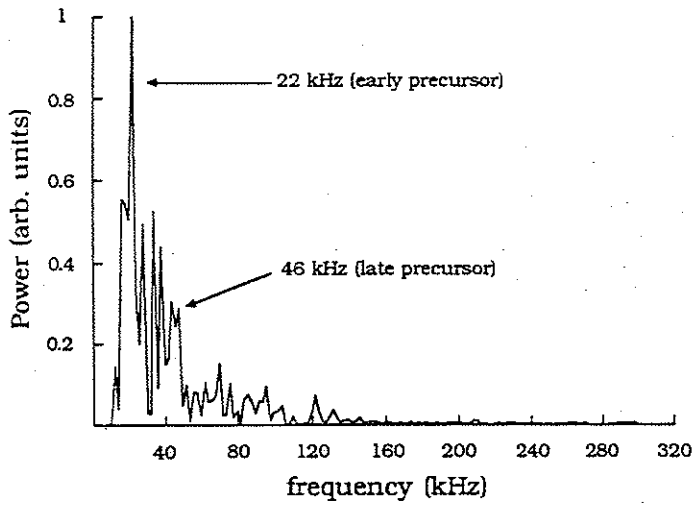

Figure 5.7c: Power spectrum of the Mirnov oscillations on the loop at ϕ = 330, θ = 90 in figure 5.7a for 0.5 ms starting at 2.75 ms, showing both the early and late precursors.

The dominant (2,1) magnetic precursor to the giant sawteeth in magnetic limiter discharges also has a frequency of 30-40 kHz, and grows exponentially during the last 150 μs before the SXR collapse with a growth rate $\gamma_{2,1} = 2.4 \pm .1 \times 10^4\ s^{-1}$ (figure 5.8). The (2,1) structure is distorted over the last few cycles in a manner consistent with an odd m/even n mode of twice the frequency of the (2,1) mode. Osborne reproduced this distortion assuming rigid toroidal rotation in nonlinear, three dimensional MHD code runs with both (2,1) and (3,2) islands.[6]

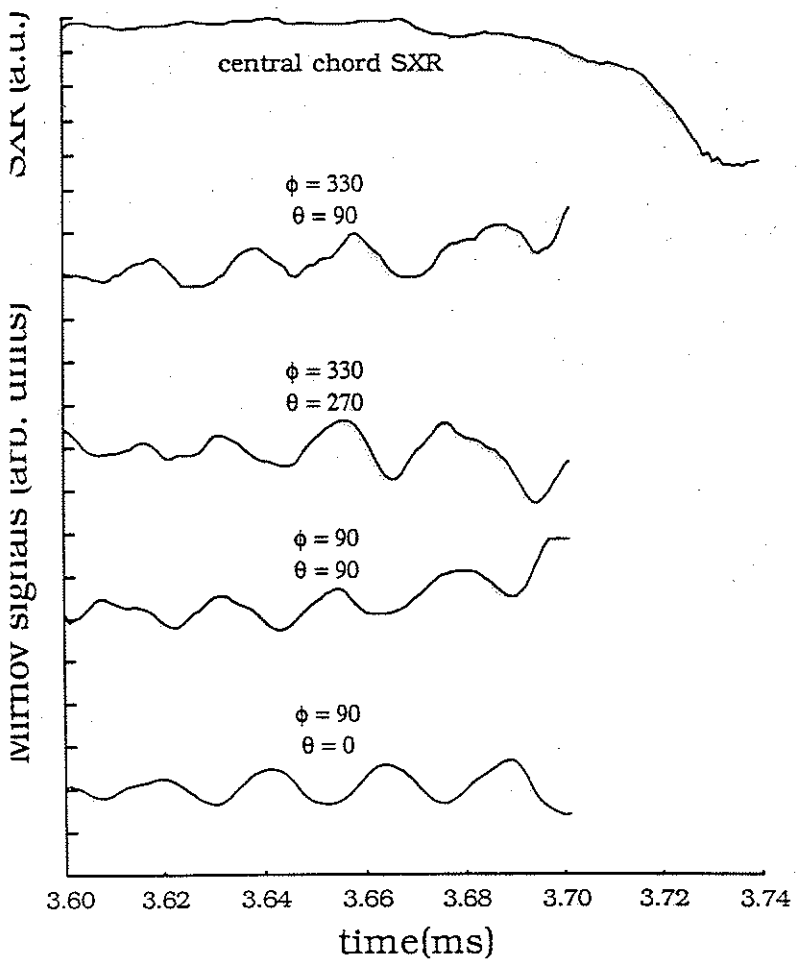

Figure 5.8a: Mirnov oscillations before a giant sawtooth in a magnetic limiter discharge. Four probes spaced 90 and 180 degrees apart poloidally, showing the dominant m = 2 character of the oscillation. The last few cycles are distorted in a manner consistant with the presence of a (3,2) mode.

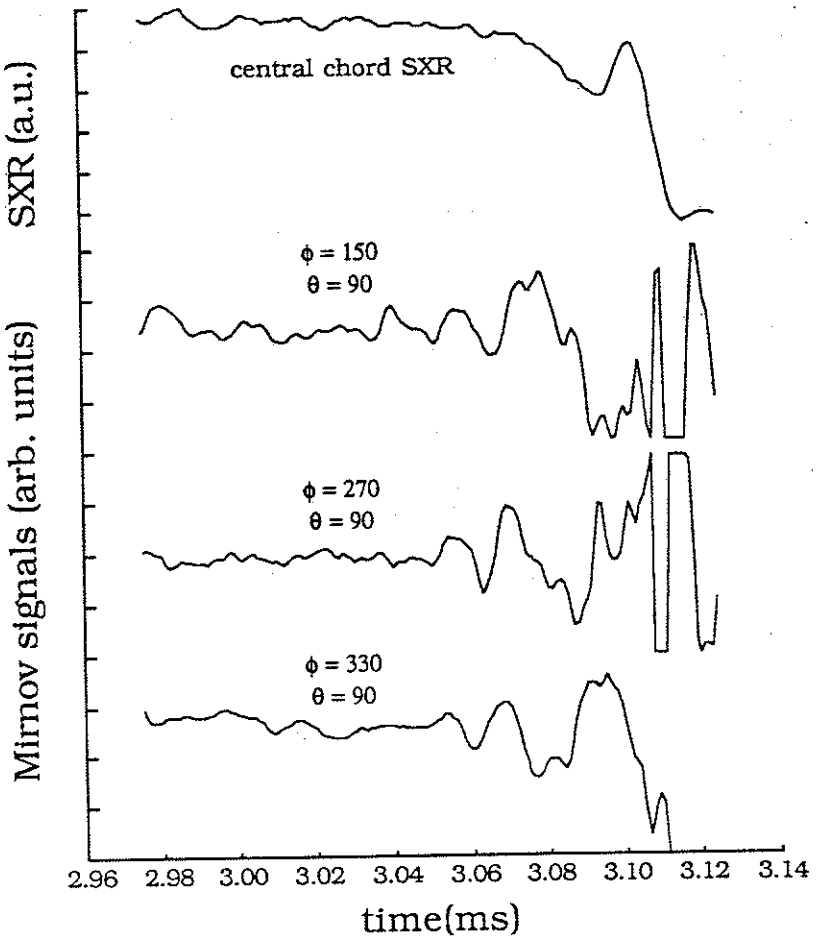

Figure 5.8b: Mirnov oscillations before a giant sawtooth in a magnetic limiter discharge. Four toroidally spaced probes on the outer midplane, showing the n = 1 character of the signal.

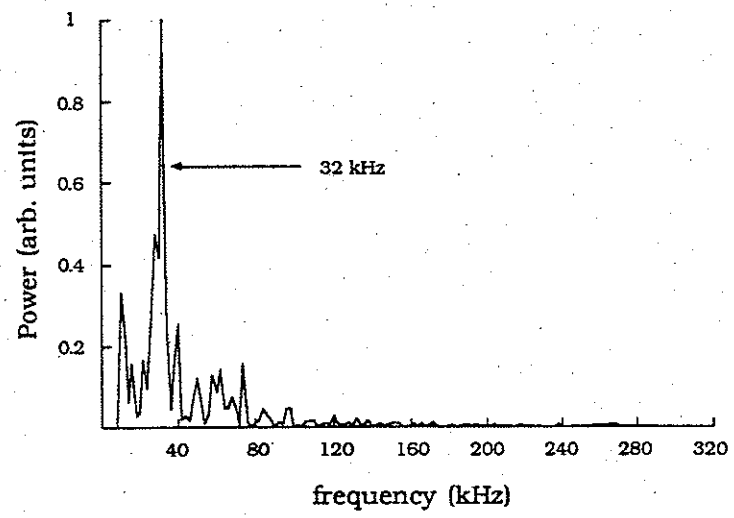

Figure 5.8c: Power spectrum of the Mirnov oscillations on the loop at ϕ = 330, θ = 90 in figure 5.8a for 0.5 ms starting at 3.2 ms, showing the dominant (2,1) mode.

In material limiter discharges, the (2,1) mode has a frequency of 15-20 kHz, half that in magnetic limiter discharges, and rises with a growth rate $\gamma_{2,1} = 2 \pm .1 \times 10^4\ s^{-1}$ as the SXR signal rises (figure 5.9). This oscillation continues for nearly 0.5 ms as the central chord SXR signal rises toward the giant sawtooth collapse at 2.55 ms. The mode is lost or locks at 2.25 ms as the SXR signal shows a quick rearrangement of the profile in the center of the discharge (figures 5.6b and 5.10). Since the Tokapole II device lacks the appropriate coil sets to detect the presence of a stationary island, these two possibliities cannot be distinguished.

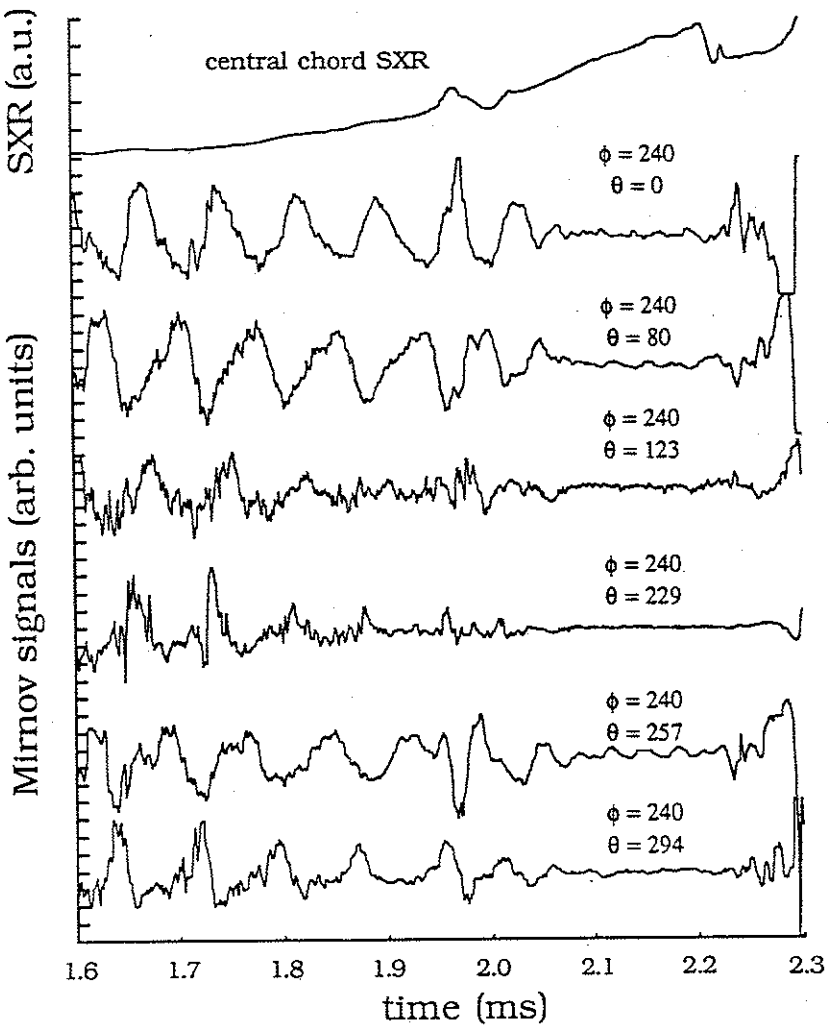

Figure 5.9a: Mirnov oscillations on a six coil poloidal array in a material limiter discharge during the first giant sawtooth ramp, showing the m = 2 character of the signal.

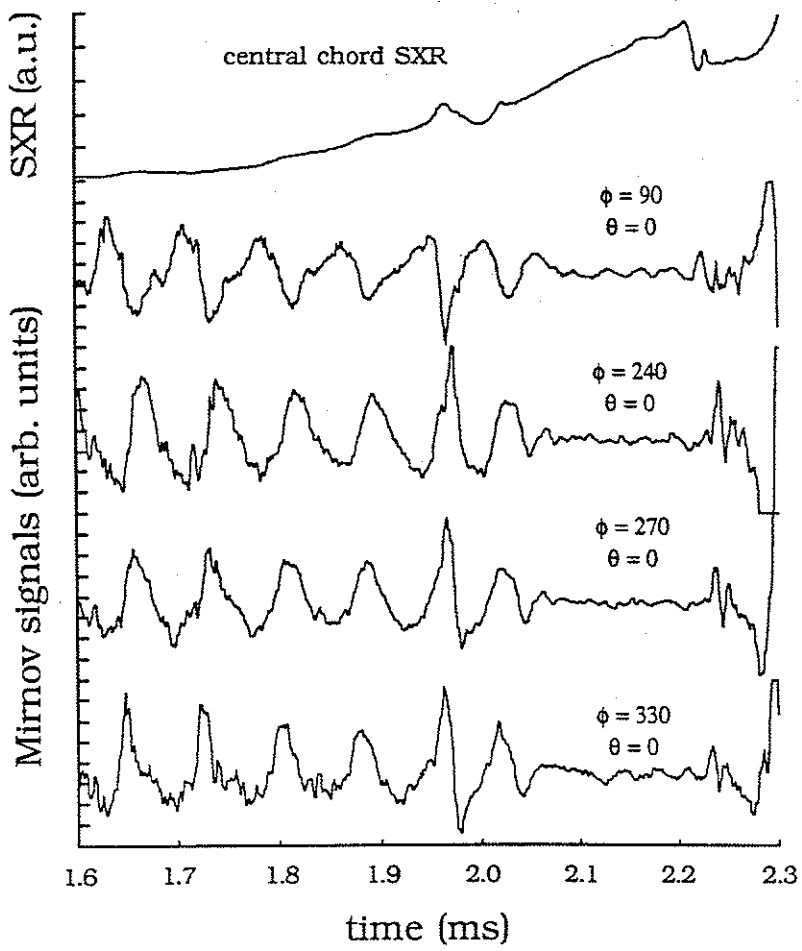

Figure 5.9b: Mirnov oscillations on a four coil toroidal array in a material limiter discharge during the first giant sawtooth ramp, showng the n = 1 character of the signal.

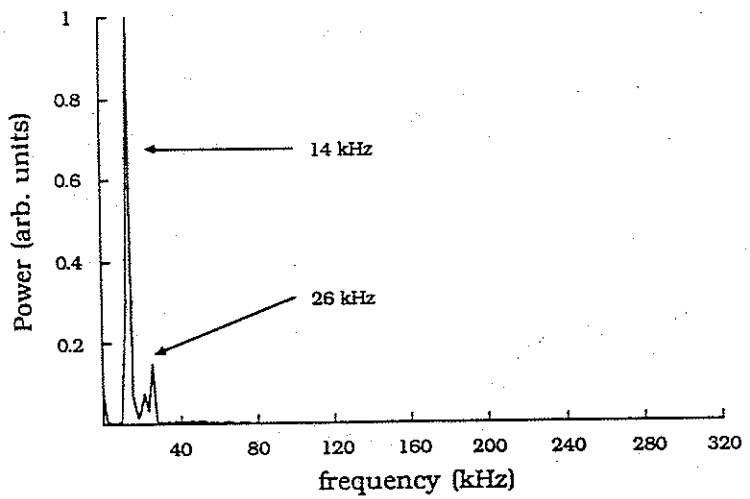

Figure 5.9c: Power spectrum of Mirnov oscillations on the loop at ϕ = 240, θ = 0 in figure 5.9a for 0.5 ms starting at 1.5 ms. The saturated (2,1) oscillation at 14 kHz dominates the power spectrum.

The mode remains locked or absent for ≈ 200 μs while the central chord SXR signal rises sharply without precursors (figure 5.10). At 2.4 ms, a brief SXR collapse of amplitude $\delta I/I$ ~ 30% occurs, and ~ 40 μs later the (2,1) mode reappears with a frequency of 40-50 kHz (as in magnetic limiter discharges) and a growth rate $\gamma_{2,1} = 4.8 \pm 0.6 \times 10^4\ s^{-1}$, twice $\gamma_{2,1}$ in magnetic limiter discharges. The explosive (2,1) growth lasts only 50 μs before the giant sawtooth collapse, compared to 150 μs in magnetic limiter configuration, and is distorted prior to the collapse similar to the odd m/even n distortion seen in the magnetic limiter discharges. A burst of high frequency, turbulent activity lasts for 50 μs following

the giant sawtooth collapse. The discharge does not survive the giant sawtooth (major disruption) and during the magnetic energy quench the (2,1) mode reappears briefly with a frequency of 15-20 kHz (figure 5.11).

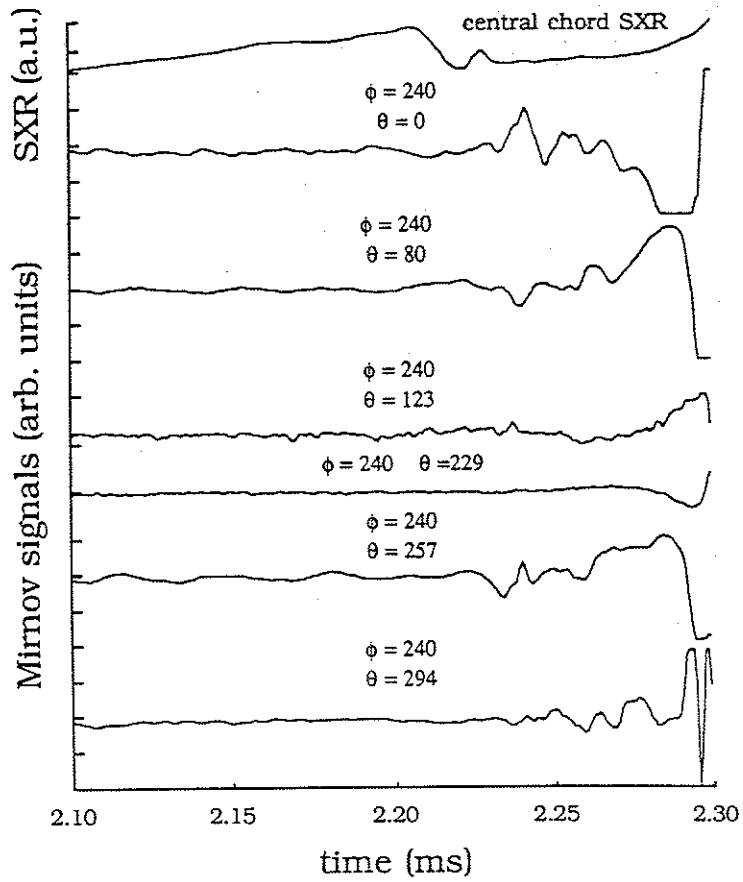

Figure 5.10a: Mirnov oscillations on a six coil poloidal array in a material limiter discharge 200 μs before the giant sawtooth collapse at 2.30 ms.

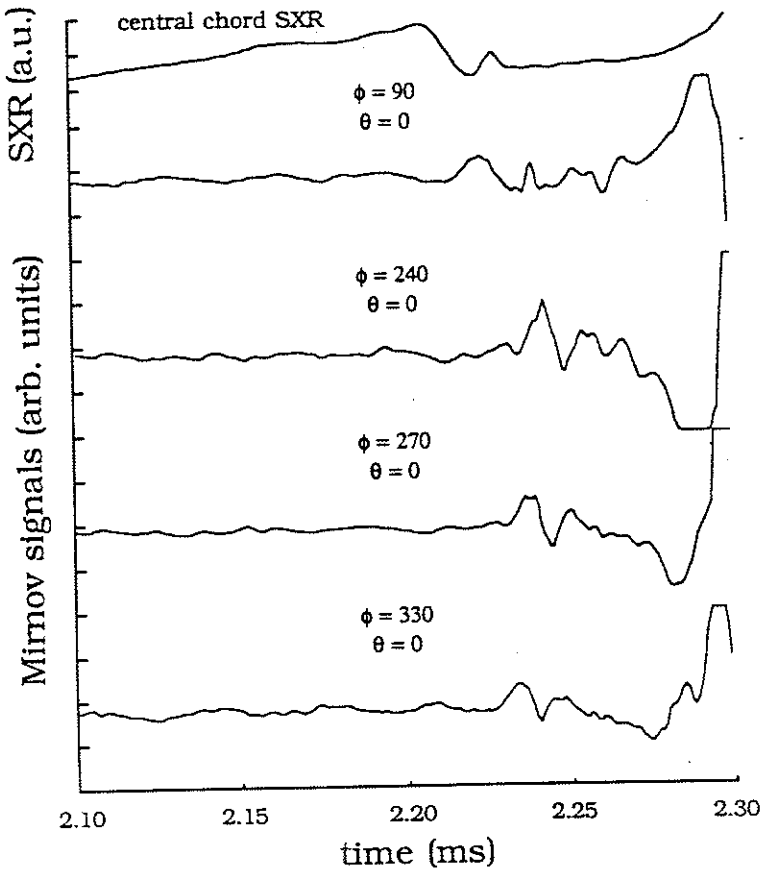

Figure 5.10b: Mirnov oscillations on a four coil toroidal array in a material limiter discharge 200 μs before the giant sawtooth collapse at 2.30 ms.

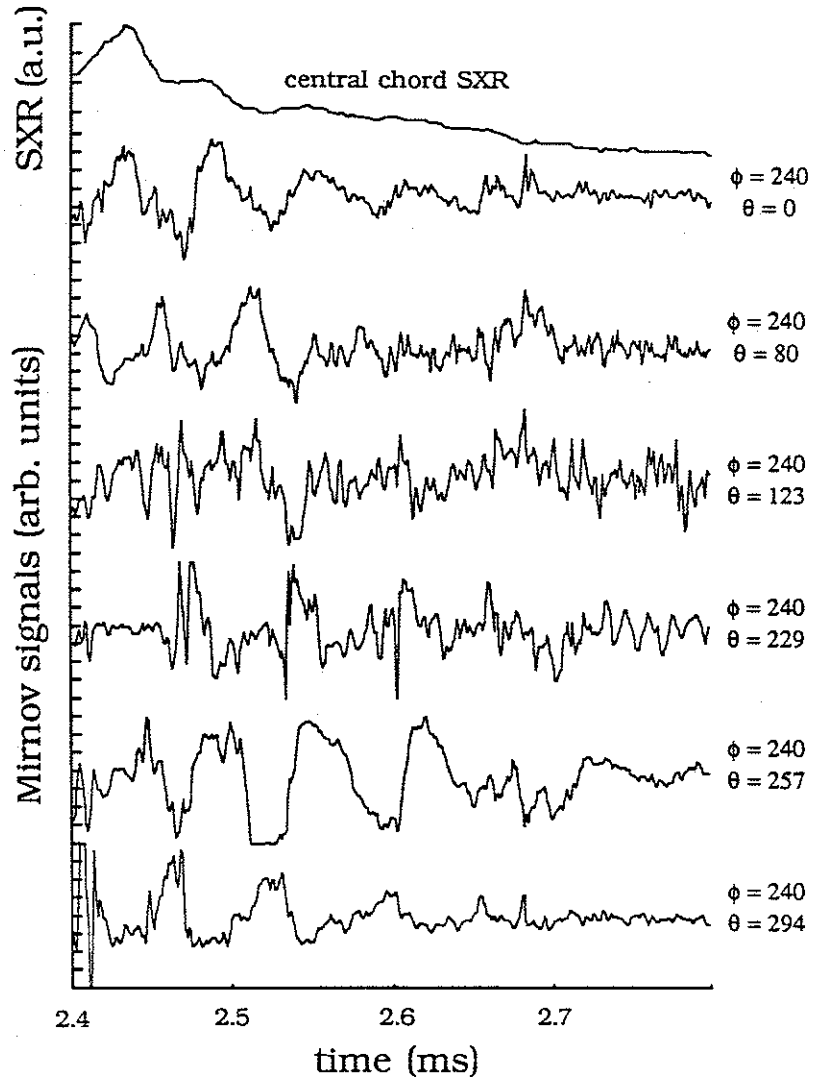

Figure 5.11a: Mirnov oscillations on a six coil poloidal array in a material limiter discharge following the giant sawtooth collapse, during the magnetic energy quench of the discharge. The successor oscillation is also m = 2.

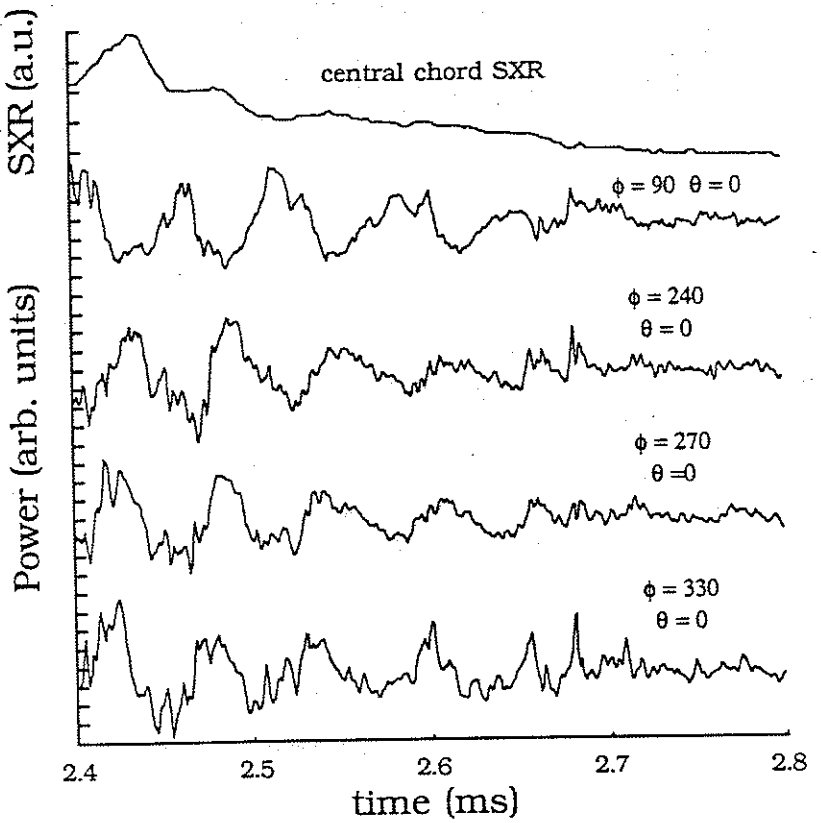

Figure 5.11b: Mirnov oscillations on a four coil toroidal array in a material limiter discharge following the giant sawtooth collapse, during the magnetic energy quench of the discharge. The successor oscillation is also an n = 1 oscillation.

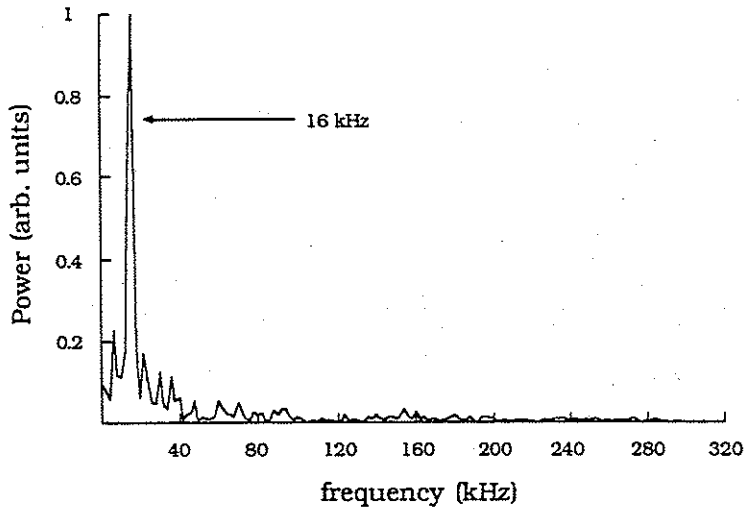

Figure 5.11c: Power spectrum of the Mirnov oscillations on the Mirnov loop at φ = 240, θ = 0 in figure 5.11a for 0.5 ms starting at 2.4 ms. The power spectrum of the (2,1) successor oscillation during the magnetic energy quench appears similar to the (2,1) precursor of figure 5.9c.

V.A.1.d. Scrape-off Profile Evolution:

External disruptions have been imaged using time resolved ion density, electron temperature, and electron pressure profiles in the divertor scrape-off region, and through the study of vacuum ultraviolet line emission from several light impurities (H, C, N, and O). The VUV data provide information on changes in the vicinity of the particular impurity ionization state, and are limited because the most easily studied lines are near the divertor separatrix or in the scrape-off region, and not in the central current channel.

Profile measurements are hindered by the lack of shot-to-shot reproducibility for the fast changes associated with sawtooth collapses. Scrape-off profile changes from small sawteeth are of small amplitude and brief duration, so these disruptions could not be imaged due to inadequate reproducibility. The larger amplitude and longer duration associated with giant sawteeth allow time-resolved profiles of these disruptions to be obtained.

Shots were selected from the datasets displaying similar giant sawteeth on the poloidal SXR array. Profiles were constructed using shots with similar (± 20%) ion saturation current and admittance signals on a stationary monitor probe at r = 13 or 15 cm in the divertor scrape-off region over the last 100 μs before the central chord SXR collapse. Profiles were calculated in 15 μs steps, averaging over 10 μs. To emphasize changes due to the disruptions, the pre-disruption profiles (40-50 μs before collapse) were subtracted from each subsequent profile. The resulting Δn_{ion}, ΔT_e, and ΔP_e profiles are plotted in figures 5.12, 5.13, and 5.14 for a disruption in a typical magnetic limiter discharge. No significant differences in evolution of the scrape-off profiles have been observed in material limiter discharges.

From figures 5.12-5.14, it is evident that the giant sawtooth is mostly a density perturbation, with the scrape-off density rising abruptly by factors of 3-10 just beyond the separatrix and n_i^{core} dropping 15% (figure 5.12b). T_e responds 40-50 μs later, rising by factors of 1-3. The increases in scrape-off T_e and P_e persist for up to

300 μs after the disruptions, while the density increase is quickly lost, within ~ 100 μs. For all the profiles, the perturbation does not appear to diffuse away, but rather to relax inward in minor radius. The substantial density perturbation of the giant sawteeth distinguishes these disruptions from typical internal disruption sawteeth that are mostly an electron temperature perturbation (10-30%), with only a minor 1%-5% density perturbation.[8,9]

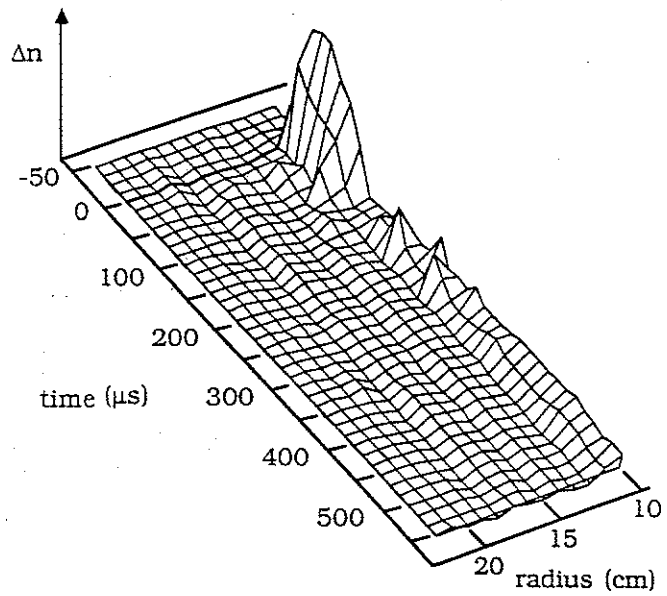

Figure 5.12a: Surface plot of the change in scrape-off ion density following a giant sawtooth in a magnetic limiter discharge. $\Delta n_i = n_i(t - t_o) - n_i(t_o)$ where t_o is 50 μs before the fast collapse of the central chord SXR signal. The profiles are shown in 15 μs steps from t = -50 μs (before the crash) to t = + 500 μs.

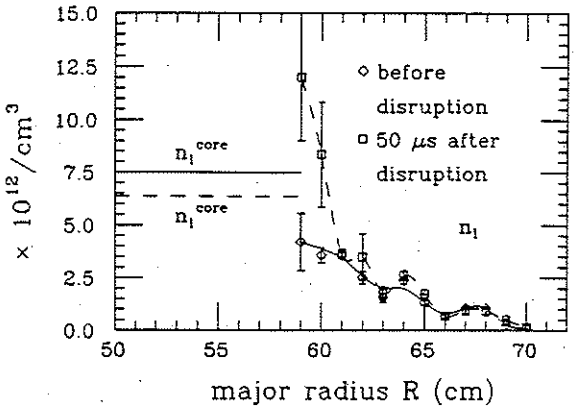

Figure 5.12b: Comparison of scrape-off density profiles 50 μs before (solid) and after (dashed) the giant sawtooth collapse. The sawtooth collapse generates a hollow density profile with a 15% drop in n_i^{core}.

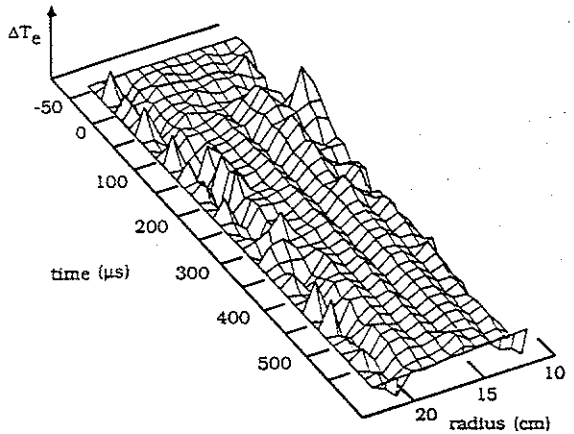

Figure 5.13: Surface plot of the change in scrape-off T_e following a giant sawtooth in a magnetic limiter discharge. $\Delta T_e = T_e(t - t_o) - T_e(t_o)$ where t_o is 50 μs before the disruption the fast collapse of the central chord SXR signal. The profile is shown in 15 μs steps from t = −50 μs (before the crash) to t = + 500 μs.

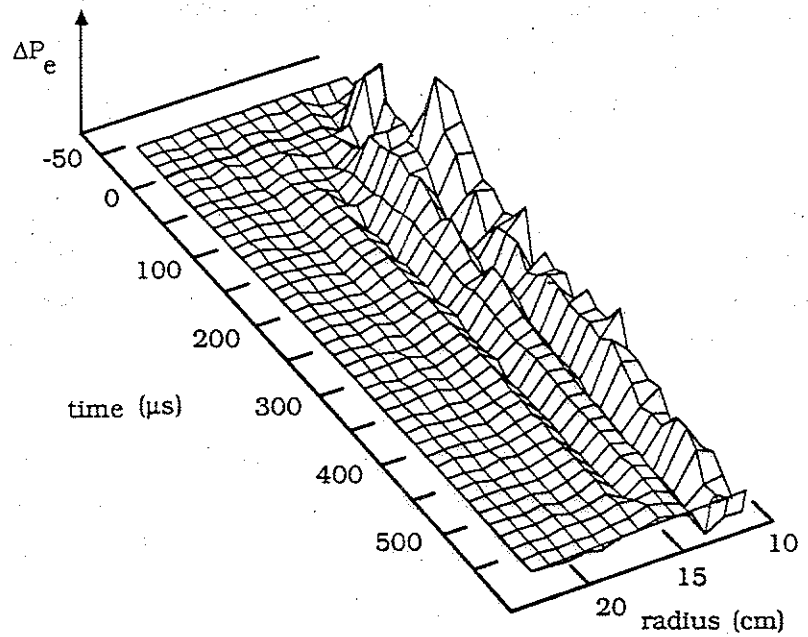

Figure 5.14: Surface plot of the change in scrape-off P_e profile following a giant sawtooth in a magnetic limiter discharge. $\Delta P_e = P_e(t - t_o) - P_e(t_o)$ where t_o is 50 μs before the fast collapse of the central chord SXR signal. The profile is shown in 15 μs steps from t = −50 μs (before the crash) to t = + 500 μs.

The structure of the Δn_i perturbation is consistent with a rapid expansion in minor radius following the disruption, typical of major disruptions in other tokamaks (Section II.B.1). No evidence for a large post-disruptive major radius shift following the collapse is seen in figures 5.12-5.14. As discussed in Section V.B.3, this is well understood in terms of: 1) experimental SXR emissivity profiles that suggest any inward shift in major radius is limited to 1-3 cm,

2) equilibrium modeling of pre- and post-disruption current density profiles[6] that predicts only a 1-2 cm shift in the magnetic axis, and 3) the decay index of the effective vertical field of the divertor rings, (equivalently, the deep magnetic well of the octupole divertor ring field) which predicts theoretically a major radius shift of ~ 2 cm.[10] The drop in central current channel density (figure 5.12b) seems too small to result from complete loss of confinement in the central current channel, and the profile changes in figures 5.12-5.14 appear to be axisymmetric (n = 0).

Line emission from the light impurities hydrogen, carbon, nitrogen, and oxygen (Section III.B.4) displays spikes (inverted sawteeth) at the time of the small and giant sawteeth in magnetic and material limiter discharges (figure 5.15). The impurity ionization states for Carbon III, Nitrogen III, and Oxygen III, IV, and V are just inside the divertor separatrix, while the hydrogen Lyman α intensity peaks near the wall. The spikes do not result in enhanced emission levels in the magnetic limiter discharges. These spikes, similar to "H_α spikes" on other tokamaks, arise from the localized density increase near the separatrix following the sawteeth. H_α spikes are generally interpreted as indicating plasma expansion, consistent with the scrape-off profiles in figures 5.12-5.14.

The behavior of the Oxygen VI line is somewhat different (figure 5.15). In magnetic limiter discharges, the O VI emission is only mildly altered by the giant sawteeth, indicating that this

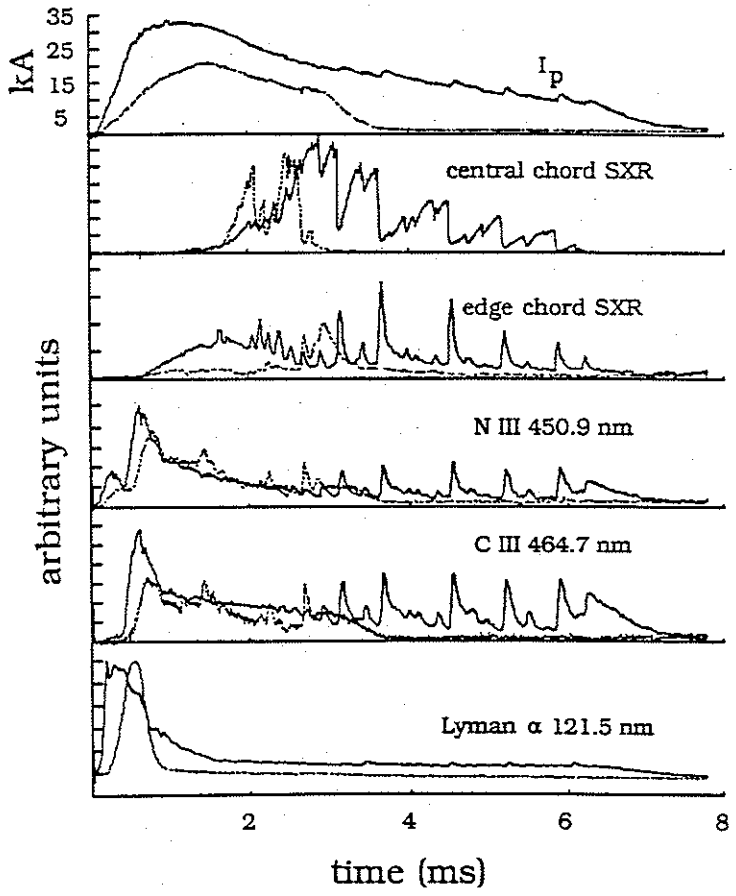

Figure 5.15a: Emission from light impurity lines in typical (solid) magnetic and (broken) material limiter discharges. The lines are: hydrogen Lyman α 121.5 nm (H_α), Carbon III 464.7 nm (C III), and Nitrogen III 450.9 nm (N III) The absolute magnitudes are meaningful for I_p, the edge and central SXR chords, and the C III and N III signals; the H_α signal is normalized to a peak value of 1.

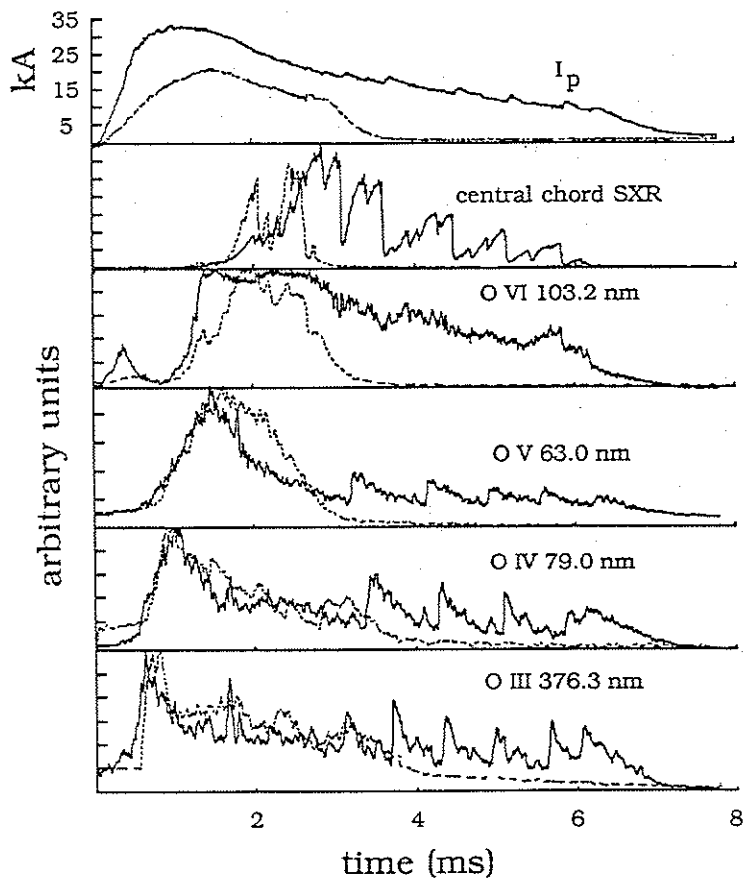

Figure 5.15b: Emission from light impurity lines in typical (solid) magnetic and (broken) material limiter discharges. The lines are: Oxygen III 376.3 nm (O III), Oxygen IV 79.0 nm (O IV), Oxygen V 63.0 nm (O V), and Oxygen VI 103.2 nm (O VI). The absolute magnitudes are meaningful for I_p, the edge and central SXR chords; the oxygen series are all normalized to peak values of 1.

ionization state is near the giant sawtooth inversion radius (just inside the separatrix). In material limiter discharges, however, the O VI emission displays giant sawteeth, indicating that the ionization state is now inside the inversion radii for the giant sawteeth.

Together with the SXR measurements, these O VI measurements indicate that confinement in the central current channel is abruptly lost during the giant sawtooth collapse. The existence of the O VI ionization state closer to the magnetic axis in the material limiter discharges indicates that either the central $T_e(0)$ is lower, the oxygen level higher (accumulation) near the axis, or both despite the more peaked character of the SXR emissivity, density and temperature profiles. In the absence of internal disruptions ($1.1 \leq q(0) \leq 1.3$), this provides a mechanism for restricting the current density on axis, which plays a crucial role in the triggering of major disruptions in the coupled tearing mode/transport simulations (Section II.B.2.c)

No change in impurity levels in the plasma periphery is evident in magnetic limiter discharges following the spikes (figure 5.15). In the material limiter discharges, the impurity radiation is enhanced in the 200-300 μs after the spike (figure 5.15). This impurity buildup on a relatively long time scale following the giant sawtooth will be shown in Section V.B.3 to be responsible for the radiative collapse that terminates the discharge in the material limiter configuration. Sources for this impurity influx are the

limiter plates at the separatrix and increased interaction with the divertor rings and supports.

V.A.2. $1 < q_a < 2$ Discharges:

As q_a is lowered at constant B_t and n_l to $q_a \sim 2$ in magnetic limiter discharges, the SXR signal makes a transition from the small and giant sawteeth discussed in Section V.B.1 to only small sawteeth (figure 5.16). A typical $q_a \approx 1.9$ magnetic limiter discharge is shown in figure 5.17. Small sawteeth onset at 1.6 ms and continue until 5.6 ms when q_a rises above 2 as the current drops. After this, the sawteeth appear progressively more "giant-like." The small sawteeth have a (1,1) SXR precursor and no dominant magnetic precursor, and are therefore identified as internal disruptions. These results suggest that the (2,1) mode responsible for the small and giant sawteeth at $2 < q_a < 3$ is stabilized as the plasma current is increased and the $q = 2$ surface approaches the divertor separatrix. With the increase in plasma current, $q(0)$ drops below 1 and internal disruptions appear.

A similar SXR sawtooth transition occurs at $q_a \sim 1.5$ in material limiter discharges as well, despite the reduction of plasma and current in the divertor scrape-off region and the concomitant steepening of the current profile at the edge of the central current channel (figure 5.18). The transition in Mirnov signals in the material limiter configuration as q_a is lowered from 3 to 1.3 is shown in figure 5.19 for the discharges in figure 5.18. The

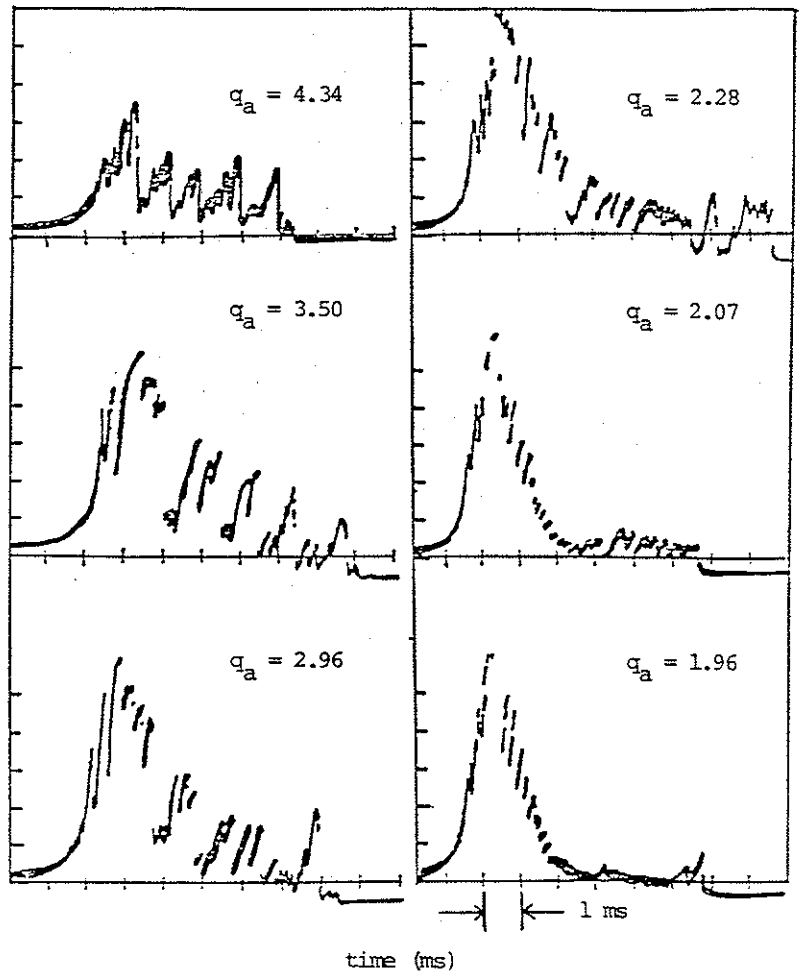

Figure 5.16: Sequence of central chord SXR signals in magnetic limiter discharges showing the transition from small and giant sawteeth at $q_a > 2$ to only small sawteeth at $q_a \approx 2$ (from reference 6).

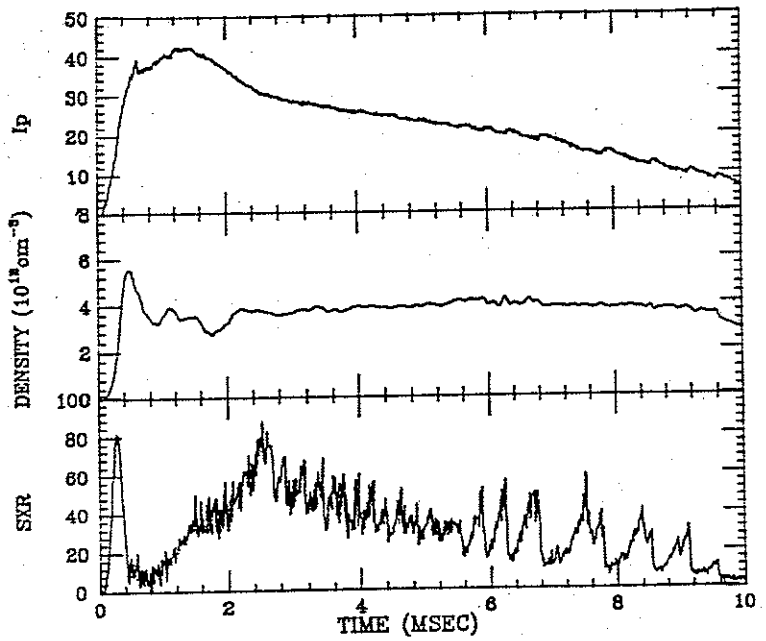

Figure 5.17: Plasma current I_p, line average density n_l, and central chord SXR signal in a magnetic limiter discharge with $q_a \sim 1.9$.

disappearance of the giant sawteeth is correlated with the loss of the coherent (2,1) oscillation on the Mirnov signals. As the (2,1) oscillation is lost, the broadband fluctuation level increases.[11] This behavior is identical to magnetic limiter discharges; the only difference is the q_a value at which the transitions occur.

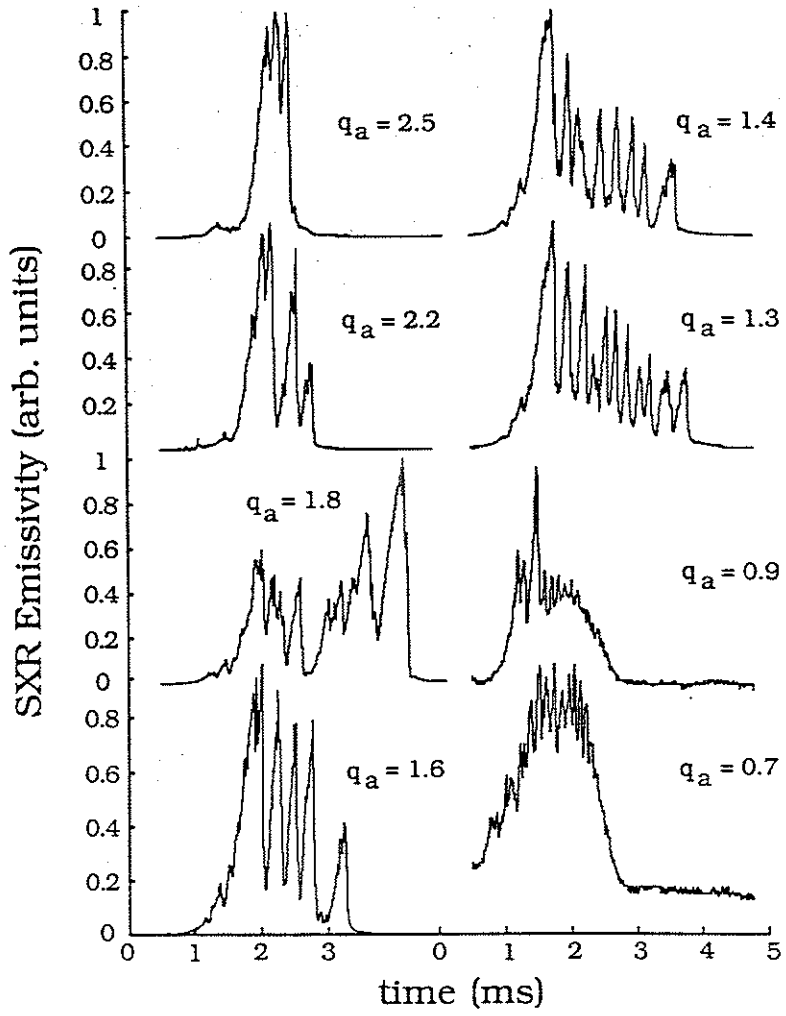

Figure 5.18: Sequence of central chord SXR signals, normalized to peaks of 1 to emphasize changes in relative amplitudes, for material limiter discharges with $1.3 \leq q_a \leq 3$.

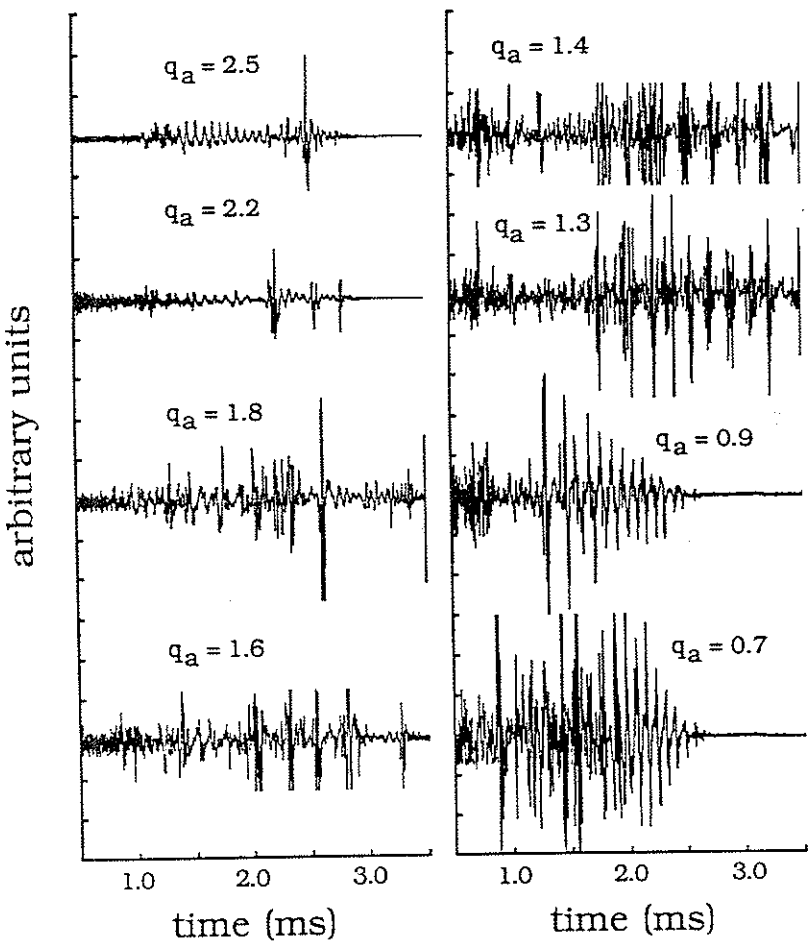

Figure 5.19: Sequence of Mirnov signals for a probe just outside the separatrix in the material limiter discharges of figure 5.18.

V.A.3. Current Termination in External Disruptions:

A key feature of Tokapole II operation in the magnetic limiter configuration is the absence of abrupt current termination over the entire operating range $0.4 < q_a < 4$. This lack of major disruption is particularly dramatic in light of the reproducibility of external disruptions (minor disruptions) that appear as major disruptions in most respects (abrupt thermal quench of the central current channel, negative gap voltage spike, initial plasma current rise during thermal quench, and exponentially growing (2,1) mode coupled just before the disruption to an odd m/even n mode). Also remarkable is the ease with which the stability barriers at $q_a = 2$ and $q_a = 1$ are passed during routine operation.

As a rule, divertor tokamaks have been less susceptible to major disruptions than limiter tokamaks (Section II.B.1.a). There is a marked tendency for external disruptions to appear as repetitive minor disruptions, particularly during current rampdown at the end of the discharge. Divertor tokamaks have not, however, been able to entirely avoid major disruptions. In material limiter operation on PDX, discharges were less susceptible to major disruption when operated with top and bottom rail limiters or an outboard pump limiter rather than against the inboard belt limiter.

Many tokamaks utilize precise plasma position control via active feedback of vertical field coils to reduce the number and severity of major disruptions. Extensive conditioning of the vacuum vessel and limiter, gettering, and careful gas puff control have also

proved effective in reducing the number and severity of disruptions in many devices. These techniques reduce plasma-limiter contact, reduce the impurity influx resulting from hard plasma contact with the limiter, or permit current profiles favorable to (2,1) tearing mode stability.[12-14]

This body of operational experience from many tokamak devices suggests that, if the giant sawteeth observed in magnetic limiter discharges in Tokapole II are really major disruptions with current termination suppressed by the magnetic limiter configuration, then operation with material limiter plates should result in abrupt current termination.

A magnetic limiter discharge that survives five minor disruptions is compared in figure 5.20 with a material limiter discharge that terminates after the first disruption. In each configuration, an abrupt thermal quench of the central current channel is indicated by the SXR signals in the expanded views of figure 5.21. After a brief (~ 120 μs) 7% rise, the plasma current returns to its initial level in each discharge. The discharge current does not collapse until 250-300 μs after the disruption in the material limiter discharge. The current collapses exponentially with an L/R time consistent with a 90 eV plasma compared to the linear rampdowns seen in hard disruptions on other devices (Section II.B.1.a). Typical current rampdown rates are $\Delta I_p/\Delta t$ ~ 10-20 kA/ms.

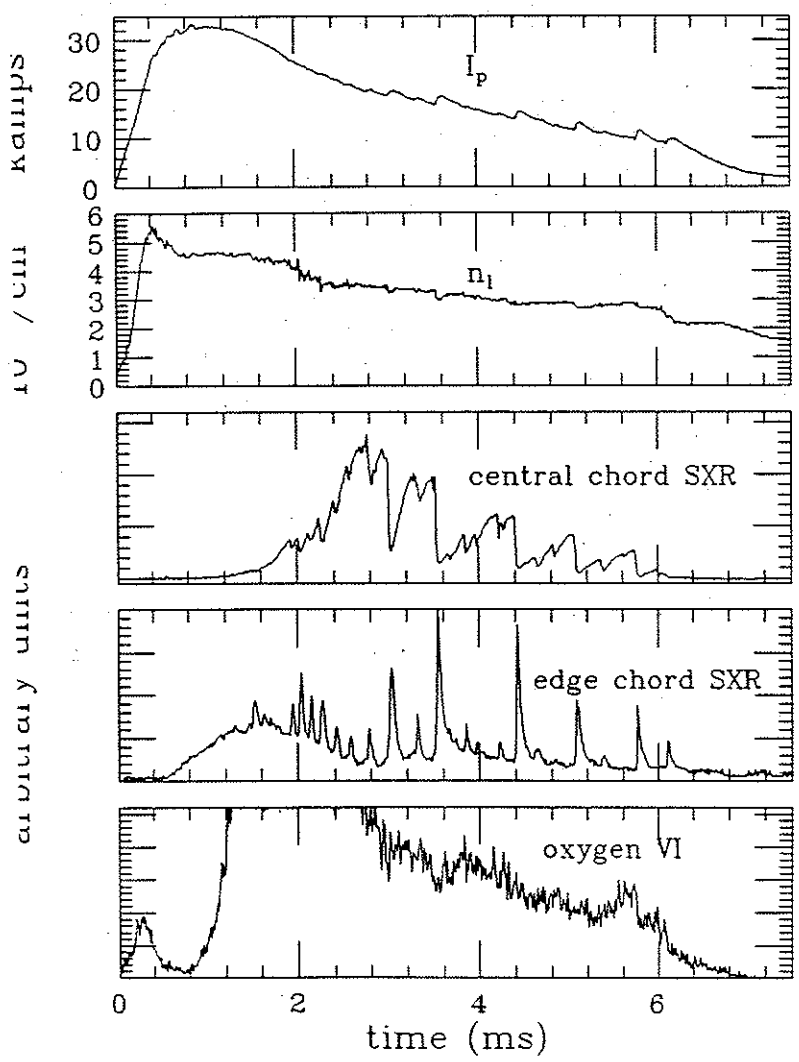

Figure 5.20a: Plasma current I_p, line average density n_l, central and edge chord SXR, and O VI line emission in a magnetic limiter discharge with $q_a \approx 2.5$.

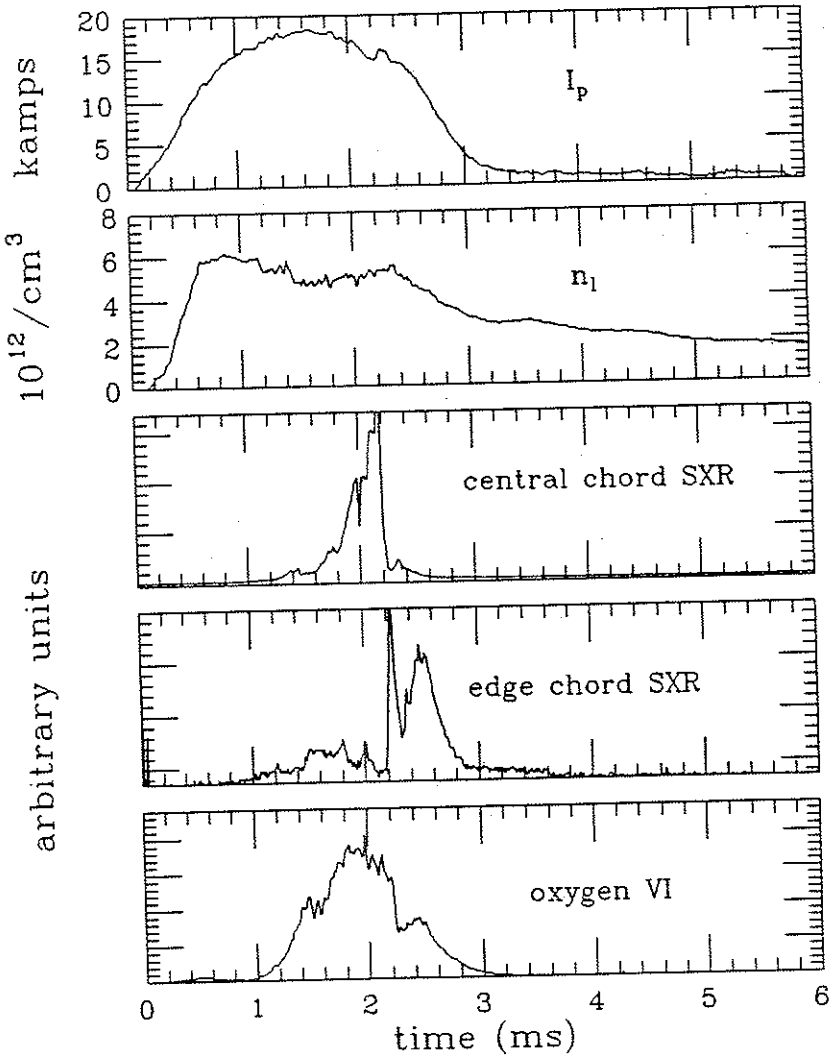

Figure 5.20b: Plasma current I_p, line average density n_l, central and edge chord SXR, and O VI line emission in a material limiter discharge with $q_a \approx 2.5$

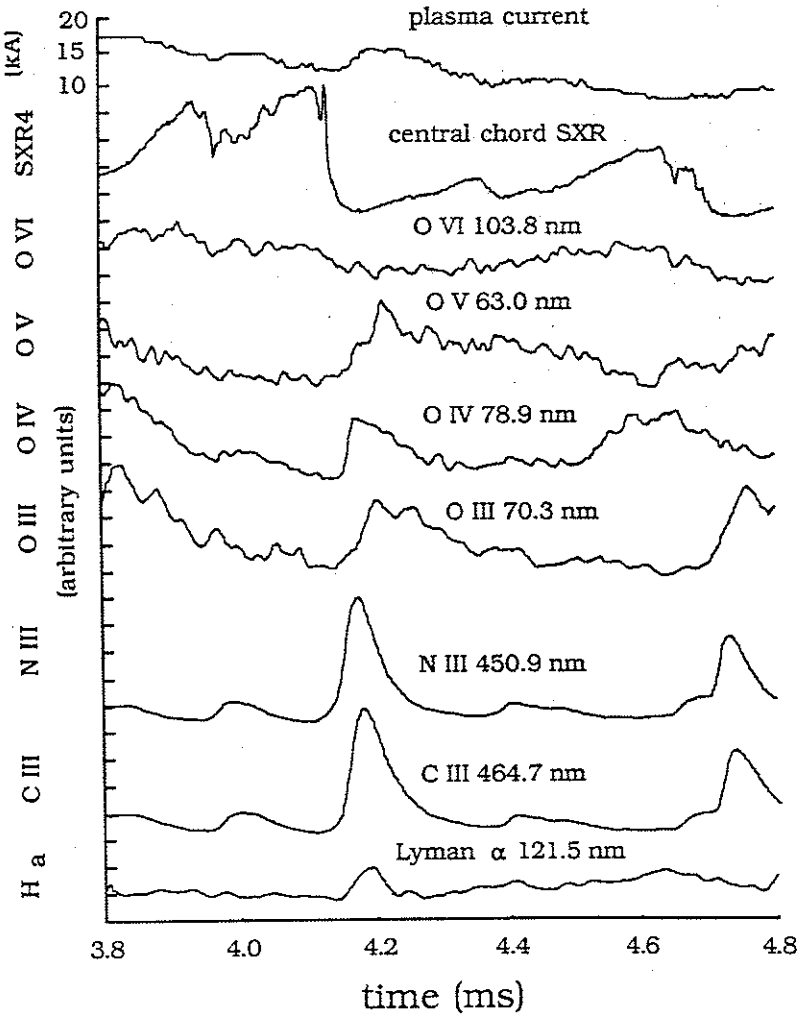

Figure 5.21a: Expanded view of plasma current I_p, central chord SXR, and the light impurity lines O VI, O V, O IV, O III, N III, C III, and H_α about a disruption in a magnetic limiter discharge with $q_a \approx 2.5$.

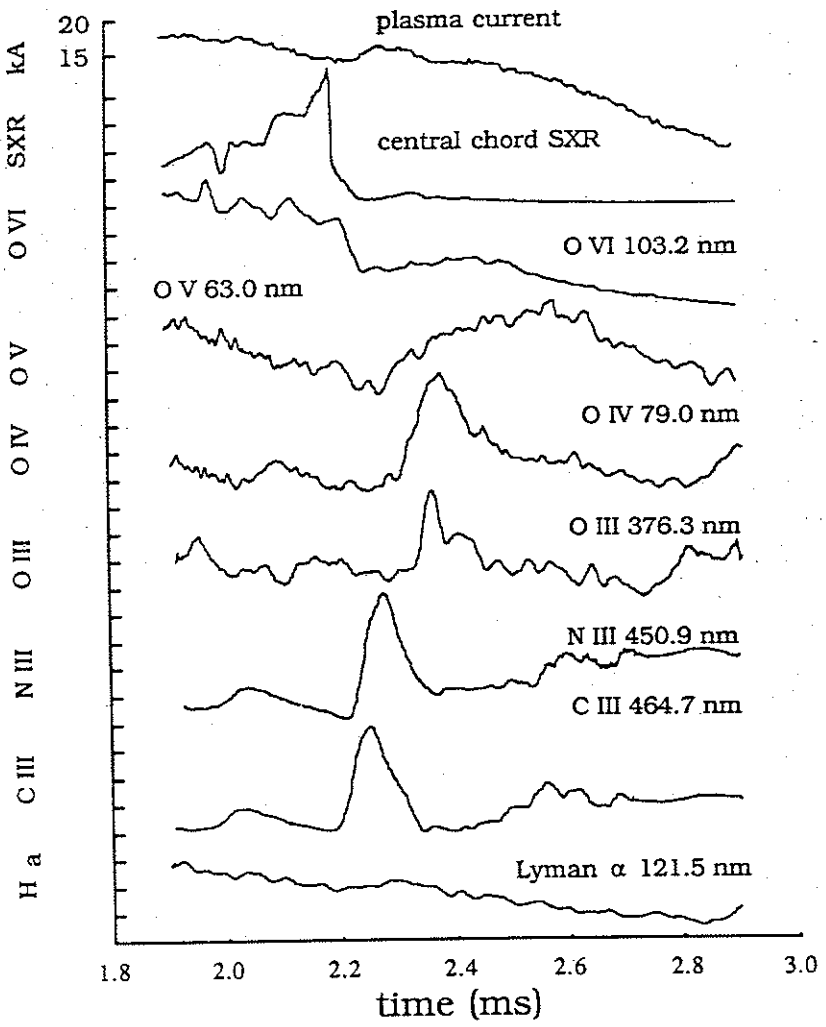

Figure 5.21b: Expanded view of plasma current I_p, central chord SXR, and the light impurity lines O VI, O V, O IV, O III, N III, C III, and H_α about a disruption in a material limiter discharge with $q_a \approx 2.5$.

No difference in light impurity behavior in the plasma periphery is seen prior to the external disruption in the magnetic and material limiter discharges (figure 5.21). Enhancement of metallic impurities (responsible for SXR emission; Section IIIB.4) in the central current channel is indicated by comparison of central chord SXR levels for consecutive discharges with constant n_l^{core} (figure 5.22). Assuming similar $T_e(0)$, equation 3.33 suggests an enhancement in impurity concentration greater than 30% since the increased impurity level should lower $T_e(0)$ as well.

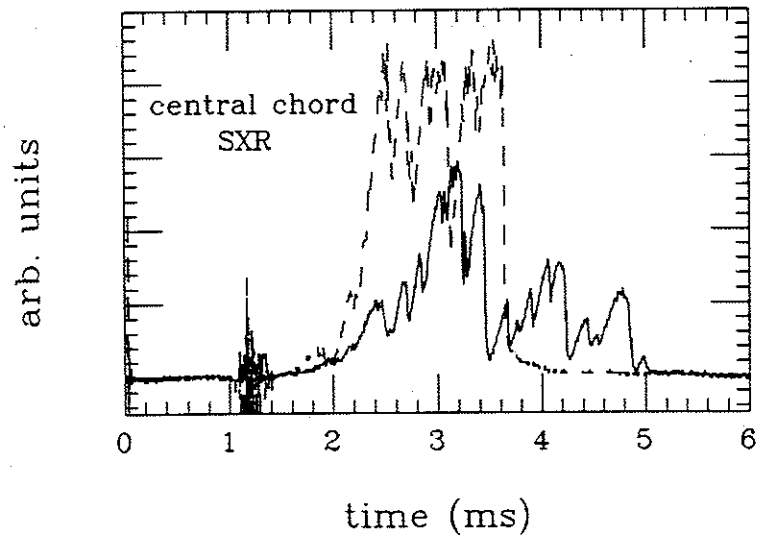

Figure 5.22: Comparison of central chord SXR signal in consecutive magnetic (solid) and material (dashed) limiter discharges with $q_a \approx 2.5$.

Impurity accumulation has been seen on other tokamak devices.[3,15] Accumulation of impurities in the center of the

discharge raises the resistivity near the axis, lowers the current density, and generates a hollow current profile that enhances the current gradient at the q = 2 surface in the outer regions of the discharge. This effect is important, in the absence of internal disruptions, for triggering major disruptions in coupled tearing mode/transport simulations (Section II.B.2.c).

Following the disruption in material limiter discharges, the light impurity levels increase (figure 5.21) during the 250-300 μs delay before current quench. Since this impurity increase is not seen following the giant sawteeth in the magnetic limiter discharges, it likely results from an enhanced plasma/limiter interaction associated with the minor radius expansion. Heavy gettering of the limiter plates and/or increased gas puff during the discharge increases the likelihood of surviving the disruption. Gettering is expected to reduce the impurity influx by "burying" the impurities under a relatively clean titanium surface (limiter surfaces gettered for 1-2 hours at .15g/hr sublimation rates). Additional gas puffing during the discharge cools the edge plasma, reducing the sputtering of material from the limiter and peaking the profile to one more favorable for (2,1) mode stability.

Enhanced plasma/limiter interaction following disruption is confirmed by monitoring the Chromium I (Cr I) line emission with a photomultiplier tube and filter positioned to view the tip of the inboard limiter plate (figure 5.23). The Cr I emission increases abruptly at disruption for the chord viewing the inboard limiter.

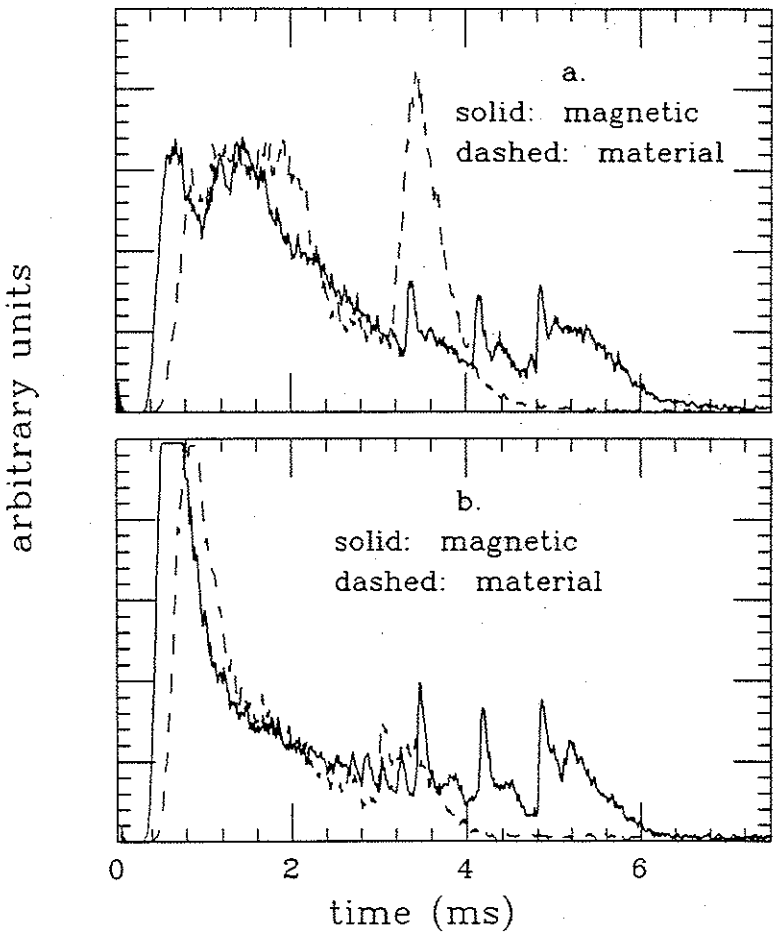

Figure 5.23: Comparison of Cr I emission along identical chords in magnetic (solid) and material (dashed) limiter discharges with $q_a \approx 2.5$. (a) Central chord viewing the inboard limiter tip during the material limiter discharge. (b) Central chord away from the limiters in the material limiter discharge.

Comparison with a central chord away from the limiters verifies

that the enhanced Cr I emission is localized to the vicinity of the inboard limiter, indicating vaporization of significant amounts of limiter material.

Further correlation of the current quench with the strength of the interaction with the inboard limiter was obtained by fixing the outboard limiter plate at the divertor separatrix while retracting the inboard limiter in 0.5 cm steps from the separatrix to the vacuum vessel wall. Between 1 and 2 cm outside the separatrix, the probability of recovery increased dramatically, with more soft disruptions occurring (figure 5.24). In figure 5.24a, the first disruption occurs at 2.24 ms, with the central chord SXR signal dropping ~ 30% in 75 μs. This soft disruption has no effect on the plasma current, and no increase in Cr I emission is seen. The discharge terminates following the second disruption at 2.60 ms, with nearly a 40-fold increase in Cr I. In figure 5.24b, the material limiter discharge is terminated in a "stair-step" manner, with two disruptions occurring at 2.3 ms and 3.3 ms. In the first disruption, 32% of the plasma current is lost, correlated with a 9-fold increase in Cr I. The discharge terminates with the loss of the remaining current correlated with an 18-fold increase in Cr I.

With the inboard limiter retracted 2-3 cm from the divertor separatrix, discharges behave identically to magnetic limiter discharges. Despite the presence of the outboard limiter plate at the separatrix, the discharges survive all external disruptions without any loss in plasma current until the current decays away

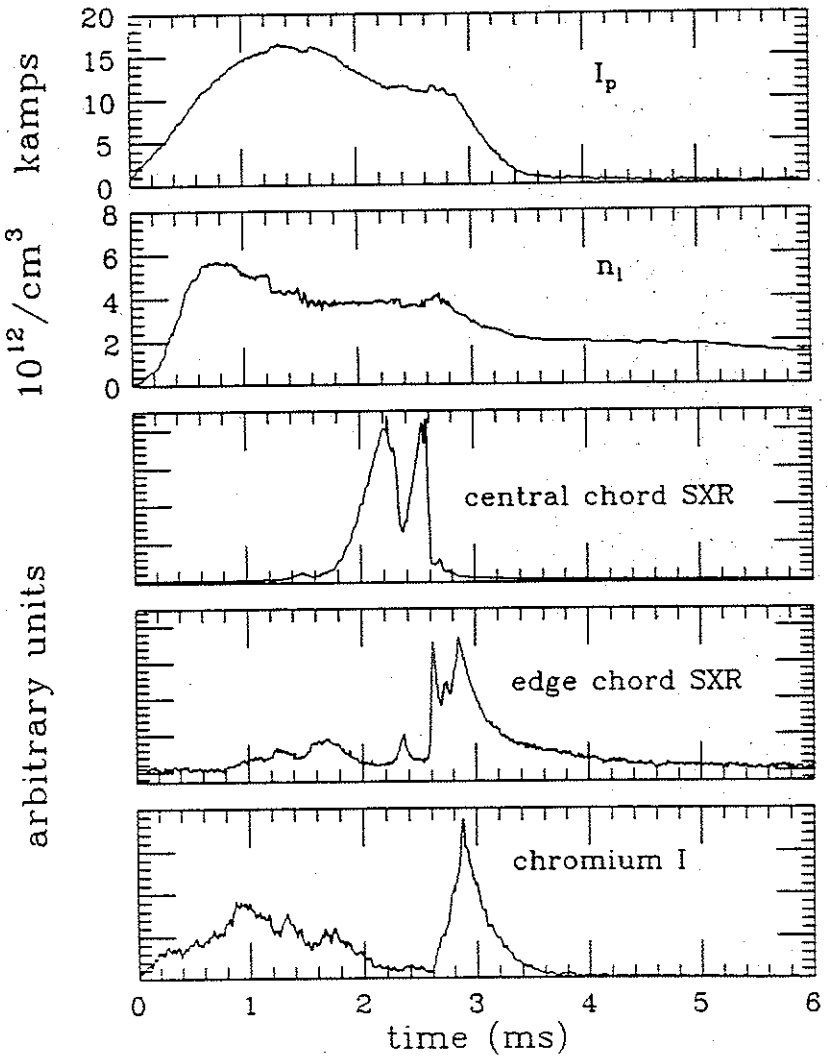

Figure 5.24a: Material limiter $q_a \approx 2.5$ discharges with the limiter plates retracted ~ 1.5 cm beyond the separatrix, displaying a soft minor disruption prior to the major disruption.

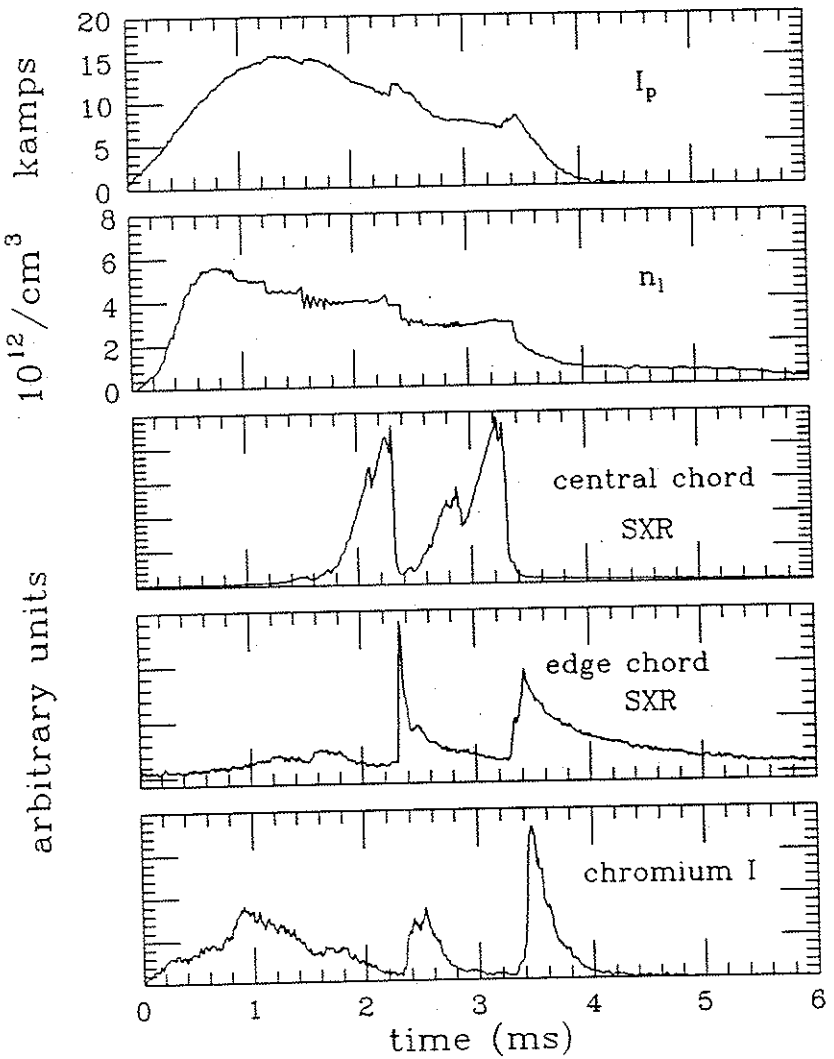

Figure 5.24b: Material limiter $q_a \approx 2.5$ discharges with the limiter plates retracted ~ 1.5 cm beyond the separatrix, displaying a hard minor disruption prior to the major disruption.

Inserting the outboard limiter inside the separatrix did not alter this behavior, although it did degrade the discharges somewhat and pushed the magnetic axis inward. Due to port availability, it was not possible to view the outboard limiter tip with the Cr I monitor without also viewing the inboard plate.

The importance of the inboard plate agrees with observations on PDX,[16] and can be understood in terms of standard major disruption behavior. The expulsion of poloidal flux from the plasma accompanying the rapid minor radius expansion and drop in plasma inductance results in an equilibrium position for the post-disruption profile at a smaller major radius than for the pre-disruption profile. On a fast (Alfvén) time scale, the discharge shifts inward in major radius unless, as in most tokamaks, an actively coupled vertical field maintains the equilibrium position. While no vertical field is used during normal operation in Tokapole II, a passive vertical field is provided by the divertor ring field. The large negative decay index of this vertical field is very effective in limiting shifts in major radius.[10] The four-fold divertor geometry additionally stabilizes the discharge against vertical instabilities that arise when the decay index along the midplane is too negative.

Shifts in major radius of the plasma current profile have been inferred from changes in the SXR emissivity profile following the giant sawtooth collapse in magnetic limiter discharges. Direct magnetic measurements in a non-perturbing manner in Tokapole II are difficult due to the large separatrix-to-wall distance and

presence of plasma and current in the scrape-off region. As discussed in Section III.B.4, the SXR emissivity and electron temperature are closely coupled. For well confined discharges, one expects the electron temperature and plasma current to be closely coupled as well.

SXR emissivity profiles obtained for magnetic and material limiter discharges are shown in 200 μs steps in figure 5.25. The profiles were taken shot-by-shot with a swiveling SXR detector viewing chords passing through the midplane. Discharges were selected with shot-to-shot variations in SXR emissivity, as determined by a fixed central chord SXR detector, of less than 20%. Variations within this range were normalized out using the low frequency portion of the central chord signal.

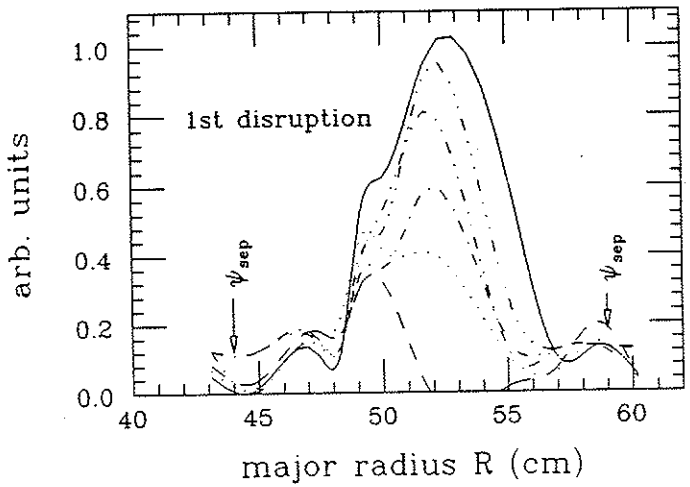

Figure 5.25a: Evolution of SXR emissivity profile in 0.2 ms steps beginning 100 μs before the first disruption in a magnetic limiter discharge.

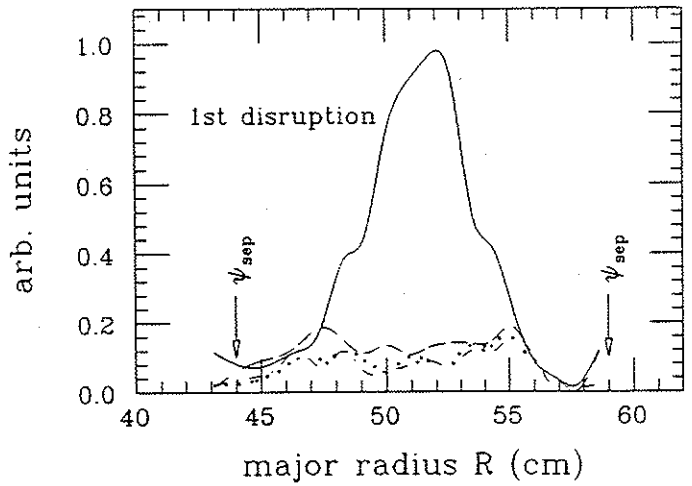

Figure 5.25b: Evolution of SXR emissivity profile in 0.2 ms steps beginning 100 μs before the first disruption in a material limiter discharge.

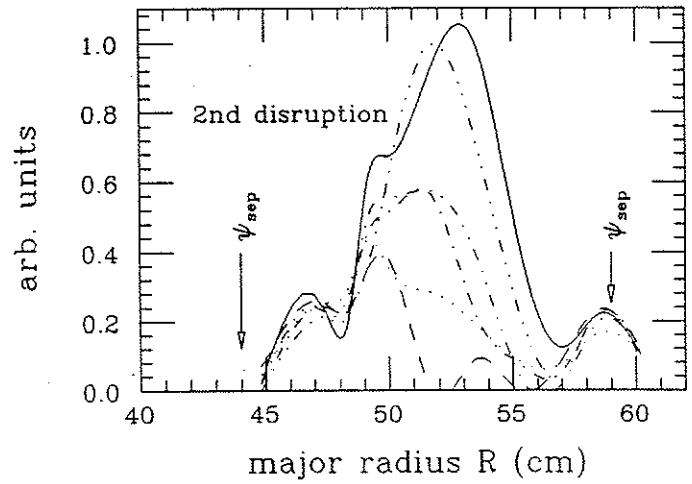

Figure 5.25c: Evolution of SXR emissivity profile in 0.2 ms steps beginning 100 μs before the second disruption in the magnetic limiter discharge.

The profiles in figure 5.25 indicate that the discharge shifts

inward 1-3 cm in magnetic limiter discharges. During the reheat following the giant sawtooth, the profile peaks and shifts outward to nearly the same major radius as before the disruption. Due to the loss of nearly all the SXR signal in the material limiter discharges (figure 5.25b), profile motion must be inferred from the magnetic limiter measurements. While the magnitude of major radius shift is small, it is sufficient to preferentially enhance the plasma/limiter interaction at the inboard limiter due to the limited minor radius expansion seen in figure 5.12. The observed shift agrees with the empirical observation that withdrawal of the inboard limiter plate 2-3 cm is sufficient to suppress termination. The shift is also consistent with the profile evolutions presented in Section V.B.1.c (shifts much larger than this would be dramatically evident on the "Δ" profiles), and is consistent with the shift expected due to the negative decay index of the divertor ring vertical field.[10]

V.B. Comparison with Resistive MHD Code Computations:

Studies of disruptive instabilities in Tokapole II have been hampered by the inability of available resistive MHD codes (e.g. HIB[17,18]) to adequately model the magnetic limiter configuration. E. Uchimoto has developed the three-dimensional resistive MHD initial value code "RPD"[1,2] that is capable of handling the divertor separatrix and the plasma current in the scrape-off region outside the separatrix. Dr. Uchimoto's research results[19] are extensively excerpted here for the convenience of the reader.

The code numerically advances the nonlinear 3-D compressible full resistive MHD equations. The RPD code Fourier analyzes dependent variables in the toroidal direction and uses a finite difference representation in the two Cartesian directions of a constant toroidal angle plane to allow it to evolve the separatrix and scrape-off region. A complete code description, and the results of extensive convergence tests and benchmarking in divertor and non-divertor configurations, is available in reference 19.

Detailed simulation of the Tokapole II experiments would require accurate central current channel profile information, which is not available. Thus, the RPD code was applied to the experiments by constructing pairs of equilibria with and without current outside the separatrix to simulate the magnetic and material limiter configurations. The current profile was taken smoothly to zero near the separatrix in material limiter simulations consistent with the effect of the limiters in these discharges. The pairs of equilibria differ from the experiment in two respects: the code uses an inverse aspect ratio $R_0/r_{wall} = 5$ compared with the experimental value of 2.27, and the code removes only current outside the separatrix, compared with the limiters that remove plasma and current. Using these pairs of equilibria, the position of the $q = 2$ surface was varied with respect to the separatrix to simulate varying q_a in the experiments.

Due to constraints on available CPU time, complete scans of the (2,1) resistive tearing and (1,1) resistive internal kink mode

behavior versus position of the mode rational surface were carried out only for the linear calculations. Nonlinear calculations with either the (2,1) or (1,1) mode dominant are continuing but will not be available for this thesis. Additional work is focusing on the variation of the saturated (2,1) island width with the radius of the q = 2 surface in each configuration and the role of stochastic effects near the separatrix.

The code provides qualitative agreement with the experimental results over the operational range of $0.4 < q_a < 4$. Results from simulation of the (2,1) resistive tearing mode are presented in this section. Results from (1,1) resistive internal kink simulations will be presented in Chapter Six.

V.B.1. Linear Results:

A matched pair of equilibria used in the linear RPD code runs for the (2,1) resistive tearing mode is shown in figure 5.26. The location of the q = 2 surface was varied by lowering q(0) and raising q_a for a sequence of similar equilibria. The variation of the linear growth rate $\gamma_{2,1}$ versus q(0) in the magnetic and material limiter discharges (figure 5.27) displays three key features: 1) the magnetic limiter configuration is generally more stable (lower $\gamma_{2,1}$) than the material limiter configuration at any given q(0) (equivalently, radius of the q = 2 surface), 2) the proximity of the q = 2 surface to the divertor separatrix stabilizes the (2,1) tearing mode in each configuration, and 3) the stabilization of the (2,1)

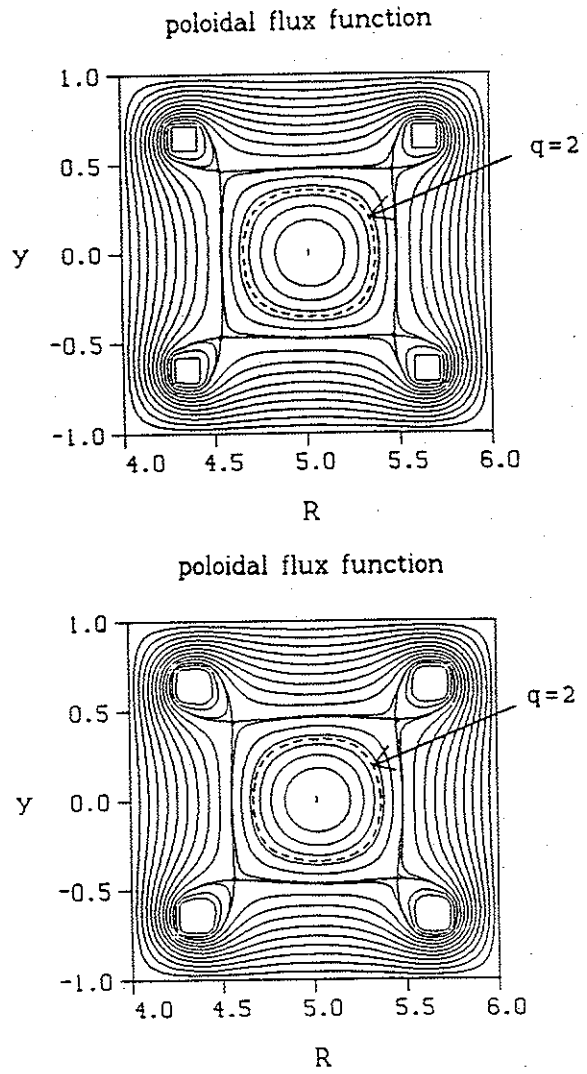

Figure 5.26a: Contours of the equilibrium poloidal flux function ψ with the position of the q = 2 surface indicated for a pair of matched $2 < q_a < 3$ equilibria in (top) magnetic and (bottom) material limiter discharges.

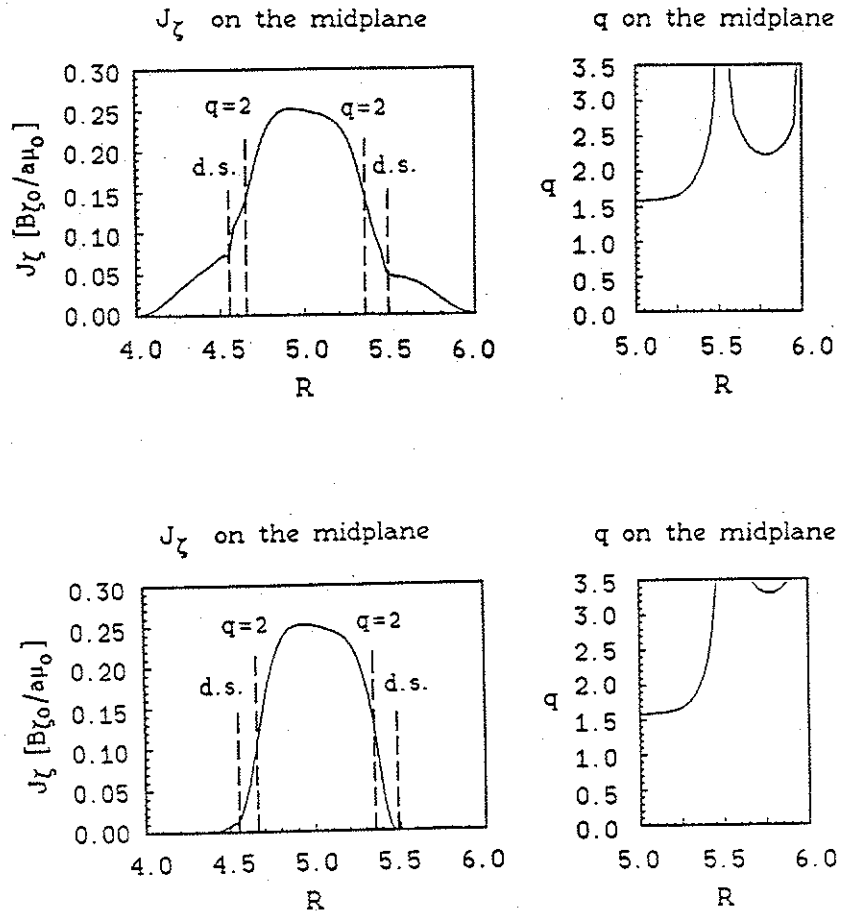

Figure 5.26b: Toroidal current density profile J_ζ and the safety factor profile q(R) in a pair of matched $2 < q_a < 3$ equilibria for (top) magnetic and (bottom) material limiter discharges.

mode from proximity of the q = 2 surface to the separatrix requires lower q(0) and q_a in the material limiter configuration.

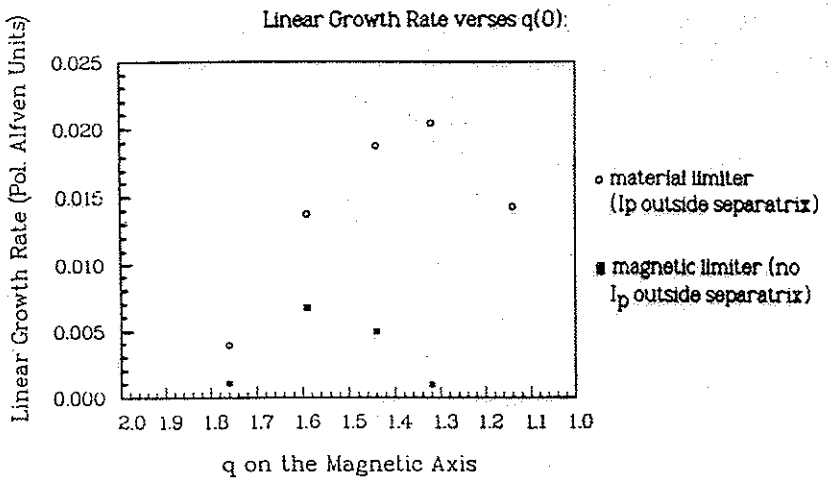

Figure 5.27: Variation of the linear growth rate $\gamma_{2,1}$ of the (2,1) tearing mode, normalized to the poloidal Alfvén time τ_{Hp}, verses q(0), the safety factor on axis. Lowering q(0) lowers q_a and moves the q = 2 surface closer to the separatrix (to the right in the plot).

All three of these effects are seen in the experiment. $\gamma_{2,1} = 4.8 \pm .6 \times 10^4\ s^{-1}$ before disruption in material limiter discharges, roughly twice $\gamma_{2,1}$ before disruption in magnetic limiter discharges ($2.1 \times 10^4\ s^{-1}$) (Section V.B.1.c). In each configuration, lowering q(0) and q_a, thereby moving the q = 2 rational surface closer to the separatrix (by increasing the plasma current at constant B_t) stabilizes the external disruptions associated with the giant

sawteeth. Stabilization of the (2,1) mode requires much lower q(0) and q_a in the material limiter discharges than in the magnetic limiter discharges.

It is not possible to use identical current profiles inside the separatrix in the pairs of magnetic and material equilibria and maintain equilibrium. Consequently, it is of considerable interest to determine whether the lower liner growth rate of the (2,1) tearing mode in the magnetic limiter code runs arises as a result of profile effects near the q = 2 surface or from an interaction of the tearing mode with the separatrix or the plasma current outside the separatrix.

Since Δ' in the tearing mode stability condition ($\Delta' = 0$; Section II.B.2.d) is determined entirely by the equilibrium current density profile in the ideal MHD region outside the tearing layer,[13,20,21] removing current outside the separatrix alters the Δ' stability criterion both by changing the current density gradient at the q = 2 surface and by altering of the wings of the current profile in the divertor scrape-off region.

To determine if the change in the (2,1) tearing mode stability arises from alteration of the current gradient at the q = 2 rational surface or from the presence or absence of current in the divertor scrape-off region, an equilibrium was generated that matched the magnetic limiter profile exactly inside the divertor separatrix and was "chopped" to zero at the separatrix instead of varying smoothly to zero over a small but finite radius as in the material limiter

equilibria. Calculations indicate that the lower linear growth rate of the (2,1) tearing mode in magnetic limiter discharges versus material limiter discharges results from alteration of the plasma current profile near the mode rational surface. The improved stability seen in each configuration as the q = 2 surface approaches the separatrix may also arise from the increasing noncircularity near the separatrix. Any effect from the presence of current outside the separatrix, initially believed to be stabilizing to the tearing modes, is small and possibly destabilizing, although this latter result is only preliminary.[22]

V.B.2. Nonlinear Results:

Due to restrictions on CPU time, it has not been possible to investigate the nonlinear evolution of the (2,1) tearing mode in the magnetic and material limiter configurations extensively. In particular, simulations of the giant sawteeth with q(0) < 1.5 and both (3,2) and (2,1) perturbations initialized have not been performed. This case involves potentially interesting saturation and stochastic effects that might arise near the divertor separatrix.[23]

The (2,1) tearing mode saturates for an equilibrium with the q = 2 surface far from the divertor separatrix. The saturated magnetic island structure is shown in figure 5.28. The island structure is determined by using RPD magnetic field calculations as input to the TUBE[24] field line tracing code. Such a saturated (2,1) mode is seen in the material limiter configuration for $2 < q_a < 3$

discharges. The large extent of the saturated island, over 30% of the plasma minor radius, makes eventual overlap with the (3,2) magnetic island seem reasonable. The large extent of the saturated island is also consistent with the detection of the (2,1) mode activity on the Mirnov coils outside the separatrix.

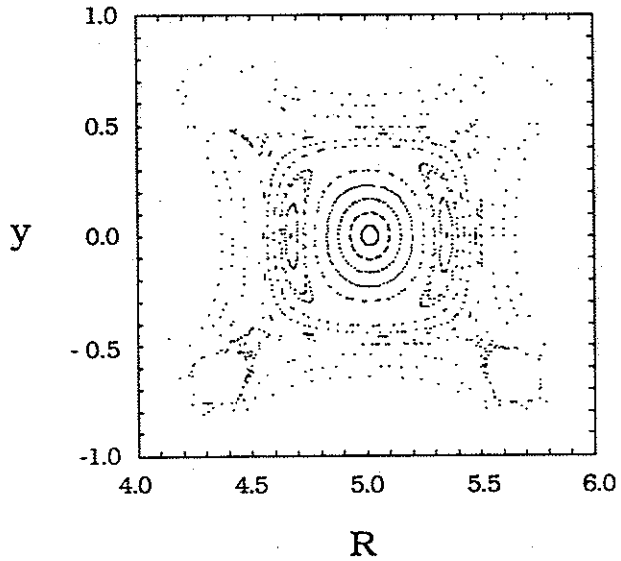

Figure 5.28: The saturated magnetic island structure obtained in nonlinear RPD computations of the (2,1) tearing mode with the q = 2 surface far from the separatrix.

For an equilibrium with the q = 2 surface close to the divertor separatrix, the (2,1) tearing mode reaches the separatrix and a stochastic field region develops from just inside the q = 2 surface to just outside the divertor separatrix prior to saturation. The stochastic field structure is shown in figure 5.29. Studies to determine whether the divertor separatrix affects the growth of the

stochastic field region are continuing.

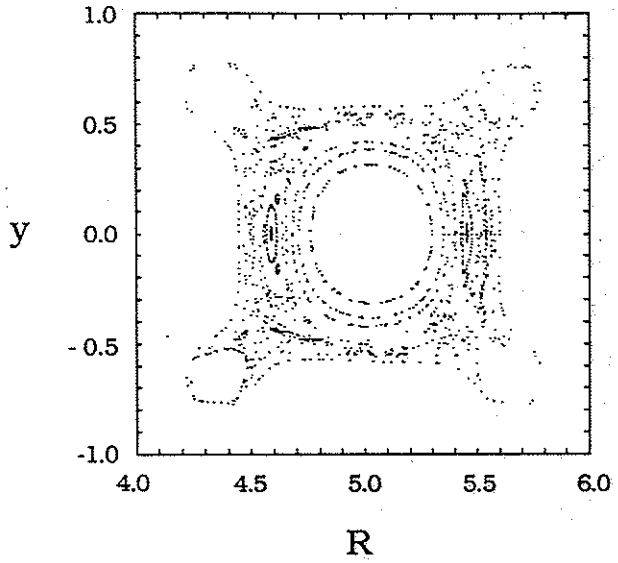

Figure 5.29: Magnetic field structure obtained in a nonlinear RPD code run showing the development of stochasticity prior to nonlinear saturation in an equilibrium with the q = 2 surface near the separatrix.

If the large stochastic field region shown in figure 5.29 enhances radial transport, the self-consistent profile modifications will leave the q = 2 rational surface in a region of cold plasma and high resistivity. This region might be sufficiently high resistivity and "vacuum-like" to allow the (2,1) island to slip with respect to the core plasma rotation and lock (Section II.B.2.e).[25] The loss of the stabilizing effect of rotation might then trigger a major disruption. This may be a plausible explanation for the mechanism the appears to lock the (2,1) mode in the material limiter discharges.

V.C. Summary and Conclusions:

External disruptions appear in magnetic limiter discharges as small sawteeth with $\tau \approx 200$ μs and as giant sawteeth with $\tau \approx .6$-1 ms. A (2,1) magnetic precursor with a frequency of 40-50 kHz and growth rate $\gamma_{2,1} \approx 2 \times 10^4$ s^{-1} has been identified for both sawteeth. The (2,1) mode is coupled to an odd m/even n mode, consistent with a (3,2) mode rotating rigidly toroidally with the (2,1) mode, during the last 150 μs before the giant sawteeth. SXR measurements suggest the presence of such an odd $m > 1$ mode in the plasma interior, but insufficient chords are available to determine the mode structure. The various characteristics of the two classes of external disruptions are listed in Table 5.1 for both the magnetic and material limiter configurations.

The SXR collapses in both small and giant sawteeth are nearly toroidally symmetric. The giant sawteeth often propagate across the minor cross section inward from the $q = 2$ surface near the plasma edge. Scrape-off density, temperature, and pressure profiles indicate that during the transport phase of the disruption the plasma expands into the scrape-off region in an axisymmetric fashion.

While the nature of the small sawteeth is not entirely understood, the giant sawteeth are major disruptions likely resulting from an interaction of the (2,1) and (3,2) tearing modes. Small sawteeth at $q_a > 3$ may fit the (2,1) mode simulations with low shear/high q(0) of Kleva, et al.[4] Measured scrape-off density

Table 5.1

MHD Characteristics of External Disruptions in Tokapole II

	Small Sawteeth:	
characteristic:	material limiters	magnetic limiters
amplitude:	5-20% of central SXR	5-20% of central SXR largest at $q = 2$ surface
period	200 μs	200-250 μs
inversion radius:	inside $q = 2$ ($q = 1$?)	$q = 2$
mode structure:		
SXR:	none	even m: 20 kHz odd $m > 1$: 50 kHz odd m: 140-175 kHz
Mirnov:	saturated (2,1) mode: 15-20 kHz	(2,1) mode: 25-30 kHz 40-50 kHz
	Giant Sawteeth:	
characteristic:	material limiters	magnetic limiters
amplitude:	80-100% of central SXR	80-100% of central SXR
period	400-800 μs	600-1000 μs
inversion radius:	at/inside $q = 2$	at/inside $q = 2$
mode structure:		
SXR:	odd $m > 1$: 25-30 kHz	odd $m > 1$: 25-30 kHz
Mirnov:	saturated (2,1) mode: 15-20 kHz until 50 μs before collapse	explosively growing (2,1) mode: 30-40 kHz; $\gamma_{2,1} = 2 \times 10^4$ s^{-1}
	explosively growing (2,1) mode: 15-20 kHz; $\gamma_{2,1} = 4 \times 10^4$ s^{-1}	distortion consistent with (3,2) mode just before collapse
	distortion consistent (3,2) mode	

profiles and n_l^{core} clearly demonstrate a rapid minor radius expansion that generates a hollow density profile in the central current channel. It is also possible that the current profiles following major disruption have $q(0) \geq 1.5$ (the inferred $1.1 \leq q(0) \leq 1.3$ corresponds to the current profile just before major disruption) and sufficiently low shear that this model may explain the small sawteeth during the reheat between giant sawteeth as well. However, the localization of the sawtooth collapse in the region near the $q = 2$ surface is more suggestive of partial disruptions localized to the region between the $q = 3/2$ and $q = 2$ surfaces.

The axis $q(0)$ inferred from equilibrium code fits to discharge parameters just before the first giant sawtooth is near, but above 1. This suggests that the major disruptions may be triggered by restriction of the current density near the axis by $m = 1$ instability, or by the presence of a magnetic island in the center that overlaps the (2,1) island in the periphery. The (3,2) island may be responsible (consistent with SXR measurements of an odd m > 1 precursor), or the (1,1) mode may appear briefly just before the disruption. Scrape-off density profiles, light impurity VUV measurements, and the evolution of global plasma parameters (I_p, n_l, T_e^{cond}) suggest that the disruption causes a minor radius expansion, and not complete loss of confinement in the central current channel.

These conclusions are generally confirmed by comparison with material limiter configuration data. The profiles are steepened in

the vicinity of the $q = 2$ surface by the presence of the limiters at the separatrix and in some discharges by impurity accumulation in the plasma core. The increased $\gamma_{2,1} = 4.8 \pm .6 \times 10^4\ s^{-1}$ is consistent with a steepened current density gradient. Major disruptions in the material limiter configuration also show coupling to an odd m/even n mode just before the disruption.

The trigger to the major disruption in the material limiter configuration appears to be mode locking of the (2,1) island following nearly 0.5 ms of saturation. RPD code simulations demonstrate the formation of a large stochastic field region between the $q = 2$ surface and the divertor separatrix that could lead to loss of confinement in this region, allowing the (2,1) island to lock in the resulting high resistivity plasma. The (2,1) mode persists for 200-300 μs after the disruption, consistent with a radiative collapse rather than complete destruction of confinement.

Clearly, the magnetic limiter configuration suppresses abrupt current termination in the $2 < q_a < 3$ discharges. Even in the material limiter configuration, current termination results from a radiative collapse due to enhanced impurity levels following interaction with the inboard limiter plate, and not from complete loss of confinement in the central current channel. The persistence of the (2,1) island after the disruption, and the 200-300 μs delay between the thermal and magnetic quenches confirm this interpretation. The current rampdown is exponential—not linear, and $\Delta I_p/\Delta t \approx$ 20-25 kA/ms. Including the 200-300 μs delay, this gives

a magnetic quench time τ_{mq} of 0.7-0.8 ms, compared to an expected 0.1-0.2 ms in a device of Tokapole II size (figure 2.9).[26] Even if the delay is excluded, τ_{mq} is still 0.4-0.5 ms. It is tempting to conclude that hard disruption is suppressed even in the material limiter configuration. Since the limiters remove plasma and current outside the separatrix, the divertor separatrix itself would be responsible for any such effect.

Access to major disruption-free operating regimes at $q_a < 2$ in magnetic limiter discharges and $q_a < 1.5$ in material limiter discharges is routine and requires no special techniques to control the (2,1) tearing mode. This behavior is well understood in terms of proximity of the q = 2 surface to the divertor separatrix. The origin of the (2,1) stabilization as the q = 2 surface approaches the separatrix is the decreased current density gradient at the q = 2 surface. Additional stabilization appears to arise from noncircularity of the flux surfaces near the divertor separatrix.[22] It is known from an independent numerical study of the effects of toroidicity and noncircularity on tearing mode stability[27] that these effects can stabilize the (2,1) mode in discharges with broad current profiles, while in discharges with peaked profiles, these effects are less pronounced. These results are in agreement with the Tokapole II experiment and RPD code simulations.

REFERENCES

[1]E. Uchimoto, J.D. Callen, and L. Garcia, Bulletin of the American Physical Society, 30, 1421 (1985).

[2]E. Uchimoto and J.D. Callen, Sherwood Theory Meeting, paper 1D18 (1987).

[3]S. Tsuji, et al., Nuclear Fusion, 25, 305 (1985).

[4]R.G. Kleva, J.F. Drake, and D.A. Boyd, Physics of Fluids, 29, 475 (1986).

[5]K. McGuire and D.C. Robinson, Nuclear Fusion, 19, 505 (1979).

[6]T.H. Osborne, Ph.D. Thesis, University of Wisconsin (1984).

[7]M.W. Phillips, University of Wisconsin—PLP 765 (1978).

[8]G.L. Jahns, et al., Nuclear Fusion, 18, 609 (1978).

[9]Equipe TFR, Plasma Physics and Controlled Fusion Research, (Proc. 6th Conf., Berchtesgaden, 1976), 1, (IAEA, Vienna, 1977), 279.

[10]M. Okabayashi, et al., Nuclear Fusion, 21, 271 (1981).

[11]D. Graessle, et al., submitted to Physical Review Letters.

[12]H.P. Furth, P.H. Rutherford, and H. Selberg, Physics of Fluids, 16, 1054 (1973).

[13]P.H. Rutherford, Physics of Plasmas Close to Thermonuclear Conditions, (Proc. of the Course, Varenna, 1979),(Comm. of the European Communities, Brussels, 1980), 1, 129.

[14]R.B. White, Reviews of Modern Physics, 58, 183 (1986).

[15]W. Engelhardt, et al., Plasma Physics and Controlled Nuclear Fusion Research, (Proc. 7th Conf., Innsbruck, 1978), 1, (IAEA, Vienna, 1979), 123.

[16]K. McGuire, et al., Journal of Nuclear Materials, 121, 329 (1984).

[17]W. Park, et al., Proc. of the US-Japan Theory Workshop on 3-D MHD Studies for Toroidal Devices, (Oak Ridge National Laboratory, Oak Ridge, TN, May, 1981).

[18]R. Izzo, et al., Physics of fluids, 26, 2240 (1983).

[19]E. Uchimoto, Ph.D. Thesis, University of Wisconsin (1988).

[20]H.P. Furth, J. Killeen, and M.N. Rosenbluth, Physics of Fluids, 6, 459 (1963).

[21]W.M. Manheimer and C. Lashmore-Davies, MHD Instabilities in Simple Plasma Configuration, Naval Research Laboratory, Washington, D.C., 1984.

[22]E. Uchimoto, private communication, 1987.

[23]D. Skinner, et al., Physics of fluids, 30, 1218 (1987).

[24]N.J. O'Neill and A.A. Mirin, NMFECC LIBRIS Library.

[25]A. Bondeson, "Disruptions in Tokamaks", Theory of Fusion Plasmas, (Proc. of the Course, Varenna, 1987), in press.

[26]K. Yamazaki and G.L. Schmidt, Proc. of the 6th Int. Conf. on Plasma Surface Interactions in controlled Fusion Devices, Nagoya, 1984.

[27]R.C. Grimm, et al., Plasma Physics and Controlled Fusion Research, (Proc. 9th Int. Conf., Baltimore, 1982), 3, (IAEA, Vienna, 1983), 35.

Chapter 6
INTERNAL DISRUPTIONS IN TOKAPOLE II

In order to understand the stability of low q_a discharges, internal disruptions have been studied in the magnetic limiter configuration for several years.[1,2] To ascertain the effect of the magnetic limiter configuration on the stability of these discharges, internal disruptions were studied in the material limiter configuration for this thesis. The principal conclusion of this study is that the partial reconnection of the internal disruption sawteeth required to permit $q_a < 1$ discharges to be obtained is a characteristic of the internal disruptions, and not the result of the magnetic limiter configuration.

Material limiter $q_a < 1$ discharges have been obtained with sawteeth displaying characteristics similar to those in magnetic limiter discharges. Internal magnetic probe measurements confirm that $q(0)$ is 0.5-0.8 for $q_a \approx 0.8$, and remains less than one throughout 10-15 internal disruptions. Toroidal current density profiles of the central current channel have been constructed from the magnetic probe data. The profiles are broad and appear qualitatively similar to those obtained in magnetic limiter discharges. Integration of the current density profile, with reasonable extrapolation to the separatrix, yields a toroidal current within 2-5% of I_p, indicating that the limiter plates are effective in removing toroidal current in the scrape-off region. These data

confirm that partial reconnection is not unique to the magnetic limiter configuration, and does not result from the presence of plasma current in the scrape-off region.

Characteristics of internal disruptions in the external disruption-free regimes of $1 < q_a < 2$ and $q_a < 1$ are presented in this chapter. Characteristics of internal disruptions are presented in Section VI.A.1 for $1 < q_a < 2$ and in Section VI.A.2 for $q_a < 1$. Experimental results are compared with numerical computations of the (1,1) resistive kink mode in Section VI.B. Summary and conclusions are presented in Section VI.C.

VI.A. Characteristics of Internal Disruptions for $0.5 < q_a < 2$:

VI.A.1. $1 < q_a < 2$ Discharges:

Sawteeth are obtained in magnetic limiter discharges that display typical internal disruption characteristics, including (1,1) SXR precursors, inversion of the sawtooth collapse at the q = 1 surface, and an axisymmetric collapse. In material limiter discharges, sawteeth are obtained that are similar to the magnetic limiter sawteeth except for the lack of a clear (1,1) SXR precursor.

VI.A.1.a. SXR Sawteeth:

SXR sawteeth in magnetic limiter $1 < q_a < 2$ discharges have a period of $\tau \approx$ 150-200 μs and a (1,1) SXR precursor of frequency $f \approx$ 45 kHz. The m = 1 structure of the precursor can be seen on the poloidal array of figure 6.1a. The (1,1) structure of the precursor is

shown in figure 6.1b, where three swivel SXR detectors are distributed to follow the pitch of a magnetic field line lying on the q = 1 surface. The last two oscillations of the precursor are in phase on the three detectors, confirming the (1,1) structure.

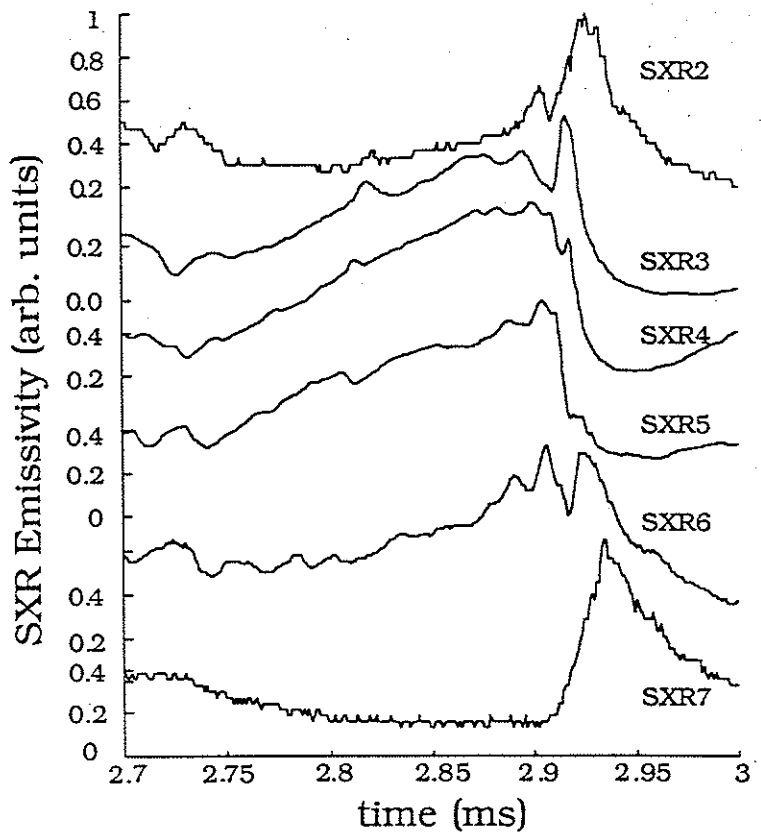

Figure 6.1a: The m=1 precursor structure on the poloidal SXR array in a magnetic limiter $q_a \sim 1.9$ discharge.

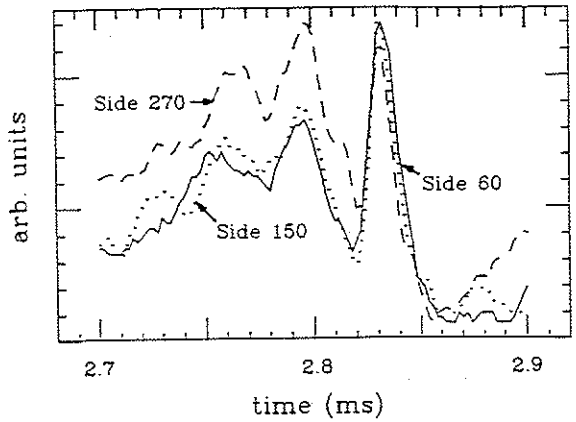

Figure 6.1b: The (1,1) structure of the SXR precursor in a magnetic limiter q_a ~ 1.88 discharge is seen on 3 detectors distributed poloidally and toroidally to follow field lines in the q = 1 surface. The constant amplitude of the precursor confirms the (1,1) structure.

The sawteeth invert at $(x-x_0)$ = -5.5 and +6.2 cm, and $(y-y_0)$ = ±6.2 cm with respect to the magnetic axis at (x_0,y_0) = (+2,0). The inversion radii agree well with the inversion radius of ion saturation current signals[1] and the location of the q = 1 surface in equilibrium code fits.

Sawteeth in material limiter $1 < q_a < 1.5$ discharges generally do not have a dominant SXR precursor (figure 6.2). The period $\tau \approx$ 100-150 μs, somewhat smaller than in the magnetic limiter discharges. The inversion radii at $(x-x_0, y-y_0)$ = (±5, ±5.5) cm are inside the inversion radius in the magnetic limiter discharges. These changes are consistent with peaking of the profiles seen in the

material limiter discharges (Section IV.B). External disruptions in material limiter $q_a > 1.5$ discharges complicate interpretation of the data for this operating regime.

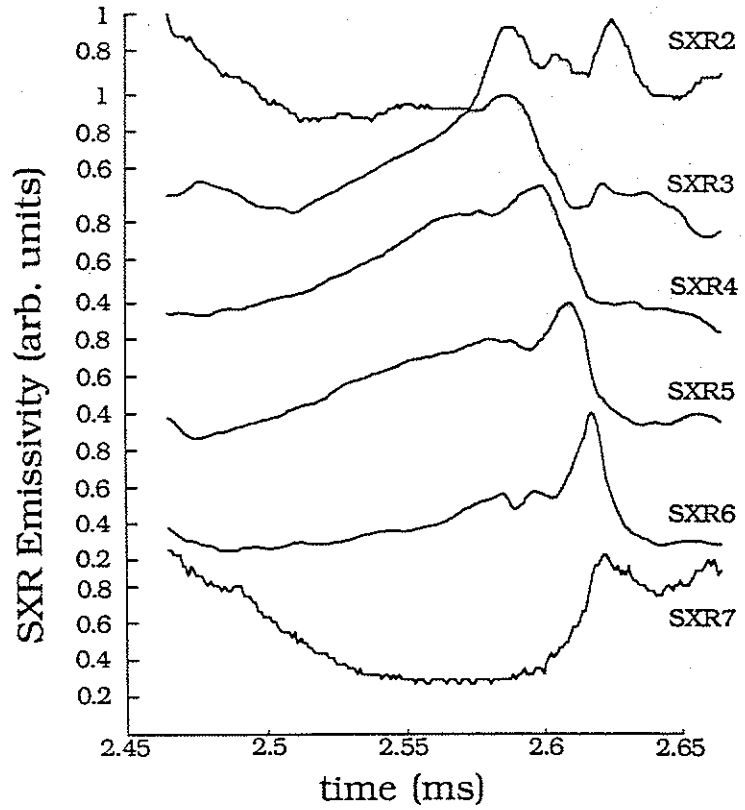

Figure 6.2: A sawtooth on the poloidal array in a material limiter $q_a \approx 1.5$ discharge. No SXR precursor is seen.

VI.A.1.b. Mirnov Signals:

No magnetic precursor is seen on the Mirnov coils for sawteeth in the $1 < q_a < 2$ magnetic and $1 < q_a < 1.5$ material limiter

discharges (figure 6.3). The power spectra lack the signature of a single dominant mode seen at higher q_a. Bursts of MHD activity are correlated with the sawtooth collapse. The broadband magnetic turbulence level has been measured (10 kHz ≤ f ≤ 370 kHz)[3] and rises as q_a decreases to 2.

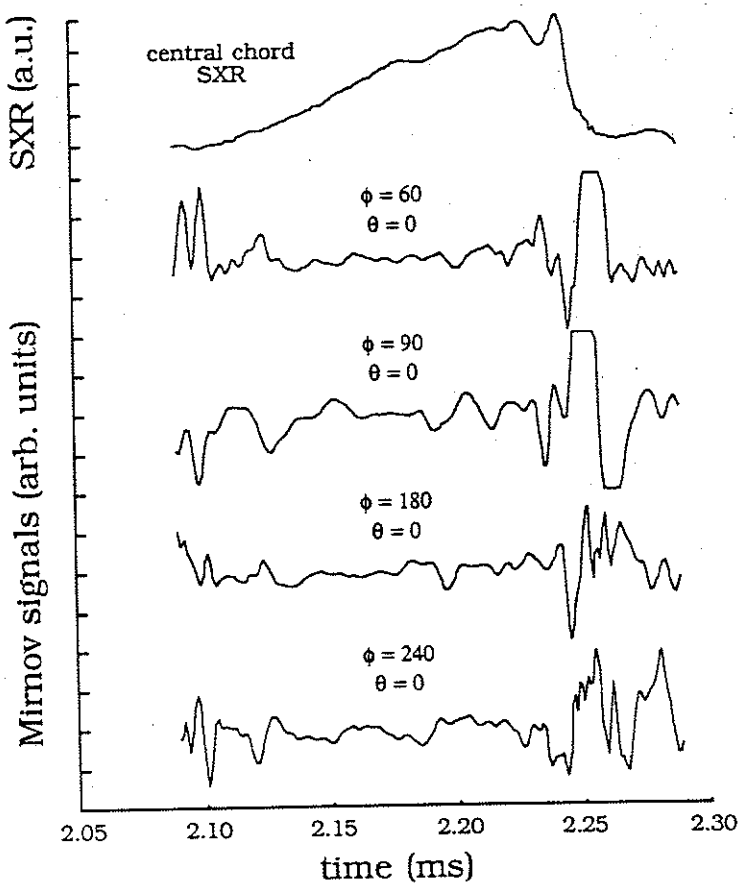

Figure 6.3a: Mirnov signals from poloidally spaced probes during a sawtooth in a $q_a \approx 1.8$ magnetic limiter discharge.

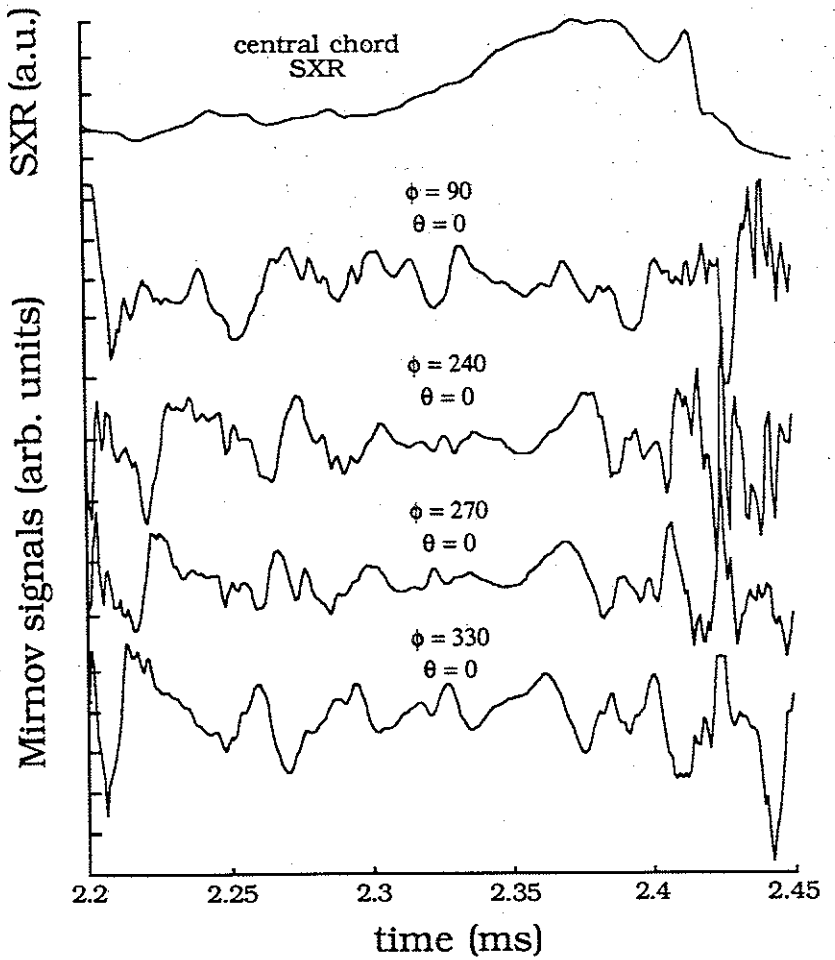

Figure 6.3b: Mirnov signals from poloidally spaced probes during a sawtooth in a $q_a \approx 1.5$ material limiter discharge.

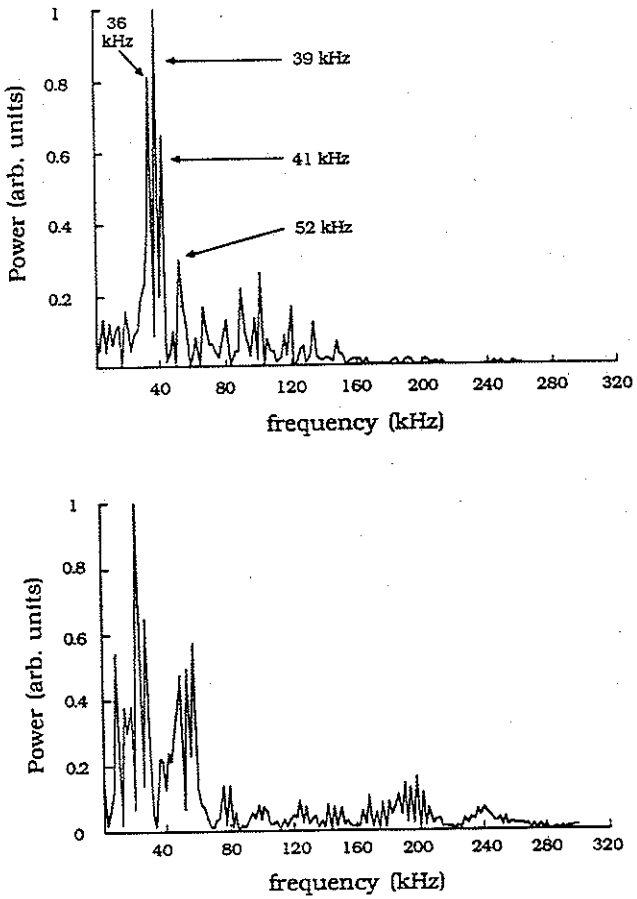

Figure 6.3c: Power spectra for 0.5 ms during sawteeth in (top) magnetic (figure 6.3a: ϕ=240/θ=0) and (bottom) material limiter (figure 6.3b: ϕ=240/θ=0) discharges.

VI.A.2. $q_a < 1$ Discharges:

VI.A.2.a. SXR Sawteeth:

As q_a is lowered below 1 in magnetic limiter discharges, the

SXR sawtooth period shortens to τ ~ 125-150 μs. No SXR precursors are seen (figure 6.4a). At still lower $q_a < 0.4$, the period shortens to 75-100 μs. The sawteeth appear more sinusoidal and are phase locked to highly distorted low frequency magnetic field oscillations on the Mirnov coils (Section VI.A.2.b).

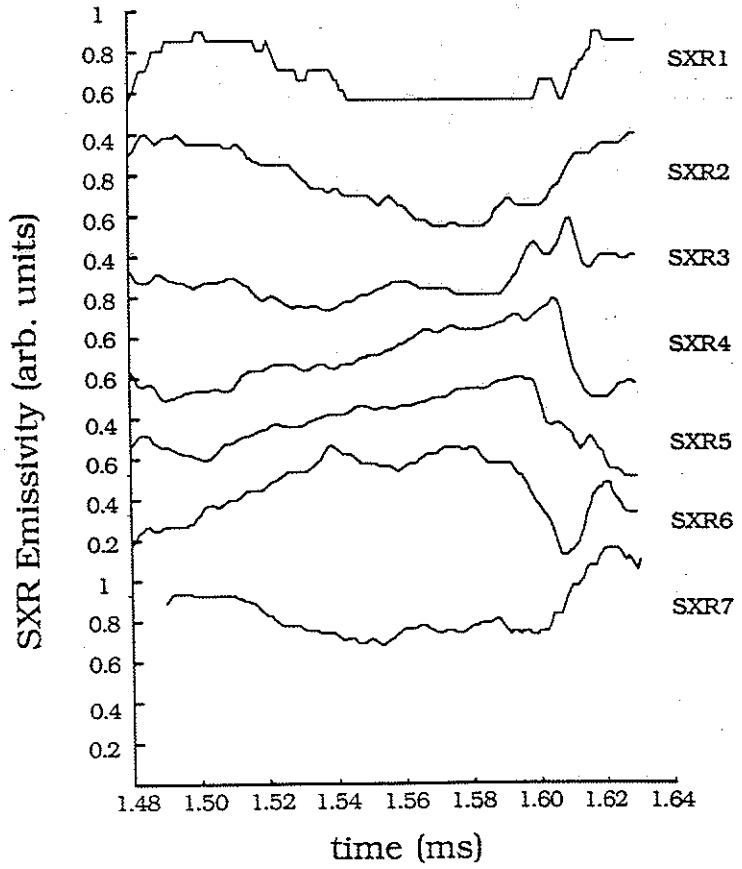

Figure 6.4a: Typical sawtooth on the poloidal array for a magnetic limiter $q_a < 1$ discharge.

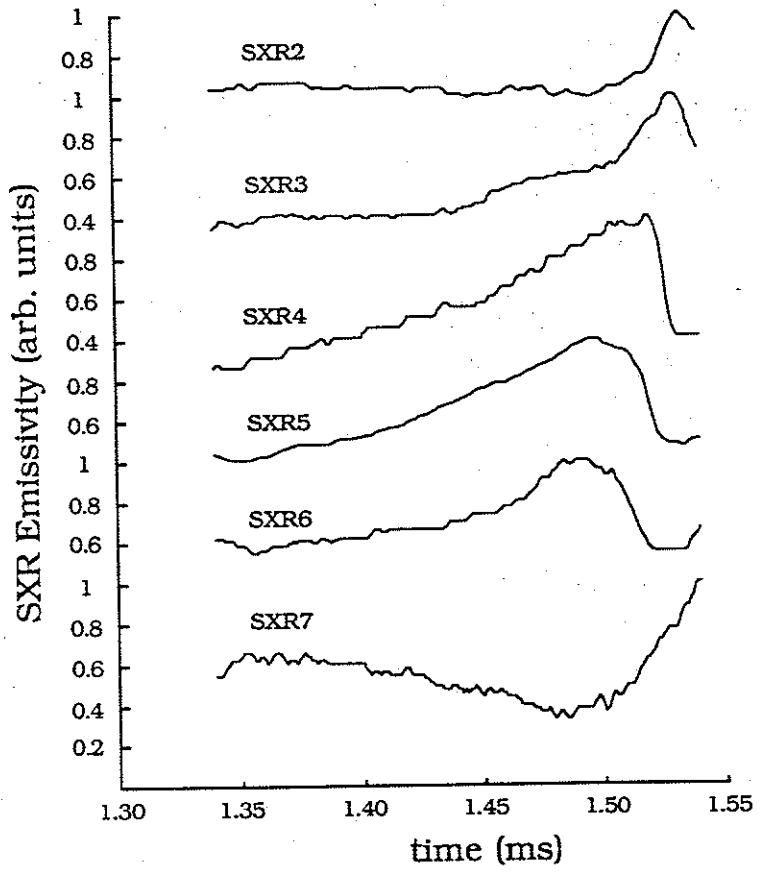

Figure 6.4b: Typical sawtooth on the poloidal array for a material limiter $q_a < 1$ discharge.

Sawteeth with similar characteristics are seen in material limiter $q_a < 1$ discharges (figure 6.4b). The sawtooth period $\tau \approx$ 100-125 μs, and no SXR precursors are seen.

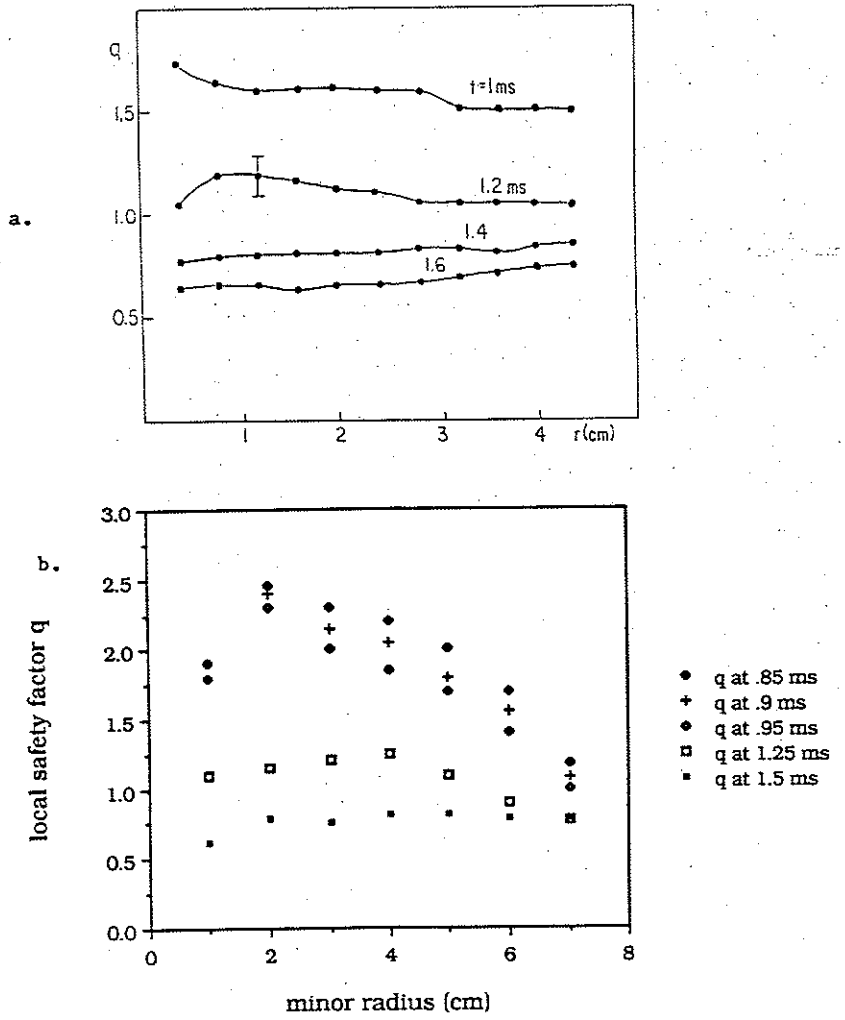

Figure 6.5: Evolution of $q(\psi)$ during startup in (a) $q_a < 1$ magnetic and (b) $q_a < 1$ material limiter discharges. Sawteeth onset between 1.4 and 2.0 ms in the magnetic limiter configuration[1] and between 1.2 and 1.4 ms in the material limiter configuration.

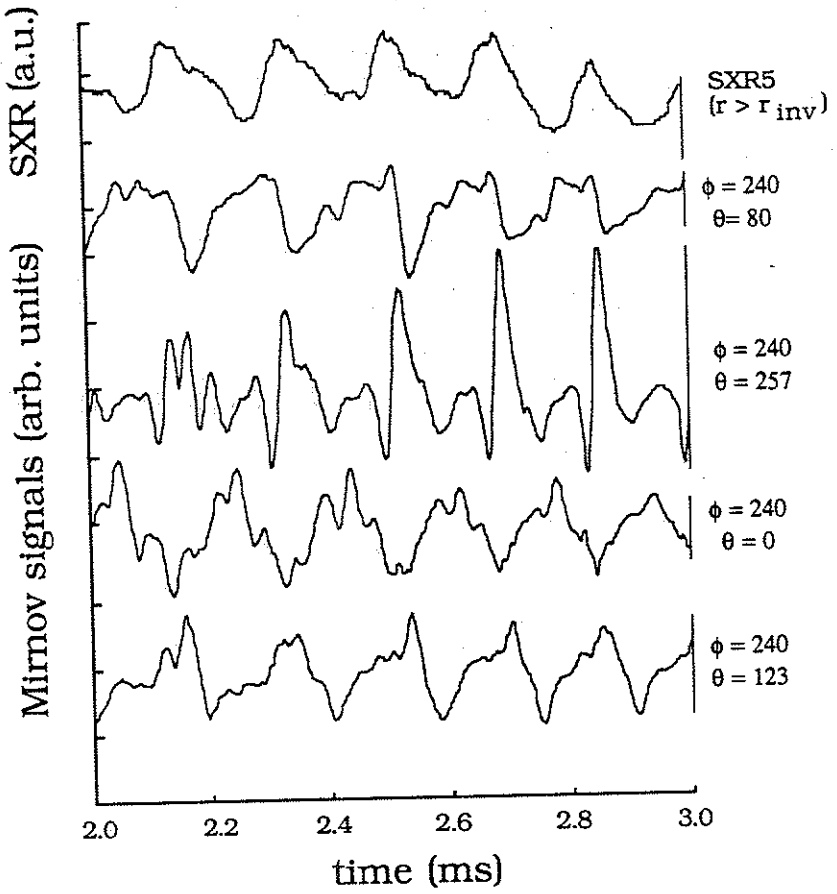

Figure 6.7a: Distorted m = 1 oscillation on Mirnov loops during sawtooth activity in q_a < 0.4 magnetic and material limiter discharges. Signals from poloidally spaced probes selected to show the m = 1 character of the oscillation.

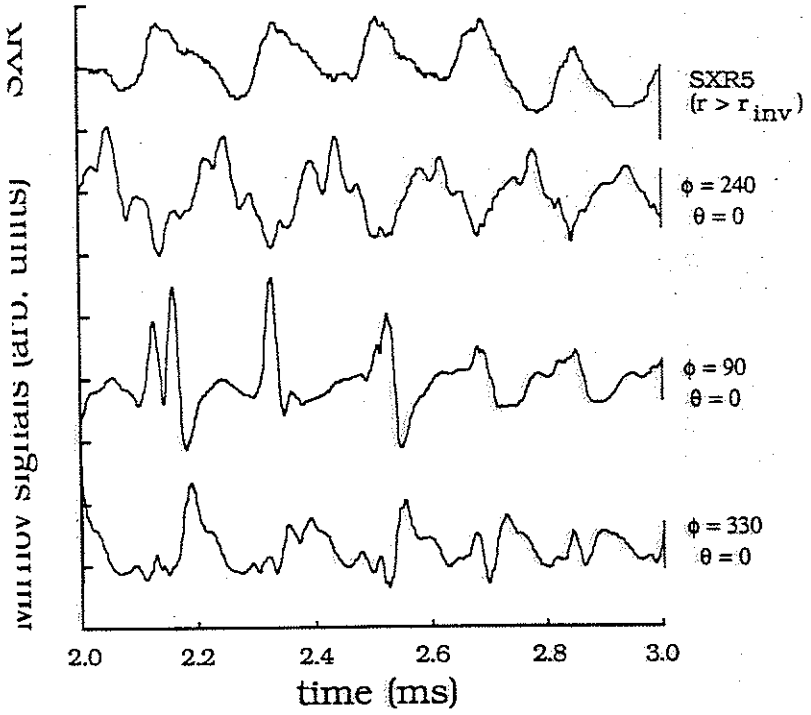

Figure 6.7b: Distorted m = 1 oscillation detected on Mirnov loops during sawtooth activity in q_a < 0.4 magnetic and material limiter discharges. Signals from toroidally spaced probes selected to show the n = 1 character of the oscillation.

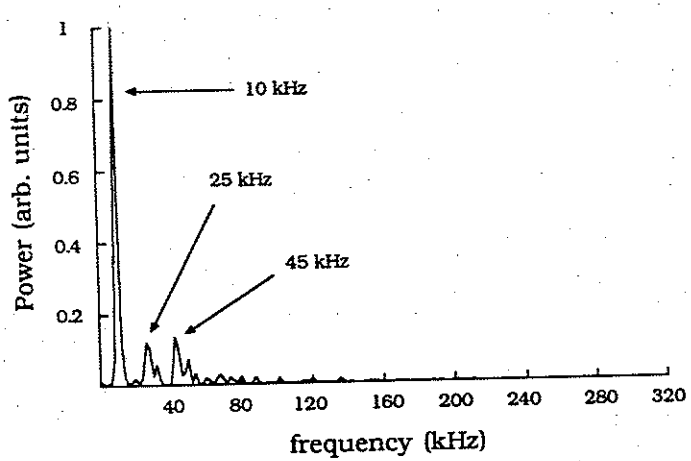

Figure 6.7c: Power spectrum of the distorted m = 1 oscillation during sawtooth activity in q_a < 0.4 magnetic and material limiter discharges, showing a single dominant mode.

No evidence for any low frequency, long wavelength activity resonant on the q = 0.5 surface in q_a < 1 discharges has been seen, up to m = 3. These measurements, together with the broadband internal fluctuation measurements, suggest that the plasma inside the q = 1 surface may be fully turbulent without good flux surfaces. This would be consistent with a sawtooth model proposed recently by Stodiek.[5] These measurements should be extended to include intermediate mode numbers m ≈ 6-10. Also useful would be measurement of the magnetic fluctuation level inside and outside the q = 1 surface during a sawtooth oscillation to clarify the role of turbulence versus reconnection in the sawtooth collapse.

VI.A.2.c. q Profile Evolution:

Flux-surface-averaged safety factor profiles have been measured in q_a < 1 magnetic limiter discharges.[6,7] The profiles are flat across most of the central current channel (figure 4.45). Sawteeth onset after the q = 1 surface enters the plasma (figure 6.5). Unlike "ultra low q" experiments on the REPUTE device,[8] no preferred curvature of the q(ψ) profile is seen when the q = 1 surface enters the plasma.[1]

The reconnection and mixing models of sawteeth described in Section II.C.2.a predict that, if the helical flux is reconnected into the center of the discharge, q(0) should rise close to 1. With an L/R time in these discharges of 2 ms, the current profile could not evolve quickly enough to drop q(0) to 0.6 within one sawtooth period (150 μs). Therefore, the observation of q(0) ≈ 0.6 just before and jsut after a sawtooth collapse confirms that q(0) remains < 1, and the sawtooth must reconnect only partially into the center of the discharge. An explanation of the sawtooth collapse in terms of one of the turbulent models described in Section II.C.2.b may be necessary.

Measurements of the local q profile along the midplane, neglecting flux surface noncircularity, have been made in material limiter discharges. These profiles display essentially the same features as local q profiles in magnetic limiter discharges, as shown in figure 6.8. The profiles are flat and less than one across much of

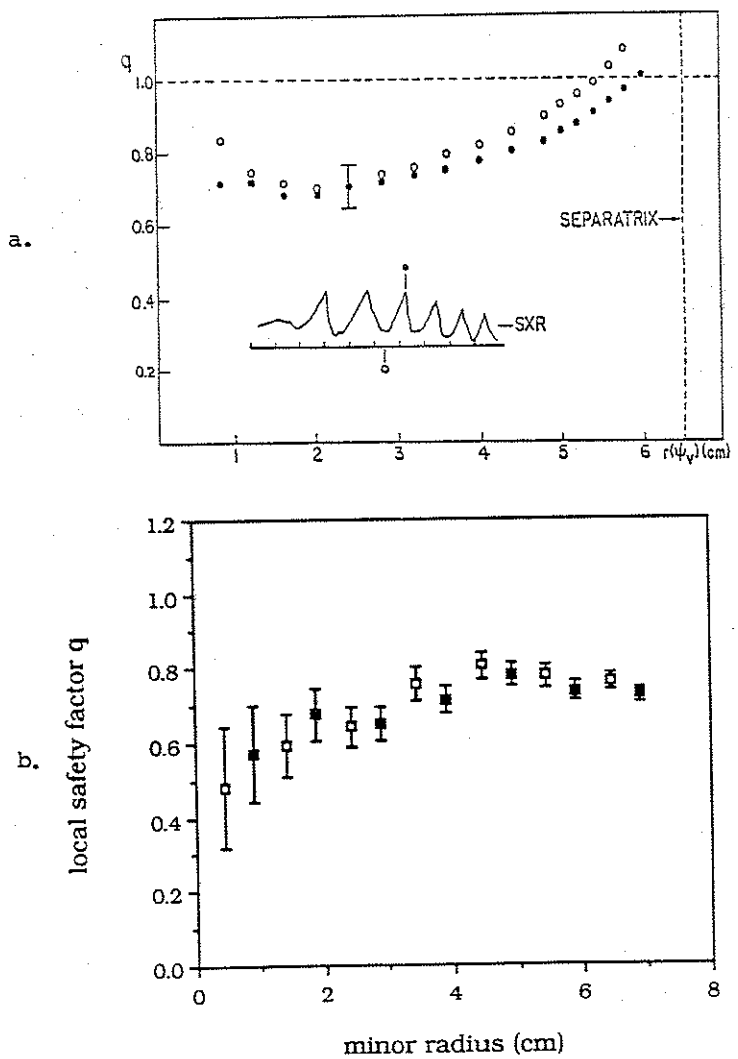

Figure 6.8: q profiles before (solid) and after (open) a sawtooth in (a) magnetic and (b) material limiter $q_a < 1$ discharges. The magnetic limiter profile is the flux surface averaged $q(\psi)$;[1,6] The material limiter profile is the local q along the midplane, neglecting noncircularity.

the central current channel. Near the axis, where noncircularity is small, q(0) remains less than one during the sawtoothing portion of the discharge. Thus, partial reconnection is not unique to the magnetic limiter configuration.

VI.B. Comparison with Resistive MHD Code Computations:

Eijiro Uchimoto has used his 3-D resistive MHD initial value code RPD[9-11] (Section V.B) to simulate the (1,1) resistive kink in the magnetic and material limiter configurations. Key results are excerpted here for comparison with experiment. Results of linear code runs are presented in Section VI.B.1. Only limited nonlinear code runs have been performed to date and the results are presented in Section VI.B.2.

VI.B.1. Linear Results:

A sample pair of magnetic and material limiter equilibria with $q_a \approx 0.8$ used as input to a linear RPD code run is shown in figure 6.9. The q = 1 surface is located at $r \approx .6r_{sep}$. The position of the q = 1 surface and q_a were varied in pairs of equilibria to investigate the effects of the divertor separatrix and central current channel boundary conditions on the linear stability of the resistive kink.

As a rule, the (1,1) resistive kink is less sensitive to variations in profile or edge boundary conditions than the (2,1) resistive tearing mode (Section V.B.1). This may be due in part to the fact that, in the ideal limit, the (1,1) internal kink is never more than

Partial reconnection of the (1,1) resistive kink mode has been seen in at least one computation of a $q_a < 1$ magnetic limiter configuration (figure 6.11). While this result is, to our knowledge, unique, it is not, however, universal. Other nonlinear runs have demonstrated total reconnection. Studies are continuing to find the parameters that determine the extent of reconnection in the simulations.

Nonlinear evolution of the (1,1) resistive kink in divertorless geometry (with similar toroidicity and noncircularity as the divertor geometry) with the RPD code produces total reconnection of the (1,1) magnetic island. The sequence of field line puncture plots shown in figure 6.12 are in excellent agreement with the classic simulation of sawtooth reconnection of Sykes and Wesson[17] (figure 2.19). By contrast, the sequence of field line puncture plots in figure 6.11 for the partial reconnection case repeat at subsequent times if the evolution is continued, with the original magnetic axis never quite disappearing.

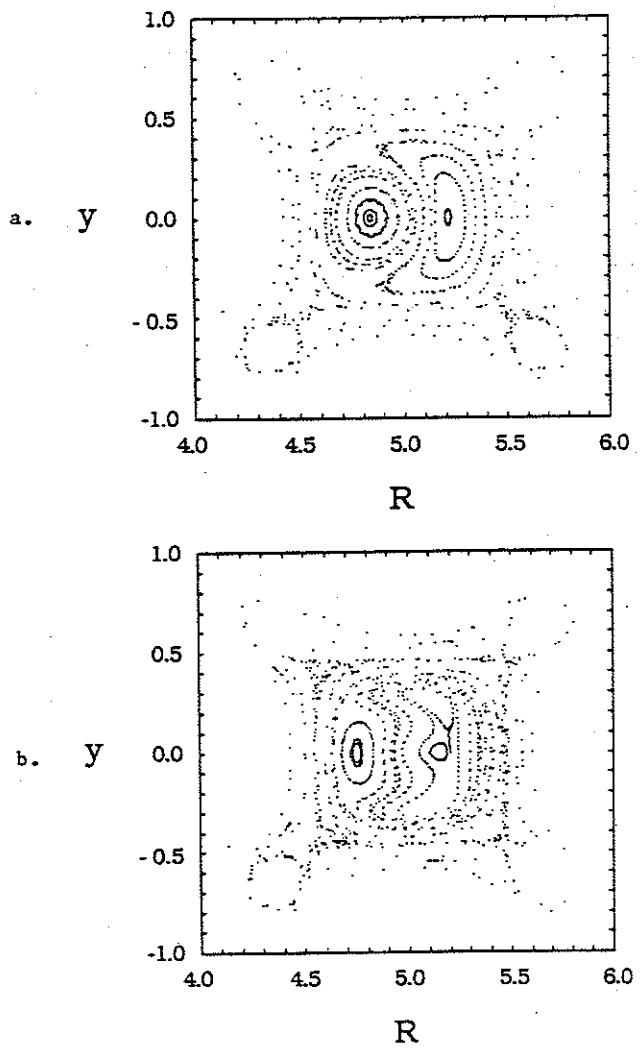

Figure 6.11a and 6.11b: Sequence of magnetic field puncture plots showing partial reconnection of the (1,1) resistive kink in a $q_a < 1$ discharge. The plots are at (a) $100\tau_{Hp}$, and (b) $125\tau_{Hp}$ [(c) and (d) on next page]. The sequence repeats if the calculation is continued.

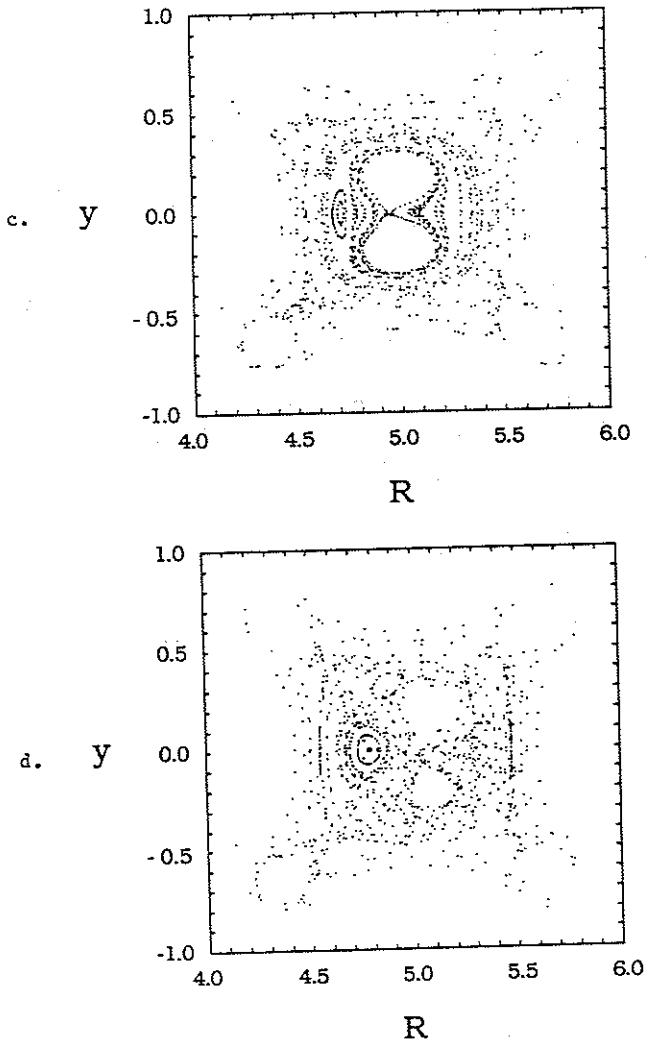

Figure 6.11c and 6.11d: Sequence of magnetic field puncture plots showing partial reconnection of the (1,1) resistive kink in a $q_a < 1$ discharge. The plots are at (c) $175\tau_{Hp}$, and (d) $200\tau_{Hp}$ [(a) and (b) on previous page]. The sequence repeats if the calculation is continued.

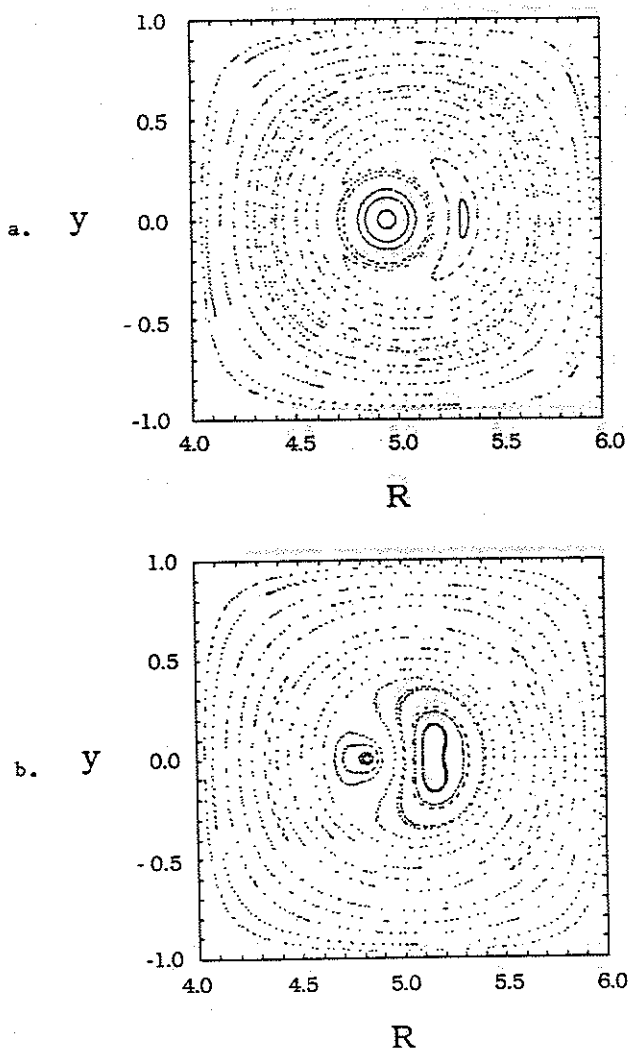

Figure 6.12a and 6.12b: Sequence of magnetic field puncture plots demonstrating total reconnecton of the (1,1) resistive kink in divertorless geometry. The plots are at (a) $200\tau_{Hp}$, (b) $250\tau_{Hp}$, (c) $265\tau_{Hp}$, and (d) $300\tau_{Hp}$ [(c) and (d) on following page].

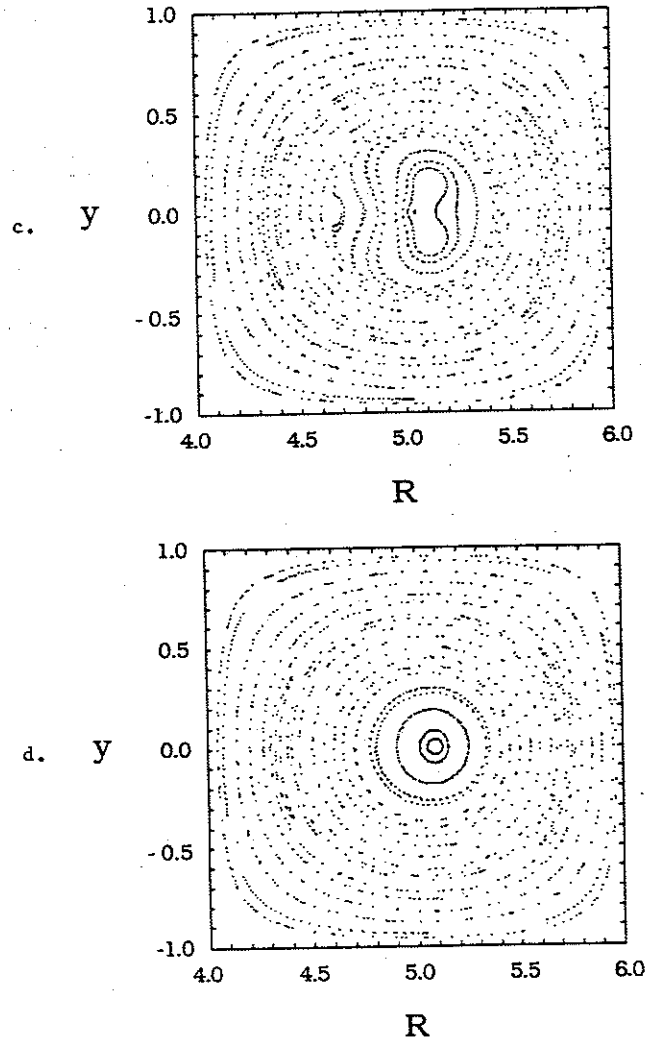

Figure 6.12c and 6.12d: Sequence of magnetic field puncture plots demonstrating total reconnecton of the (1,1) resistive kink in divertorless geometry. The plots are at (a) $200\tau_{Hp}$, (b) $250\tau_{Hp}$, (c) $265\tau_{Hp}$, and (d) $300\tau_{Hp}$ [(a) and (b) on preceding page].

VI.B.2.b. Stochasticity in $q_a < 1$ Discharges:

Investigations of magnetic field stochasticity have been carried out using the RPD code to generate magnetic field input to the TUBE field line tracing code.[11,14,15] Stochasticity develops as the (1,1) island interacts with the divertor region (figure 6.13), but is localized mostly about the island separatrix. The mode continues to grow after stochasticity onsets. The progress of a single field line, launched from the inner island separatrix along the device midplane at the time the island reached the divertor separatrix, is shown in figure 6.14.[18]

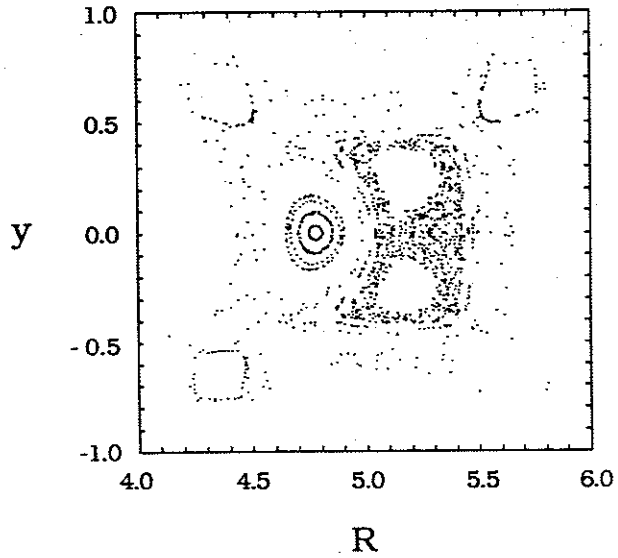

Figure 6.13: Magnetic field puncture plot showing the stochastic field region about the island separatrix.

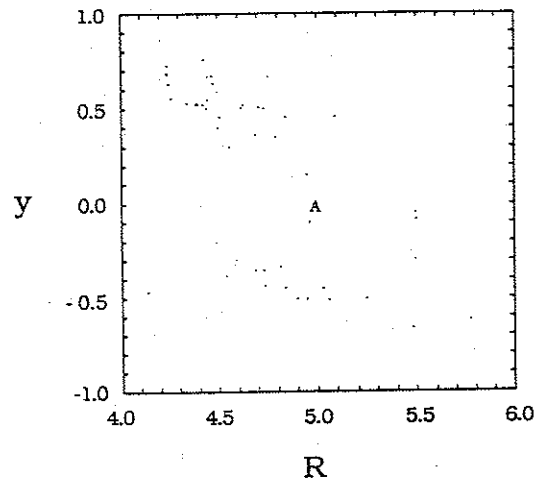

Figure 6.14: Progression of a single magnetic field line, launched from the inner island separatrix along the device midplane ("A" in the puncture plot) at the time the island reached the divertor separatrix.

Complete reconnection has been seen in computations involving large stochastic field regions, implying that partial reconnection arises from some mechanism other than stochasticity Additional nonlinear calculations are being conducted to clarify this issue. Self-consistent profile modifications due to the enhanced transport associated with large stochastic field regions are beyond the scope of the RPD code, and their impact has not been evaluated. These effects might alter the current profile sufficiently to saturate the resistive kink before complete reconnection.

VI.C. Summary and Conclusions:

Internal disruptions have been identified in both magnetic and material limiter configurations for discharges with $q_a \leq 2$.

Characteristics of the MHD activity in both magnetic and material limiter configurations are summarized in Table 6.1.

In the magnetic limiter configuration, internal disruptions have a (1,1) SXR precursor and no magnetic precursor for discharges with $1 < q_a < 2$. The sawtooth collapse is axisymmetric, and inverts at the q = 1 surface inferred from equilibrium code fits to the discharge parameters. The period $\tau \approx 200$ μs agrees well with the empirical formula of McGuire and Robinson, equation 2.8

Internal disruptions in the material limiter configuration for discharges with $1 < q_a < 1.5$ are similar to the sawteeth in the magnetic limiter configuration except that the (1,1) SXR precursor is not generally seen. The sawtooth period shortens to $\tau \approx$ 125-150 μs.

For discharges with $q_a < 1$ in both magnetic and material limiter configurations, sawteeth are observed without SXR or magnetic precursor. These sawteeth have a period $\tau \approx$ 100-150 μs (generally longer in magnetic versus material limiter discharges). Measurements of $q(\psi)$ profiles in each configuration confirm that $q(0)$ is much less than 1 (≈ 0.6) and remains stationary over many sawtooth oscillations, inconsistent with complete reconnection of the (1,1) island into the magnetic axis. The measurements of $q(0) \approx$ 0.6-0.8 have been confirmed recently by axis q measurements on TEXTOR[19] and TEXT.[20]

Table 6.1

MHD Characteristics of Internal Disruptions in Tokapole II

$1 < q_a < 2$:		
characteristic:	material limiters	magnetic limiters
amplitude:	50-80% of central SXR	10-40% of central SXR
period	100-150 μs	150-200 μs
inversion radius:	q = 1	q = 1
mode structure:		
SXR:	none	(1,1) mode: 45 kHz
Mirnov:	none	none
$0.5 < q_a < 1$:		
characteristic:	material limiters	magnetic limiters
amplitude:	50-80% of central SXR	30-80% of central SXR
period	100-150 μs	100-150 μs
inversion radius:	q = 1	q = 1
mode structure:		
SXR:	none	none
Mirnov:	none	none
$q_a < 0.5$:		
characteristic:	material limiters	magnetic limiters
amplitude:	5-20% of central SXR	5-20% of central SXR
period	200 μs	200 μs
inversion radius:	q = 1	q = 1
mode structure:		
SXR:	distorted sine wave	distorted sine wave
Mirnov:	(1,1) mode: 5 kHz phase locked to "sawteeth"	(1,1) mode: 5 kHz phase locked to "sawteeth"

Internal and external magnetic fluctuation measurements in the frequency range 10 kHz ≤ f ≤ 2 MHz confirm high levels of magnetic turbulence in these discharges.[3,4] In the frequency range 10 kHz ≤ f ≤ 370 kHz, the magnetic fluctuation level increases toward the center of the discharge. Outside the separatrix (also outside the q = 1 surface), the fluctuation level increases during the sawtooth collapse. These results, and the measurement of partial reconnection, appear consistent with predictions of the turbulent sawtooth models (Section II.C.2.b). In this context, partial reconnection is characteristic of the sawtooth oscillations, and not the result of magnetic limiter operation. Magnetic fluctuation measurements inside and outside the q = 1 surface during sawtooth oscillations could elucidate the sawtooth collapse mechanism.

The ability to obtain $q_a < 1$ discharges in the material limiter configuration with global characteristics and disruptive behavior similar to $q_a < 1$ magnetic limiter discharges demonstrates that the presence of plasma and/or current in the divertor scrape-off region does not enable $q_a < 1$ operation. Insensitivity of the resistive kink stability to details of the profiles and boundary conditions seen in RPD code simulations[11,14,15] are consistent with this result. The numerical study of the effects of toroidicity and noncircularity on the (1,1) mode by Grimm, et al.[12] also demonstrated that toroidicity and noncircularity have little effect on the (1,1) resistive kink and tearing modes.

No preferred shape to the $q(\psi)$ profile has been seen when the

$q = 1$ stability barrier is crossed, contrary to results from the REPUTE device.[8] $q(\psi)$ profiles have been seen that have $dq/dr < 0$, $dq/dr > 0$, and that are flat at the time the $q = 1$ surface enters the plasma. No "overshoot" in the plasma current rise is needed to enter the $q_a < 1$ regime. The corresponding loop voltage and initial current ramp rate are both significantly less than the corresponding values required in the REPUTE device, although each is larger than in typical tokamak devices.

REFERENCES

[1]T.H. Osborne, Ph.D. Thesis, Unversity of Wisconsin (1984).

[2]T.H. Osborne and N.S. Brickhouse, University of Wisconsin—PLP 908.

[3]D.E. Graessle, S.C. Prager, and R.N. Dexter, submitted to Physical Review Letters; University of Wisconsin—PLP 995; PLP 1024; Bulletin of the American Physical Society, 32, 1903 (1987).

[4]M.A. LaPointe, Bulletin of the American Physical Society, 33, 1903 (1987); University of Wisconsin—PLP 1025; private communication.

[5]W. Stodiek, Bulletin of the American Physical Society, 32, 1742 (1987).

[6]T.H. Osborne, R.N. Dexter, and S.C. Prager, Physical Review Letters, 49, 734.

[7]T.H. Osborne, R.N. Dexter, and S.C. Prager, Physics of Fluids, 26, 350 (1983).

[8]Z. Yoshida, et al., NEUT Research Report 85—01.

[9]E. Uchimoto, J.D. Callen, and L. Garcia, Bulletin of the American Physical Society, 30, 1421 (1985).

[10]E. Uchimoto and J.D. Callen, Sherwood Theory Meeting, paper 1D18 (1987).

[11]E. Uchimoto, Ph.D. Thesis, University of Wisconsin (1988).

[12]R.C. Grimm, et al., Plasma Physics and Controlled Fusion Research, (Proc. 9th Int. Conf., Baltimore, 1982), 3, (IAEA, Vienna, 1983),35.

[13]R.A. Moyer, et al., Bulletin of the American Physical Society, 32, 1774 (1987).

[14]Z. Chang, et al., Bulletin of the American Physical Society, 32,

1774 (1987).

[15]E. Uchimoto and J.D. Callen, Proceedings of the 12th Conference on the Numerical Simulation of Plasmas, (San Francisco, CA, September 20—24, 1987), paper PM23.

[16]N.J. O'Neill and A.A. Mirin, NMFECC LIBRIS Library.

[17]A. Sykes and J.A. Wesson, Physical Review Letters, 37, 140 (1976).

[18]Z. Chang, private communication.

[19]G.H. Wolf, et al., Plasma Physics and Controlled Fusion, 28, 1413 (1986).

[20]W.P. West, D.M. Thomas, and J.S. DeGrassie, Physical Review Letters, 26, 2758 (1987).

Chapter 7
CONCLUSIONS AND SUGGESTIONS FOR FUTURE WORK

VII.A. Summary and Conclusions:

Disruptive instabilities have been studied in the magnetic and material limiter configurations over the range of safety factor $0.4 < q_a < 4$. Features of disruptive behavior in the magnetic and material limiter discharges versus q_a are summarized in figure 7.1, which is an extension of the magnetic limiter summary of figure 1.2. Comparison of results for external and internal disruptions in the two configurations has led to several significant results regarding the disruptive stability of the magnetic limiter configuration.

The most dramatic demonstration of an effect of the magnetic limiter configuration on disruptive stability is the fact that most of the discharges in the Tokapole II device lie outside the stable operating space of the Hugill plot for other tokamaks. In the magnetic limiter configuration, the stability barriers at $q_a \approx 2$ and $q_a \approx 1$ are both routinely passed without a close fitting conducting wall, and without employing external windings, fast current ramp rates, or careful profile control as required in other tokamaks.

External disruptions are no longer seen on SXR and Mirnov diagnostics in magnetic limiter discharges with $q_a < 2$. The lack of

external disruptions is the result of stabilization of the (2,1) tearing mode due to the proximity of the q = 2 surface to the divertor separatrix. Numerical computations suggest that this effect likely is due to the decreasing current density gradient near the separatrix. The increasing noncircularity of the flux surfaces near the separatrix may also play a role in stabilizing the (2,1) tearing mode in the broad current profiles of the low q_a discharges.

Key Features of Disruptive Behavior
in Tokapole II Discharges

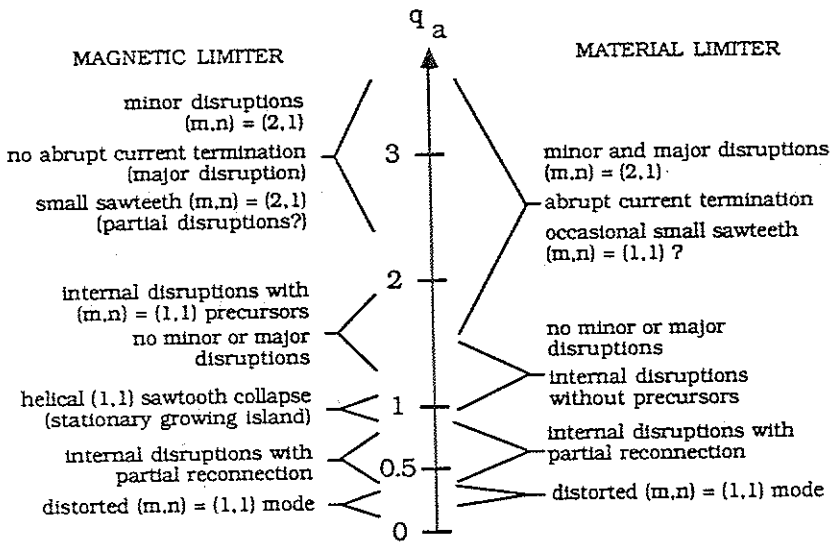

Figure 7.1

An external disruption-free operating regime is obtained in the

material limiter configuration for q_a < 1.5. SXR and Mirnov measurements again confirm the absence of the (2,1) mode. The lower q_a necessary to enter the external disruption-free regime relative to the magnetic limiter configuration is predicted in the RPD code runs. It arises from differences in the current density gradients between the two configurations near the separatrix that result in a lower (2,1) tearing mode growth rate in the magnetic limiter configuration. Because of the enhanced (2,1) mode growth rate in the material limiter configuration, the q = 2 surface must be moved closer to the separatrix to stabilize the mode. In each configuration the linear stabilization of the (2,1) tearing mode arises from a decreasing current density gradient and the increased noncircularity near the separatrix.

The existence of the external disruption-free regime in material limiter as well as magnetic limiter discharges is consistent with the argument that access to this regime results from profile and noncircularity effects, and not because of the presence of plasma (acting as a conducting wall) or current outside the separatrix.

External disruptions have been identified in both magnetic and material limiter configurations with characteristics during the precursor and transport phases similar to external disruptions in other tokamaks. The magnetic limiter configuration suppresses current termination in the final phase of the disruption by

eliminating the plasma interaction with the inboard limiter following the disruption. Material limiter discharges terminate in a radiative collapse resulting from an enhanced impurity level following the disruption.

It has not been possible, even in the material limiter configuration, to trigger hard disruptions with a steep, linear current rampdown rate. The radiative collapse is delayed 100-300 μs after the lose of confinement in the central current channel, as indicated by central chord SXR and O VI signals, and the exponential decay is consistent with the L/R time of a 90 eV plasma. It appears that, even in the material limiter configuration, the final phase of the disruption is softened by the magnetic separatrix geometry. This could result from the small post-disruptive major radius shift due to the large negative decay index of the vertical field provided by the divertor rings. Still, other tokamaks suffer major disruptions without loosing equilibrium due to the post-disruptive shift. The lack of hard major disruptions in the Tokapole II device might be associated with the stabilizing effects of noncircularity or high shear near the separatrix, or with the relatively high resistivity ($S \approx 10^4$). High shear could stabilize the ideal kink mode that, in some models, is the final stage of a major disruption. High resistivity could suppress the formation of a narrow neutral current sheet at the island X-points that drives the nonlinear destabilization of higher order tearing modes. This

nonlinear destabilization leads to destruction of the flux surfaces due to island overlap.

In both magnetic and material limiter configurations, partial reconnection of sawtooth oscillations permits discharges with $q(\psi) < 1$ to be obtained. This partial reconnection is confirmed experimentally by measuring the evolution of the safety factor profile. Originally, it was believed that the magnetic limiter configuration caused the partial reconnection.[1,2,3] Partial reconnection in the material limiter configuration indicates that partial reconnection is characteristic of sawteeth in the Tokapole II device, and not the result of the magnetic limiter configuration. Recent mesurements of $q(0) \approx 0.7$–0.8 in TEXTOR[4] and TEXT[5] are consistent with partial reconnection and support the conclusion that $q(0) < 1$ is characteristic of sawtooth oscillations, at least in these devices.

VII.B. Suggestions for Future Work:

The plasma physics research group at the University of Wisconsin has acquired a large amount of experience in the study of disruptions and magnetic fluctuations on the Tokapole II device. This leaves the group remarkably well placed to perform an extremely important and difficult measurement that could clarify the issue of turbulence versus reconnection in internal disruptions.

Time resolved measurements of the q profile, and of magnetic

fluctuation levels inside and outside the q = 1 surface, throughout a complete sawtooth cycle would provide valuable information concerning the extent of turbulence during each phase of the sawtooth oscillation. If these measurements are coupled with simultaneous Mirnov measurements to ascertain the influence of long wavelength MHD modes (e.g. (1,1), (2,1) and (3,2)), a complete picture of the sawtooth oscillation could be developed.

These measurements would be most valuable if performed in discharges with $q_a > 1$. Previously, it has not been possible to insert magnetic probes into the center of such discharges, as required to make these measurements. The development of "micro-probes" might minimize the perturbation sufficiently to obtain "normal" sawteeth. The use of multiple coil probes with sets of transverse and axial coils spaced across the minor radius to the separatrix would permit the data to be acquired in a single shot, eliminating the difficulties due to the lack of adequate reproducibility generally associated with placing a probe into the plasma core.

An additional issue is the plasma performance in $q_a < 1$ discharges. Available ohmic input powers have been limited by the mechanical strength of the original divertor rings and supports. An upgrade of the Tokapole II device has recently been completed that enables the plasma current in $q_a < 1$ discharges to be doubled while holding q_a constant with an improved toroidal field capability. This may permit investigation of hotter, longer $q_a < 1$ discharges of

lowered resistivity and improved performance. Such discharges could be utilized to address the issue of confinement at such low q values.

A typical feature of MHD modes in the Tokapole II device is the absence of SXR and/or Mirnov precursors. This may be due to the lack of plasma rotation over much of the operating space in both configurations. It would be very useful to search for locked modes with SXR imaging and saddle coils to determine if such modes affect the stability of the discharges. Locked modes have been observed recently on several other tokamaks, where they generally lead to poor plasma performance.

REFERENCES

[1]T.H. Osborne, Ph.D. Thesis, Unversity of Wisconsin (1984).

[2]T.H. Osborne, R.N. Dexter, and S.C. Prager, Physical Review Letters, 49, 734.

[3]T.H. Osborne, R.N. Dexter, and S.C. Prager, Physics of Fluids, 26, 350 (1983).

[4]G.H. Wolf, et al., Plasma Physics and Controlled Fusion, 28, 1413 (1986).

[5]W.P. West, D.M. Thomas, and J.S. DeGrassie, Physical Review Letters, 26, 2758 (1987).

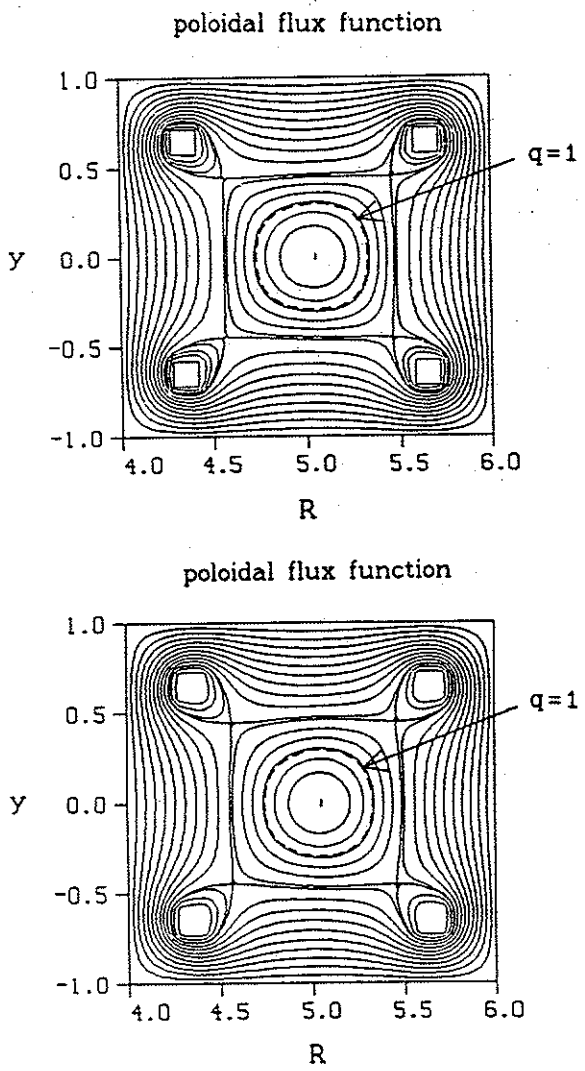

Figure 6.9a: Equilibrium poloidal flux contours for a pair of matched (top) magnetic and (bottom) material limiter $q_a < 1$ equilibria used as input to linear RPD code runs.

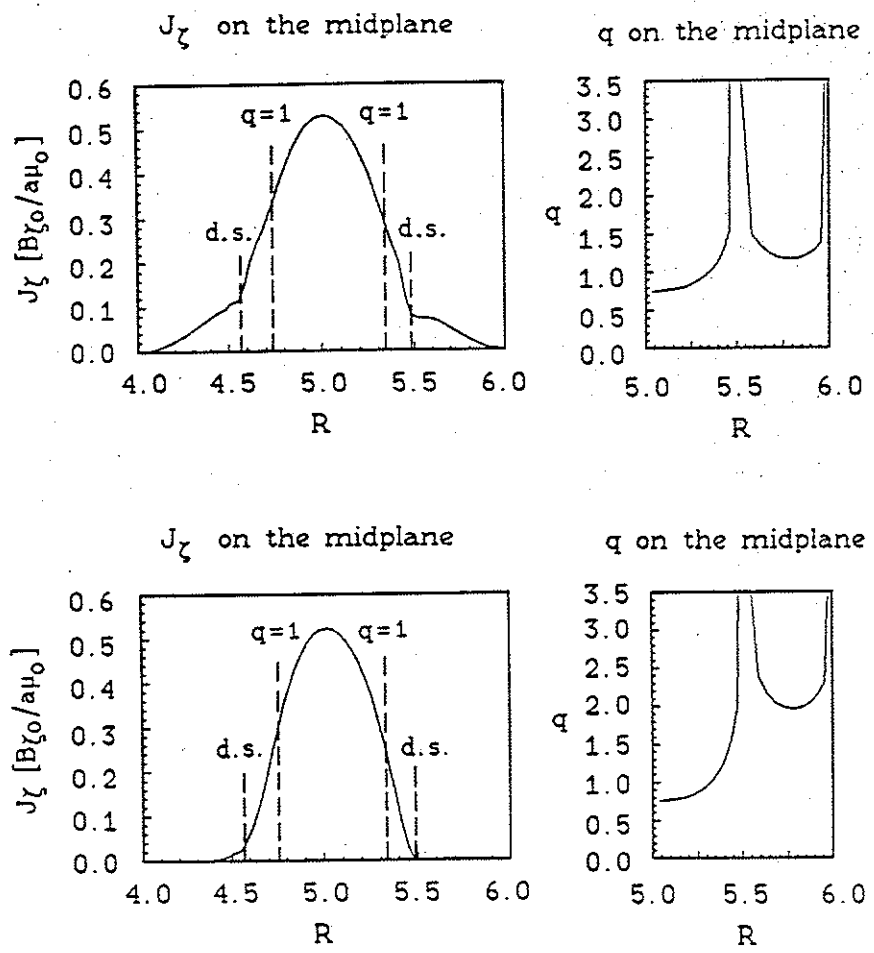

Figure 6.9b: Toroidal current density profile J_ζ and q(R) profiles on the midplane for a pair of matched (top) magnetic and (bottom) material limiter $q_a < 1$ equilibria used as input to linear RPD code runs.

marginally stable for any profile, contrary to the ideal limit of the

tearing mode which may be absolutely stable for appropriate current profiles. The structure of the (1,1) mode eigenfunction, which is localized inside the q = 1 surface, also suggests that this mode may be less sensitive to edge boundary conditions outside the q = 1 surface.

The linear growth of the (1,1) resistive kink stops increasing as the q = 1 surface is brought closer to the divertor separatrix in the magnetic limiter configuration (figure 6.10). While the linear growth rate $\gamma_{1,1}$ is less than that in the material limiter configuration, it does not drop to 0. The magnetic limiter configuration is therefore stabilizing to the (1,1) resistive kink, but the mode does not become linearly stable as was observed for the (2,1) tearing mode.

This insensitivity of the (1,1) resistive kink to the proximity of the q = 1 surface to the separatrix is qualitatively consistent with experimental results, where the (1,1) mode manifests itself as sawteeth in each configuration regardless of the value of q_a between $0.5 \leq q_a \leq 1$. Grimm, et al. have shown that toroidicity and noncircularity also have little effect on the (1,1) mode stability.[12] Simulating partial reconnection would, of course, require nonlinear calculations. A limited number of nonlinear runs have been performed and the results are discussed in the next section.

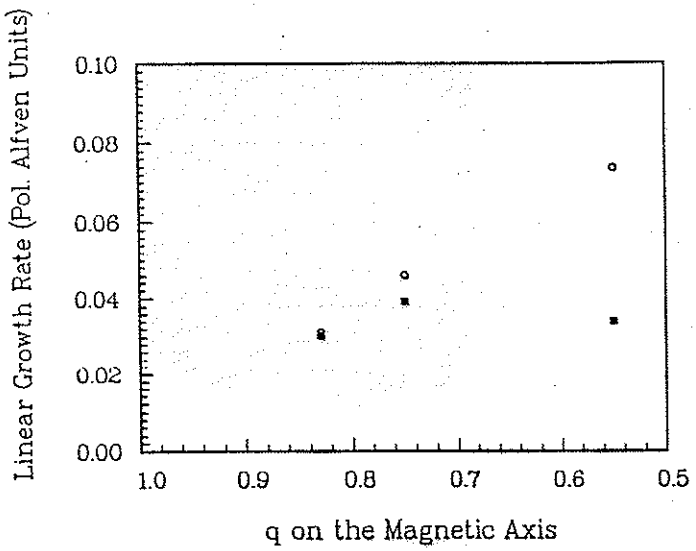

Figure 6.10: Linear growth rate $\gamma_{(1,1)}$ of the (1,1) resistive kink, normalized to the poloidal Alfvén time τ_{Hp}, versus q(0) (equivalently, nearness of the q = 1 surface to the separatrix.) Results are plotted for magnetic (solid squares) and material (open circles) limiter configurations.

VI.B.2. Nonlinear Results:

Nonlinear (1,1) resistive kink behavior has also been evaluated by Uchimoto using the RPD code.[11,13-15] Stochastic effects due to magnetic island interaction with the divertor separatrix and higher order satellite islands have been investigated using the magnetic field line tracing code TUBE[16] and RPD code output.[11,14]

VI.B.2.a. Nonlinear Evolution: